Chapter 9

Multi-wavelength Properties of TeV Blazars

In previous sections, we have investigated the rapid variability and spectral evolution of TeV blazars, highlighting the X-ray observations by *ASCA* and *RXTE* . However, the overall spectral energy distribution of blazars generally ranges over a very wide range from radio to TeV γ-ray bands and such spectra are one of the most important features allowing us to understand these sources. To reveal the multi-frequency properties of TeV blazars, we have to carry out multi-frequency monitoring campaigns of the source in various states of activity.

Results from previous campaigns strongly suggest correlated variations in X-ray and TeV γ-ray fluxes, while variability is much less pronounced in other energy bands (e.g., Macomb et al. 1995; Buckley et al. 1996). However, a problem remains that most of the data are taken either *non*-simultaneously (but contemporaneous within a week; e.g., Macomb et al. 1995) or are very sparsely sampled (e.g., Buckley et al. 1996).

From the X-ray studies of rapid variability, we now know that the characteristic variability time scale of TeV blazars are very short, ranging from 0.3 day to $\sim$ 1 day (§ 8.2.3). TeV flux variations are sometimes faster rapid variability as short as an hour had been reported (Gaidos et al. 1996). Thus the discussion based on those *quasi*-simultaneous data may be incomplete. We need *exactly* simultaneous monitoring, especially in the X-ray and TeV energy bands, to correctly understand the sources. In the following, we summarize the results from *truly* simultaneous campaigns of TeV blazars conducted from 1996 to 1998. Observations logs are given in § 6.4.

9.1 Mrk 421

X-ray/TeV γ-ray correlation

Figure 9.1 shows the long term variability of Mrk 421 in X-ray and TeV γ-ray energy bands. Two remarkable flares were observed in TeV energy band in 1996 May, where flux reached up to ~ 10 Crab and rapidly decreased to the quiescent level on time scale as short as an hour (Gaidos et al. 1996; indicated by an arrow in Figure 9.1). Importantly, *RXTE* observations also revealed that Mrk 421 was very bright and extremely active during 1996 May observations (e.g., § 8.1).

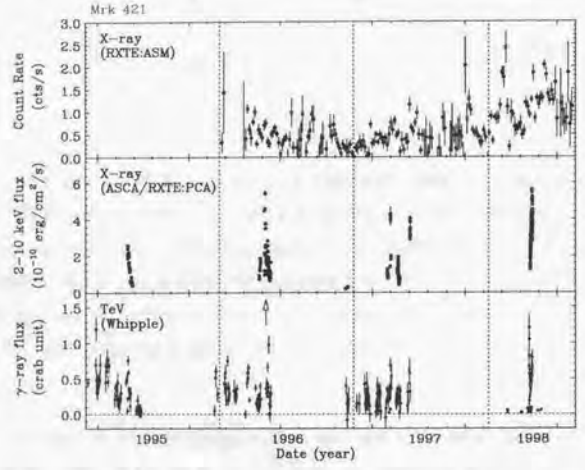

Figure 9.1: X-ray and TeV γ-ray flux variation from 1995 to 1998. *top* and *middle* : X-ray flux (2–10 keV; this work), *bottom* : TeV γ-ray flux above 350 GeV (roughly estimated from McEnery et al. 1997 and private communication with M.Catanese). TeV γ-ray flux are given in unit of Crab flux. TeV data from May 7, 1996 (6.2 Crab) is suppressed and represented here by an arrow.

During 1998 April observation, *ASCA* recorded a higher flux than that observed in 1996 May – to our knowledge, this is the record high flux ever observed for this source in the X-ray band. The campaign started from a pronounced high amplitude flare recorded by *BeppoSAX* and *Whipple* (Maraschi et al. 1999b), and high activity of the source continues during the whole campaign both in X-ray and TeV γ-ray.

Simultaneous observations by TeV telescopes revealed that the TeV flux was also in a high state, although extremely rapid variability as short as an hour was not observed

during this campaign. Such a correlation is more clearly seen in multiband light curves taken at April 1998 (Figure 9.2). This figure combines the results from TeV telescopes (*Whipple* , *HEGRA* and *CAT*), X-ray observations (*ASCA* , *BeppoSAX* and *RXTE*) and *EUVE*. Light curves are normalized by their average values. It should be noted that the rapid flares observed in the X-ray energy band were also detected at TeV energies (e.g., flares at MJD 50924.5 and 50928.0). During this campaign, the X-ray flux was gradually increasing on a time scale of ~ 10 days, which is the same trend as that observed in TeV flux variation.

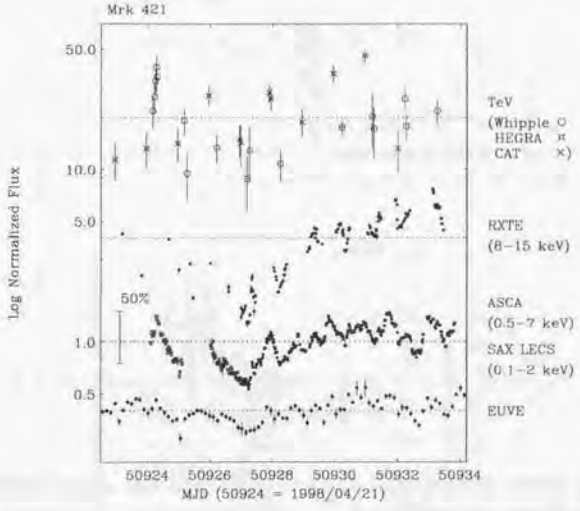

Figure 9.2: Multiband flux variations of Mrk 421 during 1998 campaign. TeV data: *Whipple* , *HEGRA* , and *CAT*. X-ray data: ASCA, *RXTE* , and *BeppoSAX*. UV data : *EUVE*. All light curves are normalized by their average values. Figure adopted from Takahashi et al (1999; in preparation).

In Figure 9.3, we plot the keV X-ray flux (2–10 keV) versus TeV γ-ray flux (in Crab units) obtained from observations in 1997 and 1998. In the plot, each point is calculated from the period when both *ASCA* and *Whipple* observed the source simultaneously. A clear correlation was found for the first time, where [TeV γ-ray flux] $\propto$ [X-ray flux]$^{0.92\pm0.12}$. We also plot in Figure 9.4 the flux correlation between UV and TeV data. Since the UV flux variation is small compared to the X-ray variation, correlation slope is steeper, where [TeV γ-ray flux] $\propto$ [UV flux]$^{2.71\pm0.67}$.

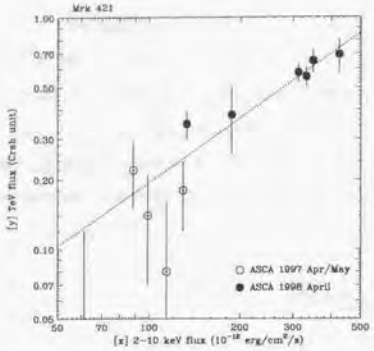

Figure 9.3: Correlation between X-ray flux (2−10 keV) and TeV γ-ray flux (> 350 GeV). X-ray flux measurements come from *ASCA* data, while TeV fluxes are *Whipple* data. TeV fluxes are given in unit of Crab flux. Dashed line shows the best-fit line of [TeV flux] $\propto$ [keV flux]$^{0.92}$.

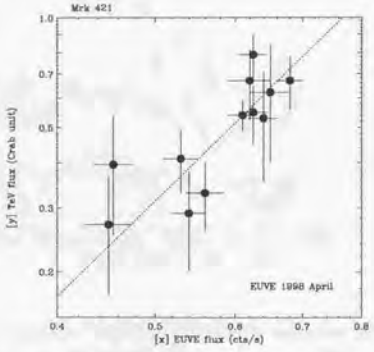

Figure 9.4: Correlation between *EUVE* count rate and TeV γ-ray flux (> 350 GeV). TeV fluxes are given in unit of Crab flux. Dashed line shows the best-fit line of [TeV flux] $\propto$ [keV flux]$^{2.7}$.

Evolution of Multi-frequency Spectrum

Evolution of multi-frequency spectrum of Mrk 421 is given in Figure 9.5. Open circles come from Macomb et al (1995), while other symbols (#1−4) represent our new results taken exactly simultaneously in X-ray (also *EUVE*) and TeV γ-ray bands.

Several important features are seen in the figure. First, the slope of X-ray photon

spectra ($\Gamma_{\rm X-ray} \sim 3$; see § 7.3) are steep, and very similar to those in the TeV energy band ($\Gamma_{\rm TeV} \sim 3$; Aharonian et al.1999b). Second, the amplitude of TeV flux variation is less or almost comparable with that in the X-ray energy bands (see also Figure 9.3). Third, although X-ray flux changed dramatically in various seasons, only small changes are implied in the synchrotron peak position, as we have quantitatively discussed in § 7.3.3.

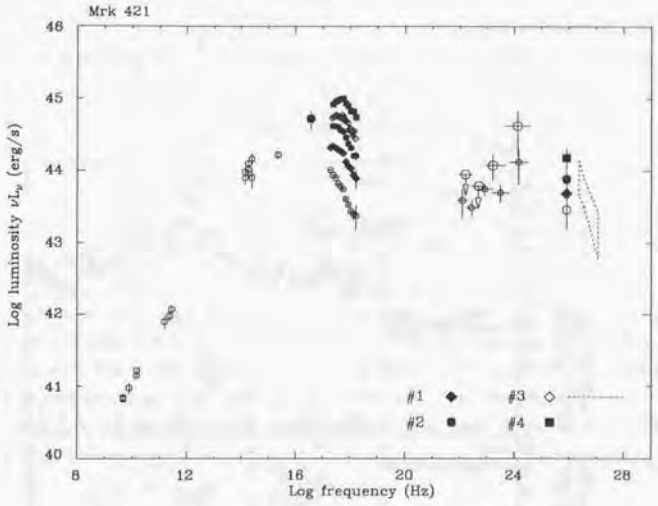

Figure 9.5: Multi-frequency spectra of Mrk 421 in various source activities. Truly simultaneous data for *EUVE*, X-ray and TeV γ-ray bands were plotted with non-simultaneous archival data. #1 : data from MJD 50571.15 to MJD 50571.20 (May 3, 1997; this work), #2 : data from MJD 50927.13 to MJD 50927.29 (Apr 24, 1998; this work). #3 : data from MJD 50927.84 to MJD 50927.90 (Apr 24, 1998; this work), #4 : data from MJD 50933.22 to MJD 50933.27 (Apr 30, 1998; this work). Open circles are published data from Macomb et al (1995). For #1−4, TeV data are provided by *Whipple* Chereukov observatory (private communication with M.Catanese), while TeV data (*HEGRA*) for #4 come from Aharonian et al (1999b).

9.2 Mrk 501

X-ray/TeV γ-ray correlation

Figure 9.6 shows a long term variability of Mrk 501 comparing the X-ray and TeV γ-ray energy bands. One finds that the source was in a historically high state during the 1997 pointings. This clearly suggests that the flux variation in both X-ray and TeV γ-ray energy bands is well correlated on time scales of months to years. During the flare in 1997 April/May, flux reached ~ 4 Crab in the TeV energy bands (Catanese et al. 1997), which was the factor 40 increase of flux compared to that reported in the quiescent state (Quinn et al. 1995; 1999).

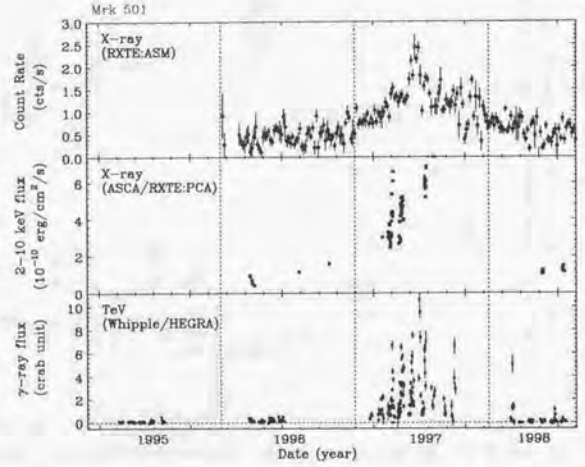

Figure 9.6: X-ray and TeV γ-ray flux variation from 1995 to 1998. *top* and *middle* : X-ray flux (2–10 keV; this work), *bottom* : TeV γ-ray flux above 350 GeV (Quinn et al .1999) and Aharonian et al (1999a; above 1 TeV). TeV γ-ray flux are given in unit of Crab flux.

The light curves during the first multi-wavelength campaign conducted in 1996, which included γ-ray detectors, are shown in Figure 9.7. These observations have two important results. Firstly, EGRET detected GeV γ-ray emission for the first time at 3.5 σ level, which was also confirmed by the follow up observations in 1996 April/May (Table 9.1; Kataoka et al. 1999). Secondly, since the observations were conducted when the source was relatively low emission state, this establish the 'baseline' spectral energy distribution of Mrk 501 compared to the high state emission in 1997.

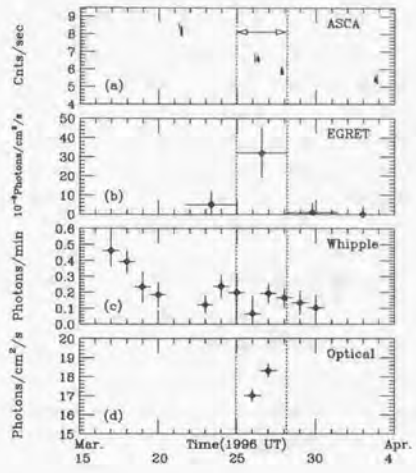

Figure 9.7: Time history of Mrk 501 during the March 1996 campaign. (a): X-ray (*ASCA*: 0.7 – 10 keV), (b): GeV (*EGRET*: 100 MeV – 10 GeV), (c): TeV (*Whipple*: above 350 GeV) and (d): Optical (R – band: 650 nm). The *ASCA* count rates are from the summed SIS0 and SIS1 data, extracted from a circular region centered on the target with a radius of 3 arcmin. The time interval marked with arrows is when EGRET detected Mrk 501 at 3.5 σ significance for the first time. All errors are 1 σ. Figure from Kataoka et al (1999).

Multi-wavelength observations of Mrk 501 during the high state in 1997 demonstrated a clear correlation of fluxes in the X-ray band and TeV γ-ray bands (Catanese et al. 1997). Large amplitude flux change as well as spectral evolution were reported in the X-ray energy band by *BeppoSAX* observations (Pian et al. 1998). Based on three ToO observations conducted in Apr 7, 11 and 16 with *BeppoSAX* , they presented that (1) 2–10 keV flux increased to more than 5×10^{-10} (erg/cm^2/s) and (2) synchrotron peak shifted to higher energies $\sim$ 100 keV, both of which are consistent with our results (§ 8.3.3).

ASCA and *RXTE* observations reported in this thesis were based on much larger samples, which were taken at various phases of source activity. Figure 9.8 shows the flux variations of X-ray and TeV γ-ray bands taken at April/May 1997, when the source was in a very high state. One finds a clear correlation in both energy bands on a time scale of a day, as well as on longer time scales.

X-ray and TeV γ-ray fluxes are plotted in Figure 9.9, based on *truly* simultaneous

Table 9.1: EGRET results for Mrk 501

EGRET VP [a]	Interval	Aspect [b]	Exposure [c]	Significance (σ)	Flux [d]
9.5	12-Sep-1991 — 19-Sep-1991	3.3°	2.28	0.5	< 11
201.0	17-Nov-1992 — 24-Nov-1992	2.5°	1.12	1.7	9±6
202.0	24-Nov-1992 — 01-Dec-1992	5.8°	1.06	1.1	8±7
516.5	21-Mar-1996 — 03-Apr-1996	3.1°	1.47	2.1	10±5
	(25-Mar-1996 — 28-Mar-1996)		0.46	3.5	32±13
519.0	23-Apr-1996 — 07-May-1996	1.2°	2.10	4.0	18±5
	(E>500 MeV)		2.97	5.2	[e]6±2
617.8	04-Apr-1997 — 15-Apr-1997	3.0°	0.82	1.5	9±7

a: EGRET Viewing Period

b: Angle between the source and the EGRET instrument

c: Exposure in unit of 10^8 cm^2 s

d: Flux (E>100 MeV) in units of 10^{-8} cm^{-2}s^{-1}

e: Flux (E>500 MeV) in units of 10^{-8} cm^{-2}s^{-1}

[e]The error is 1 σ.

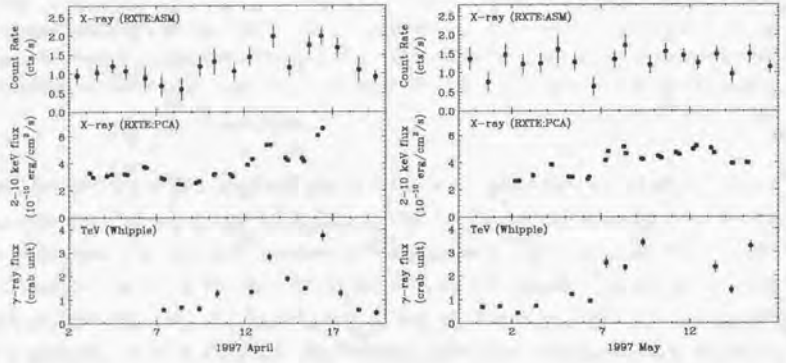

Figure 9.8: X-ray and TeV γ-ray flux variation in 1997. *left* : April 1997, *right* : May 1997. *top* and *middle* : X-ray flux (2−10 keV; this work), *bottom* : TeV γ-ray flux above 350 GeV (Quinn et al .1999). TeV γ-ray fluxes are given in unit of Crab flux.

data. One finds a clear correlation, but different from that found in Mrk 421. For Mrk 501, we obtained a quadratic relation, where [TeV γ-ray flux] $\propto$ [X-ray flux]$^{1.96\pm0.07}$.

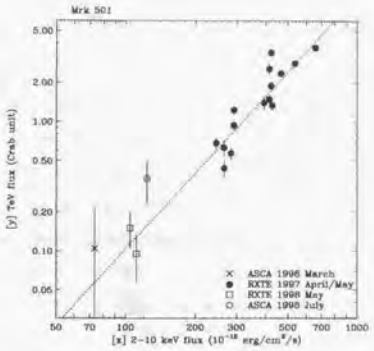

Figure 9.9: Correlation between X-ray flux (2−10 keV) and TeV γ-ray flux (> 350 GeV). X-ray fluxes come from *ASCA* and *RXTE* data, while TeV fluxes are *Whipple* data. TeV fluxes are given in unit of Crab flux. Dashed line shows the best-fit line of [TeV flux] $\propto$ [keV flux]$^{1.96}$.

Evolution of Multi-frequency Spectrum

Evolution of the multi-frequency spectrum of Mrk 501 is shown in Figure 9.10. Open circles are data from public archive (taken from Kataoka et al. 1999), while other symbols represent our new results derived from simultaneous monitoring in the X-ray and TeV γ-ray bands. For the data obtained in March 1996, we also plot the EGRET and optical data.

Compared to the results for Mrk 421, some significant differences are implied in the multiband specta. First, the changes in X-ray flux are accompanied by large shift in the position of the synchrotron peak, as shown in § 7.3.3 and 8.3.3. Second, the slope of X-ray spectra varies widely, ranging from $\Gamma_{\rm X-ray} \sim 1.7$ to 2.5 (see § 7.3, 8.3), while the photon index in the TeV energy band is almost unchanged and steeper: $\Gamma_{\rm TeV} \sim 2.5$ (e.g. Petry et al. 1997; Aharonian et al. 1999a). Third, amplitude of TeV flux variation is much larger than that in the X-ray energy band (see also Figure 9.9).

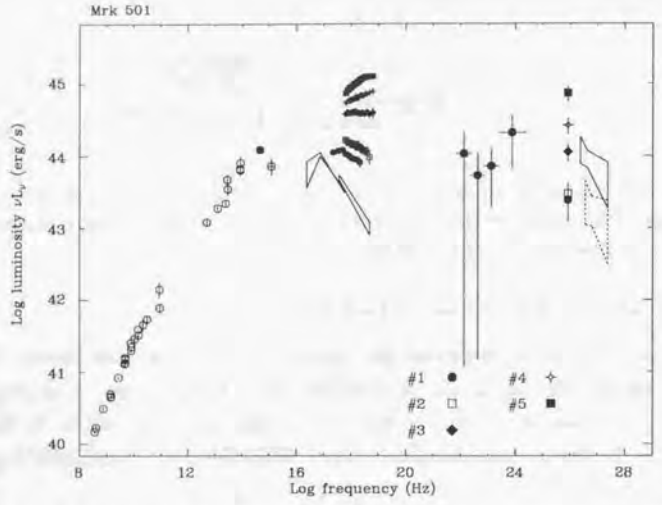

Figure 9.10: Multi-frequency spectra for Mrk 501 in various source activities. Truly simultaneous data in optical, X-ray, GeV γ-ray and TeV γ-ray bands were plotted with non-simultaneous archival data. #1 : data from MJD 50166.96 to MJD 50170.17 (Mar 25-28, 1996; Kataoka et al. 1999a), #2 : data from MJD 50960.29 to MJD 50960.39 (May 27, 1998; this work), #3 : data from MJD 50545.36 to MJD 50545.46 (Apr 7, 1997; this work), #4 : data from MJD 50550.33 to MJD 50550.43 (Apr 12, 1997; this work), #5 : data from MJD 50554.38 to MJD 50554.48 (Apr 16, 1997; this work). Open circles : NASA/IPAC Extragalactic data base (NED). Solid figure : *ROSAT* (Comastri et al. 1997), *GINGA* (Makino et al. 1991), *HEGRA* (Aharonian et al. 1997). Dashed figure : *HEGRA* (Bradbury et al. 1997).

9.3 PKS 2155−304

Flux Variation

Figure 9.11 shows the long term variability of PKS 2155−304 in X-ray and TeV γ-ray energy bands. The detection of the TeV γ-ray emission was reported only recently by Chadwick et al (1999). When the highest TeV emission was detected in 1997 November, *RXTE* observation also recorded the highest X-ray flux ever observed (§ 8.3). At the same epoch, the EGRET observed the source and found that GeV γ-ray flux increased by factor 3 compared to that in the 1996 observation (Sreekumar & Vestrand 1997). This probably implies the correlation of emission in various energy bands, but needs further study.

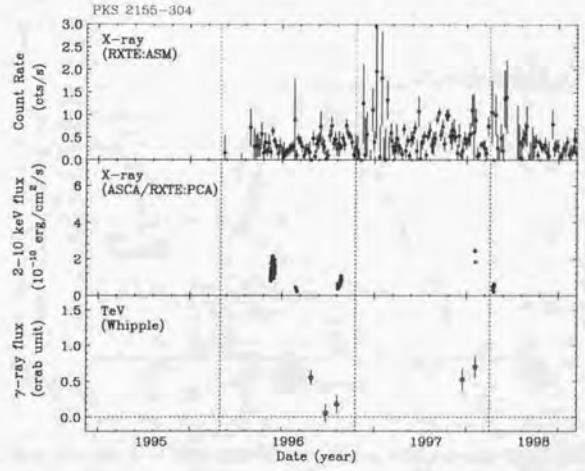

Figure 9.11: X-ray and TeV γ-ray flux variation from 1995 to 1998. *top* and *middle* : X-ray flux (2−10 keV; this work), *bottom* : TeV γ-ray flux above 300 GeV (roughly estimated from Chadwick et al. 1999). Note that the TeV γ-ray emission was detected only recently. TeV γ-ray flux are given in unit of Crab flux.

Evolution of Multi-frequency Spectrum

Evolution of multi-frequency spectra of PKS 2155−304 is given in Figure 9.12. Open circles are data from archive. In this figure, TeV flux is given as an averaged flux from all

observations, including 1997 November (Chadwick et al. 1999). We also plot the EGRET spectrum estimated from the flux in Sreekumar & Vestrand (1997), assuming a spectral form reported in Vestrand et al (1995).

In contrast to the sparse sampling of γ-ray observations, lower energy band data are even better sampled than other TeV blazars. Filled circles are simultaneous data from optical to X-ray obtained in 1994 May campaign (Urry et al. 1997; Kataoka et al. 2000). Compared to Mrk 421 and Mrk 501, X-ray flux variation seems to be rather *chaotic*; when the source was in the brightest state (1997 November; #2), the spectrum was very steep, suggesting that synchrotron peak exists at much lower energies than X-ray energy band. However, for 1994 May data when the source was rather fainter, synchrotron peak existed at ~ 1 keV (§§ 7.3.3, 8.3.3).

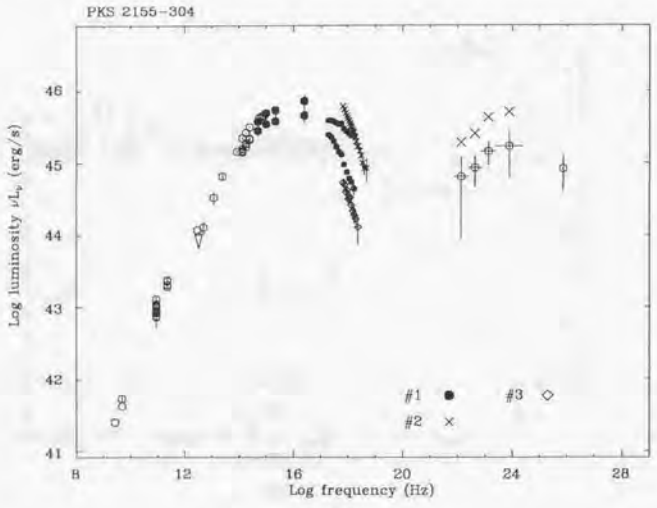

Figure 9.12: Multi-frequency spectra for PKS 2155−304 in various states of source activity. Truly simultaneous data in *IUE*, *EUVE*, X-ray bands were plotted with non-simultaneous archival data. #1 : data from MJD 49491.23 to MJD 49493.33 (Mar 19-21, 1994; Urry et al. 1997; Kataoka et al. 2000). #2 : data from MJD 50772.96 to MJD 50772.97 (Nov 20, 1997; this work), #3 : data from MJD 50291.66 to MJD 50291.68 (July 27, 1996; this work). Open circles : NED data base. Lower EGRET data are from Vestrand, Stacy & Sreekumar (1995), while upper EGRET data are estimated from Sreekumar & Vestrand (1997). TeV γ-ray data come from Chadwick et al. (1999). #2 is when the source was the brightest, while #3 is when the source was the faintest in the X-ray energy band.

9.4 1ES 2344+514

Flux Variation

Figure 9.13 shows the long term variability of 1ES 2344+514 in X-ray and TeV γ-ray energy bands. Only a very few observations had been conducted before the detection of TeV γ-rays as the third TeV blazar (Catanese et al. 1998). Unfortunately, no X-ray observations had been conducted when the *Whipple* telescope detected TeV γ-rays (1995 December 20); no *RXTE* ASM data are available on this source before 1997. More data are required to test a correlated variability in various energy bands.

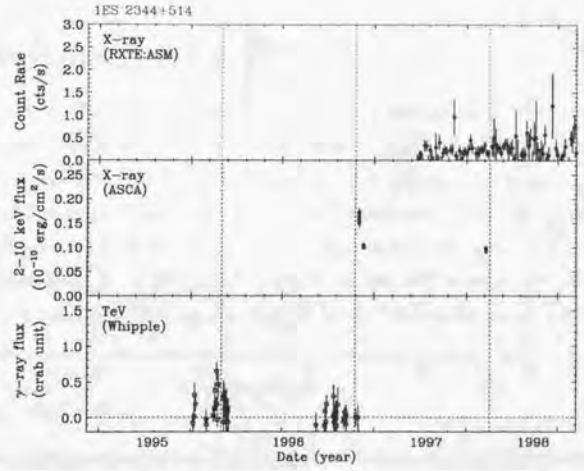

Figure 9.13: X-ray and TeV γ-ray flux variation from 1995 to 1998. *top* and *middle* : X-ray flux (2−10 keV; this work), *bottom* : TeV γ-ray flux above 350 GeV, from Catanese et al. 1998. Note that, TeV γ-rays were not detected above 2 σ level for 1996/97 observational seasons.

Evolution of Multi-frequency Spectrum

Evolution of multi-frequency spectrum of 1ES 2344+514 is given in Figure 9.14. Open circles are data from the public archive. Three TeV points are from Dec. 20 1995 (highest flux), averaged flux from 1995 to 1996, and upper limit from 1996 and 1997 observations. No EGRET detection has been reported for this source.

1ES 2344+514 is also the faintest TeV blazar in the X-ray energy band. However,

spectral evolution correlated with a flux change, similar to that for Mrk 501, is suggested as shown in Figure 9.14. When the source was in a quiescent state, it showed a steep spectrum with photon index of $\Gamma_{\rm X-ray} \sim 2.3$. It hardened to ~ 1.8 when the source becomes brighter (Giommi et al. 1999; § 8.3). This supports an idea that the synchrotron peak largely moves with the flux change as that were observed in Mrk 501 (§ 7.3.3). Further observations are necessary for confirmation.

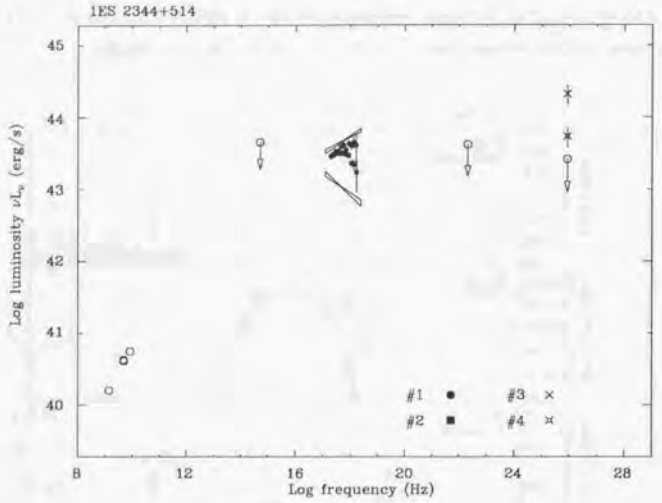

Figure 9.14: Multi-frequency spectra for 1ES 2344+514 in various source activities. No simultaneous data with X-ray observations has been available. #1 : data from MJD 50458.68 to MJD 50458.84 (Jan 10, 1997; this work), #2 : data from MJD 50471.23 to MJD 50471.40 (Jan 23, 1997; this work), #3 : TeV data on 1995 Dec 20 (TeV flare; Catanese et al. 1998), #4 : TeV average flux from 1995 to 1996 (Catanese et al. 1998). Open circles : Perlman et al. 1996; Patnaik et al. 1992; Gregory & Condon 1991. Solid figure: *BeppoSAX* (Giommi et al. 1999). Upper limit for TeV emission was derived from 1996/1997 observations (Catanese et al. 1998).

Chapter 10

Discussion

10.1 Summary of Results

We have observed 4 TeV blazars with X-ray satellites *ASCA* and *RXTE*. These observations provide the highest quality spectral and timing information over a very wide energy range of 0.7−20 keV. It is noted that 30 X-ray observations were conducted simultaneously with *Whipple* Cherenkov telescopes (TeV), and 7 observations are also contemporaneous with EGRET on-board *CGRO* (GeV). To our knowledge, our current work is based on the largest sample of X-ray/GeV/TeV γ-ray data for TeV blazars, obtained in various states of source activities. In the following, we briefly summarize major results contained in this thesis.

X-ray Time Variability

Unprecedented big campaigns for Mrk 421 (1998; 7days) and PKS 2155−304 (1996; 12 days) revealed more than 10 flares with time scales of about a day which occured during the observations, indicating that variabilities in TeV blazars are more dynamic and complicated than we had imagined. Successive occurrence of flare events had been proposed by previous observations (e.g., Buckley et al. 1996), but data were too short and/or too undersampled to study in detail the time profile. We thus confirmed for the first time that rapid flares repeat day-by-day in those TeV blazars.

This naturally leads us to an idea that there exists some *prefered* time scale for variability of blazars. Structure function of TeV blazar variability showed a roll-over around 1 day, which we interpret as the characteristic time scale of rapid variability in blazars. Time scale was ~ 0.5 day for Mrk 421, 0.3 day for PKS 2155−304 and ~ 1 day for Mrk 501. Notably, these time scales reflect the typical rise/decay time of individual flare events.

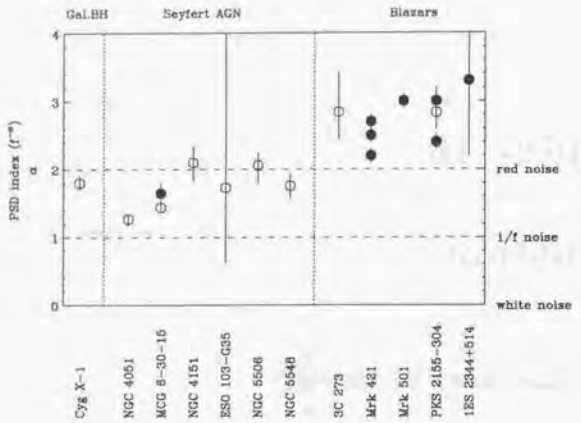

Figure 10.1: Comparison of PSD slopes for various black hole systems. *Open circle* : Hayashida et al (1998). *Filled circle* : Estimated from Structure Function analysis (this work). The power law indices for PSD (α for $f^{-\alpha}$) are simply estimated from SF index (β) as $\alpha = \beta + 1$.

On a shorter time scale ($\lesssim$ 0.3 day), slopes of SFs (β) are quite steep, ranging from 1.2 to 2.3 for all TeV blazars (this corresponds to the PSD index where $f^{-\alpha}$ of $\alpha = 2 \sim 3$). This clearly indicates that the physical processes operating in TeV blazars are strong red-noise type ($\beta \sim 1$) or actually no significant process exits ($\beta \sim 2$) up to the characteristic time scale described above ($\sim$ 1 day). As we can see in Figure 10.1, this is very different from other types of mass-accreting black hole systems, whose variabilities are well characterized by a fractal, flickering noise ($0 < \beta < 1$).

It is also remarked that the most of the flare events were characterized by nearly equal rise-time and decay-time, thus forming a quasi-symmetric time profile. To evaluate the time asymmetry of the light curves in various energy bands, we used an applied technique introduced by Kawaguchi et al. (1998). We discovered that the symmetry of the time profile tends to break down at lower X-ray energies both for Mrk 421 (Figure 7.14) and PKS 2155−304 (Figure 8.10).

Another important discovery is the detection of 'hard-lag' flares. Such an *unusual* behaviour was first implied for PKS 2155−304 (Sembay et al. 1993), but was not confirmed due to limited photon statistics and short coverage of previous observations. We confirmed that the *paradigm* that the soft X-ray variations always lag behind the hard X-ray variations ('soft lag') was *not* generally true – in fact, we detected complicated

mixture of 'soft lag' and 'hard lag' during the 7-day observation of Mrk 421 in 1998. As many authors have suggested, variability amplitude tends to become larger as photon energy increases, but some clear exceptions were found, which may possibly related to the hard-lag behaviours (Figure 7.24).

X-ray Spectral Evolution

In the X-ray band, photon spectra of those TeV blazars are well represented by a power law form, but smoothly steepening to higher energies. Using 5-year complete samples of *ASCA* and *RXTE* data, we confirmed a general trend that the spectra tend to steepen when the sources become fainter (e.g., Giommi et al. 1990). It is also noted that low luminosity TeV blazars tend to have flatter spectrum (Figure 7.27), possibly indicating a smooth connection to other types of blazar classes, such as LBLs and QHBs (see Figure 2.11; Ghisellini et al. 1998; Kubo et al. 1998).

The peak of the synchrotron component (LE component) was detected with *ASCA* (in conjunction with the data in other wavelengths) for all TeV blazars. More remarkably, we found that the position of the peak shifts from lower to higher energy when the source becomes brighter. We showed that the spectral evolution of Mrk 421 indicates very little change in the peak position (0.5 − 2 keV), while Mrk 501 records largest shift ever observed (1 − 100 keV; Catanese et al. 1997 and Pian et al. 1998). For the first time, we succeeded to quantify the correlation between the peak luminosity (L_p) and the peak energy (E_p) (Figure 8.19). We found $E_p \propto L_p^{0.4}$ for Mrk 421 and $E_p \propto L_p^{1.6}$ for Mrk 501. This naturally indicates that the origin of the flare may be quite different in those two objects.

Inter-band Variability

The results from several previous campaigns had suggested that the variability in blazars correlates in multi-frequency bands (e.g., Macomb et al. 1995; Buckley et al. 1996). However, non-simultaneity of observations and/or rather sparse sampling prevented us from concluding the inter-band variability. In the present work, Mrk 421 and Mrk 501 were intensively monitored in both X-ray and TeV γ-ray bands, providing *exactly* simultaneous X-ray and TeV flux information in various phases of source activity. We found that variations in keV and TeV bands are well correlated on time scale of a day to years. We found that the amplitude of variation is comparable in both energy bands for Mrk 421 ([X-ray flux] $\propto$ [TeV flux]; see, Figure 9.3), while quadratic for Mrk 501 ([X-ray flux]$^2 \propto$ [TeV flux]; see, Figure 9.9).

10.2 Dynamics of Rapid Variability

In the following, we discuss dynamical time scales which characterize the rapid variability in blazars. For simplicity, we will consider the synchrotron process as the dominant cooling process for high energy electrons, ignoring the inverse Compton cooling. This approximation is valid for TeV blazars because (1) the synchrotron luminosity is generally greater than the Compton luminosity, and (2) the reduction of the cross section in the Klein-Nishina regime significantly decreases the Compton scattering efficiency. More detailed discussion will be given in § 10.6.

10.2.1 Synchrotron Cooling

The non-thermal emission of the low energy (LE) component is most likely produced by synchrotron emission from high energy electrons (see, § 2, § 3). X-ray energy band is considered to be the highest part of LE component for TeV blazars. Cooling rate of a single electron by synchrotron radiation is given in equation (3.34). Thus the time $t_{\rm cool}$ when an an electron loses half of its energy would roughly be (in the observer's frame)

$$t_{\rm cool}(\gamma) \simeq 5 \times 10^8 B^{-2}\gamma^{-1}\delta^{-1}({\rm sec}), \tag{10.1}$$

where γ is the electron Lorentz factor. Since the peak observed frequency of the synchrotron emission is related to γ by equation (3.32), we found a simple relation,

$$t_{\rm cool}(E_{\rm keV}) \simeq 1.2 \times 10^4 B^{-3/2} E_{\rm keV}^{-1/2}\delta^{-1/2}({\rm sec}), \tag{10.2}$$

where $E_{\rm keV}$ is the observed photon energy in keV and δ is a beaming factor (Takahashi et al. 1996). Since the cooling time is proportional to γ^{-1}, higher energy electrons cool much faster than lower energy electrons, which may account for the 'soft-lag' behaviour often observed in TeV blazars.

By calculating the Discrete Correlation Function (DCF) in various photon energies, Takahashi et al. (1996) found that the soft X-ray ($E < 1$ keV) variability lagged behind that for hard X-ray band ($E > 2$ keV) by 4×10^3 sec, consistent with our present analysis (Figure 7.20). They associated the soft-lag with the difference of cooling time with respect to the energy and derived a magnetic field $B \sim 0.2\,(\delta/5)^{-1/3}$ (G). Importantly, this was the first case where the magnetic field was calculated only from the observed X-ray variability.

Similar approach was adopted by Kataoka et al. (2000) for the PKS 2155−304 flare in 1994 (§ 7.2.5). Since the X ray light curve during the flare was very symmetric, they evaluated the time lags in various energy bands with more direct method than the DCF, and compared the results with those obtained from DCF. They fitted the light curves to

a Gaussian and searched for the time shift of the peak of the flare. In this model, the photon count rate at an arbitrary time t is expressed as: $f(t) = C_0 + C_1 \times \exp\left[-(t - t_p)^2/2\sigma^2\right]$, where C_0 is a constant offset, C_1 is the amplitude of the flare component, t_p is the peaking time, and σ is the duration of the flare, respectively. The light curves were divided into 10 logarithmic-equal energy bands from 0.5 keV to 7.5 keV (for the SIS data) and 0.7 keV to 7.5 keV (for the GIS data; 9 bands). A Gaussian provides a sufficient fit of the resultant energy-binned light curves; the χ^2 probability of the fit was $P(\chi^2) \geq 0.1$ for 12 of 19 light curves. Note here that there was not any systematic (preferential) trend for the data whose probability $P(\chi^2)$ are less than 0.1. In Figure 10.2, we show examples of the Gaussian fit, which turned out to be a good representation of the data.

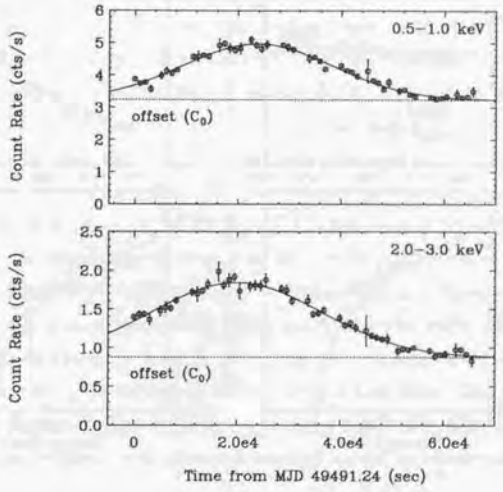

Figure 10.2: A Gaussian fit to the time profile of PKS 2155−304 during the flare in 1994. The count rates of both SIS detectors are summed. The solid line corresponds to the best fit with a Gaussian function given in the text. Upper Panel: Light curve in the 0.5 − 1.0 keV band; $\chi^2_{red} = 1.5$ for 49 dof. Lower Panel: Light curve in the 2.0 − 3.0 keV band: $\chi^2_{red} = 1.1$ for 49 dof (figure from Kataoka et al. 2000).

Figure 10.3 (a) shows the dependence on energy of the flare duration derived from fitting the energy-binned light curves. This result is consistent with a constant fit of σ = 1.5 × 10^4 sec. Figure 10.3 (b) shows the energy dependence of the flare amplitude, defined as the ratio of the normalization of the flare to the constant offset: $Ap \equiv C_1/C_0$.

The flare amplitude becomes larger as the photon energy increases. This is mostly due to the decrease in the constant offset (C_0) at higher energies. In other words, the spectrum during the flare is harder than that in the quiescent state. Figure 10.3 (c) is the lag of the peak time, calculated from the difference of t_0 of the Gaussian, as compared to that measured in the 3.0−7.5 keV band. As shown in the figure, the hard X-ray (3.0−7.5 keV) variability leads the soft X-rays (0.5−1.0 keV) by ~ 4 ksec. Finally, Figure 10.3 (d) shows the time lag measured from DCF technique, as was the case for the Mrk 421 (Takahashi et al. 1996). Lag is consistent with that estimated from the Gaussian fitting.

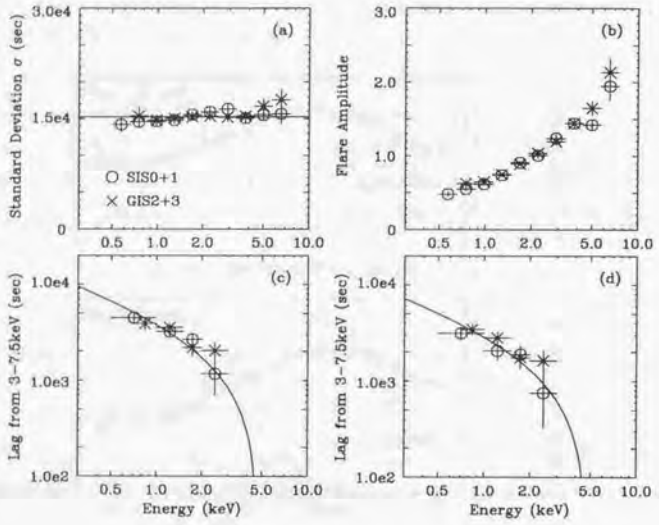

Figure 10.3: Measurement of the parameters describing the 1994 May flare of PKS 2155−304. The circles are combined SIS data, while the crosses are combined GIS data. (a): The flare duration, estimated by the standard deviation, σ, of the Gaussian fits at various X-ray energies. The solid line is a constant fit ($\sigma = 1.5 \times 10^4$ sec). (b): The flare amplitude ($A_\beta \equiv C_1/C_0$) at various X-ray energies, determined by a Gaussian fit. (c): Time lag of photons of various X-ray energies versus the 3.0−7.5 keV band photons, calculated from the peaking time determined by a Gaussian fit. The solid line is the best fit with a function (10.2). The best fit parameter is $B = 0.11$ G for $\delta = 25$. (d): Time lag of photons of various X-ray energies versus the 3.0−7.5 keV band photons, calculated using the discrete correlation function (DCF). The solid line is the best fit with a function (10.2). The best fit parameter is $B = 0.13$ G for $\delta = 25$ (figure from Kataoka et al. 2000).

Importantly, two methods mentioned above yielded consistent values for B. They found the magnetic field for PKS 2155−304 to be $B = (0.12 \pm 0.02)(\delta/25)^{-1/3}$ (G).

10.2.2 Smoothing by Light Travel Time

From results of Mrk 421 and PKS 2155−304, one can approximate the typical values of the magnetic field B of Mrk 421 and PKS 2155−304 as $B \sim 0.1 - 0.2$ (G), when a beaming factor is $\delta \simeq 10$. In order to derive the magnetic field from the time lag, we need a complete sample of flares. Unfortunately, we do not have any samples of 'complete flares' for Mrk 501 and 1ES2344+514. With the magnetic field of $B \sim 0.1$ (G), we can estimate the cooling times of electrons which emit photons of various energies from equation (10.2): $t_{\rm cool}$(0.1 keV; UV) $\simeq 4 \times 10^4$ (sec), $t_{\rm cool}$(1 keV; soft X-ray) $\simeq 1 \times 10^4$ (sec) and $t_{\rm cool}$(10 keV; hard X-ray) $\simeq 4 \times 10^3$ (sec). In the X-ray band, cooling time is much *shorter* than the decay time of an each flare event. As is clearly seen in the light curves of Mrk 421 (e.g., Figure 7.2; see also Figure 10.4) and PKS 2155−304 (Figure 10.2), typical time scale of the decay in a flare is 0.3−0.5 day for these sources. It should be also noted that the time scale of the rise in a flare is also 0.3−0.5 day (see also, § 7.2.3; 8.2.3).

This clearly indicates that a mechanism other than synchrotron cooling, actually determines the decay-time of each flare. The most natural interpretation is the *smoothing* of rapid variabilities by source light travel time (e.g., Chiaberge & Ghisellini. 1999; Kataoka et al. 2000). Rapid variability on time scale shorter than R/c, where R is the emission region size, cannot be observed, because of the relaxation (smoothing) by the light travel effects over the source on a light-crossing time scale. The observational fact that rise and decay time-scales of the short term flares are nearly comparable, bears important consequences (Figure 10.2). In fact, it is highly unlikely that these time scales are directly associated with the particle acceleration and cooling time scales, since a priori there is no reason for them to be equal, and observed equality would be accidental (Ghisellini et al. 1997).

This simple idea was confirmed by a detection of energy-dependence of time-asymmetry of the light curves (Figure 7.14, 8.10). We found two important properties in the light curves : (i) time profiles of TeV blazars are almost symmetric, but in the strict sense, they are characterized by the 'rapid rise and gradual decay', and (ii) the symmetry of the time profile more strongly breaks down at lower energies (§ 7.2.3; 8.2.3). It should be noted that both of these are most naturally interpreted by the balance of cooling time ($t_{\rm cool}$) and light travel time ($t_{\rm crs} = R/c$). Since cooling time becomes comparable with the source light travel time only at lower energy bands, smoothing of rapid time variability should be more important at high energy X-ray band, forming a symmetric time profile. We show an example of time profile of a flare in Figure 10.4 (Mrk 421 in 1998: time-region

#2) which clearly demonstrates the fact that the hard X-rays decayed more rapidly than the soft X-rays and UV photons.

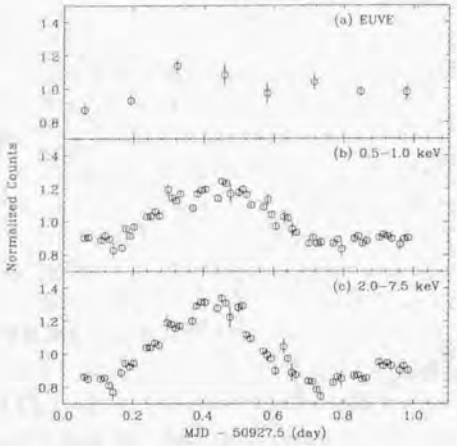

Figure 10.4: Time profiles of a flare of Mrk 421 observed in 1998 (time-region # 2). *top* (a): *EUVE* (~0.1 keV), *middle* (b): *ASCA* SIS (0.5−1.0 keV), *bottom*(c): *ASCA* SIS 3.0−7.5 keV. Note that time profile of the flare becomes more symmetric at higher energy bands and amplitude of variability is larger as increasing photon energy.

We also note that the importance of light travel time (t_{crs}) is implied from another reason. In Figure 10.5, we show the time profiles of different types of flares observed for Mrk 421 in 1998. For the flare in time-region #2 (see, Figure 7.8), we can see a symmetric triangular shape whose rise-time and decay-time are nearly equal. However, for the flare in time-region #9, we can see a plateau in the light curve. For this particular flare (#9), after the flux reached the maximum, it remained almost constant for 0.4 day (Figure 10.5). This indicates that, for the flare in time-region #9, the electron and photon distributions would have enough time to reach a 'new' equilibrium state, and form a *plateau* in the light curve (e.g., Mastichiadis & Kirk 1997; Chiaberge & Ghisellini 1999; see also § 11).

Assume that the flares are explained by a shock front propagating through the emission region, supplying freshly accelerated electrons only in the front's vicinity (Kirk, Rieger & Mastichiadis 1998). A plateau in the light curve appears only when the duration of a change in electron injection (t_{inj}) is larger than t_{crs}. This corresponds to a physical condition in which shock velocity is much slower than the speed of light, because the injection process take R/V_s to influence the whole region, where V_s is the shock velocity.

In this case, newly accelerated electrons are injected to the emission region for $t_{inj} > t_{crs}$. On the other hand, a symmetric triangular shape of the light curve corresponds to a highly relativistic shock, $V_s \sim c$. In any case, present observational data indicate that the balance of duration of an injection event t_{inj} and source light travel time t_{crs} is important to describe the rapid variability in blazars.

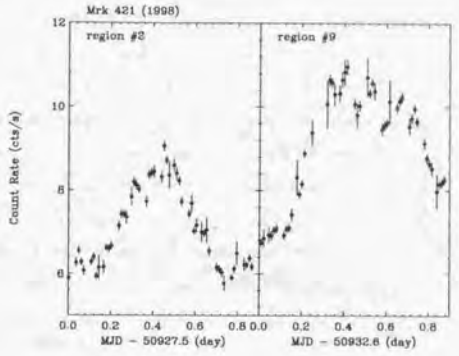

Figure 10.5: Time profiles of two different flares of Mrk 421 observed in 1998. SIS light curves of energy band 1.0−1.5 keV are plotted. *left* : time-region #2, *right* : time-region #9 (see, § Figure 7.8). Note that a plateau appears in the light curve of #9, whose duration of flare is longer than that of #2.

10.2.3 Acceleration of Electrons

As we have seen in previous sections, electrons with higher energy cool faster than electrons with lower energy ($t_{cool} \propto \gamma^{-1}$). Thus if the nature of rapid variability of the system (*flare*) is controlled by *instantaneous* injection of electrons up to γ_{max} and energy loss by radiative cooling, soft X-ray variations should *always* lag behind those in the hard X-ray band. However, we are aware that there were observations in which no time-lags or opposite sign of lags were reported (e.g., Sembay et al. 1993; Figure 7.19; Figure 7.21). Curiously, such observations were only little studied or forgotten in previous works, probably because it cannot be understood by a simple synchrotron cooling scenario. Another reason might be that observations were too short to cover the whole flare duration, thus reducing a motivation for strongly arguing the presence of such *unusual* behaviour.

Uninterrupted observation of Mrk 421 in 1998 revealed that the actual situation is much complex than we had expected. Sign of lags had changed flare by flare (Figure 7.23). In some flares, we actually detected completely opposite behaviour, where the soft X-ray

variations *preceded* that in the hard X-rays ('hard lag'; see, Figure 10.6). It is clearly shown that the time variation in lower energy band lags behind that in the higher energy band. Mechanism other than the synchrotron cooling is necessary to account for the *slower* response for higher energy electrons.

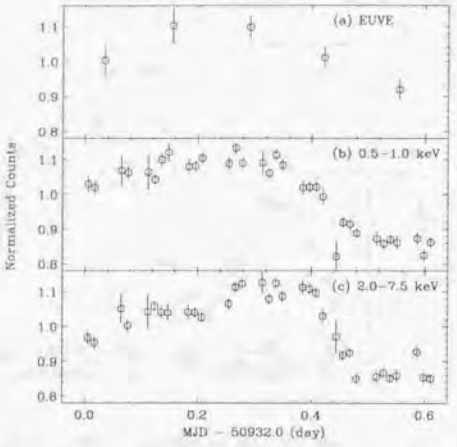

Figure 10.6: Time profiles of a flare of Mrk 421 observed in 1998 (time-region # 8). *top* (a): *EUVE* (~0.1 keV), *middle* (b): *ASCA* SIS (0.5–1.0 keV), *bottom*(c): *ASCA* SIS 3.0–7.5 keV. Note that the time variation in higher energy band lags behind that in the lower energy band (*hard lag*), and variability amplitude is almost equal through *EUVE* to *ASCA* .

Since the cooling time of electrons is a function of B and δ (equation (10.1)), it might be expected that the magnetic filed and/or beaming factor changed flare by flare. However, this is not plausible for two reasons. First, even if the magnetic field is variable, one cannot account for the hard lag ('zero-lag' at most; see equation 10.2). Second, since the synchrotron emissivity is proportional to B^2 (e.g., equation (3.34)), changes in magnetic field inevitably would cause a large-amplitude variations also in the lowest energy bands (e.g., radio/optical) as well as X-ray bands. This has not been observed. Optical flux (R band) for Mrk 421 during the 1998 ASCA observation (24–30 April) showed only small fluctuation within 12.6±0.1 (fag) (Mattox 1999, private communication). Changes of beaming factor, e.g., due to the bending of jet (Wagner et al. 1993) might explain the changes of cooling time. However, it is not plausible because the fluctuation of beaming factor produce completely *coherent* variations in energy (see, also § 11.7). Such coherent variability have never been observed for Mrk 421, although this might had been the case

for a particular flare of 2155−304 observed in 1991 (see, Edelson et al. 1995).

In TeV blazars, we believe that most natural interpretation of 'hard lag' behaviour is based on the acceleration of electrons at shock front postulated to exist in blazar jets. Such a shock is expected to be produced by several different ways, for examples, by a collision of emission blob with surrounding materials in the vicinity of the jet (e.g., BLR; see, § 2) and/or by a collision of blobs moving with different bulk Lorentz factors (*internal shock* scenario; e.g., Ghisellini 1999; see also the discussion below). As we described in § 3.1, when the low energy electrons are injected into the shock front, they are gradually accelerated to higher energies up to the maximum Lorentz factor $\gamma_{\rm max}$, where radiative loss and energy gain are equally balanced. The efficiency of acceleration is expressed by the *acceleration time scale*, $t_{\rm acc}$ (see, § 3.1.4). In practice, $t_{\rm acc}$ would be dependent on the electron energy in accordance with shock acceleration process. For example, $t_{\rm acc}$ $(\gamma) \propto \gamma$ for diffusive acceleration with a 'gyro-Bohm' process (e.g., Inoue & Takahara, 1996) and $\propto \gamma^{1/3}$ for fully developed Kolmogorov turbulence. Although we assume $t_{\rm acc}$ to be constant for simplicity, the following discussion can be applied for the case that the acceleration time has some dependences on energy (see, § 3.1.3).

10.2.4 Application of Acceleration/Cooling Model to Data

Let's assume a simple case where electrons with mono-energetic Lorentz factor γ_0 ($\ll \gamma_{\rm max}$) are picked up (injected) into the acceleration process at a shock front, and subsequently drift away from into the downstream flow. Drifted electrons will be cooled by synchrotron process in a homogeneous magnetic field B, in which electrons emit most of the radiation (emission region). We define the magnetic field strength around the shock front $B_{\rm s}$ ($\neq B$ in general) and the shock velocity $V_{\rm s}$. We note that $t_{\rm acc}$ and $\gamma_{\rm max}$ would be a function of $B_{\rm s}$ and $V_{\rm s}$, but a detailed description is beyond the scope of this thesis (e.g., $t_{\rm acc} \propto B_{\rm s}^{-1} V_{\rm s}^{-2}$ and $\gamma_{\rm max} \propto B_{\rm s}^{-1/2} V_{\rm s}$ for diffusive acceleration with a 'gyro-Bohm' process; Inoue & Takahara, 1996).

From the equation (3.21), we obtain an upper limit on the electron energy which can be accelerated at time t,

$$\gamma(t) = \left(\frac{1}{\gamma_{\rm max}} + \left[\frac{1}{\gamma_0} - \frac{1}{\gamma_{\rm max}}\right]\exp(-t/t_{\rm acc})\right)^{-1}. \qquad (10.3)$$

What is important is that the higher energy electrons require *longer time to be accelerated*, which produces opposite sign of time-lag expected from the synchrotron cooling process. 'Hard lag' thus appears as a delay in the start time of the flare for higher X-rays. When the variation at observed photon energy E_1 is found to be lagged behind the variation at

energy E_0 ($E_0 < E_1$) for Δt (sec), one finds a simple relation.

$$\Delta t \simeq \frac{t_{acc}}{2}\delta^{-1}\ln(\frac{E_1}{E_0}). \tag{10.4}$$

The combination of 'soft-lag' by radiative cooling in the emission region, and 'hard-lag' by acceleration process (equation (10.2) and (10.4)) can be applied for the explanation of the observed behaviour of flare-by-flare changes in sign of the time-lag. If we take the acceleration process into account, the time lag can be expressed as,

$$\Delta t(E_0, E_1) \simeq 1.2 \times 10^3 B^{-3/2}\delta^{-1/2}(E_0^{-1/2} - E_1^{-1/2}) - \frac{t_{acc}}{2}\delta^{-1}\ln(\frac{E_1}{E_0}) \ \ (\mathrm{sec}), \tag{10.5}$$

where $\Delta t(E_0, E_1)$ is the time lag of the light curves at observed photon energy E_0 from that at the energy E_1 (in unit of keV; $E_0 < E_1$).

We applied this simple model to Mrk 421 data obtained in 1998. We fixed the magnetic field in the emission region and beaming factor to $B = 0.2$ (G) and $\delta = 10$, as calculated from the time-lag for 1994 data (Takahashi et al. 1996). Regarding this point, we note that the time-lag for Mrk 421 in 1994 is well represented by synchrotron cooling term only, because the energy dependence of the cooling time derived from the time lag is consistent with the synchrotron cooling process. We do not need to introduce an additional acceleration term. This corresponds the physical case in which the electron populations are rapidly ($t_{acc} \simeq 0$) accelerated from γ_0 to γ_{max}.

Since flare-by-flare changes of B are unlikely (see above), we fixed the magnetic field to 0.2 G and fit the 1998 data with only one free parameter, t_{acc}. Figure 10.7 shows the model fit to the time-lag for time-region #2−9 (see, Figure 7.8). Best fit models are given as a solid line. Upper panel shows the case where the magnetic field was larger/smaller by factor of 2 than the assumed value (0.2 G), but t_{acc} is fixed at the best fit value. The lower panel corresponds to the case when the acceleration time changed by factor of 2, but B is fixed to 0.2 G.

One finds that all the data are consistent with this simple model ($P(\chi^2) > 0.1$) and that parameters (B and t_{acc}) are well constrained within a factor of 2. The calculated acceleration time ranges from 1×10^3 sec to 6×10^3 sec in observer's frame. Since the cooling time of electrons which emit X-ray photons at 1 keV is $t_{cool} \simeq 5 \times 10^3$ (sec) for $B = 0.2$ (G) and $\delta = 10$, the derived acceleration time is nearly equal to the cooling time. We should note that if $B_s \simeq B$, the acceleration time (t_{acc}) and cooling time (t_{cool}) are expected to be balanced for electrons that emit photons in the X-ray energy bands. The steep X-ray photon spectra of TeV blazars ($\Gamma_{X-ray} > 2$; Figure 7.27 and 8.14) imply that the X-ray band corresponds to the highest part of the LE component, thus reflecting the electron population close to the γ_{max}. However, if the magnetic field is compressed around the shock, i.e. $B_s \gg B$, acceleration time can be much shorter than the cooling time, even in the X-ray energy bands.

Variability or flaring behaviour can arise from a number of reasons. When the shock front overruns a region of the jet in which the local electron density is enhanced, the number of electrons picked up and injected into the acceleration process is expected to increase (Kirk, Rieger & Mastichiadis 1998). In this case, we do not expect any changes in acceleration time, thus variations of observed time-lags for each flare event cannot be explained. On the other hand, if the density change is associated with a change in the magnetic field in the shocked region (B_s) or changes in the shock velocity (V_s), acceleration time *can* also vary. In such situation, time-lags may also vary, corresponding to the balance of the acceleration time and the cooling time, as was the case for Mrk 421 flares in 1998.

Although the full description of the shock process is necessary to deepen the current discussion, a simple model in which electrons are accelerated in the 'accelerated region' and injected to a 'emitting region' for the radiation can qualitatively explain properties of the complicated time profiles observed in Mrk 421. Present results, which indicate t_{cool}(X-ray) $\geq t_{acc}$, might indicate the tangled magnetic field around the shock (B_s) is enhanced as compared to that in the emitting region (B).

As a summary, our current discussions assumed a single emitting region associated with a single shock front (one-zone homogeneous model). The structure of jet is assumed to be globally smooth, but locally the jet may include tangled regions, e.g., with enhanced plasma density. Various types of flares can be produced when the shock overruns such a tangled region. We found that this picture qualitatively accounts for the observed properties of TeV blazars.

10.2.5 Comment on Multiple Emission Models

Instead of assuming a single emission region, one might expect multiple emission regions and shock fronts in the jet, all of which are characterized by different physical quantities (e.g., region size and magnetic field density). These quantity may vary independently. Complex features observed from Mrk 421 in 1998 could be generated by the superpositions of flares originating in different emitting regions. When a flare arises in a blob with strong magnetic field, the observed lag becomes small, while larger lag would be observed when the magnetic field is relatively small.

Such a situation seems to be realistic in some sense, however, we prefer one-zone model for several reasons: (1) rapid variability in TeV blazars is well correlated in the X-ray and TeV γ-ray bands, suggesting that same spatial region and same population of relativistic

electrons dominated the emission (Figure 9.3; 9.6). (2) clear correlation between the flux and the photon index, as well as shift of the synchrotron peak (e.g., Figure 8.19) rules out superpositions of photon spectra which are produced in different emission region characterized by different physical parameters. (3) spectral energy distribution of TeV blazars is well represented by one-zone homogeneous model (see also, § 11)

Also note that our discussion based on one-zone model is not affected as long as individual emitting region is concerned. Balance of 4 time scales, $t_{\rm cool}$, $t_{\rm acc}$, $t_{\rm crs}$ and $t_{\rm inj}$ must be held even when we assume a complicated multiple emission region model.

10.2.6 Cooling Time vs Escape Time

In the previous sections, we considered four timescales which characterize the rapid variability in blazars. We would like to comment here on another dynamical time scale; $t_{\rm esc}$. Many authors have assumed that the relativistic electrons are injected into the emission region with a specified distribution and escape on a timescale $t_{\rm esc}$ (e.g., Inoue & Takahara. 1996). After particles escape from the emission region, these particles no longer radiate. For low-energy electrons whose cooling time is longer than $t_{\rm esc}$, they cannot cool completely before leaving the source, thus the spectral form becomes similar to that of the injection. However, for the high energy electrons of $t_{\rm cool} < t_{\rm esc}$, they lose most of the energy before leaving the source. If the electron injection spectrum is a power law form of $\propto \gamma^{-s}$, it breaks by one power in the index ($\propto \gamma^{-s-1}$) for $\gamma > \gamma_{\rm br}$, where $\gamma_{\rm br}$ is the electron Lorentz factor which satisfies $t_{\rm cool}(\gamma_{\rm br}) = t_{\rm esc}$.

There is a good observational reason to believe that escape, or equivalently, sudden energy loss by adiabatic expansion is important. In fact, the photon spectral index starts to deviate from that in the radio (millimeter) band by ~ 0.5 around IR/optical band for TeV blazars (e.g., § 9). Thus the electron loss by escape, rather than cooling, is more important for low energy electrons which emit photons from radio to optical band. In the X-ray energy band, cooling time is expected to be much shorter than $t_{\rm esc}$. Since we are dealing with the rapid variability observed in the X-ray energy band, $t_{\rm esc}$ is not crucial. But $t_{\rm esc}$ could be important when the cooling time is longer than $t_{\rm esc}$ (see also, § 10.6).

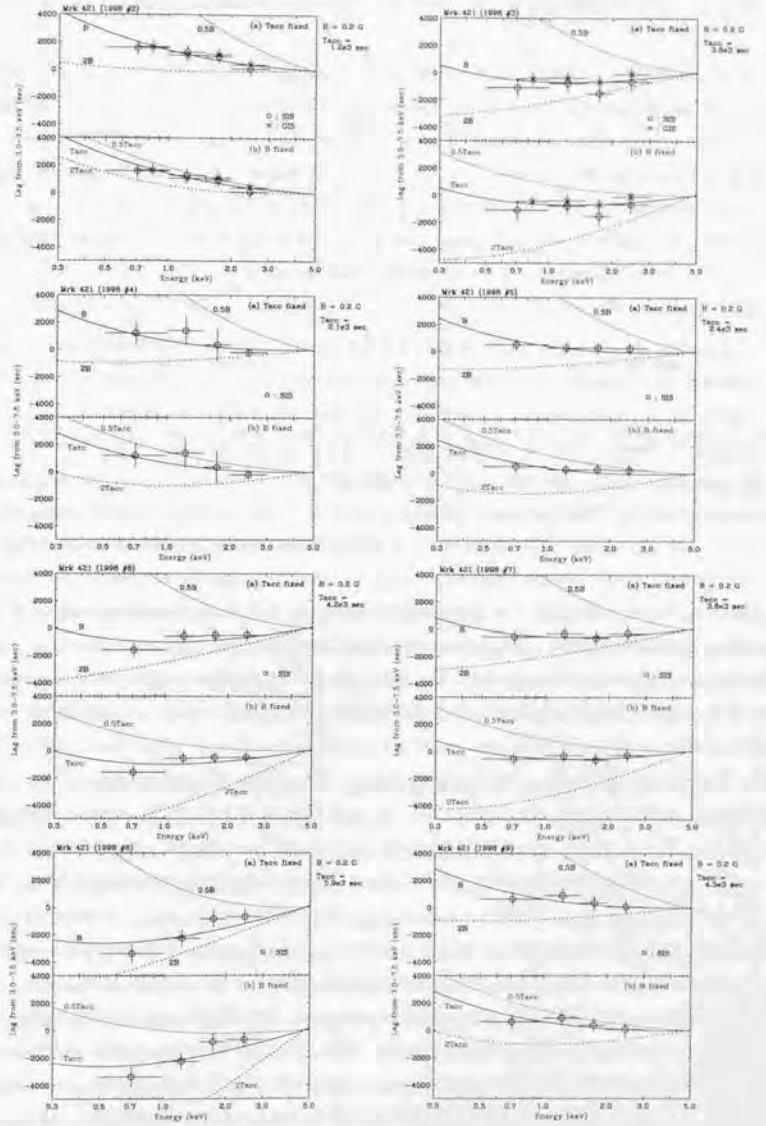

Figure 10.7: Fit with acceleration plus cooling model. Data from 1998 observation of 421. Acceleration time is given in observer's frame (assuming $\delta = 10$).

10.3 Properties of Short-Time Variability in Blazars

As we have seen in Figure 10.1, rapid time variability of TeV blazars is clearly different from that of Galactic black holes and galaxies. This is most probably due to different physical origins and/or locations where the X-ray photons are produced, and hence, different time variability is observed. In fact, X-ray photons are considered to be emitted almost isotropically from the most inner part of the accretion disk for Galactic black holes and Seyfert galaxies (see, e.g., Tanaka et al. 1995; Dotani et al. 1997), while non-thermal emission from relativistic electrons in the relativistic jet is thought to be the origin of X-ray photons for blazars (see, § 2).

For TeV blazars, we showed that time variability shows strong red-noise type behaviour, and variability shorter than *characteristic* time scale is strongly suppressed. This is more clearly seen in Figure 10.8, in which variability of different time scales are separately shown. For the case of Cyg X−1 (*left*), similar time variability is seen in various time scales. Existence of time variability in the shortest time scale well explains an observed flat PSD index of Cyg X−1 (1.7−1.8; Figure 10.1). For the case of Mrk 421 (*right*), however, time variability changes dramatically in various time scales. On the shortest time scales (< 0.2 day), time variability seems to be absent and the light curve is almost constant. On longer time scales (< 2.0 day), variability which is often called a 'flare' appears. Rise-time and decay-time of a flare are what we have derived as the *characteristic* time scale using SF analysis. Although the last panel is somewhat undersampled, large amplitude variations are clearly seen, which are similar to that in the middle panel.

Despite the long history of X-ray astronomy, the physical processes which may account for the *canonical* (quasi-fractal) time variability of Galactic black holes and Seyfert galaxies are still under debate. The situation is more severe for blazars, where only few studies have been performed to investigate the nature of rapid variability in blazars. In the X-ray band, Tagliaferri et al. (1991) have studied *EXOSAT* observations of PKS 2155−304 (exposure of about 1 day), and found that the power spectrum follows a power-law with an index −2.5±0.2, which is exactly consistent with our SF analysis. Hayashida et al. (1998) also found very steep power spectra for both PKS 2155−304 and 3C 273 as were given in Figure 10.1. In the optical band, Paltani et al. (1997) studied the time variability based on 15 nights data. They also reported that the PSD is well described by a power-law with an index −2.4, comparable with the index found in the X-ray domain. No PSD studies had been reported for variabilities in Mrk 421, Mrk 501 and 1ES 2344+514 prior to this thesis.

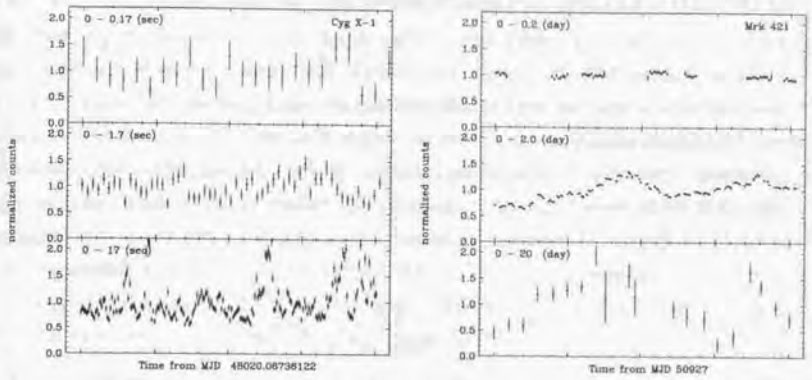

Figure 10.8: Self-similarity of rapid variabilities in Cyg X−1 and Mrk 421. Variabilities of different time scales are separately shown. *left* : time variability in Cyg X−1. Data come from Hayashida et al (1998). *top*: 0−0.17 (sec), *middle*: 0−1.7 (sec), and *bottom*: 0−17 (sec). Start time is MJD 48020.06736122 (1990/05/09). *right* : time variability in Mrk 421. *top*: 0−0.2 (day), *middle*: 0−2 (day), and *bottom*: 0−20 day. Start time is MJD 50927.0 (1998/04/23).

The absence or suppression of rapid time variability (≤ 1 day) in blazars implies that there exists a *prefered location* in which X-ray photons are produced. Characteristic time scale of each flare event, $t_{\rm obs} \sim 1$ day, indicates that the size of the emission region is $\sim 10^{16}$ cm in the source frame, if the emitting blob is moving with the Lorentz factor of $\Gamma \sim 10$. Since the jet is collimated within a narrow cone with angle $\theta \simeq 1/\Gamma$, one finds that the X-ray emission site is $D \sim 10^{17}$ cm from the base of the jet. Absence of rapid variability shorter than ~ 1 day rules out the X-ray emission inside of this. Similarly, more distant region, as expected from radio emitting region (which is ≥ 1 pc; see also § 10.4), is also ruled out because it cannot explain the rapid time variability as short as 1 day.

There are several reasons which may account for this 'critical' distance $D \sim 10^{17}$ cm. First, even if the X-rays are actually produced at the base of the jet, and hence close to the accretion disk, the produced X-rays should be inevitably absorbed by photon-photon interactions, with associated pair production. A simple calculation reveals that the optical depth to pair production for X-ray and γ-ray photons well exceeds unity at the base of the jet ($\tau_{\gamma-\gamma} \geq 100$), thus we cannot observe both emissions in this region. Second, the shock fronts themselves may be absent at the base of the jet, and high energy electrons which are fully accelerated to emit X-rays, would be absent for distance closer than $D \sim$

10^{17} cm. In the following, we suggest a possible interpretation which may account for this preferred location of the shock fronts. This is called *internal shock scenario* and first introduced in the field of modeling γ-ray bursts. Very recently, Ghisellini (1999) pointed that this idea successfully explains some of observed characteristics in blazars.

Let's assume a central engine is not working continuously, but produces different blobs of material moving with different bulk Lorentz factors. For simplicity, we consider two relativistic blobs, blob-1: Lorentz factor is Γ_1 and emitted at $t = 0$, blob-2: Lorentz factor is Γ_2 ($\Gamma_2 = a\Gamma_1$; $a > 1$) and emitted at $t = \tau$. Assuming that blobs are initially separated by a few Schwarzschild radii ($\sim 3R_g$), blob-2 cathes up the blob-1 at a distance of

$$D = c\tau\Gamma_1^2(\frac{2a^2}{a^2-1}) \sim 10R_g\Gamma_1^2. \tag{10.6}$$

Despite the uncertainties in parameters a and τ, a distance at which two blobs collide is roughly estimated as $\sim 10\ R_g\ \Gamma_1^2$.

A radial distance of the jet at D is

$$R = D\sin\theta \simeq D\theta \simeq D/\Gamma_1. \tag{10.7}$$

Observed time scale is shortened by $\simeq 1/\Gamma_1$, because of the beaming effect (§ 3.7). Thus we obtain the observed time scale for blazars,

$$t_{\rm obs} \sim D/(c\Gamma_1^2) \sim 10R_g/c. \tag{10.8}$$

In this scenario, we expect that *no* significant time variability would be observed for distance closer than D, because blobs are smoothly moving in the jets and shock fronts are absent in this region. Thus it is natural that rapid time variability shorter than $D/(c\ \Gamma_1^2)$ is strongly suppressed, as was indicated from temporal studies of X-ray light curves of TeV blazars.

Based on the discussion above, it is intriguing to estimate the mass of central black holes in TeV blazars. Since the Schwarzschild radius is expressed as

$$R_g/c \simeq 1.1 \times 10^{-10}(\frac{M}{M_\odot}) \quad ({\rm day}), \tag{10.9}$$

we obtain $M \sim 5{\times}10^8\ M_\odot$ for $t_{\rm obs} = 0.5$ (day). Interestingly, this result is also consistent with the typical mass of central black holes postulated to exist in active galactic nuclei (e.g., Hayashida et al. 1998).

10.4 X-ray Flares and Implications on the Jet Structure

In § 7.3.3 and 8.3.3, we found that the position of the synchrotron peak shifts from lower to higher energy when the source becomes brighter. The correlation was most clear for Mrk 421 ($E_{\rm p} \propto L_{\rm p}^{0.4}$) and Mrk 501 ($E_{\rm p} \propto L_{\rm p}^{1.6}$), where $L_{\rm p}$ is the peak luminosity and $E_{\rm p}$ is the peak energy (§ 7.3.3; 8.3.3). The difference of spectral evolution in both objects implies that quite different mechanisms were at work when the sources went into the flaring states.

Since the peak luminosity is proportional to the number of photons at peak ($n_{\rm ph}(E_{\rm p})$) multiplied by the peak energy, a simple relation can be found:

$$L_{\rm p} \propto E_{\rm p} n_{\rm ph}(E_{\rm p}) \propto \gamma_{\rm p}^2 n_{\rm e}(\gamma_{\rm p}), \tag{10.10}$$

where $\gamma_{\rm p}$ is the Lorentz factor of electron which emits photon of energy $E_{\rm p}$ and $n_{\rm e}(\gamma_{\rm p})$ is the number of electrons at $\gamma_{\rm p}$. We thus find the relations,

$$n_{\rm e}(\gamma_{\rm p}) \propto \gamma_{\rm p}^{3.6} \quad ({\rm Mrk421}), \tag{10.11}$$

$$n_{\rm e}(\gamma_{\rm p}) \propto \gamma_{\rm p}^{-0.8} \quad ({\rm Mrk501}). \tag{10.12}$$

This implies that for the case of Mrk 421, increase of $\gamma_{\rm p}$ by a factor of 2 requires more than factor 10 *increase* in number of electrons at peak energy. On the other hand, the same amount of increase of $\gamma_{\rm p}$ requires *decreases* in number of electrons by a factor of 2 for the case of Mrk 501. Such variations in spectral behaviors may be associated with the difference of physical conditions in relativistic jets, which is discussed below.

Assume that a substantial amount of gas (e.g., in a form of clouds) is distributed in the jet. In these clouds, density of low-energy electrons is enhanced as compared to the ambient, but other physical quantities such as magnetic field strength are unchanged. Those clouds essentially provide a plentiful source of low-energy electrons for the shock front. When a shock front overruns one of such clouds, fresh electrons are successively injected and assumed to undergo continuous acceleration by repeatedly crossing and recrossing the shock front, as well as simultaneously cooling by synchrotron radiation (e.g., Kirk, Rieger & Mastichiadis 1998). In this scenario, number of electrons increases significantly, but only small changes are implied for the maximum Lorentz factor as were observed in Mrk 421.

On the other hand, when clouds are absent or very sparsely distributed in the jet, flares may be produced in several diffent manners. For an example, if the shock overruns the enhanced tangled-magnetic field region, this may cause changes in acceleration time

of electrons, and hence increase the maximum Lorentz factor (see also, § 10.2.4). Importantly, regardless of detailed models for flaring behaviour, total number of electrons is *conserved* in this case. During the flare, acceleration can be assumed to be more efficient than radiative cooling, thus the present electron population as a whole will be accelerated to higher energies, but no additional electrons are supplied into the shock.

In latter case, numbers of electrons at the peak ($n_e(\gamma_p)$) will *decrease*, reflecting the power-law shape of an electron population. If the differential number density of electrons is expressed as $N_e \propto \gamma^{-2}$ (standard shock; § 3.1.5), electron number decreases as $n_e(\gamma_p) \propto \gamma_p N_e(\gamma_p) \propto \gamma_p^{-1}$. Importantly, this relation is very close to the case we have observed in Mrk 501 (equation (10.12)).

Present discussion based on the X-ray spectral evolution suggests very important implications for internal jet structures of Mrk 421 and Mrk 501. Only a small shift of synchrotron peak observed in Mrk 421 may be associated with electron clouds *filling* the jet, while the jet of Mrk 501 seems to be relatively empty. During the flare of Mrk 421, kinetic power of the shock is equally distributed to large number of low-energy electrons newly injected into the shock, thus increasing the number of high energy electrons. Large shifts of synchrotron peak observed in Mrk 501, on the other hand, is possible only when the internal jet is rather sparse and transparent to the shock propagation. Kinetic power of the shock is spent to *increase* the energies of individual electrons and hence *number-conservative*.

It may thus be worthwhile to compare our X-ray implications to the VLBI results. Accurate measurements of changes in the parsec-scale jet structure imaged with VLBI provide constraints on the jet kinematics and geometry. When combined with estimates of the Doppler beaming factor (determined, for example, from the X-ray time variability), the apparent motion of the jet components can be used to constrain the Lorentz factor of the jet and the angle of the jet to the line-of-sight. Although VLBI observations do not yet have an enough resolution to image the region production of the X-ray/γ-rays ($\sim$ 0.01 pc), they provide the highest resolution structual information available, and can image the region immediately downstream.

VLBI maps of Mrk 421 and Mrk 501 at 18 cm are separately shown in Figure 10.9. Both objects are observed in a space VLBI project using the *HALCA* satellite and 12 ground stations (Giovannini et al. 1998). It is interesting that the subparsec- and parsec-scale jets of Mrk 421 and Mrk 501 appear to be weak relative to those of other blazars (Marscher et al. 1999). Most importantly, superluminal motions have been detected only for Mrk 501 ($v = 6.7\ c$; Giovannini et al. 1998), while subluminal motions were implied for Mrk 421 ($v \simeq 0.3\ c$; Piner et al. 1999). An apparent velocity of Mrk 501 implies that

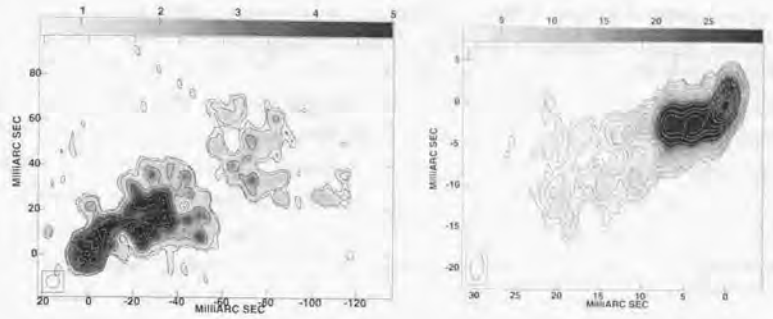

Figure 10.9: Global Space VLBI map of Mrk 421 (*left*) and Mrk 501 (*right*). In these figures, 1 mas corresponds to 0.9 pc. Superluminal motions were detected only for Mrk 501 ($v \sim 6.7\ c$). Figures from Giovannini et al (1998).

the real jet velocity has to be $\geq 0.989\ c$ and the jet has to be oriented at an angle smaller than 17 deg (Giovannini et al. 1998). By assuming that the bulk and pattern jet velocity are comparable, Giovannini et al (1998) derive that the beaming factor of Mrk 501 as $\delta \sim 1.3-5.6$. For the case of Mrk 421, the results are consistent with *no-beaming*.

In any case, the estimated beaming factors for both sources are relatively low compared with the lower limits derived from time variabilities in other wavebands; for examples, Takahashi et al. (1996) derived $\delta \geq 5$ for Mrk 421 and Kataoka et al. (1999) derived $\delta \geq 6$ for Mrk 501 using the X-ray/TeV γ-ray time variability (see also, § 10.6). Marscher (1999) disscussed that rather low superluminal apparent speeds and lackluster variability properties of the radio jets evidences that the bulk flow of the jets *decelerates* from X-ray/TeV γ-ray emitting section ($\sim$ 0.01 pc) to the radio emitting region ($\sim$ 1 pc). The weak subparsec- and parsec-scale jets of those objects are readily understood as the consequence of heavy energy and momentum loss in the upstream of the jet where most of the energy and momtentum of the relativistic electrons are transfered to the radiation in the X-ray and TeV γ-rays.

Remarkably, very different manners of X-ray spectral evolutions of Mrk 421 and Mrk 501 presented in this thesis is exactly consistent with those VLBI observations. Our X-ray observations predict that relativisitc outflows of Mrk 421 will be decelerated faster than that for Mrk 501, because the jet of Mrk 421 is filled with low-energy materials and kinetic

energy of outflows are more efficiently dissipated during the propagation. The absence of superluminal motion of Mrk 421 in radio bands thus indicates that the high energy outflow has been sufficiently decelerated when it reaches to more distant, radio emitting region.

10.5 Implications from Inter-band Correlation

From the *truly* simultaneous observations of Mrk 421 and Mrk 501, we found that the flux variations in the X-ray and TeV γ-ray bands are well correlated on time scale of *hours to years*. These results imply that the same spatial region and the same population of relativistic electrons are responsible for the emission, as is predicted from the simple synchrotron self-Compton (SSC) scenario. The amplitude of variation was comparable in both energy bands for Mrk 421 ([TeV flux] $\propto$ [X-ray flux]$^{0.92\pm0.12}$), while quadratic for Mrk 501 ([TeV flux] $\propto$ [X-ray flux]$^{1.96\pm0.07}$). In this section, we briefly discuss inter-band correlations expected from the simple SSC model and interpret the difference of Mrk 421 and Mrk 501.

Consider the electron population whose number density is given by N_e. Since energy loss rate of a single electron is proportional to the magnetic field density U_B (equation (3.34)), one finds a simple relation between the observed synchrotron luminosity and physical quantities as

$$L_{\rm sync} \propto \delta^4 N_e B^2, \tag{10.13}$$

where δ is the beaming factor of emission blob. If the emission is taking place in the Thomson regime ($\gamma h\nu \ll m_e c^2 \delta$), similar relation for the SSC flux is simply given by

$$L_{\rm SSC} \propto N_e L_{\rm sync} \propto \delta^4 N_e^2 B^2. \tag{10.14}$$

When the scattering takes place in the Klein-Nishina regime ($\gamma h\nu > m_e c^2 \delta$), the situation is more complicated because the cross-section for the inverse Compton process reduces significantly. Corresponding relation for SSC luminosity in the Klein-Nishina regime is

$$L_{\rm SSC}^{\rm KN} \propto N_e L_{\rm sync}^{\rm eff} \propto \delta^4 N_e N_e^{\rm eff} B^2, \tag{10.15}$$

where $L_e^{\rm eff}$ and $N_e^{\rm eff}$, respectively, are the synchrotron luminosity and electron energy density *effectively* involved in the inverse Compton process.

In previous sections, we concluded that the variability of Mrk 421 is most probably due to the changes in number of electrons (N_e), rather than changes in δ or B. Above relations thus predict $L_{\rm SSC} \propto L_{\rm sync}^2$ for Thomson scattering, while $L_{\rm SSC} \propto N_e^{\rm eff} L_{\rm sync}$ for Klein-Nishina regime. Observational results imply that the X-ray spectrum and TeV γ-ray spectrum have similar slopes, whose differential photon indices are ~ 3.0. This indicates that the both emissions come from the *same*, high energy end of the electron distribution. Thus the above prediction can be directly compared with the observed relation of Mrk 421. From simultaneous observations in X-ray and TeV γ-ray bands, we found a relation [TeV

flux] $\propto$ [X-ray flux]. This suggests that the SSC process are operating in the Klein-Nishina regime, keeping $N_e^{\rm eff}$ almost constant.

This prediction is plausible because the seed photons that are Comptonized to produce TeV flux are *not* X-ray photons (Takahashi et al. 1996; Ghisellini & Maraschi 1996). Assuming a typical value for B of 0.1−0.2 G and δ of 10, we expect that the Lorentz factor of electrons which emit X-ray photons is $\gamma \sim 10^5$ (equation (3.32)). We thus expect $\gamma\ h\nu_{\rm X-ray} \sim 10\ m_e c^2 \delta$, which implies the scattering takes place in the Klein-Nishina regime. Seed photons for TeV γ-ray production are more likely to be optical/UV photons:

$$\nu_{\rm seed} \simeq m_e c^2 \delta / h\gamma \sim 10^{15-16}({\rm Hz}), \tag{10.16}$$

where h is the Planck constant. In this energy band, variability is small compared to that in the X-ray band (e.g., Buckley et al. 1996; Figure 9.2) and we can approximate $N_e^{\rm eff}$ to be constant. Thus X-ray and TeV γ-ray correlation of Mrk 421, [TeV flux] $\propto$ [X-ray flux], is accurately consistent with the SSC scenario operating in the Klein-Nishina regime.

For the case of Mrk 501, however, quadratic relation of [TeV flux] $\propto$ [X-ray flux]^2 does *not* simply mean that the SSC process is operating in the Thomson regime. There are two reasons to explain this relation; (1) spectral evolution of Mrk 501 implies that large changes in $\gamma_{\rm max}$ (§ 10.4). (2) X-ray spectrum of Mrk 501 is flatter (1.7−2.5 in photon index) than that in the TeV γ-rays ($\sim$ 2.5 in photon index), suggesting that electrons responsible for emission in both bands are different in energy. For the latter point, we should note that the correlation of fluxes between UV (not X-ray) and TeV energy bands for Mrk421 is [TeV flux] $\propto$ [UV flux]$^{2.7\pm0.7}$, which is similar to the relation found for Mrk 501 (Figure 9.4).

When the $\gamma_{\rm max}$ varies significantly during the flare, evolution of synchrotron/self-Compton luminosity cannot be simply written as equation (10.13)−(10.15), because the observed energy range is only limited in X-ray and TeV γ-ray bands. To evaluate the effects of the reduction of cross section in the Klein-Nishina regime, we approximate the spectral energy distribution (SED) of Mrk 501 as two broken power-laws (Figure 10.10). Lower component is synchrotron radiation, while upper is SSC radiation. For simplicity, we assume both components are *self-similar* and spectral index (in νF_ν space) is α ($>$ 0) below the break and β ($<$ 0) above the break, respectively.

We assume a flare in which $\gamma_{\rm max}$ increased by factor ξ ($>$ 1). We denote initial X-ray/TeV γ-ray fluxes as F_s and F_c, respectively. Initial break (*peaks*) in the synchrotron component is ν_s, while it is ν_c for the SSC component. Since the synchrotron frequency is $\propto \gamma^2$, ν_s increases by factor ξ^2 during the flare. In the Thomson regime, we expect ν_c to increase by factor ξ^4, because $\nu_c \propto \gamma^2\ \nu_s$ (equation (3.44)). Thus for the case of

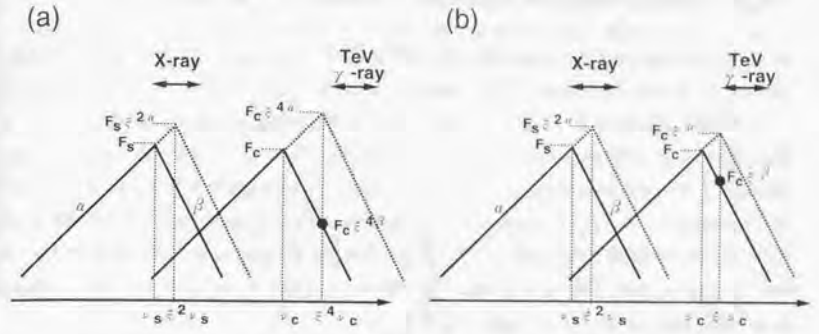

Figure 10.10: Schematic view of spectral evolution of Mrk 501. (a) : spectral evolution in Thomson regime, (b) : spectral evolution in Klein-Nishina regime. For Mrk 501, appropriate values for α and β are 0.2 and −0.5, respectively.

Mrk 501, the X-ray flux during the flare is roughly be $F_s\ \xi^{2\alpha}$ and TeV γ-ray flux is $F_c\ \xi^{4\alpha}$ (Figure 10.10), compared with the initial values of F_s and $F_c\ \xi^{4\beta}$. Thus the index of correlation $k_{\rm TM}$ between X-ray and TeV γ-ray flux is ([TeV flux] $\propto$ [X-ray flux]$^{k_{\rm TM}}$)

$$k_{\rm TM} \simeq \frac{4(\alpha-\beta)}{2\alpha}. \tag{10.17}$$

Selecting the appropriate values of α and β ($\alpha \sim 0.2$ and $\beta \sim -0.5$ for Mrk 501), we finally obtain $k_{\rm TM}$(Mrk 501) $\sim$ 7. This is much larger than the observed relation.

In the Klein-Nishina regime, we expect ν_c increased by factor ξ, because the maximum energy of Comtpon scattered photon is limited to $\gamma_{\rm max}\ m_e c^2$. The X-ray flux during the flare is roughly be $F_s\ \xi^{2\alpha}$ while TeV γ-ray flux is $F_c\ \xi^{\alpha}$, compared with the initial values of F_s and $F_c\ \xi^{\beta}$. Thus the index of correlation $k_{\rm KN}$ between X-ray and TeV γ-ray flux is ([TeV flux] $\propto$ [X-ray flux]$^{k_{\rm KN}}$)

$$k_{\rm KN} \simeq \frac{\alpha-\beta}{2\alpha}. \tag{10.18}$$

Selecting the appropriate values of α and β ($\alpha \sim 0.2$ and $\beta \sim -0.5$ for Mrk 501), we obtain $k_{\rm KN}$(Mrk 501) $\sim$ 2. This value is exactly consistent with the observed relation.

In summary, different correlations between X-ray/TeV γ-ray fluxes found in Mrk 421 and Mrk 501 are due to the different origins of the spectral evolution : number of electrons increased for Mrk 421, while maximum Lorentz factor increased for Mrk 501. Importantly, both observed relations are consistent if the Synchrotron self-Compton scattering takes place in the Klein-Nishina regime.

10.6 Constraints on the Physical Parameters

In § 10.2, we derived the magnetic field strength B by comparing observed time lags in various X-ray energy bands. The magnetic field of Mrk 421 and PKS 2155−304 were successfully determined to be $B \simeq 0.1$−0.2 G, assuming the beaming factor δ of 10. However, we should note that these constraints had been obtained only from the time-variability. Several important physical quantities are still unknown. Even in the one-zone SSC scenario, we need 7 parameters to specify the model, which cannot be determined only from the time variability constraints. In the following, we consider the constraints that can be derived from the multi-frequency spectra and compared with the limit obtained from 'time-lags' in the X-ray light curves.

One can find similar discussions in Bednarek & Protheroe (1997; 1999), Tavecchio, Maraschi & Ghisellini (1998) and Kataoka et al (1999). Following approach has two advanteges compared to the previous works (1) multi-frequency spectra taken at various states of activities are evaluated by polynomial fits for each TeV blazar, and (2) our discussion is more flexible and less affected by the uncertainties in the observational data.

10.6.1 Allowed Parameter Region

To specify the spectral energy distribution, we need the magnetic field B, region size R, beaming factor δ, escape time $t_{\rm esc}$, and the electron injection spectrum as input parameters (§ 3; see, also § 11). We adopt a specific form for the injected electron spectrum, $Q(\gamma) = q_o\, \gamma^{-s} \exp(-\gamma/\gamma_{\rm max})$, where $\gamma_{\rm max}$ is the maximum Lorentz factor of electrons. Seven free parameters listed here are required to specify the model.

Importantly, all these parameters can be calculated from seven observables: synchrotron maximum frequency, $\nu_{\rm s}^{\rm max}$; Compton maximum frequency, $\nu_{\rm C}^{\rm max}$; synchrotron break frequency, $\nu_{\rm s}^{\rm br}$; variability time scale, $t_{\rm var}$; synchrotron luminosity, $L_{\rm s}^{\rm tot}$; Compton luminosity, $L_{\rm C}^{\rm tot}$; and radio (millimeter) spectral index, α. The slope of injected electrons is simply related with α as $s = 2\alpha + 1$ (e.g., Blumenthal & Gould. 1970; § 3.3.2). Since the radio (millimeter) band is thought to be the uncooled portion of the electron distribution (§ 10.2.6, see also below), $\nu_{\rm s}^{\rm br}$ is the frequncy where the spectral index starts to deviate from that in the radio (millimeter) band.

Despite the equal numbers of observables and parameters (7 observables for 7 parameters), the model cannot be specified uniquely. The reasons are; (1) the region size is described by an inequality $R \leq c t_{\rm var} \delta$ (2) most of the present data are not well sampled and not obtained simultaneously, (3) multi-frequency spectra of blazars track smooth curves, hence we cannot clearly define the accurate positions of 'maximum frequency' or 'break frequncy', (4) Klein-Nishina effects probably reduce the Compton flux significantly at TeV energy band, which may cause the underestimate of the seed photon (i.e., synchrotron photon) density.

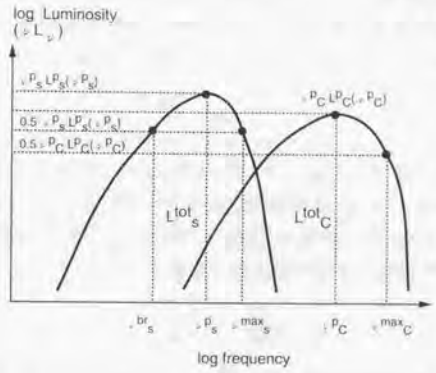

Figure 10.11: Definition of parameters from polynomial (cubic) fit. Spectral energy distribution of a TeV blazar is schematically shown. Horizontal axis is 'log frequency', while vertical axis is 'log νL_ν luminosity'.

To constrain the physical paramters, we first need to determine 7 observables. For this purpose, the multi-frequency spectrum of each TeV blazar was fitted with polynomial function of a form: $\log(\nu L_\nu) = a + b \log\nu + c\,(\log\nu)^2 + d\,(\log\nu)^3$, where a, b, c, d are the constants (Comastri et al. 1995). Since there are at least two components in the multi-frequency spectrum, we fitted the lower component (LE component; radio to X-rays) and the higher component (HE component; γ-rays) with separate polynomial functions. We determined 'observables' from the best fit cubic functions, which are schematically shown in Figure 10.11.

A relation $R \leq c t_{\rm var} \delta$ gives only an upper limit on the dimension of the source. But if we choose very small number for R, extremely high Doppler factor is required from the transparency condition (see below). Following Tavecchio, Maraschi & Ghisellini (1998), we limit ourselves in the range, $R = \xi c t_{\rm var} \delta$ $(1/3 < \xi < 1)$. The escape time of electrons, $t_{\rm esc}$, is also quite uncertain, but it needs to be longer than light travel time over the source (R/c). It is, however, not plausible that $t_{\rm esc}$ is much larger than R/c. If so, *no* break ($\nu_{\rm s}^{\rm br}$) would be observed in the spectral energy distribution up to $\nu_{\rm s}^{\rm max}$, which contradicts the obserations. We thus adopt a limit to $t_{\rm esc}$ as $t_{\rm esc} = \eta\, R/c$ $(1 < \eta < 10)$.

First constraint on parameters is derived as follows. The maximum Lorentz factor of

electrons is approximately related to the observable $\nu_s^{\rm max}$,

$$\gamma_{\rm max} \simeq [\frac{\nu_s^{\rm max}}{3.7\times10^6 B\delta}]^{1/2}, \tag{10.19}$$

where the electron pitch angle with respect to the magnetic field was set to be $\pi/2$ (equation 3.33). Since the Compton-scattered spectrum extends up to $\nu_C^{\rm max}$, the maximum electron energy must be larger $h\nu_C^{\rm max}$ in the source frame. We thus obtain the first constraint,

$$h\nu_C^{\rm max} \leq \gamma_{\rm max} m_e c^2 \delta \simeq [\frac{\nu_s^{\rm max}}{3.7\times10^6 B}]^{1/2} m_e c^2 \delta^{1/2}. \tag{10.20}$$

The second relation can be derived using the ratio of *total* luminosities of the synchrotron radiation and the total luminosity of the self-Compton radiation. As we have seen in equation (3.48), this ratio is directly related to the ratio between the radiation and the magnetic field densities inside the source as,

$$\frac{L_C^{\rm tot}}{L_s^{\rm tot}} = \frac{U_s^{\rm avail}}{U_B}, \tag{10.21}$$

where $U_s^{\rm avail}$ indicates the synchrotron photons which can effectively involved in the inverse-Compton scattering, below the Klein-Nishina limit. We conveniently express $U_s^{\rm avail}$ as $U_s^{\rm avail} = (1/\kappa)\, U_s$, where U_s is the *total* soft photon density and $\kappa > 1$. If the scattering takes place purely in the Thomson regime, κ is equal to 1. Since U_s is related to $L_s^{\rm tot}$ as

$$U_s = \frac{L_s^{\rm tot}}{4\pi R^2 c \delta^4}, \tag{10.22}$$

we find a relation

$$U_B = \frac{1}{\kappa} U_s \frac{L_s^{\rm tot}}{L_C^{\rm tot}} = \frac{1}{4\pi R^2 c \delta^4 \kappa} (\frac{L_s^{\rm tot\,2}}{L_C^{\rm tot}}). \tag{10.23}$$

Considering the reduction of cross section in the Klein-Nishina regime, we assume $1 < \kappa < 10$ in the following. This range of κ is valid as long as $\gamma_{\rm max}$ is not too large (e.g., $\gamma_{\rm max} \leq 10^6$; Figure 3.8). Thus we finally obtain the second constraint

$$\frac{1}{4\pi R^2 c \delta^4} (\frac{L_s^{\rm tot\,2}}{L_C^{\rm tot}}) (\frac{1}{10}) < U_B < \frac{1}{4\pi R^2 c \delta^4} (\frac{L_s^{\rm tot\,2}}{L_C^{\rm tot}}). \tag{10.24}$$

The third constraint is derived from the balance between cooling and electron-escape time scale (e.g., Sikora, Begelman & Rees 1994; Inoue & Takahara 1996). An injection of a power-law energy distribution of electrons up to a certain maximum energy (as expected from shock acceleration) into the radiating region should yield a steady-state electron distribution with a break in its index at a characteristic energy $\gamma_{\rm br}$. $\gamma_{\rm br}$ is estimated from a similar relation with equation (10.19),

$$\gamma_{\rm br} \simeq [\frac{\nu_s^{\rm br}}{3.7\times10^6 B\delta}]^{1/2}. \tag{10.25}$$

By equating the cooling time of electrons at $\gamma_{\rm br}$ with electron escape time, we obtain

$$t_{\rm cool}(\gamma_{\rm br}) = \frac{3 m_e c^2}{4(U_B + U_s^{\rm avail})\sigma_{\rm T}\gamma_{\rm br} c} = t_{\rm esc}, \tag{10.26}$$

where $\sigma_{\rm T}$ is the Thomson cross section (see, equation (3.34), (3.47)). Combining with equation (10.21) and $t_{\rm esc} = \eta\, R/c\, (1 < \eta < 10)$, we finally obtain the third constraint,

$$\frac{3 m_e c^2}{4 U_B \sigma_{\rm T} \gamma_{\rm br} R} (\frac{1}{10}) < \frac{L_C^{\rm tot}}{L_s^{\rm tot}} + 1 < \frac{3 m_e c^2}{4 U_B \sigma_{\rm T} \gamma_{\rm br} R}. \tag{10.27}$$

An additional constraint is derived from the condition of transparency of γ-rays to pair production absorption. Importantly, the transparency condition does not depend on the specific emission mechanisms, therefore it can place a strong and *independent* constraint on the minimum value of the Doppler factor in the SSC model. Following Dondi & Ghisellini (1995) and Tavecchio, Maraschi & Ghisellini (1998), conditions can be written

$$\delta > [\frac{\sigma_{\rm T} d_{\rm L}^2}{5hc^2} \frac{F(\nu_{\rm tgt})}{t_{\rm var}}]^{\frac{1}{4+2\beta}}, \tag{10.28}$$

where $\nu_{\rm tgt}$ is the frequency of *target* photons for pair production, related with γ-ray photons ν_γ as $1.6\times10^{40}/\nu_\gamma$. β is the spectral energy index of target photons, $F(\nu_{\rm tgt})$ is the flux density of target photons per frequency, and $d_{\rm L}$ is the luminosity distance, respectively.

All of above four conditions (equation (10.20), (10.24), (10.27) and (10.28)) are written in terms of two physical parameters: the magnetic field and the beaming factor. Each constraint then corresponds to an allowed region in the (δ,B) plane. On the other hand, the X-ray observation of 'time-lags' strongly limit B and δ along a narrow line $B \propto \delta^{-1/3}$ (e.g., equation (10.2)). Thus this provides a crucial test to examine whether the limits from spectral energy distribution and time-variability are mutually consistent. In the next section, we evaluate the allowed parameter space (δ, B) for each TeV blazar.

10.6.2 Individual Target

To evaluate the SED for each TeV blazar, we collected the non-simultaneous data from the literature and combined with our simultaneous X-ray/TeV γ-ray data (see § 9). Since the constraints described above basically assume a *steady state* emission, lowest fluxes in the literature were plotted as an approximate *quiescent* state. Balance of cooling time and escape time ($t_{\rm cool}(\gamma_{\rm br}) = t_{\rm esc}$) is only expected when the electron population has enough time to reach an equilibrium state. Similarly, the ratio between the radiation and the magnetic field densities (equation 10.21) holds when the photon distribution is in an equipartition (e.g., § 11). In the following, however, we also use simultaneous data in

various flaring states to check the consistency of parameters derived from the spectra in the quiescent state.

The results of polynomial fit are summarized in Table 10.1. We define $\nu_s^{\rm br}$ as the frequency where synchrotron luminosity reaches a half of its peak value ($\nu_s^{\rm p} L_\nu(\nu_s^{\rm p})$), while $\nu_s^{\rm max}$ is the frequency where the synchrotron luminosity decreased to a half of the peak (Figure 10.11). Since 1ES 2344+514 has not been detected by EGRET (Figure 9.14), we conveniently assume a best-fit polynominal function of Mrk 501 for the Compton radiation of 1ES 2344+514.

It should be noted that for Mrk 421 and PKS 2155−304, the total synchrotron luminotisy $L_s^{\rm tot}$ is larger than the total Compton luminosity $L_C^{\rm tot}$ by a factor of 2−3, while nearly equal for the case of Mrk 501. Also note that the maximum synchrotron frequency becomes larger for fainter sources (see, also Figure 7.27).

Table 10.1: Results of polynominal (cubic) fit

source	α	$\nu_s^{\rm br}$ (Hz)	$\nu_s^{\rm p}$ (Hz)	$\nu_s^{\rm max}$ (Hz)	$\nu_s^{\rm p} L_s(\nu_s^{\rm p})$ (erg/s)	$L_s^{\rm tot}$ (erg/s)	$\nu_C^{\rm p}$ (Hz)	$\nu_C^{\rm max}$ (Hz)	$\nu_C^{\rm p} L_C(\nu_C^{\rm p})$ (erg/s)	$L_C^{\rm tot}$ (erg/s)
Mrk 421	0.3	14.4	15.8	17.2	44.3	45.2	24.2	25.7	44.0	44.8
Mrk 501	0.4	13.8	15.7	17.6	44.0	44.9	23.0	24.8	44.1	45.0
PKS 2155 −304	0.2	14.6	16.0	17.3	45.7	46.5	24.2	25.7	45.3	46.2
1ES 2344 +514	0.5	14.1	16.0	17.9	43.3	44.2	23.0	24.8	43.4	44.3

Frequencies and luminosities are all given in *log*.

radio (millimeter) spectral index, α ; synchrotron break frequency, $\nu_s^{\rm br}$; synchrotron peak frequency, $\nu_s^{\rm p}$; synchrotron maximum frequency, $\nu_s^{\rm max}$; synchrotron peak luminosity, $\nu_s^{\rm p} L_s(\nu_s^{\rm p})$; total synchrotron luminosity, $L_s^{\rm tot}$; SSC peak frequency, $\nu_C^{\rm p}$; SSC maximum frequency, $\nu_C^{\rm max}$; SSC peak luminosity, $\nu_C^{\rm p} L_C(\nu_C^{\rm p})$; total SSC luminosity, $L_C^{\rm tot}$;

The 7 input observables for the allowed parameter space are summarized in Table 10.2. $t_{\rm var}$ was determined from the characteristic time scale of the X-ray time variability found in this thesis (§ 8.2.3). We assume $t_{\rm var} = 1$ day for 1ES 2344+514, because its variability time scale is completely unknown, but longer than ~ 0.5 day (Figure 8.11). Other input quantities are same as Table 10.1, except for additional errors in the values of $\nu_C^{\rm max}$ and $L_C^{\rm tot}$. We add systematic errors of factor 3 and factor 2 in the values of $\nu_C^{\rm max}$ and $L_C^{\rm tot}$, respectively. This is because the Compton component is evaluated only from GeV/TeV γ-ray data, thus quite uncertain. On the other hand, the quality of the

synchrotron spectrum is much better than the Compton specturm, so we can neglect the errors on $\nu_s^{\rm max}$ and $L_s^{\rm tot}$.

Table 10.2: Input observables for individual TeV blazars

source	α	$\nu_s^{\rm br}$ (Hz)	$\nu_s^{\rm max}$ (Hz)	$L_s^{\rm tot}$ (erg/s)	$\nu_C^{\rm max}$† (Hz)	$L_C^{\rm tot}$† (erg/s)	$t_{\rm var}$ (sec)
Mrk 421	0.3	14.4	17.2	45.2	$25.7^{+0.5}_{-0.5}$	$44.8^{+0.3}_{-0.3}$	4.3×10^4
Mrk 501	0.4	13.8	17.6	44.9	$24.8^{+0.5}_{-0.5}$	$45.0^{+0.3}_{-0.3}$	1.0×10^5
PKS 2155 −304	0.2	14.6	17.3	46.5	$25.7^{+0.5}_{-0.5}$	$46.2^{+0.3}_{-0.3}$	3.0×10^4
1ES 2344 +514	0.5	14.1	17.9	44.2	$24.8^{+0.5}_{-0.5}$‡	$44.3^{+0.3}_{-0.3}$	1.0×10^{5}‡

Frequencies and luminosities are all given in *log*.

radio (millimeter) spectral index, α ; synchrotron break frequency, $\nu_s^{\rm br}$; synchrotron maximum frequency, $\nu_s^{\rm max}$; total synchrotron luminosity, $L_s^{\rm tot}$; SSC maximum frequency, $\nu_C^{\rm max}$; total SSC luminosity, $L_C^{\rm tot}$; variability time scale, $t_{\rm var}$;

† Uncertainties of factor 3 in the value of $\nu_C^{\rm max}$ and factor 2 in the value of $L_C^{\rm tot}$ are taken into account.

‡ ; assumed to be equal to Mrk 501, because EGRET detection has not been reported.

Mrk 421

In Figure 10.12, we show the parameter space for Mrk 421 (*right*). Thin region is the allowed space derived from the *quiescent* SED of Mrk 421 (Table 10.2 and Figure 10.12 (*left*)). Uncertainties of factor 3 in the value of R, factor 10 in $t_{\rm esc}$ and the reduction of Compton flux in the Klein-Nishina regime (up to factor 10) are considered. We also investigate the allowed parameter space for various flaring states plotted in Figure 9.5. Filled area is the overlapped region. The solid vertical line is the lower limit from the transparency condition derived from TeV γ-ray/optical correlation in time variability (Buckley et al. 1996; equation (10.28)).

We also plot the equipartition condition for the magnetic field density and synchrotron photon density, $U_B = U_s^{\rm avail}$. Dashed line with a label 'TM' is the case when all the scattering takes place in the Thomson regime, although this is unlikely for the TeV blazars (see the discussion in § 10.5). A line with a label 'KN' is the case when the scattering takes place in the Klein-Nishina regime, reducing the effective seed photon density by a factor of $\kappa = 10$. Both lines assume $R = c\, t_{\rm var}\, \delta$ for simplicity.

Importantly, this equipartition line divides the *synchrotron cooling dominant* region and *Compton cooling dominant* region in the δ−B plane. Synchrotron cooling approximation (see, § 10.2.1) is only valid in the right of this line, while in the left, Compton

cooling is more effective. Thus current allowed region for Mrk 421 indicates that the synchrotron cooling is more dominant than Compton cooling process, even in the Thomson scattering limit. This is consistent with the fact that $L_s^{\rm tot}$ is larger by factor ~ 3 than $L_C^{\rm tot}$ (Figure 9.5).

Finally, we superpose a constraint from the observed time-lags in various X-ray energy band (Takahashi et al. 1996). Synchrotron cooling is assumed to be dominant cooling process. The line is appeared as a flat solid line ($B \propto \delta^{-1/3}$) with measurement errors on the lag (dotted lines). It is extremely important that this line, which is completely independent of the spectral constraints, is nicely in agreement with the parameter region allowed by those constraints.

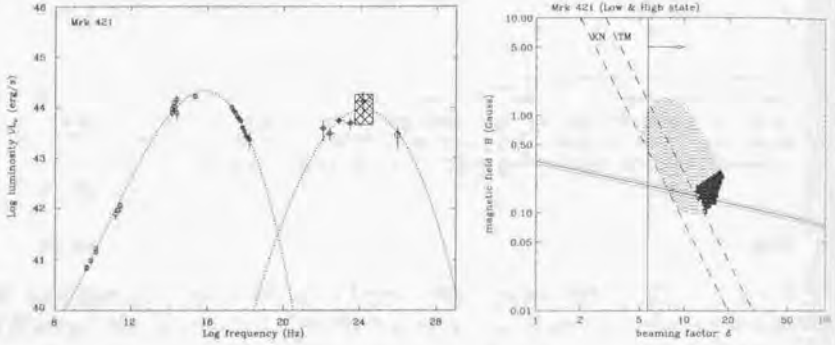

Figure 10.12: *left*: polynomial (cubic) fit of νF_ν spectrum of Mrk 421. Hatched region is the uncertainty associated with the estimates of $\nu_C^{\rm p}$ (factor 3) and $L_C^{\rm p}$ (factor 2). *right* : the parameter space (δ, B) allowed by the one-zone SSC model for Mrk 421 data. Thin region is the allowed space using only SED data for quiescent state (*left*), while thick region is the overlapped region for various source activities (Figure 9.5). Solid line put in dashed lines is a limit derived from X-ray observation of 'time-lags', assuming the synchrotron cooling process. Vertical line is the limit from TeV γ-ray/optical transparency condition. Dashed lines show the equipartition between U_B and $U_s^{\rm avail}$, which divides the dominance of synchrotron/Compton cooling processes. Lines for Thomson limit and Klein-Nishina limit are separately shown.

Mrk 501

Figure 10.13 shows the parameter space for Mrk 501 (*right*). Thin region is the allowed space derived from the *quiescent* SED of Mrk 501 (Table 10.2 and Figure 10.13 (*left*)). Uncertainties in parameters are same as that for Mrk 421. Filled area is the overlapped

region with those derived for various flaring states (Figure 9.10). The solid vertical line is the lower limit from the transparency condition derived from TeV γ-ray/optical correlation in time variability (Catanese et al. 1997; equation (10.28)).

The equipartition condition for magnetic field density U_B and synchrotron density $U_s^{\rm avail}$ is shown as dashed lines. A line for pure Thomson limit and Klein-Nishina limit (s = 10) are separately shown. One finds that synchrotron cooling is dominant as long as scattering takes place in the Klein-Nishina regime. Unfortunately, no X-ray observation of 'time-lags' are reported, hence only spectral constraints are shown in the figure.

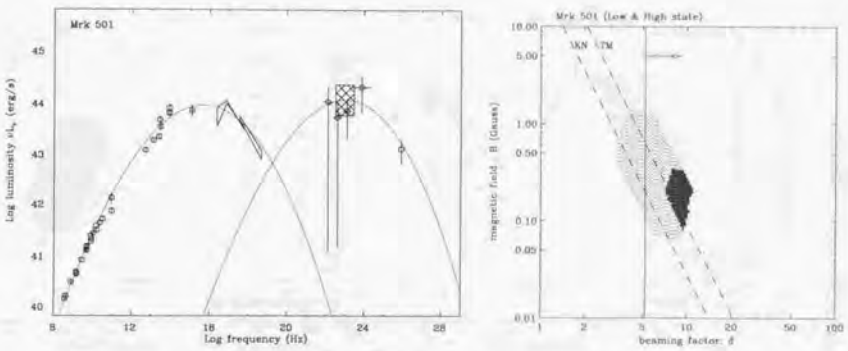

Figure 10.13: *left*: polynomial (cubic) fit of νF_ν spectrum of Mrk 501. Hatched region is the uncertainty associated with the estimates of $\nu_C^{\rm p}$ (factor 3) and $L_C^{\rm p}$ (factor 2). *right* : the parameter space (δ, B) allowed by the one-zone SSC model for Mrk 501 data. Thin region is the allowed space using only SED data for quiescent state (*left*), while thick region is the overlapped region for various source activities (Figure 9.10). Vertical line is the limit from TeV γ-ray/optical transparency condition. Dashed line shows the equipartition between U_B and $U_s^{\rm avail}$, which divides the dominance of synchrotron/Compton cooling processes. Lines for Thomson limit and Klein-Nishina limit are separately shown.

PKS 2155−304

Figure 10.14 shows the parameter space for PKS 2155−304 (*right*). Thin region is the allowed space derived from the *quiescent* SED of PKS 2155−304 (Table 10.2 and Figure 10.14 (*left*)). Uncertainties in parameters are assumed to be same as that for Mrk 421. Filled area is the overlapped region for those derived from *non*-simultaneous EGRET observations (see Figure 9.12). Transparency conditions cannot be calculated because no correlation of variability have been reported between synchrotron and Compton components.

Equipartition condition for U_B and $U_s^{\rm avail}$ are given as dashed lines, both for Thomson and Klein-Nishina case ($\kappa = 10$). Synchrotron cooling approximation is valid as long as scattering takes place in the Klein-Nishina regime. Also note that $L_s^{\rm tot}$ is larger by factor $\simeq$ 2 than $L_C^{\rm tot}$, which implies that synchrotron cooling dominates in this source (Figure 9.12). Another constraint from the observed time-lags in various X-ray energy bands (Kataoka et al. 2000) is given in narrow solid-dotted lines ($B \propto \delta^{-1/3}$). Similar to the case of Mrk 421, this line is exactly consistent with the parameter region *independently* determined from the spectral constraints.

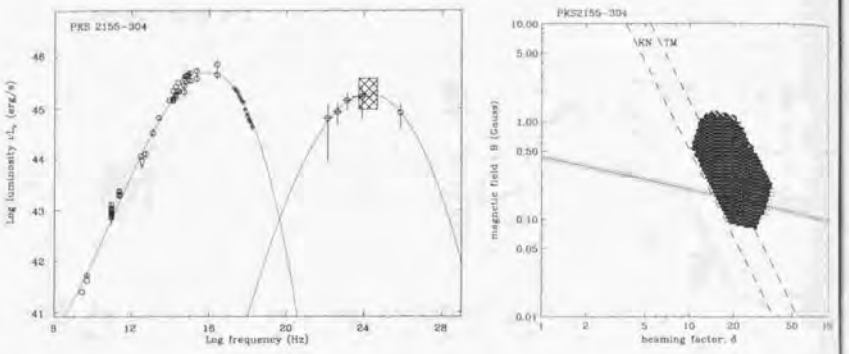

Figure 10.14: *left*: polynomial (cubic) fit of νF_ν spectrum of PKS 2155−304. Hatched region is the uncertainty associated with the estimates of $\nu_C^{\rm P}$ (factor 3) and $L_C^{\rm P}$ (factor 2). *right* : the parameter space (δ, B) allowed by the one-zone SSC model for PKS 2155−304 data. Thin region is the allowed space using only SED data for quiescent state (*left*), while thick region is the overlapped region with a higher state (Figure 9.12). Solid line put in dashed lines is a limit derived from X-ray observation of 'time-lags', assuming the synchrotron cooling process. Dashed lines show the equipartition between U_B and $U_s^{\rm avail}$, which divides the dominance of synchrotron/Compton cooling processes. Lines for Thomson limit and Klein-Nishina limit are separately shown.

1ES 2344+514

Figure 10.15 shows the parameter space for 1ES 2344+514 (*right*). Thin region is the allowed parameter space derived from the *quiescent* SED of 1ES 2344+514 (Table 10.2 and Figure 10.15 (*left*). Since the data are too sparse especially in the γ-ray (EGRET) range, we conveniently assumed a polynomial function of Mrk 501, just by changing the normalization. Luminosity ratio, $L_s^{\rm tot}/L_C^{\rm tot}$, is assumed to be equal in these two sources. Thus following 'allowed region' may be fault if the Compton spectrum of 1ES 2344+514

is completely different from the Mrk 501. Transparency conditions cannot be calculated because any correlations of time variability has not been reported.

The equipartition condition for magnetic field density U_B and synchrotron density $U_s^{\rm avail}$ is shown as dashed lines. Line for pure Thomson limit and Klein-Nishina limit (κ = 10) are separately shown. One finds that synchrotron cooling is dominant as long as scattering takes place in the Klein-Nishina regime. More observations in various energy bands are awaited for this source.

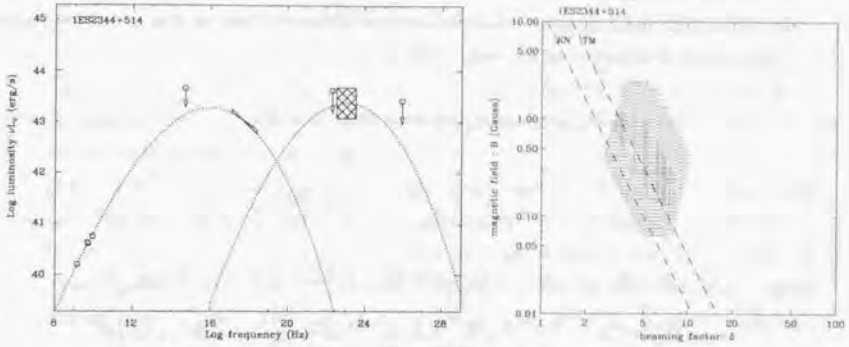

Figure 10.15: *left*: polynomial (cubic) fit of νF_ν spectrum of 1 2344+514. Hatched region is the uncertainty associated with the estimates of $\nu_C^{\rm P}$ (factor 3) and $L_C^{\rm P}$ (factor 2). *right* : the parameter space (δ, B) allowed by the one-zone SSC model for 1ES 2344+514 data. Thin region is the allowed space using only SED data for quiescent state (*left*), while thick region is the overlapped region for various source activities (Figure 9.14). Dashed line shows the equipartition between U_B and $U_s^{\rm avail}$, which divides the dominance of synchrotron/Compton cooling processes. Lines for Thomson limit and Klein-Nishina limit are separately shown.

Summary

In summary, the calculated physical quantities for TeV blazars are shown in Table 10.3 (5 of 7 parameters). We assumed parameters in the overlapped region of (δ, B) space, although these might be over-constraints if the photon distributions are far from equipartition in the flaring states. The limits listed here are only from the spectral constraints and additional constraints from observed 'time-lags' are not taken into account. Allowed space would be more tightly constrained for Mrk 421 and PKS 2155−304, if those limits are combined ($B \simeq 0.1$−0.2 G). Remaining two physical quantities are easily derived from these 5 parameters. The range of $t_{\rm esc}$ is just R/c−$10R/c$. Normalization of input electrons

q_e can be determined *uniquely* to agree with observed $L_\nu^{\rm tot}$, but it is difficult to express it in an analytical form.

Importantly, our derived parameter (Table 10.3) indicates that the magnetic field strength B and the maximum Lorentz factor $\gamma_{\rm max}$ of TeV blazars are very similar in the quiescent state. Since we assumed parameters in the overlapped region of (δ, B) space, these two parameters are not changed even in the flaring states. On the other hand, $\gamma_{\rm max}$ and q_e can vary in various states of source activity, as suggested from the different way of spectral evolution observed in Mrk 421 and Mrk 501 (§ 9). For an example, we expect that the $\gamma_{\rm max}$ of Mrk 501 increased to $\sim 5\times10^6$ when the source was in the high state, while B and δ stayed constant (see, § 11.7).

Table 10.3: Output physical quantities for individual TeV blazars

source	s	δ	B (G)	$R^\dagger$ (pc)	$\gamma_{\rm max}$
Mrk 421	1.6	12–18	0.1–0.3	$(1.6–7.4)\times10^{-3}$	$(0.9–1.8)\times10^6$
Mrk 501	1.8	7–11	0.1–0.4	$(1.9–10)\times10^{-3}$	$(1.9–3.8)\times10^5$
PKS 2155 −304	1.4	10–36	0.08–1.2	$(1.0–10)\times10^{-3}$	$(0.5–1.6)\times10^5$
1ES 2344 +514	1.9	3–10	0.06–2.5	$(0.8–8.4)\times10^{-3}$	$(1.3–7.1)\times10^5$

Resultant allowed parameter regions determined from the quiescent spectral energy distributions. Limits from observed 'time-lags' are not taken into account. Allowed space would be more tightly constrained for Mrk 421 and 2155−304, if 'time-lags' are considered ($B \simeq 0.1–0.2$ G). electron injection spectral index, s; beaming factor, δ; magnetic field strength, B; emission region size, R; maximum Lorentz factor of electron, $\gamma_{\rm max}$.
†: Uncertainties of factor 3 in the value of B is taken into account.

10.7 Motivation to develop a 'NEW' theoretical model

From detailed discussion in this chapter, we found that the spectral and temporal behaviour of TeV blazars is well explained by a simple one-zone SSC scenario. One of the most important discoveries is that the rapid X-ray time variability in blazars are probably characterized by 4 dynamical time scales: acceleration time $t_{\rm acc}$, cooling time $t_{\rm cool}$ and source light travel time t_{crs} and injection time $t_{\rm inj}$. It is, however, unfortunate that the most of the previous models consider *steady state* emission only, in spite of rapid variability which is often seen in blazars.

Very recently, several authors have started to develop *time-dependent* SSC model to

interpret the rapid variabilities and spectral evolutions of blazars. Mastichiadis & Kirk (1997) and Dermer (1998) considered time-dependent SSC models where the variability is on time scales longer than R/c (see, also § 2.3.2). However, our current results strongly predicts that the cooling time of the highest electrons is much shorter than t_{crs}, thus rapid variability could be relaxed (smoothed) by light travel time effects over the source. Chiaberge & Ghisellini (1999) and Kataoka et al. (2000) took this relaxation effect into account, but their models neglected the time scale for electrons to be accelerated ($t_{\rm acc}$).

Kirk & Mastichiadis (1998) considered more sophisticated scenario where a thin shock front propagates through the emission region with a finite velocity V_s, supplying freshly accelerated electrons only in the front's vicinity. They argued that the balance of acceleration and cooling processes plays an important role to characterize blazar's variability, in particular at $\gamma \sim \gamma_{\rm max}$. However, their model neglects the effects of smoothing of rapid variability by light-crossing time scale.

As a consequence, a time-dependent model which considers 4 dynamical time scales properly, has not been developed so far. To confirm many ideas discussed in this thesis and investigate the relative importance of those dynamical time scales, we developed a *new* time-dependent SSC code. This model is an improved version of a model presented in Kataoka et al. (2000). We introduced an acceleration term in the time dependent particle kinetic equation in the model. Thus all the relevant time scales, $t_{\rm acc}$, $t_{\rm cool}$, t_{crs} and $t_{\rm inj}$, are accurately considered in the code.

Since our code follows the full time evolution of electrons and photons in the source, we can study both the spectral evolution and temporal variability in blazars. For example, clockwise and anti-clockwise loop pattern can be simulated for various types of flares. Those results will be directly compared with the observational data (e.g., Figure 7.16). Our SSC code is also viable to predict possible variability patterns which may be observed in future, with a variety of balances of 4 dynamical time scales.

In § 10.6, we have investigated the allowed regions and successfully put constraints in the parameter space. In the next chapter, we will apply these *self-consistent* solutions to the observational data. We will also discuss the effects of cross section reduction in the Klein-Nishina regime, as well as relative importance of synchrotron/Compton cooling process in the next chapter.

Chapter 11

Time-Dependent SSC Model

11.1 One-zone Homogeneous SSC Model

We derive the standard solution for the one-zone homogeneous SSC model, assuming a *spherical geometry* of radius R.

For a general source at a distance d_L from the observer, the spectral energy flux $F(\nu)$ is determined by the photon emission coefficient j_ν and the absorption coefficient α_ν by

$$F(\nu) = \frac{1}{4\pi d_L^2} \int d^3\vec{r} \ [4\pi j_\nu(\vec{r}) \exp(-\int \alpha_\nu(\vec{r'}) ds')]. \tag{11.1}$$

This is an integral over the volume of the source with an exponential absorption factor involving a line integral from the source point ($\vec{r}$) through to the exterior of the source in the direction of the observer. For the synchrotron case, j_ν and α_ν are respectively given in equation (3.37) and (3.40).

Gould (1979) applied the solution for the synchrotron emission from a homogeneous sphere for which j_ν and α_ν are constants over the volume. The integration is trivial (see, Appendix I), yielding the synchrotron luminosity $L_{sync}(\nu)$ ($\equiv 4\pi d_L^2 F_{sync}(\nu)$)

$$L_{sync}(\nu) = 4\pi^2 R^2 \frac{j_\nu}{\alpha_\nu} (1 - \frac{2}{{\tau_\nu}^2}[1 - e^{-\tau_\nu}(\tau_\nu + 1)]), \tag{11.2}$$

where τ_ν is the optical depth in the blob along the line of sight and expressed as $\tau_\nu = 2\alpha_\nu R$. The electron pitch angle with respect to the magnetic field is set to $\alpha = \pi/2$.

We calculate the inverse Compton emission incorporating the effects of cross section reduction in the Klein-Nishina regime. The differential photon production rate, $q(\epsilon)$, is calculated from equation (3.49). Note that for the SSC model, $n(\epsilon_0)$ is the number density of *synchrotron photons produced by the same electrons*, per energy interval. To be exact, $n(\epsilon_0)$ varies depending on the position in the emission blob and we have to take this effect

into account (Gould 1979). Approximately, we calculated $n(\epsilon_0)$ at the center of the blob with the correction factor $C_{\rm corr} = 0.75$ (see Appendix I). Thus we have

$$n(\epsilon_0) = \frac{4\pi}{hc\epsilon_0} C_{\rm corr} \frac{j_\nu}{\alpha_\nu}(1 - e^{-\alpha_\epsilon R}). \tag{11.3}$$

The Compton luminosity is obtained from the integration of equation (11.1) for the case of the SSC radiation

$$L_{\rm SSC}(\nu, t) = 4\pi^2 R^2 \frac{j_\nu^{\rm SSC}}{\alpha_\nu^{\rm SSC}}(1 - \frac{2}{\tau_\nu^{\rm SSC 2}}[1 - e^{-\tau_\nu^{\rm SSC}}(\tau_\nu^{\rm SSC} + 1)]), \tag{11.4}$$

where $j_\nu^{\rm SSC}$ is the emission coefficient of the Compton emission given in equation (3.53) and $\alpha_\nu^{\rm SSC}$ is the absorption coefficient of the Compton emission, respectively. Since the optical depth for the self absorption, $\tau_\nu^{\rm SSC}$, is negligibly small for the Compton emission, we approximated it as zero:

$$L_{\rm SSC}(\nu, t) \simeq \frac{16}{3}\pi^2 R^3 j_\nu^{\rm SSC}. \tag{11.5}$$

11.2 Application to the Time-Dependent Model

11.2.1 Assumptions

Our kinetic code was developed as an application of a homogeneous SSC model for the steady state, which represents spectra of TeV blazars in the quiescent state. In the code, we assume a model in which electrons are accelerated at a shock front and cool by synchrotron and inverse Compton radiation in the homogeneous magnetic field behind it. Similar to Kirk, Rieger & Mastichiadis (1998), we treat two spatial zones: one around the shock front, in which the particles are continuously accelerated (acceleration region), and one downstream of the shock front, in which the electrons emit most of the radiation (emission region). The emission region has a spherical volume of radius R. We assume both regions are connected closely in space. The electrons in the shock's vicinity will escape from the acceleration region at a constant rate $r_{\rm esc}$, and are *uniformly* injected into the emission region. Thus the injection rate of electrons into the emission region is exactly the same as the escape rate from the acceleration region. The shematic view of our modeling is given in Figure 11.1.

Thus we need two kinetic equations of electrons corresponding to each region. For the acceleration region, we have

$$\frac{\partial N_s(\gamma, t)}{\partial t} = \frac{\partial}{\partial \gamma}[(\beta_s \gamma^2 - \frac{1}{t_{{\rm acc},s}}\gamma) N_s(\gamma, t)] + q_s \delta(\gamma - \gamma_0) - \frac{N_s(\gamma, t)}{t_{{\rm esc},s}}, \tag{11.6}$$

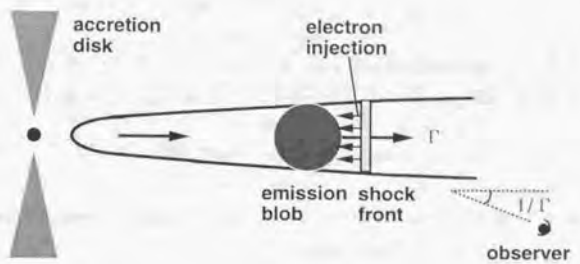

Figure 11.1: Schematic view of the model adopted in this thesis. The electrons are accelerated only in the shock's vicinity and escape at a constant rate. All of them are injected into the emission blob where they radiate.

and for the emission region,

$$\frac{\partial N_e(\gamma, t)}{\partial t} = \frac{\partial}{\partial \gamma}[(\gamma_{\rm sync} + \gamma_{\rm SSC}) N_e(\gamma, t)] + Q(\gamma, t) - \frac{N_e(\gamma, t)}{t_{\rm esc}}, \tag{11.7}$$

where N_s and N_e is the number density of electrons per unit energy (see, § 3.6). The suffix s indicates the quantities in the acceleration region, while others are those in the emitting region. For simplicity, we approximate β_s as a constant value. For acceleration region, we assume low energy electrons are injected only at γ_0 ($\simeq 1$), and gradually accelerated to higer energies in a time scale characterized by $t_{{\rm acc},s}$. The maximum energy to which the electrons can be accelerated is determined by the balance of cooling and acceralation efficiency; $\beta_s \gamma_{\rm max}^2 = \gamma_{\rm max}/t_{{\rm acc},s}$.

11.2.2 Connection between Acceleration Region and Emission Region

The kinetic equation for the shock region (11.6) can be solved analytically, if we assume β_s and $t_{{\rm acc},s}$ has no dependence on energy. This corresponds to the case of $\xi = 0$ for equation (3.16). The solution is expressed as (see, § 3.1.5 or Kirk, Rieger, & Mastichiadis 1998)

$$N_s(\gamma, t) = \frac{A}{\gamma^2}(\frac{1}{\gamma} - \frac{1}{\gamma_{\rm max}})^{\frac{t_{{\rm acc},s} - t_{{\rm esc},s}}{t_{{\rm esc},s}}} \qquad (\gamma_0 < \gamma < \gamma_1(t)), \tag{11.8}$$

where

$$A = q_s t_{{\rm acc},s} \gamma_0^{\frac{t_{{\rm acc},s}}{t_{{\rm esc},s}}}(1 - \frac{\gamma_0}{\gamma_{\rm max}})^{-t_{{\rm acc},s}/t_{{\rm esc},s}}, \tag{11.9}$$

$$\gamma_{\rm max} = (\beta_s t_{{\rm acc},s})^{-1}, \tag{11.10}$$

$$\gamma_1(t) = (\frac{1}{\gamma_{\rm max}} + [\frac{1}{\gamma_0} - \frac{1}{\gamma_{\rm max}}]\exp(-t/t_{{\rm acc},s}))^{-1}, \quad (11.11)$$

As a result, the spectrum of accelerated electrons is well approximated by a power law up to a cut-off at the energy at which radiative losses balance energy gains:

$$N_s(\gamma,t) \simeq q_s t_{{\rm acc},s} \gamma^{-(1+\frac{t_{{\rm acc},s}}{t_{{\rm esc},s}})}. \quad (11.12)$$

Assume that the electron injection function $Q(\gamma,t)$ for the emission region is characterized by a power law in the same energy range ($\gamma_0 < \gamma < \gamma_{\rm max}$),

$$Q(\gamma,t) \simeq q_e \gamma^{-s}. \quad (11.13)$$

Since the electrons escape from the acceleration region in a time scale $t_{{\rm esc},s}$, and are injected into the emitting region, we have relations which connect the quantities in these two regions,

$$q_e \simeq q_s \frac{t_{{\rm acc},s}}{t_{{\rm esc},s}}, \quad (11.14)$$

$$s \simeq 1 + \frac{t_{{\rm acc},s}}{t_{{\rm esc},s}}, \quad (11.15)$$

$$\gamma_{\rm max} \simeq (\beta_s t_{{\rm acc},s})^{-1}. \quad (11.16)$$

11.2.3 Numerical Approach

In order to follow the time evolution of the radiation from the emission region, we have to solve a differential equation (11.7). Since we do not have analytical solution for this equation, due to the high non-linearity of the process involved, we have to solve the equation numerically.

Consider a well-defined electron population in the emission region, characterized by $N_e(\gamma,t)$. Given the electron population, the synchrotron emission including the self-absorption can be calculated using the spherical solution for the radiative transfer equation (11.2). The inverse Compton emission incorporating the effects of cross section reduction in the Klein-Nishina regime is calculated by equation (11.4).

The right-hand side of the equation (11.7) is now described by the quantities at time t, and solved numerically to obtain the electron population at time $t+\Delta t$. We adopted an implicit difference scheme by Chang & Cooper (1970), with some modifications for our purposes, since we are dealing with a kinetic equation with injection/escape terms and no diffusion term. This scheme is suitable for finding non-negative and particle number conserving solutions. Details of the techniques in calculations are given in Appendix J.

11.2.4 Light Travel Time Effects

In order to incorporate the light-travel time effects properly in the calculation, we divide the source into $(2t_{\rm crs}/\Delta t)$ slices of ΔR thickness for each, where $t_{\rm crs}$ $(= R/c)$ is the source light-crossing time and Δt is a time-step of the calculation. The interval Δt must be shorter than the shortest relevant time scale, e.g., radiative cooling times or acceleration time scale. We define $\Delta R \equiv c\Delta t$. The schematic view of this division of the emission blob into slices is given in Figure 11.2.

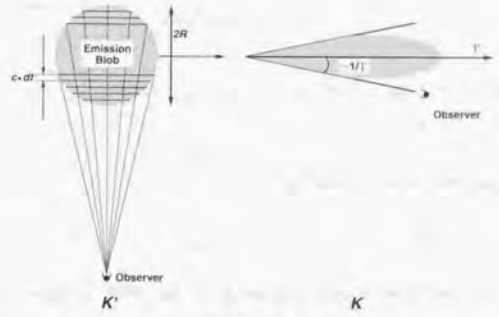

Figure 11.2: The schematic view of the division of the emission blob into 'slices'. Left Panel: Source frame (K'). Right Panel: Observer's frame (K). The emission blob is first cut into slices in the source frame and contributions from each shell are summed. In the observer's frame, the radiation is concentrated in a narrow cone with a half angle $\theta \simeq 1/\Gamma$.

We first consider the slices in the source frame K', with line of sight placed at 90° with respect to the surface of the slices. In the observer's frame K, emission will be concentrated in the forward direction within a narrow cone of half-angle $1/\Gamma$ (§ 3), if the blob moves with a Lorentz factor Γ ($\simeq \delta$ for our case). Volume of each slice is expressed as

$$\Delta V(k) = \pi(R-k)(R+k)\Delta R, \quad (11.17)$$

where k is the distance of the slice from the center of the sphere. Thus the 'weight' function normalized to the spherical volume $V_0 = 4\pi R^3/3$ is

$$w(k) = \frac{3(R-k)(R+k)\Delta R}{4R^3}. \quad (11.18)$$

This function is illustrated in Figure 11.3. The observer will see, at any given time, photons produced in different parts of the source, characterized by an electron distribution

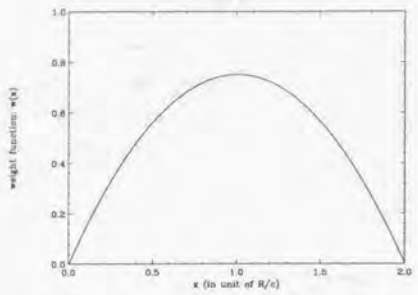

Figure 11.3: Weight function of 'slices' for spherical geometry. An integration of $w(x)$ from 0 to $2R/c$ is normlized to 1.

of a different age. This is expressed as

$$L_{\rm mod}(t) = L(t) \times w(R) + L(t - \Delta t) \times w(R - c\Delta t) ..... + L(t - 2R/c) \times w(R). \quad (11.19)$$

where $L(t)$ is the total luminosity emitted from the blob at time t and $L_{\rm mod}(t)$ is the *observed* luminosity at time t. Thus the observed spectra is a sum of different spectra, emitted from different slices at different times.

11.3 Acceleration of Electrons

11.3.1 Electron Injection at γ_0

We discuss the time evolution of electron spectrum in the acceleration region, based on the discussion in the previous section. The analytic solution (11.8) predicts a very sharp cut-off in the electron distribution at $\gamma = \gamma_1(t)$, which is reflected to the sharp cut-off in the synchrotron spectrum. However, observed photon spectra of blazars show very smooth curvature even in the X-ray band (e.g., § 9). This indicates that, in reality the broad cut-off in the electron spectrum. Such a smooth cut-off might be explained if we incorporate more realistic geometry and/or inhomogeneousness of the source. To mimic the observational photon spectra with 'broad' cut-off, we approximate the solution (11.8) in a simpler form with an exponential cut-off at $\gamma = \gamma_1(t)$. We thus obtain the approximate expressions for equations (11.8) – (11.11), holding the relations (11.14) – (11.16).

$$N_s(\gamma, t) \simeq q_s t_{{\rm acc},s} \gamma^{-(1+\frac{t_{{\rm acc},s}}{t_{{\rm esc},s}})} \exp(\gamma/\gamma_1(t)). \quad (11.20)$$

$$\gamma_1(t) = (\frac{1}{\gamma_{\rm max}} + [\frac{1}{\gamma_0} - \frac{1}{\gamma_{\rm max}}]\exp(-t/t_{{\rm acc},s}))^{-1}, \quad (11.21)$$

$$\gamma_{\rm max} = (\beta_s t_{{\rm acc},s})^{-1}, \quad (11.22)$$

In Figure 11.4, we show the time evolution of $N_s(\gamma, t)$ at $t = 0$, $t_{\rm acc}$, $4t_{\rm acc}$, $8t_{\rm acc}$ and 14 $t_{\rm acc}$. We assume here $t_{{\rm acc},s} = 10^5$ sec, $t_{{\rm esc},s} = 2.5\ t_{{\rm acc},s}$ and $\gamma_{\rm max} = 10^5$. For time $t \gg t_{\rm acc}$, the electron population does not change because $\gamma_1(t) \simeq \gamma_{\rm max}$. We divided $N_s(\gamma, \infty)$ by the escape time $t_{{\rm esc},s}$ to obtain the injection function $Q(\gamma)$ for the emitting region at the steady state (see, § 11.2.2).

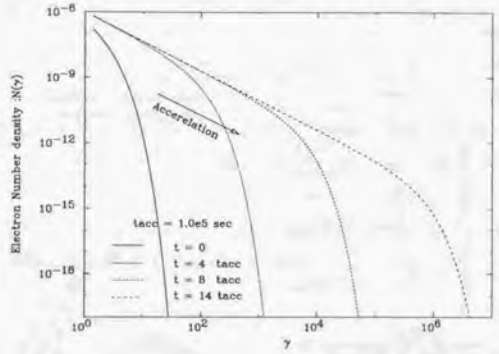

Figure 11.4: Evolution of the electron distribution which are constantly accelerated at rate $(t_{\rm acc})^{-1}$. Mono-energetic electrons ($\gamma = \gamma_0 \simeq 1$) are assumed to be injected into the acceleration region.

11.3.2 Evolution of Electron Distribution after Stopping the Injection

Assume that the 'fresh' electrons are injected only for $0 < t < t_{\rm inj}$, and injection stops after that ($t > t_{\rm inj}$). This may be one of the simplest models of flares in blazars. From the general solution of kinetic equation (3.59) with $Q(\gamma, t) \equiv 0$, one finds

$$N_s(\gamma, t) = \frac{K/t_{{\rm acc},s} - \beta_s K^2}{\gamma/t_{{\rm acc},s} - \beta_s \gamma^2} \exp(-t/t_{{\rm esc},s}) N_{s,0}(K), \quad (11.23)$$

where

$$K = [t_{{\rm acc},s}\exp(t/t_{{\rm acc},s})(\frac{1}{t_{{\rm acc},s}\gamma} - \beta_s) + \beta_s]^{-1}. \quad (11.24)$$

$N_{s,0}$ is the electron population at $t = t_{\rm inj}$.

Note that the electron population $N_{s,0}(K)$ has low-energy cut-off at $K = \gamma_0$, and high-energy cut-off at $K = \gamma_1(t_{\rm inj})$. From equation (11.24), we can calculate the shift of those cut-offs in time,

$$\gamma_0'(t) = [t_{{\rm acc},s}(\beta_s + \frac{1/t_{{\rm acc},s} - \beta_s\gamma_0}{\gamma_0 \exp(\frac{t-t_{\rm inj}}{t_{{\rm acc},s}})})]^{-1}, \tag{11.25}$$

$$\gamma_1'(t) = [t_{{\rm acc},s}(\beta_s + \frac{1/t_{{\rm acc},s} - \beta_s\gamma_1(t_{\rm inj})}{\gamma_1(t_{\rm inj})\exp(\frac{t-t_{\rm inj}}{t_{{\rm acc},s}})})]^{-1} \qquad (t > t_{\rm inj}). \tag{11.26}$$

The electron population at time $t(> t_{\rm inj})$ is well approximated by a simple function

$$N_s(\gamma, t) \simeq q_s t_{{\rm acc},s} \gamma^{-s} [\exp(-\gamma/\gamma_1'(t)) - \exp(\gamma/\gamma_0'(t))]. \tag{11.27}$$

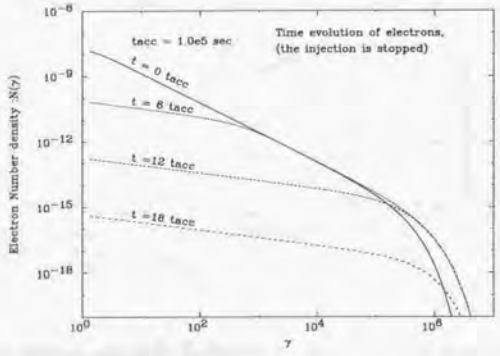

Figure 11.5: Evolution of the electron distribution after the injection has been stopped. In this particular case, the number of electrons reduces significantly at low energy, while highest energy electrons still be accelerated ($\gamma_1(t_{\rm inj}) < \gamma_{\rm max}$).

In Figure 11.5, we show an example of time evolution of electrons after the injection is stopped. We set $t_{{\rm acc},s} = 10^5$ sec, $t_{\rm inj} = 10 t_{{\rm acc},s}$, $\beta_s = 10^{-10}$, and $\gamma_0 = 1$. One finds that the maximum energy of electrons increases even after the stop of the injection, because in this particular case, $\gamma_1(t_{\rm inj}) < \gamma_{\rm max}$. Also note that the electron number density decreases significantly from low energy to higher energy.

11.4 Examples [I] – Steady State Emission

To verify the SSC code developed in this thesis, we show examples of the calculation. Further detailed modeling will be shown in the last part of this chapter, with application

to the observational data.

11.4.1 SSC Spectrum and Higher Order Comptonization

In order to follow the time evolution of the SSC spectrum, we start from the steady state solution of the Synchrotron self-Compton (SSC) model.

In Figure 11.6, we compute a SSC spectrum using our numerical code, with the same parameter set of Figure 5*a* in Band & Grindlay (1985). In the calculation, the electron population has a power law form $N_e(\gamma) = 4\times10^6\ \gamma^{-3}$, in a range $1 < \gamma < 10^4$. Source radius is $R = 2 \times 10^{14}$ cm. Our result agrees perfectly with their result. We also calculate the second order Comptonization spectrum for comparison, using the same formula (3.49). In the calculation, the incident photon density is now the photons from the first order inverse Compton scattering. Note, however, that these Componized spectra have slightly different slopes than those in Band & Grindlay (1985), especially in the lowest energy band ($\leq 10^{11}$ Hz). This is because we have neglected the self-absorption of Comptonized spectrum for simplicity. Strictly speaking, self-Compton photons are also absorbed by the electrons, although this effect is negligiblly small because the Compton flux is much lower than the synchrotron flux in this energy band.

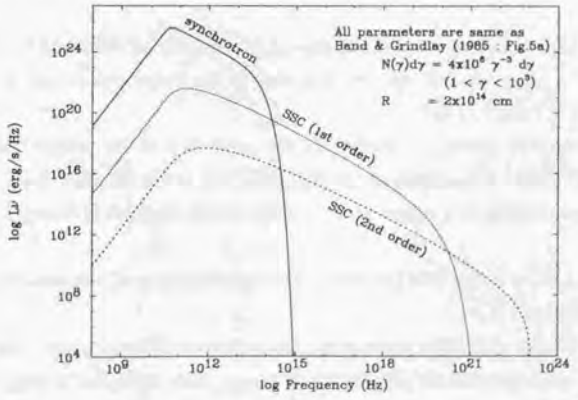

Figure 11.6: An example of synchrotron self-Compton spectrum calculated with our numerical code. All parameters are same as Figure 5*a* in Band & Grindlay (1985). We assume power law electron distribution of $N_e(\gamma){\rm d}\gamma = 4\times10^6\gamma^{-3}{\rm d}\gamma$ for $1<\gamma<10^4$ in a spherical source of $R = 2\times10^{14}$ cm.

11.4.2 Effects of the Changes in Parameters

In order to study the variety of spectral behavious observed from TeV blazars, it is important to investigate how the physical quantities in the emission region or parameters for the injected electron spectrum effects the photon spectrum. To highlight the effects caused by the changes of individual parameters, we have changed only one parameter with other parameters fixed. As a *baseline* of the spectral energy distribution, we choose magnetic field $B = 0.1$ G, region size $R = 1.0{\times}10^{16}$ cm, beaming factor $\delta = 10$, and the redshift $z = 0.1$, which are suggested from the observation (e.g., § 10). We adopt a specific form for the electron distribution from $\gamma_{\rm min}$ to $\gamma_{\rm max}$, $N(\gamma) = N_0\gamma^{-s}\exp(-\gamma/\gamma_{\rm max})$, where $\gamma_{\rm min}$ and $\gamma_{\rm max}$ is the minimum/maximum Lorentz factor of electrons, respectively. We choose $\gamma_{\rm min} = 1$, $\gamma_{\rm max} = 10^5$, $N_0 = 100.0$ (/cm^3) and $s = 2$ as a baseline.

Figure 11.7(a) shows the changes in SSC spectrum by varying the magnetic field B from 0.01 G to 1.0 G. Since the synchortron emission from a single electron is proportional to B^2 (e.g., equation (3.34)), flux becomes higher when B increases, while the ratio of synchrotron and Compton components does not vary. Also note that the peak frequency of synchrotron component increases as $\propto B$ (see, equation (3.32)).

Figure 11.7(b) is the change caused by the region size R. The flux increases as $\propto R^3$, because the total number of electrons is proportional to the volume of the emission region.

Figure 11.7(c) is the case of the change in beaming factor δ from 10 to 50. The change in the flux in a manner $\propto \delta^4$ and the blue shift of the frequency $\propto \delta$ are clearly seen (see, equation (3.71) and (3.74))

Figure 11.7(d) shows the changes in the redshift z of the source from 0.01 to 1.0. Because of the $d_{\rm L}^{-2}$ dependence of the flux, where $d_{\rm L}$ is the distance from the source, the flux changes roughly in a manner $\propto z^{-2}$ if the source redshift is changed (valid for $z \leq 1$).

Figure 11.7(e) is the changes due to the normalization of electrons N_0 and the flux changes just as $\propto N_0$.

Figure 11.7(f) shows the changes in the maximum electron Lorentz factor $\gamma_{\rm max}$ from 10^4 to 10^6. The synchrotron peak shifts as $\propto \gamma_{\rm max}^2$ (see, equation (3.32)), while the shift of the Compton peak at $\gamma_{\rm max} = 10^6$ is rather small. This is because the scattering takes place in the Klein-Nishina regime (see, § 3.4.2).

Figure 11.7(g) is the change due to the minimum electron Lorentz factor $\gamma_{\rm min}$. This does not affect the photon spectrum very much if $1 < \gamma_{\rm min} < 100$, while makes sharp cut-off in low-energy photon spectrum if $\gamma_{\rm min} > 100$.

Finally, Figure 11.7(h) shows the changes in the spectral index of electrons s from 1.5 to 2.5. This is reflected to the photon spectral index p as $p \propto (s-1)/2$ (e.g., Rybicki & Lightman, 1979), but the spectral shape is not changed for the low-energy photons for which self-absoption is dominant.

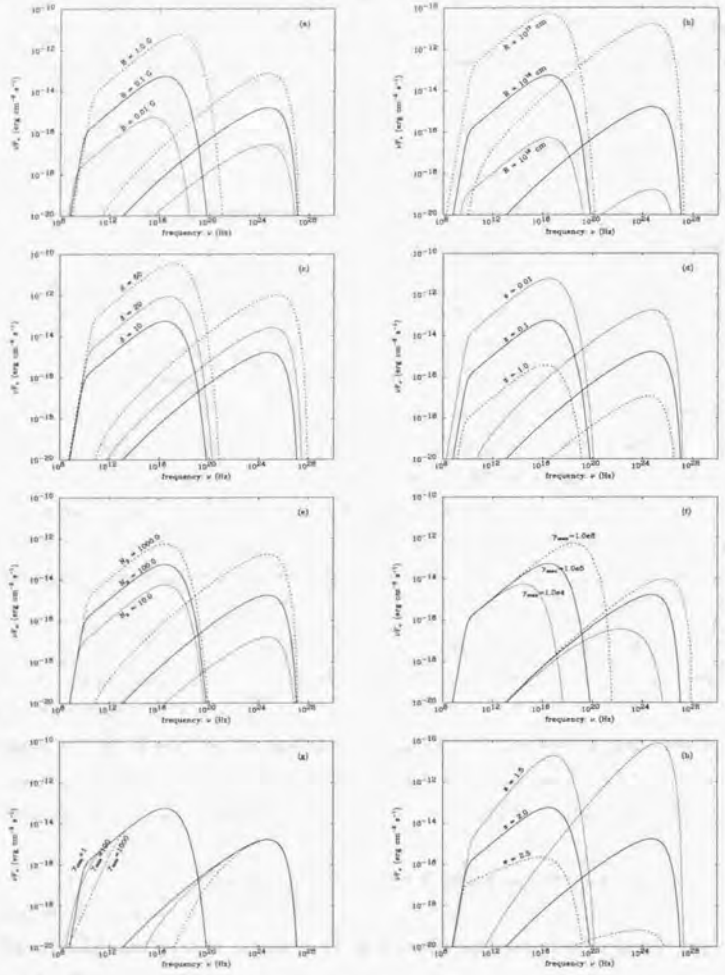

Figure 11.7: Synchortron self-Compton spectra for various parameter changes; (a) magnetic field B, (b) region size R, (c) beaming factor δ, (d) redshift z, (e) electron normalization N_0, (f) electron maximum Lorentz factor $\gamma_{\rm max}$, (g) electron minimum Lorentz factor $\gamma_{\rm min}$, and (h) electron spectral index s.

11.5 Examples [II] – Time Evolution

11.5.1 Synchrotron Cooling Model

We compare the time evolution of the electron spectrum derived from our code with the analytic solutions given by Kardashev (1962) and Makino (1998) for verification. In the calculation, we assume that electrons lose their energy only by synchrotron radiation, but not by the inverse Compon process. We also assume electron number is conserved, such that the injection rate $Q(\gamma) \equiv 0$ and the escape rate $N(\gamma)/t_{\rm esc} \equiv 0$. In this simplest case, the kinetic equation is given by

$$\frac{\partial N_e(\gamma,t)}{\partial t} = A\frac{\partial}{\partial \gamma}[\gamma^2 N_e(\gamma,t)], \tag{11.28}$$

where A is a constant

$$A \equiv \frac{4\sigma_{\rm T} U_B}{3 m_e c}. \tag{11.29}$$

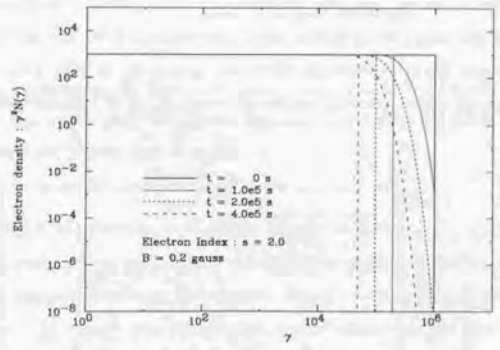

Figure 11.8: Time evolution of the electron spectrum by the synchrotron cooling process. We assume power law electron distribution of $N_e(\gamma) = N_0\gamma^{-2}$ ($1<\gamma<10^6$). The magnetic field is 0.2 G and inverse Compton losses are not taken into account. Electron spectra with sharp edges represent analytical solutions given by Kardashev (1962), while others (dull edge) are from the numerical calculation.

For the initial condition of $N_e(\gamma,0) = N_0\gamma^{-s}$ at time $t = 0$, the analytic solution of equation (11.28) is given by

$$N_e(\gamma,t) = N_0\gamma^{-s}(1 - At\gamma)^{s-2}, \qquad (\gamma At < 1) \tag{11.30}$$

and $N_e(\gamma,t) = 0$ otherwise (e.g., Kardashev 1962). In Figure 11.8, we show the time evolution of electron energy spectrum for $s = 2$ and $B = 0.2$ G calculated from our numerical code. The results obtained from analytical solutions are also given shown in the figure. Note that for all γ, analytic solution shows a sharp cut-off at $\gamma_c = 1/At$. Numerical calculation also shows cut-off at $\gamma_c = 1/At$, but rather smooth than the analytic solution.

11.5.2 Time Evolution of the SSC Spectrum and Light Curves

Once we have a numerical code that computes time evolution of the spectrum, we can simulate spectral evolution during a *flare* observed from TeV blazars. At the same time, we extract light curves by taking the light travel time effects into account.

It is very interesting to know the response to the flare-like injection of electrons in the emission region. We concentrate on a specific case defined as follows. First, no electron population exists at time $t = 0$, i.e. $N_e(\gamma, 0) = 0$. The mono-energetic electrons ($\gamma = \gamma_{\rm in}$) are injected for $0 < t < R/c$ and injection goes back to zero after R/c. For simplicity, we consider neither escape nor the acceleration of electrons. In this case, the electron population injected into the emission region is expressed by the delta-function, $Q(\gamma) = Q_0\delta\,(\gamma-\gamma_{\rm in})$, where Q_0 is a constant. Here we choose $\gamma_{\rm in} = 10^5$. The physical quantities in the emission region are assumed to be; $B = 0.1$ G, $R = 1.0\times10^{16}$ cm, $\delta = 10$ and $z = 0.1$.

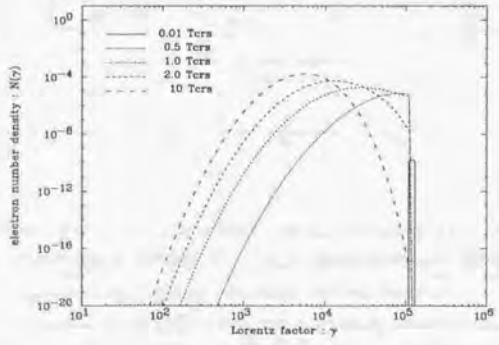

Figure 11.9: The spectral evolution of electrons at different times. We assume the mono-energetic electrons ($\gamma_{\rm in} = 10^5$) are injected only for $0<t<R/c$ ($= t_{\rm crs}$). The electron spectra at $t = 0$, $0.5t_{\rm crs}$, $t_{\rm crs}$, $2t_{\rm crs}$ and $10t_{\rm crs}$ are shown respectively.

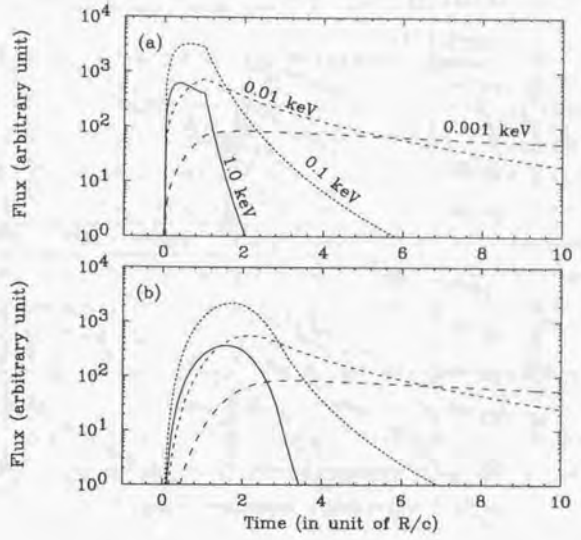

Figure 11.10: Light curves of the flux at different energy bands from 0.001 keV to 1.0 keV, in observer's frame. The upper panel (a) shows the case of ignoring the light travel time effects, while the lower panel (b) taking into account.

The time evolution of electrons is shown in Figure 11.9. For $0 < t < R/c$, accumulation of fresh electrons and the energy loss by synchrotron radiation occur at the same time, enhancing low-energy population in the number density distribution of electrons. It should be noted that the high energy end of electron distribution reaches the equilibrium state in a very short time ($\leq 0.5\,t_{\rm crs}$) and does not vary for the rest of the injection time. After $t > R/c$, total number of electrons becomes constant, but the peak of the distribution moves to lower energy, by the radiative cooling.

Figure 11.10 shows the corresponding light curves of synchrotron fluxes at various energy bands. The upper panel shows the light curves when the light travel time effects are not taken into account. Since we assume an instantaneous and uniform injection throughout the source, the rise time of the flux is much shorter than R/c, especially at $\gamma\sim\gamma_{\rm in}$. The *plateau*-like structure can be seen in the light curve, especially energy above 0.1 keV. Although the rise time varies in different energy bands, peaking time is roughly $\sim R/c$ for all energy bands. The lower panel shows the light curves, when the light travel

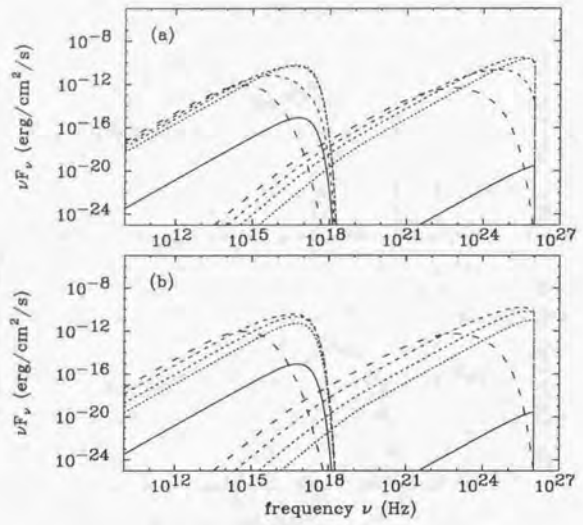

Figure 11.11: Evolution of synchrotron self-Compton spectra at different times. The dashes and solid line show the photon spectra at $t = 0,\ 0.5t_{\rm crs},\ t_{\rm crs},\ 2t_{\rm crs}$ and $10t_{\rm crs}$. Notation of lines are same as Figure 11.9.

time effects are properly taken into account. In this case, the light curve at high energy band (1.0 keV) has symmetric shape and very similar to the weight function $w(x)$, in Figure 11.3. This symmetry is broken for lower-energy light curves, which have longer decay times than R/c. In the low-energy band, time constant for the decay is dominated by the cooling effect. It should be noted that the peaking time in Figure 11.10(b) is energy dependent, such that the lower energy peaks lag behind the high energy peaks (see also, Chiaberge & Ghisellini 1999).

Finally, we show the time evolution of both the synchrotron spectra and the self-Compton spectra in Figure 11.11. The upper panel (a) shows the evolution ignoring light travel time effects, while the lower panel (b) considers smoothing by the source light-crossing time scale. It is clearly seen that the multi-frequency spectra evolves more slowly if the light travel time effect is taken into account.

11.6 Comments on the Time-Dependent Model

11.6.1 Emission from the Acceleration Region

In the previous sections, we have considered two spatial zones which are closely connected in space. One is around the shock front, in which particles are continuously accelerated, and the other is the downstream of it in which electrons emit most of the radiation (see, Figure 11.1). In our current modeling, we considered the radiation only from the latter, however, one may consider it inappropriate, because the acceleration region also has the magnetic field B_s thus can radiate. In the following, we will roughly estimate the synchrotron emission from the accelerating region (L_s), as compared to the radiation from the emitting region (L_e).

Let's denote the acceleration region size R_s and emitting region size R. Physically, R_s may corresponds to the boundary distance where inside of it, the particle effectively return to the shock front (see, § 3.1.4). Escape times from both regions are quite uncertain, however, one can envision that those values are order of region size divided by the light velocity (e.g., equation (3.14)). We then have approximate relations

$$t_{{\rm esc},s} \sim R_s/c, \quad t_{\rm esc} \sim R/c. \tag{11.31}$$

The ratio of both region sizes is given

$$\frac{R_s}{R} \sim \frac{t_{{\rm esc},s}}{t_{\rm esc}}. \tag{11.32}$$

Since the maximum Lorentz factor $\gamma_{\rm max}$ is determined by the balance between the acceleration and cooling around the shock front (equation (11.16)), the magnetic field strength B_s can be written

$$B_s = (C_s \gamma_{\rm max} t_{{\rm acc},s})^{-1/2}, \tag{11.33}$$

where C_s is a constant

$$C_s = \frac{4}{3}\frac{\sigma_{\rm T}}{m_e c}\frac{1}{8\pi}. \tag{11.34}$$

From the equation (11.12), the ratio of number density of electrons in both regions is given

$$\frac{n_s}{n_e} \simeq \frac{N_s(\gamma_{\rm min})}{N_e(\gamma_{\rm min})} = \frac{q_s t_{{\rm acc},s}}{q_e t_{\rm esc}} = \frac{t_{{\rm esc},s}}{t_{\rm esc}}, \tag{11.35}$$

where we use the relations (11.12) and (11.14).

Since the synchrotron luminosity is proportional to B^2R^3n, the ratio of synchrotron luminosities in both regions is calculated to be

$$\frac{L_s}{L_e} \simeq \frac{B_s^2 R_s^3 n_s}{B^2 R^3 n_e} = \frac{1}{B^2 C_s \gamma_{\rm max} t_{{\rm acc},s}} \left(\frac{t_{{\rm esc},s}}{t_{\rm esc}}\right)^4. \tag{11.36}$$

where we use the equation (11.32), (11.33) and (11.35). From the equation (11.15), we finally obtain,

$$\frac{L_s}{L_e} = \frac{1}{B^2 C_s \gamma_{\rm max} t_{{\rm acc},s}} \left(\frac{1}{s-1}\frac{t_{{\rm acc},s}}{t_{\rm esc}}\right)^l. \tag{11.37}$$

For example, if $B = 0.1$ G, $\gamma_{\rm max} = 10^5$, $t_{\rm esc} = 10^0$ s, $t_{{\rm acc},s} = 10^5$ s and $s = 2$, which are typical for blazars (e.g., Table 10.3), one finds that $L_s/L_e \sim 10^{-2}$. This value is probably the upper limit which corresponds to the case of $B_s \simeq B$. Note that for more shorter acceleration time $t_{{\rm acc},s}$ and stronger magnetic field B, this ratio becomes much smaller than 10^{-2}. We thus conclude that the radiation from the acceleration region is negligible compared to that in the emission region.

11.6.2 Scope for Improvement

We proceed under the assumption that electrons are injected uniformly throughout a homogeneous emission region. Such a description may be adequate as long as the injection time-scale is longer than R/c (Dermer 1998), but is unphysical for shorter time-scales since the particle injection process itself should take (at least) $\sim R/c$ to influence the whole region. In a more realistic picture, a thin shock front may propagate through the emission region with a finite velocity v_s, supplying freshly accelerated electrons only in the front's vicinity (Kirk, Rieger & Mastichiadis 1998). However, such a detailed calculation necessarily involves some additional, uncertain parameters, not to mention the assumption of a particular geometry. Instead, we will choose the injection to be uniform and instantaneous over the emission volume. Such a choice, albeit unrealistic, will allow us to clarify the role of light travel time effects on blazar variability (Below, however, we will also consider the duration of the injection to be comparable to R/c).

In our current assumption, synchrotron cooling process occurs uniformly and instantaneously over the emission region because (1) electrons are injected uniformly over the emission region and (2) the magnetic field strength is uniform throughout the blob. For the Compton scattering process, however, each electron should experience the changes in the photon field with some 'delay', which depends on the position in the emission blob. In other words, the synchrotron photons require the time $\sim R/c$ to fill up the blob to be scattered. This will cause additional delay for the response of Compton photon spectrum. However, for TeV blazars dealt in this thesis, the synchrotron cooling process must be dominant and the effects caused by Compton cooling process is small because (1) the synchrotron luminosity is greater or nearly equal to the Compton luminosity, and (2) the reduction of the cross section in the Klein-Nishina regime will significantly affect the Compton scattering efficiency. For these reasons, we approximate here that the synchrotron radiation (i.e., the soft photons for the inverse Compton scattering) instantaneously fills the whole of the emission region, just to reduce the computational time (see also Chiaberge & Ghisellini 1999).

11.7 Application to the Observational Data

11.7.1 Steady State Emission

In § 10.6.1, we successfully constrained the allowed regions for physical quantities of TeV blazars, assuming the relations expected by the homogeneous SSC scenario. In the following, we practically fit the multi-frequency spectra of TeV blazars using the one-zone SSC solution for a spherical geometry. 7 parameters for the model were determined to be consistent with the parameter regions we have constrained. For Mrk 421 and PKS 2155−304, the tightest constraint from the X-ray observations of 'time-lags' are considered as well as the spectral constraints. We summarize the 7 parameters for the SSC model in Table 11.1. Although there still remains flexibility in selected values of parameters, we note that our derived parameters are not affected by more than a factor of 2 even if taking the uncertainty of the observables into account (see, Table 10.3).

Table 11.1: Input model parameters for TeV blazars

source	s	δ	B (G)	R (pc)	$\gamma_{\rm max}$	$t_{\rm esc}$ (in R/c)	q_e ($\rm cm^{-3}s^{-1}$)
Mrk 421	1.6	14	0.13	5.9×10^{-3}	1.6×10^5	8	7.4×10^{-6}
Mrk 501	1.8	9	0.13	9.6×10^{-3}	3.1×10^5	8	3.8×10^{-5}
PKS 2155−304	1.4	28	0.14	7.7×10^{-3}	8.3×10^4	10	6.1×10^{-7}
1ES 2344+514	1.9	7	0.18	3.2×10^{-3}	4.4×10^5	6	3.2×10^{-3}

electron injection spectral index, s; beaming factor, δ; magnetic field strength, B; emission region size, R; maximum Lorentz factor of electron, $\gamma_{\rm max}$; electron escape time, $t_{\rm esc}$; electron normalization, q_e. We adopted a cutoff power law for the injected electron population : $Q(\gamma) = q_e\,\gamma^{-s}\exp(-\gamma/\gamma_{\rm max})$. We set the minimum Lorentz factor of the electrons, $\gamma_{\rm min} = 1$, for simplicity.

The input parameters for our SSC model are determined almost at the *center* of the allowed parameter region for different constraints discussed in § 10.6. To obtain the steady state solution for electron and photon spectra based on the parameters listed in Table 11.1,

we start from the initial condition $N_e(\gamma, 0) = Q(\gamma)$ and calculate the time evolution of the spectra to more than $t > 30\, t_{\rm cro}$, assuming constant injection and escape. We adopted a cutoff power law for the injected electron population: $Q(\gamma) = q_e\ \gamma^{-s}\ \exp(-\gamma/\gamma_{\rm max})$.

In Figure 11.12–11.15 (*left* panel), we show the synchrotron self-Compton model spectra at the *steady state*, superposed on the multi-frequency spectra for Mrk 421, Mrk 501, PKS 2155−304 and 1ES 2344+514. One can see that our SSC model lines are nicely consistent with the observational data, except for the discrepancy in the radio band. The discrepancy in the radio band can be an effect of the emission arising from larger distances than the location of the X-ray/γ-ray emitting region (e.g., Marscher 1980). In fact, VLBI observations of these objects have reveled that the radio emission comes from a very large region than that expected from the rapid X-ray/γ-ray time variability ($\geq$ 10 pc; see, Figure 10.9).

Right panel of each figure (Figure 11.12– 11.15) shows the ratio of electron cooling rate by synchrotron/inverse Compton radiation for the steady state. Horizontal line shows the electron Lorentz factor, while the vertical line shows the energy loss rate of an electron ($\gamma_{\rm sync,SSC}$; equation (3.34), equation (3.54)) multiplied by γ^{-2}. Those values are constant for synchrotron loss ($\gamma_{\rm sync} \propto \gamma^2$), hence normalized to a unity. Corresponding *ASCA* energy band is shown as dashed lines (0.7–10 keV; equation (3.33)). Importantly the ratio $\gamma_{\rm SSC}/\gamma_{\rm sync}$ exactly coincides with $U_{\rm sync}/U_B$ for low-energy electrons, while Compton scattering efficiency reduces significantly for the high energy electrons due to the cross section reduction in the Klein-Nishina regime. One finds that synchrotron cooling is more dominant in the X-ray band, which is in fact consistent with our previous assumption (§ 10.6).

Table 11.2 shows the energy densities of photons, magnetic field and electrons derived from the SSC fit of each source. *Effective* synchrotron photon density, $U_{\rm sync}^{\rm avail}$, was calculated simply from equation (10.21). One finds that for these TeV blazars, there exists an approximate equality between U_B and $U_{\rm sync}$, however, Klein-Nishina effect reduces the soft photon density which are effectively involved in the self-Compton scattering process ($U_{\rm sync}^{\rm (avail)}$) by a factor of several. This also confirms our previous assumption of $1 < \kappa < 10$ to be valid (§ 10.6).

More importantly, electron energy density U_e is larger than U_B and $U_{\rm sync}$ by a factor of ~ 10. This indicates that the relativistic jets are particle dominated. Even when we take ambiguities in selected input parameters into account, this conclusion does not be affected. An implication that the particle energy dominates over magnetic energy density may pose an interesting issue on the jet formation mechanism. Most of the models of bulk acceleration of jets relied on some roles of magnetic field dominated situation. The present results seems to argue against such 'magnetic driven jet' formation. An alternative mechanism for jet formation is necessary to account for this.

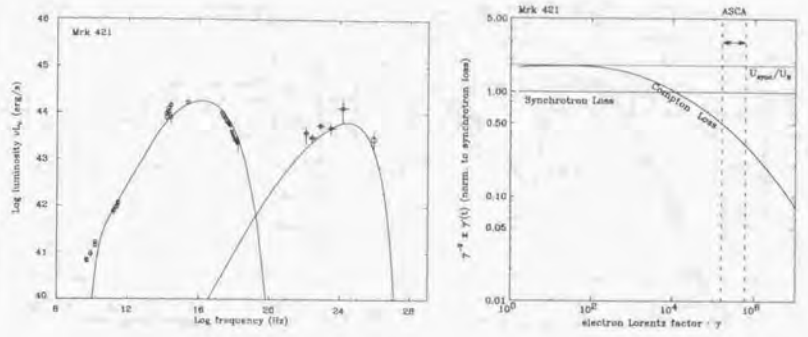

Figure 11.12: *left*: One-zone SSC model fit for the steady state emission of Mrk 421. Model parameters are given in Table 11.1. *right*: Ratio of electron cooling rate by synchrotron/inverse Compton radiation for the steady state of Mrk 421.

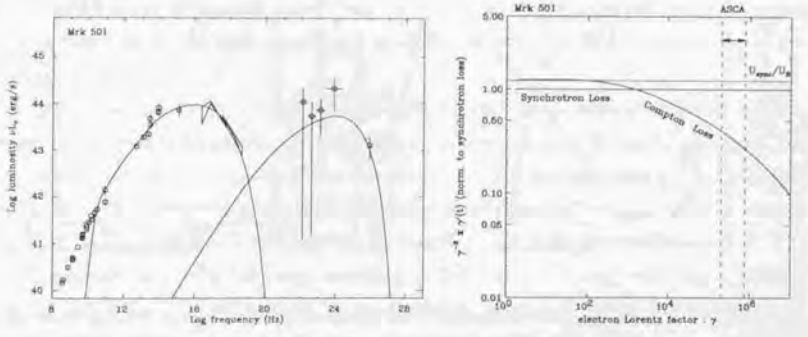

Figure 11.13: *left*: One-zone SSC model fit for the steady state emission of Mrk 501. Model parameters are given in Table 11.1. *right*: Ratio of electron cooling rate by synchrotron/inverse Compton radiation for the steady state of Mrk 501.

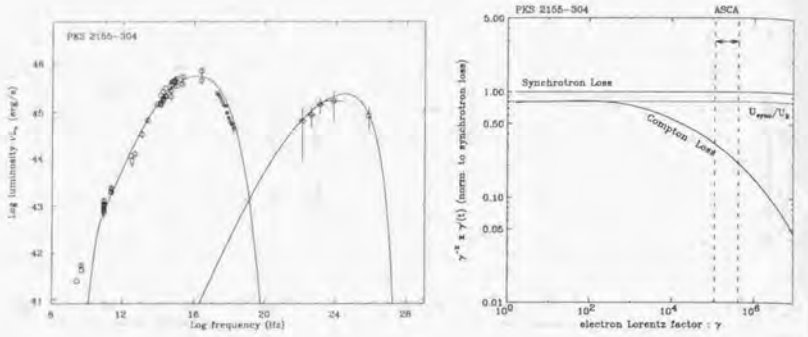

Figure 11.14: *left* : One-zone SSC model fit for the steady state emission of PKS 2155−304. Model parameters are given in Table 11.1. *right* : Ratio of electron cooling rate by synchrotron/inverse Compton radiation for the steady state of PKS 2155−304.

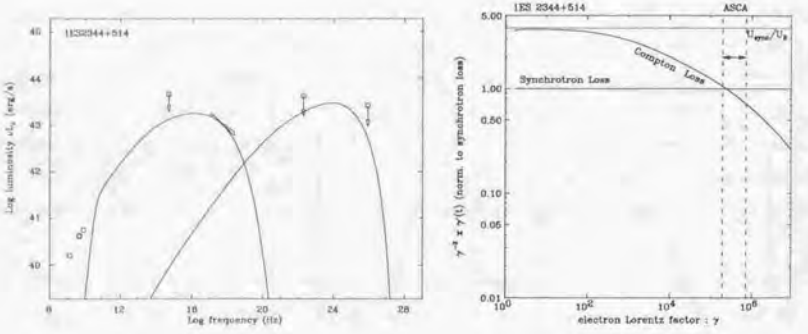

Figure 11.15: *left* : One-zone SSC model fit for the steady state emission of 1ES 2344+514. Model parameters are given in Table 11.1. *right* : Ratio of electron cooling rate by synchrotron/inverse Compton radiation for the steady state of 1ES 2344+514.

11.7.2 Modeling PKS 2155−304 Flare in 1994

Based on the physical parameters selected above, and the resultant 'steady state' spectrum as an initial condition, we model the X ray flare of PKS 2155−304 in 1994 May. This particular flare was selected because (1) the flare was isolated, excluding the effects caused by the superposition of many flare events, (2) amplitude of flare was large, and (3) 'time-lags' are observed in the various X-ray energy bands (Figure 10.2, 10.3). Since PKS

Table 11.2: Energy density of photons, magnetic field and electrons

source	U_B (erg/cm^3)	U_{sync} (erg/cm^3)	U_{sync}^{avail} (erg/cm^3)	U_{SSC} (erg/cm^3)	n_e (/cm^3)	U_e (erg/cm^3)	U_e/U_B
Mrk 421	7.1×10^{-4}	5.7×10^{-4}	2.4×10^{-4}	2.0×10^{-4}	7.0×10^{1}	3.3×10^{-3}	4.6
Mrk 501	6.6×10^{-4}	8.0×10^{-4}	3.7×10^{-4}	4.4×10^{-4}	4.8×10^{2}	6.2×10^{-3}	9.3
PKS 2155 −304	8.2×10^{-4}	6.6×10^{-4}	3.5×10^{-4}	2.8×10^{-4}	1.6×10^{1}	2.9×10^{-3}	3.5
1ES 2344 +514	1.3×10^{-3}	4.9×10^{-3}	2.0×10^{-3}	7.6×10^{-3}	9.4×10^{3}	7.3×10^{-2}	56

Energy density of photons, magnetic field and electrons derived from the steady state SSC model fit. Parameters are given in Table 11.1. magnetic field; U_B, total synchrotron photon density; U_{sync}, *effective* synchrotron photon density; U_{sync}^{avail}, self-Compton photon density; U_{SSC}, number density of electrons; n_e, energy density of electrons; U_e, ratio of electron energy density and magnetic field density; U_e/U_B. Minimum Lorentz factor of electrons is assumed to be $\gamma_{min} = 1$.

2155−304 did not show any clear trends between the peak synchrotron luminosity and peak energy (Figure 8.19), an origin of the flare is not as clear as that for Mrk 421 and Mrk 501 (§ 10.4). Various types of flaring behavior were thus investigated by changing the parameters for the injected electron spectrum and/or the physical quantities in the emission region.

In the following, we simulated the light curves, as well as the time evolution of spectra, when γ_{max} increased by a factor of 1.6 during one t_{crs} interval from the start of the flare. For this particular case, a model fit of the time-lags (§ 10.2.4) revealed that t_{acc} is consistent with zero, which corresponds to the rapid electron injection up to γ_{max}. We thus assume $t_{acc} \simeq 0$ and γ_{max} changed *instantaneously* during the flare for the present case.

We varied the injected electron spectrum as $Q_e(\gamma) = q_e\ \gamma^{-s}\ \exp(-\gamma/1.6\gamma_{max})$ for $0 \leq t \leq t_{crs}$ and $Q_e(\gamma) = q_e\ \gamma^{-s}\ \exp(-\gamma/\gamma_{max})$ otherwise. After the calculation was performed in the source frame, it was transformed into the observer's frame for comparison with the observational data. We take the time-step to be $\Delta t = 2000$ sec throughout the calculation. This corresponds to $\Delta t < 100$ sec in the observer's frame, much shorter than the variability time scales, such as the synchrotron cooling time.

In Figure 11.16, we show the calculated light curves from *EUVE* to *ASCA* energies. The flux was normalized to that for the steady state ($t = 0$), and the time axis was normalized to the source light-crossing time-scale (R/c). The symmetric light curve during the flare is reproduced quite well. Notably, the peaking time of the flare at lower energies lags behind that for higher energies, and the amplitude of the flare becomes larger as

the photon energy increases,which agree qualitatively with the observational data (Figure 10.2).

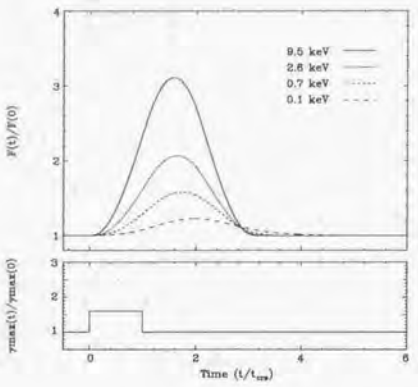

Figure 11.16: Upper Panel: Simulated light curves at different UV/X–ray energies, reproducing the rapid flare of PKS 2155−304 in 1994 May. We plotted the time evolution of the fluxes at different frequencies, normalized to the initial ($t = 0$) value. The quasi-symmetric shape of the high energy light curves and the increasing time lag of the peak with decreasing energy is clearly seen. Lower Panel: Assumed change of $\gamma_{\rm max}$ during the flare. The $\gamma_{\rm max}$ is assumed to increase by a factor of 1.6 from the initial value for $0 \leq t \leq t_{\rm crs}$. Time-axes of both panels are in units of the source light-crossing time ($t_{\rm crs}$). In the observer's frame, $t_{\rm crs}$ corresponds to 0.3 day. Figure from Kataoka et al (2000).

Importantly, the position of the peak time is determined by the balance of slices in which the emitted flux is increasing and slices in which the decaying phase has already started. For example, at the highest X ray energy band which corresponds to $\gamma \sim \gamma_{\rm max}$, the peak of the light curve will occur at a time t, where $t_{\rm crs} < t < 2t_{\rm crs}$. This is because these electrons in the slices cool much faster than $t_{\rm crs}$ and the volume which contains the flare information is maximum at the center of the sphere, which can be observed after $t_{\rm crs}$ from the start of the flare (see Figure 11.2). The whole emission region requires $2\,t_{\rm crs}$ to be completely visible to the observer. This will cause a decaying of the flux (foreside slices) and an increasing of the flux (backside slices) at the same time. However, in the lower energy band where $t_{\rm cool} \gg t_{\rm crs}$, the electrons do *not* cool effectively. The emitted flux will continue to increase even after $2\,t_{\rm crs}$. This combination of the increasing/decreasing phase of slices can cause a time lag in the position of the peak as can be seen in Figure 11.16.

The dashed lines in Figure 11.17 (a) and (b) show the spectral evolution calculated from the adopted model. The $2-10$ keV flux was obtained by integration of the calculated spectrum in the $2-10$ keV band, so it can be readily compared with the observational data. The photon spectral index was simply determined from the ratio of the fluxes at 0.7 keV to 7.5 keV. Since the *ASCA* observation started after the onset of the flare, we shifted our simulated light curves in the time-axis for comparison. The fact that the peaking time of the photon index leads that for the flux is quite well reproduced. This can be also seen in Figure 11.18, where the 'clockwise' hysteresis in the flux ($2-10$ keV) versus photon index ($0.7-7.5$ keV) plane can be clearly seen.

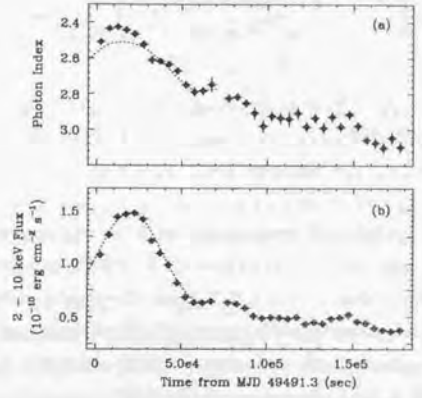

Figure 11.17: Detailed time history of PKS 2155−304 during the 1994 May campaign. Each data point corresponds to an equal 5 ksec interval and all SIS/GIS data are combined for the fit. The model is a power law with free absorption. (a): Variation of the differential photon index in the 0.7− 7.5 keV band. The dashed line is a model prediction as described in § 3. (b): Variation of the 2 - 10 keV flux in units of 10^{-10} erg cm^{-2} s^{-1}. The dashed line is a model prediction using our time-dependent code. Figure from Kataoka et al (2000).

To make a quantitative comparison of the observed and modeled light curves in different energy bands, we analyzed the light curves in the same way as that for the observational data (for comparison, see Figure 10.3). The dashed lines in Figure 11.19 (a)−(c) were calculated from a Gaussian fit of the simulated light curves, and converted to the observer's frame. Figure 11.19 (a) shows the duration of the flare, determined from the standard deviation (σ) of the Gaussian. This stays nearly constant at $\sim 1.5 \times 10^4$ sec, but the model shows a sign of increase at lower X ray energies – σ for 0.5 keV is 8 %

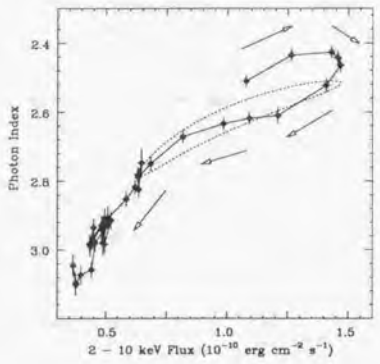

Figure 11.18: Evolution of the X-ray spectrum of PKS 2155−304, in the flux versus photon index plane. The solid line connects the observational data, while the dashed line is the model prediction from our time-dependent code. Figure from Kataoka et al (2000).

longer than that for 5.0 keV. Although we do not detect any such increase (broadening) in the observed X-ray light curves, flares observed by *EUVE* and *IUE* showed considerably longer time scales than that in the *ASCA* band (Urry et al. 1997). This may suggest that the duration of the flare actually increases at lower energies, if both flares have the same origin. Also note that the Gaussian fit of the simulated light curves could make systematic errors on σ, if the symmetry of the light curves is broken only in the lowest X-ray energy bands.

The amplitude of the flare ($Ap \equiv C_1/C_0$) was calculated to be 0.5 for 0.5 keV and 1.6 for 5 keV — precisely in agreement with the observational data (Figure 11.19 (b)). We compared the light curves at 5 keV to those for the lower energies, and found a 'soft-lag' where the $0.5 - 1$ keV photons lag behind 5 keV photons about 4 ksec, quantitatively in agreement with the observational data (Figure 11.19 (c)). Importantly, this result implies that the observed time lag is well represented by the difference of the synchrotron cooling time scales.

We also computed the discrete correlation function for the model light curves. The result is given in Figure 11.19 (d). Again, we obtained a similar result as with Gaussian fits, and verified a 'soft-lag' where the $0.5 - 1$ keV photons lag behind 5 keV photons about ~ 4 ksec.

Finally, in Figure 11.20 we show the time evolution of the multi-wavelength synchrotron self-Compton spectra after the start of the flare, at $t/t_{\rm cr} = 1.0$, 1.6 and 2.4 (for

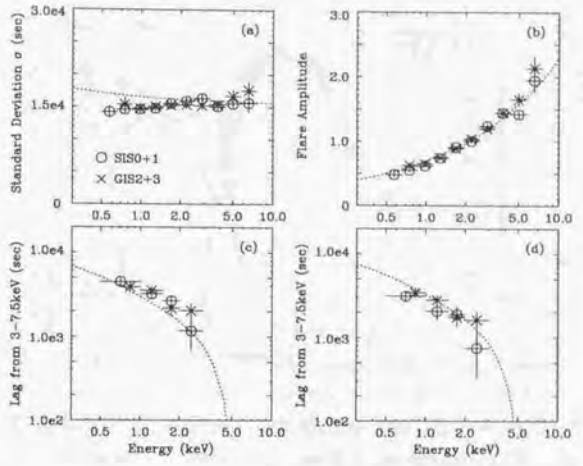

Figure 11.19: Measurement of the parameters describing the 1994 May flare of PKS 2155−304. Observational data are same as Figure 10.3, but model lines (dotted lines) are calculated using our time-dependent code.

comparison, see also Figure 11.16). The X-ray spectrum clearly becomes harder when the flux increases. Also note that the flux variation of the Compton spectrum is smaller than that for synchrotron spectrum. This is because the reduction of Compton cross section in the Klein-Nishina regime strongly suppresses the increase of the flux at the highest photon energies ($\sim h\nu_{\rm c}^{\rm max}$).

We also investigated other scenarios for the flare, such as increasing the normalization of the injected electrons ($q_{\rm e}$) or the magnetic field strength (B), but these did not give good representations of the data. In a more realistic situation, all of these parameters probably vary simultaneously, but our modeling implies that the most essential parameter during this particular flare is $\gamma_{\rm max}$.

11.7.3 Modeling Mrk 421 Flare

Next we consider variability patterns and spectral evolutions of Mrk 421. In the following, we will discuss *general* behaviours which are expected in various types of flares, rather than focusing on some particular flares which have been observed. In the subsequent analysis, we will consider a single, isolated, large amplitude variability for various changes

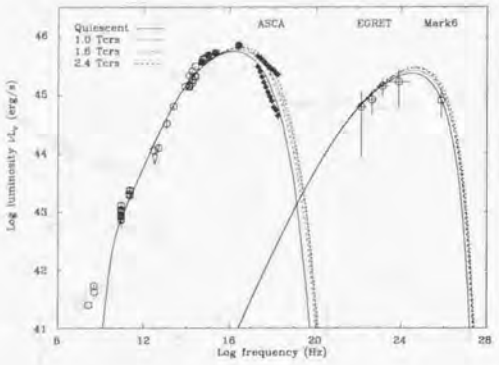

Figure 11.20: Multi-band spectrum of PKS 2155−304. The filled circles are the nearly simultaneous *IUE* and *EUVE* data reported in Urry et al. (1997). The filled squares are the X-ray data obtained with *ASCA* (this work). The solid line and dashed lines represent the time evolution of the photon spectra calculated from the time-dependent SSC model. The multi-frequency spectra at $t/t_{crs} = 0$, 1.0, 1.6 and 2.4 are shown respectively. Figure from Kataoka et al (2000).

in physical parameters. More complicated situation (e.g., Figure 7.8), however, could be easily understood as a superposition of variety of such flare events. We assume that the duration of the change is impulsive, and continues $\Delta t = t_{crs}$ for simplicity. One can find a similar discussion, although including less variety, in Mastichiadis & Kirk (1997) in which variability is assumed to continue until both electron/photon distributions reach to the 'new' equilibrium state.

Flares due to Changes in δ

We first consider the case where the beaming factor δ changes impulsively by a factor of 2 (Figure 11.21). The symmetric time profile of the flare, whose rise-time and decay-time are characterized with t_{crs}, are clearly seen. Since the beaming factor is defined as $\delta = [\Gamma(1 - \beta)\cos\theta]^{-1}$ (§ 3.7.2), such situation is physically possible if the trajectory of the emitting blob is curved (e.g., local spatial bending of the jet: e.g., Wagner et al. 1993) or Lorentz factor Γ itself has been changed. In any case, Figure 11.21 shows that the resultant variability should be *coherent* in energy, which strongly contradicts to the observation. No time lags will be observed for time variability in various energy bands.

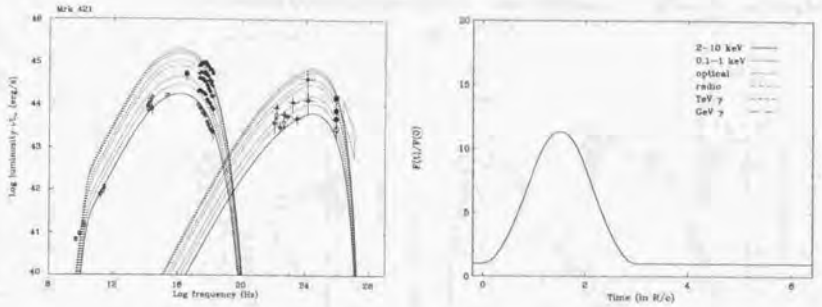

Figure 11.21: *left*: Evolution of the multi-frequency spectra of Mrk 421 in the case where the beaming factor (δ) changes impulsively by a factor of 2. Duration of the change is assumed to be t_{crs}. *right*: Plot of the flux at various frequencies (normalized to its queiscent value) for the flare that corresponds to a change in δ by a factor of 2.

Flares due to Changes in B

Next case is a flare due to the impulsive change in magnetic field strength B by factor of 3 (Figure 11.22). In this case, the whole synchrotron spectrum is blue-shifted ($\nu \propto B$) and boosted in intensity ($L_{\rm sync} \propto B^2$) although the observed amplitude becomes smaller because (1) flare duration is too short to reach a new equilibrium state and (2) strong cooling reduces the variability amplitude for the high energy electrons. Light travel time effect also reduces the amplitude because slices of increasing B and decreasing B are summed up at the same time.

It is reamarkable that the self-Compton flux, on the other hand, reduces significantly from its original value. This result is consistent with that discussed in Mastichiadis & Kirk (1997) and apparently contradicts the case we have shown in Figure 11.7 (a), in which the total electron distribution was held to be constant. Although such curious behaviour during a flare have never been observed, this case is interesting from the standpoint of the energetics in the jet.

In current case, we keep the electron injection rate $Q(\gamma)$ to be constant. Thus the electron kinetic energy input to the emission region per unit time per unit volume is

$$P_e = m_e c^2 \int_{\gamma_{\rm min}}^{\infty} (\gamma - 1) Q_e d\gamma, \tag{11.38}$$

For the high energy electrons, the sum of the synchrotron and inverse Compton energy loss (equation (3.34); 3.54) would be balanced with P_e, to reach a 'new' equilibrium state. In the situation where P_e is constant during the flare, increasing synchrotron luminosity

thus inevitably will cause the decrease in self-Compton luminosity.

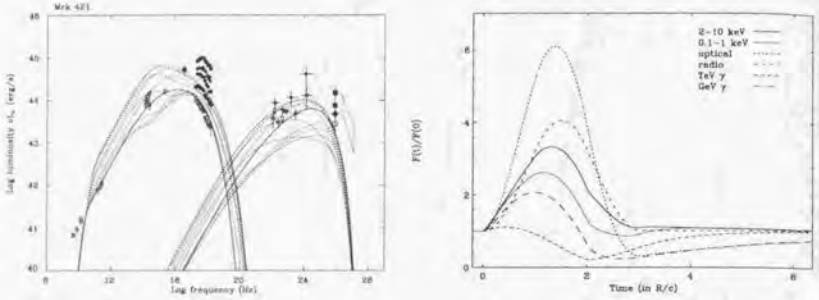

Figure 11.22: *left* : Evolution of the multi-frequency spectra of Mrk 421 in the case where the magnetic field strength B changes impulsively by a factor of 5. Duration of the change is assumed to be t_{crs}. *right* : Plot of the flux at various frequencies (normalized to its queiscent value) for the flare that corresponds to a change in B by a factor of 5.

Flares due to Changes in γ_{max}

The third case is a flare due to changes in the maximum Lorentz factor of electrons γ_{max} (Figure 11.23). γ_{max} was assumed to be changed instantaneously by factor of 5 for t_{crs}. This case of flare was good representation of the data for a particular flare observed for PKS 2155−304 (see § 11.7.2).

The result seems to describe adequately the variability of the self-Compton flux, however, X-ray spectrum becomes too flat compared to its relatively small changes in peak luminosity (Figure 11.23). Also note that the variability amplitude in the X-ray band is a factor 2 larger than that in the TeV energy band (*right* panel), which does not agree with the observational results where [X-ray flux] $\propto$ [TeV γ-ray flux] (see, Figure 9.3).

In this thesis, we found that the peak energy of the synchrotron component for Mrk 421 *did* shift during the flare, but the change was very small ($\sim 0.5 - 2$ keV) compared to the large amplitude variations in flux. We thus expect that the factor of ~ 2 changes practically expected in γ_{max}, but the *main* cause of the flux variation must be other than the changes in γ_{max}.

In this case, time lags will be observed in various energy bands. Observed lag will be consistent with that expected from the synchrotron cooling time scale in the X-ray energy band, because the synchrotron cooling is more dominant than Compton cooling

process (Figure 11.12). Amplitude becomes larger as the photon energy increases, which qualitatively agrees with the observational data (§ 7.2.2).

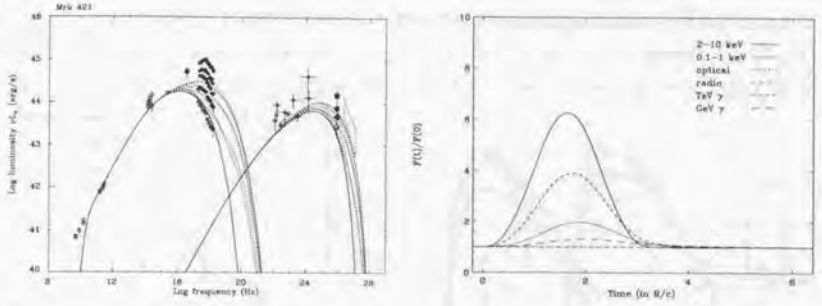

Figure 11.23: *left* : Evolution of the multi-frequency spectra of Mrk 421 in the case where the maximum Lorentz factor of electron (γ_{max}) changes impulsively by a factor of 5. Duration of the change is assumed to be t_{crs}. *right* : Plot of the flux at various frequencies (normalized to its queiscent value) for the flare that corresponds to a change in γ_{max} by a factor of 5.

Flares due to Changes in q_e

Finally, we simulate a flare due to the impulsive change in electron injection normalization q_e by a factor of 10. In this case, the model fit seems to be better than all of the previous cases from radio to γ-ray bands. Amplitude of variability becomes larger as the photon energy increases, but energy dependence is smaller than a case of the flare due to γ_{max}. Only discrepancy is the fact that the amplitude of variability in TeV band is larger than that in the X-ray band. The relation of variability amplitude in both energy bands is somewhat between the Thomson limit ([X-ray] $\propto$ [TeV γ-ray]^2) and the Klein-Nishina limit ([X-ray] $\propto$ [TeV γ-ray]) (see, § 10.5).

Time lags will be observed in various energy bands. Observed lag will be consistent with that expected from the synchrotron cooling time scale in the X-ray energy band, because the synchrotron cooling is more dominant than Compton cooling process (Figure 11.12). The symmetric time profile of the flare are only seen for high energy light curves (X-ray and TeV γ-ray). For radio−optical and GeV band, light curves are assymmetric whose rise time is characterized with t_{crs}, while decay-time is more longer cooling time (t_{cool}) or escape time (t_{esc}).

In summary, in the practical situation, we expect that both γ_{max} and q_e can vary during the flare of Mrk 421. However, large amplitude variations in flux are mostly due to the

increasing number of injected electrons (q_e). Linear correlation between the X-ray and TeV γ-ray flux can be also explained by the combination of these two types of variations. Time lags in various X-ray energy bands as well as the symmetric time profile are well represented by these simple models of the flare.

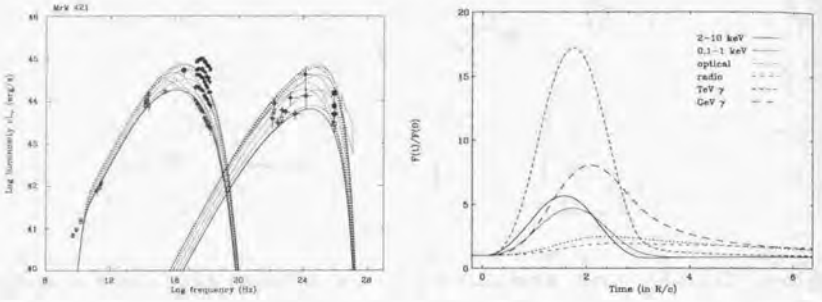

Figure 11.24: *left* : Evolution of the multi-frequency spectra of Mrk 421 in the case where the amplitude of electron injection (q_e) changes impulsively by a factor of 10. Duration of the change is assumed to be t_{crs}. *right* : Plot of the flux at various frequencies (normalized to its quciscent valne) for the flare that corresponds to a change in q_e by a factor of 10.

11.7.4 Spectral Evolutions

In the previous section, we found that the flare of Mrk 421 is well explained by the changes in q_e and $\gamma_{\rm max}$. Since for this particular source, the former is more important, we study the spectral behaviour during the flare in which q_e changes factor of 10 for $t_{\rm crs}$.

Rapid Electron Injection up to $\gamma_{\rm max}$

We first consider that fresh electrons are *instantaneously* injected into the emission region up to $\gamma_{\rm max}$. Thus for all electron energy bands, the relation $t_{\rm acc} \ll t_{\rm cool}$ holds. Although this situation may seem to be somewhat unphysical, this may occur when the tangled magnetic field in the acceleration region B_s is much stronger than that in the emitting region (see § 10 for more detail).

Figure 11.25 (*left*) shows the light curves of synchrotron component in various energy bands (the same situation as with Figure 11.24). One finds that (1) peak time of the flare lags in lower photon energy, and (2) light curves are symmetric for high energy band (t_{cool} $\ll t_{\rm crs}$), while the symmetry breaks down in the lower energy ($t_{\rm cool} \geq t_{\rm crs}$), both of which are exactly consistent with the observational data (Figure 10.2, § 7.2.3; 8.2.3).

Spectral evolutions during the flare is most conveniently expressed as a track pattern in the flux versus photon index plane. This expression is equivalent to the patterns of the brightness versus hardness, which was introduced in § 7.2.4. Figure 11.25 (*right*) shows variability patterns in various X-ray energy bands. One can see the canonical clockwise-loop in all energy-bands.

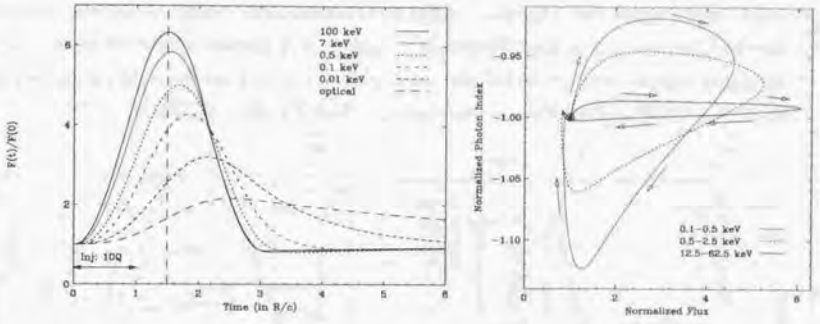

Figure 11.25: Simulation of a flare in which electron injection normalization changed by a factor of 10 for $t_{\rm crs}$. Electrons are assumed to be injected instantaneously up to $\gamma_{\rm max}$. *left* : Light curves of synchrotron component in various energy bands. *right* : Variability patterns in the flux versus photon index plane, which represents the spectral evolutions in various energy bands. One can see the canonical clockwise-loop in all energy-bands.

Acceleration of Electrons up to $\gamma_{\rm max}$

We next consider the case in which fresh electrons are mono-enegetically injected at $\gamma_{\rm min}$ for $0 < t < t_{\rm crs}$, and subsequently accelerated up to $\gamma_{\rm max}$. Acceleration time of the electrons are assumed to be $t_{\rm acc} = 8.0{\times}10^4$ (sec) in the source frame. For the SSC parameters of Mrk 421 assumed here (Table 11.1), current value of t_{acc} is roughly equal with the cooling time at ~ 1 keV. Thus this exmaple may correspond to the case in which the magnetic field in the accelerating region is almost eqaual to that in the emission region.

Figure 11.26 (*left*) shows the light curves of synchrotron component in various energy bands. Clear differences can be seen from the previous case: (1) start time of the flare is different in various energy bands, and (2) very little time-lags are observed in the X-ray energy bands. More precisely speaking, the peak time of the flare is fastest in the *ASCA*

energy band (0.5–7 keV), while in other wavelengths, peak-time will be lagged behind that in the *ASCA* band. Remarkably, hard X-ray (100 keV) variation also lags, showing the '*hard-lag*' behaviour.

This is more cleary seen in the flux versus photon index plane (Figure 11.26; *right*). In the hard X-ray energy bands, variability patterns track a loop in opposite direction, characterized with *anti*-clockwise motion. The possible patterns in 'clockwise' hysterisis were first discussed by Kirk, Rieger & Mastichiadis (1998). They argued that for the lower energy band where $t_{\rm cool} \gg t_{\rm acc}$, variability pattern is always a canonical clockwise loop, while around the maximum energy of electrons, *anti*-clockwise pattern could be observed because $t_{\rm cool} \simeq t_{\rm acc}$. Thus our simulation is consistent with their results. The balance of *soft-lag* due to the radiative cooling and *hard-lag* from the acceleration process determines whether clockwise or *anti*-clockwise loop is mainly observed.

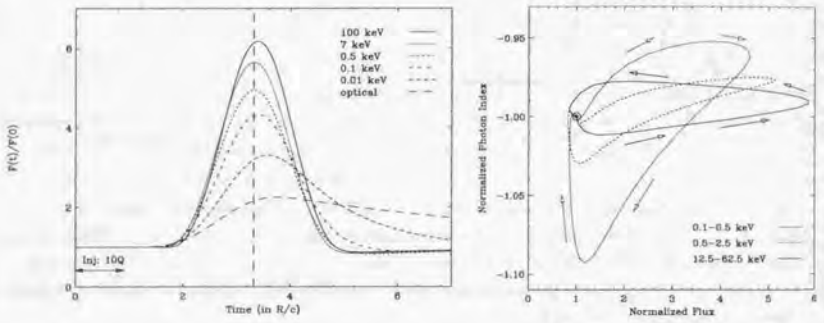

Figure 11.26: Simulation of a flare in which electron injection normalization changed by a factor of 10 for $t_{\rm crs}$. Electrons are assumed to be injected at $\gamma_{\rm min}$ and accelerated up to $\gamma_{\rm max}$ with a constant rate of $t_{\rm acc} = 8.0{\times}10^1$ sec in the source flame. *left* : Light curves of synchrotron component in various energy bands. *right* : Variability patterns in the flux versus photon index plane, which represents the spectral evolutions in various energy bands. One can see the canonical clockwise-loop in low energy bands (0.1–0.5 keV and 0.5–2.5 keV), while *unusual anti*-clockwise loop can be seen in the highest X-ray energy bands (12.5–62.5 keV).

Electron Injection Longer than $t_{\rm crs}$

Final example is where the fresh electrons are instantaneously injected into the emission region up to $\gamma_{\rm max}$ for 3 $t_{\rm crs}$. Only difference from the first case of Figure 11.25 is the duration of the flare, which was set to be $t_{\rm crs}$ in the previous case. Figure 11.27 (*left*)

shows the light curves of synchrotron component in various energy bands. One can see a *plateau* in the high energy light curves. In the low energy band (UV and optical), such structure in time profile is ambiguous, beause the rise-time of a flare itself is larger than 3 $t_{\rm crs}$. Interestingly, such a *plateau*, although not as common, has been observed for Mrk 421 during 1998 campaign (see, § 10.2; Figure 10.5). A plateau appears only when the duration of a change in electron injection ($t_{\rm inj}$) is larger than $t_{\rm crs}$, thus enough time is allowed for electrons/photons to reach a new equilibrium state.

Spectral evolution during the flare is most conveniently expressed as a track pattern in the flux versus photon index plane (Figure 11.27). As was the previous case of $t_{\rm inj} = t_{\rm crs}$, canonical clockwise-loops can be seen in all energy-bands.

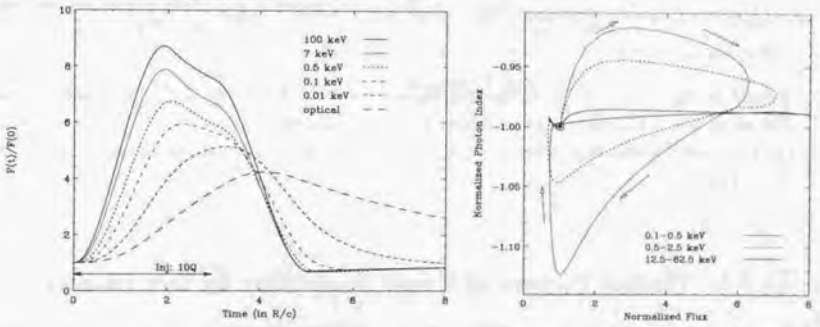

Figure 11.27: Simulation of a flare in which electron injection normalization changed by a factor of 10 for 3 $t_{\rm crs}$. Electrons are instantaneously injected at $\gamma_{\rm min}$. *left* : Light curves of synchrotron component in various energy bands. *right* : Variability patterns in the flux versus photon index plane, which represents the spectral evolution in various energy bands. One can see the canonical clockwise-loop in all energy bands (0.1–0.5 keV and 0.5–2.5 keV).

11.7.5 Modeling Mrk 501 Flare

Next we model the flaring behaviours in Mrk 501. In similarity to the case of Mrk 421, we considered various types of flares, rather than focusing on some particular flares which have been observed. Our previous discussion suggest that the flare of Mrk 501 is mostly due to the changes in $\gamma_{\rm max}$ as well as the spectral hardening during the flare (see, § 10.4).

In Figure 11.28 (*left*), we show the time evolution of Mrk 501 multi-frequncy spectrum during a single flare event. We assume $\gamma_{\rm max}$ changed by factor 20 ($\gamma_{\rm max} = 6{\times}10^6$) from the quiescent state and the electron injection spectrum hardens from $s = 1.8$ to 1.2. The

amplitudes of variation in various energy bands are qualitatively in agreement with the observation.

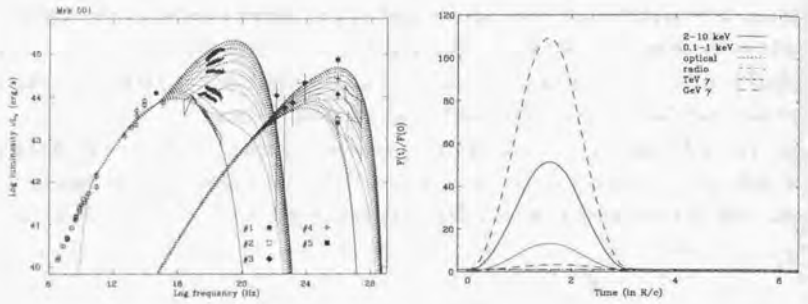

Figure 11.28: *left*: Evolution of the multi-frequency spectra of Mrk 501 in the flaring states. *right*: Plot of the flux at various frequencies (normalized to its quiescent value) for the Mrk 501 flare. During the flare, hard electron population ($s = 1.2$) with the maximum Lorentz factror of $\gamma_{\rm max} = 6\times10^6$ are injected for $t_{\rm inj} = t_{\rm crs}$.

11.7.6 Unified Picture of Rapid Variability in TeV Blazars

From the X-ray observations of TeV blazars, we have suggested in § 10 that the rapid variability events observed in blazars are well characterized by 4 dynamical scales; acceleration time: $t_{\rm acc}$, cooling time: $t_{\rm cool}$, source light travel time: $t_{\rm crs}$, and electron injection time: $t_{\rm inj}$. In this chapter, we have confirmed this scenario based on a newly developed time-dependent SSC model. Although the real situation may be much more complicated than we have imagined, those dynamical time scales should play important roles to specify time vaiability in blazars. We assumed here that the electron escape time ($t_{\rm esc}$) is always longer than $t_{\rm cool}$. Note, however, that if this relation is not correct, i.e., $t_{\rm cool} > t_{esc}$, we have to replace $t_{\rm cool}$ to t_{esc} because escape is more efficient than cooling process.

As a summary, we give a unified picture of rapid variability considering the balance of 4 dynamical time scales. Possible 24 (4!) patterns are reduced to 12 patterns by two physical constraints: (i) t_{acc} must be shorter than $t_{\rm cool}$ because magnetic field strength in the shocked region would be stronger or equal to that in the emitting region ($B \leq B_s$). (ii) $t_{\rm inj}$ must be longer than source light travel time because the particle injection process itself should take (at least) $\sim R/c$ to influence the whole emission region.

In Figure 11.29 and 11.30, we illustrate the *allowed* time profiles which can be observed

in blazars. For simplicity, we assume a 'box-shaped' (step-function like) injection profile which lasts $t_{\rm inj}$. Of course, the injection profile itself may vary in time; however, this approximation is correct as long as $t_{\rm inj} \simeq t_{\rm crs}$, since more rapid changes in injection ($< t_{\rm crs}$) are unplausible from causality. Thus results presented here will be affected only when $t_{\rm inj}$ is much larger than $t_{\rm crs}$ and variable on longer time scale.

For examples, 'soft lag' flares observed for PKS 2155−304 in 1994 May (§ Figure 10.2) correspond to the case (7), because the flare was very symmetric and peak time of the flare shows the 'soft-lag' behaviour. A *plateau*-like flare observed for Mrk 421 in 1998 (Figure 10.5) is the case (12), while hard lag flare corresponds to (6). Variability patterns which are listed here but have not been observed, remaines as a 'homework' in the future observations. Interestingly, we predict all types of the flares are characterized by rapid-rise and gradual-decay, or nearly equal rise and decay. Flares in opposite sense, i.e., gradual rise and rapid decay, will be possible only when the duration of the flare is much larger than $t_{\rm crs}$ and injection event itself has such peculiar time profile.

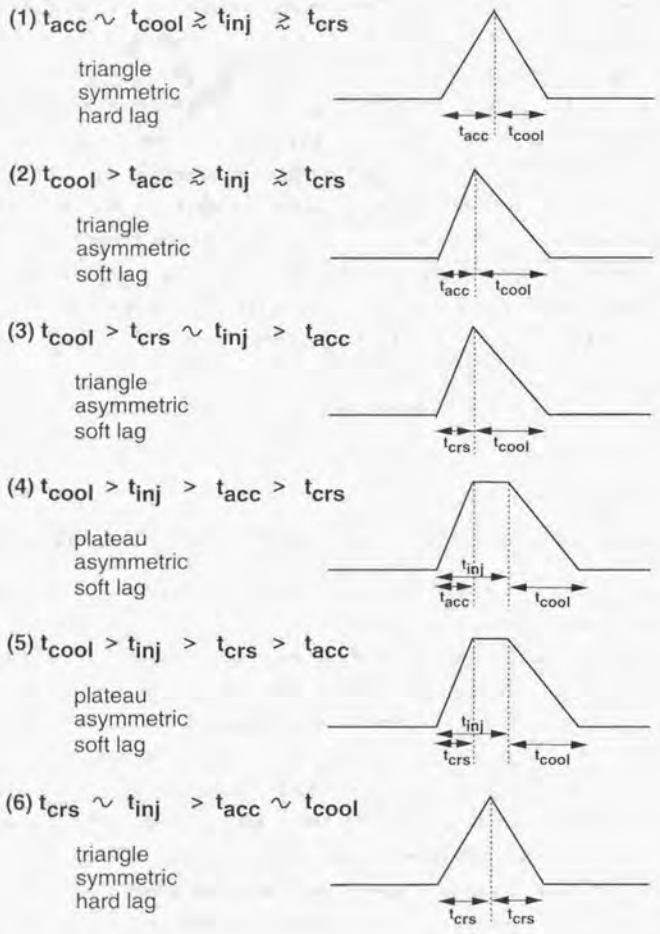

Figure 11.29:

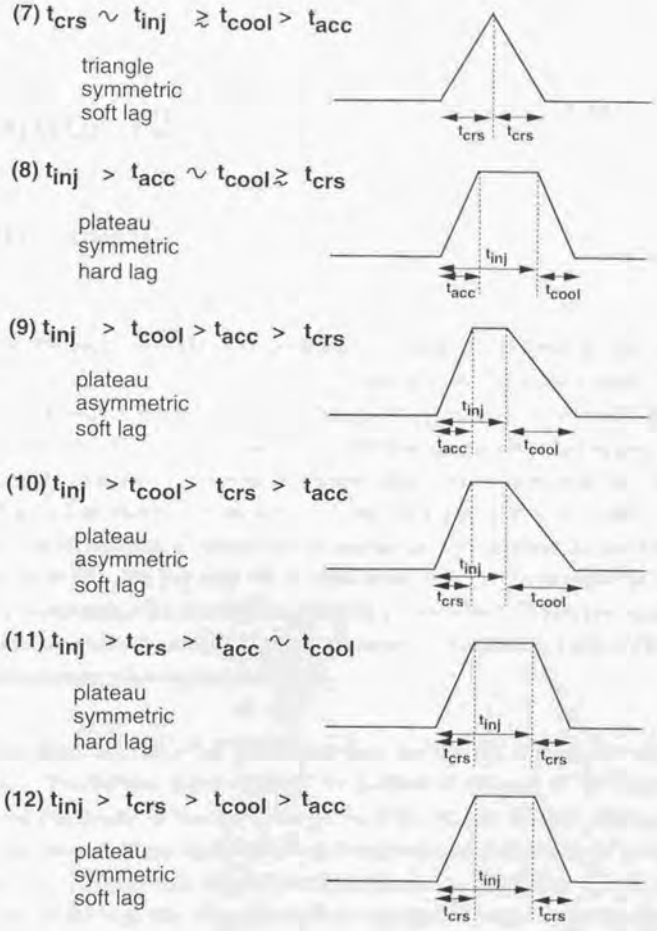

Figure 11.30: Unified picture of rapid variability in blazars. All the variability patterns are well explained by the combination of 4 dynamical time scales. These are; acceleration time : t_{acc}, cooling time : t_{cool}, source light travel time : t_{crs}, and electron injection time : t_{inj}. For simplicity, we assumed here that the electron escape time (t_{esc}) is always longer than t_{cool}. Note however that, if the relation is not correct, i.e., $t_{cool} > t_{esc}$, we have to replace t_{cool} in the figure to t_{esc} because escape is more efficient than cooling process.

Chapter 12

Conclusion

We studied the rapid variability and spectral evolution of four TeV blazars observed with the *ASCA* and *RXTE* satellites. These observations provide the highest quality spectral information as well as light curves in the X-ray energy range of 0.7−20 keV. Since the spectral energy distribution spanning over a very wide energy range and large-amplitude time variability are marked features of blazars, these sources were contemporaneously observed in various energies, including UV, X-ray, GeV and TeV γ-ray bands. We conducted a number of multi-frequency campaigns for the TeV blazars. In particular, our observations of Mrk 421 and Mrk 501 in both X-ray and TeV γ-ray bands provide the first truly simultaneous data in various phases of source activity. From the study of the time-dependent spectral evolution based on the largest samples of X-ray/GeV/TeV γ-ray data, we discovered following major results:

(1) The overall spectra of all TeV blazars form two distinct peaks in the $\nu L(\nu)$ representation. We detected and determined the position of the peak of the lower energy synchrotron component in the X-ray energy band for all TeV blazars: this position is clearly time-variable. Clear correlations were found between peak energy ($E_{\rm p}$) and peak luminosity ($L_{\rm p}$) for both Mrk 421 and Mrk 501. The relations are $E_{\rm p} \propto L_{\rm p}^{0.4}$ for Mrk 421 and $E_{\rm p} \propto L_{\rm p}^{1.6}$ for Mrk 501. Mrk 421 showed very small changes in the peak position, while Mrk 501 showed the largest shift ever observed in blazars.

(2) From the truly simultaneous data, we found that variability in the X-ray and TeV γ-ray bands is well correlated on time scale of a day to years, indicating that the same spatial region and the same population of relativistic electrons are responsible for the emission in both bands. The amplitude of flux variability was comparable in X-ray and TeV γ-ray bands for Mrk 421 ([X-ray flux] $\propto$ [TeV flux]), while quadratic for Mrk 501 ([X-ray flux]^2 $\propto$ [TeV flux]).

Clear correlation of E_p with L_p, found in Mrk 421 and Mrk 501, suggests that general characteristics of the flaring behavior are repeatable in these objects. We argue that the different properties of spectral evolution observed in Mrk 421 and Mrk 501 are due to a variety of changes in physical quantities during the flare. Data for Mrk 421 indicate that the flux variability is associated with an increase in the number of electrons, while only small changes are implied in maximum Lorentz factor of electrons ($\gamma_{\rm max}$). On the other hand, the flare of Mrk 501 is mostly due to the large changes in $\gamma_{\rm max}$ while keeping the electron number almost conservative. Although different origins of flares produce quite diffent spectral behavior, in both cases, the data are consistent with the synchrotron self-Compton (SSC) scenario operating close to the Klein-Nishina regime.

Our analysis, based on the X-ray spectral evolution suggests very important implications for internal jet structure of Mrk 421 and Mrk 501. According to the recent VLBI observations, superluminal motions have been detected only for Mrk 501, while subluminal motions were implied for Mrk 421. Only a small shift of the synchrotron peak observed in Mrk 421 indicates that electron clouds *fill* the jet, while the filling factor of the clouds in the jet of Mrk 501 appears to be much lower. During the flare of Mrk 421, kinetic power of the shock (which is presumably responsible for the acceleration of the radiating particles) causes roughly equal distribution of energy to large number of low-energy electrons newly injected into the shock; this increases the number of high energy electrons. Large shifts of the synchrotron peak observed in Mrk 501, on the other hand, are possible only when the internal jet encounters a medium that is rather sparse and transparent to the shock propagation. Kinetic power of the shock is spent to *increase* the energies of individual electrons and hence *number-conservative*. The absence of superluminal motion of Mrk 421 in the radio band indicates that the high energy outflow has been sufficiently decelerated when it reaches to more distant, radio emitting region.

From the study of time variability in the X-ray band, we found following major results:

(3) Unprecedented long observations of Mrk 421 and PKS 2155−304 revealed day-by-day flares from UV to hard X-rays, and TeV γ-ray bands. Structure function of the X-ray time series in TeV blazars showed a roll-over at $\sim$ 1 day, which is interpreted as a characteristic time scale of a single flare event. On a shorter time scales, rapid variability is strongly suppressed, implying 'strong red-noise' power spectrum density ($\propto f^{-2} \sim f^{-3}$). This is clearly different from the results obtained in Seyfert galaxies or Galactic Black Hole systems whose rapid time variability is well represented by a fractal, flickering noise ($\propto f^{-1} \sim f^{-2}$).

(4) 7-day uninterrupted observation of Mrk 421 revealed that the lags of time variability in various X-ray energy bands were relatively small compared to those found in previous observations. Detailed temporal analysis showed that time-lags changed flare by flare. Importantly, we found a signature of 'hard-lag' behavior, where soft X-ray variations *preceded* those in the hard X-ray band.

(5) We detected a general trend that the amplitude of variability became larger at increasing photon energy. However in some flares, variability in lower energy band was larger or comparable to that in the higher energy band.

(6) Time profiles of individual flare events were almost symmetric, which is characterized by a nearly equal rise-time and decay-time. Importantly, this time-scale was longer than the synchrotron cooling time for X-ray emitting electrons. From the detailed analysis, we discovered that the symmetry of the time profile tends to break down at lower energies.

The absence of rapid variability on time scales shorter than $\leq$ 1 day implies that the X-ray emission site is located $\sim 10^{17-18}$ cm ($\sim$ 100 R_g) from the base of the jet. In this region, high energy electrons lose their energy by radiative (synchrotron/inverse Compton) cooling processes, but the current paradigm is insufficient to understand all observational properties obtained in this thesis. Our results on different sign of lags in the light curve of Mrk 421 can be explained if we take the effect of electron acceleration into account. We confirmed that *usual* 'soft-lag' pattern is observed when the acceleration time of electrons is much shorter than the cooling time, while 'hard-lag' can be detected when the acceleration time of electrons is almost equal to their cooling time. Such opposite sense of lag is expected only if the electron energy is close to $\gamma_{\rm max}$, which corresponds to the X-ray energy band in the photon space.

Symmetry of the time profiles tends to break down in the lower energy bands because cooling time becomes longer than the light travel time across the source. This results in an asymmetrical time profile where the decay-time is longer than the rise-time. We argue that 4 dynamical time scales must be considered properly. These are (i) acceleration time ($t_{\rm acc}$), (ii) cooling time ($t_{\rm cool}$), (iii) source light travel time ($t_{\rm cro}$), and (iv) electron injection time ($t_{\rm inj}$). We suggest that all the variability patterns currently known for blazars are well understood by the balance of these dynamical time scales.

By considering both the spectral energy distribution and the limits from X-ray time variability, we successfully place constraints on the physical quantities relevant for the overall electromagnetic emission from TeV blazars. Based on the synchrotron self-Compton (SSC) scenario, we found that the physical parameters are similar among those objects, where the magnetic field strength $B = 0.1-0.4$ Gauss, beaming factor $\delta = 10-40$, region

size $R = 10^{-3}$–10^{-2} pc, and maximum Lorentz factor of electrons $\gamma_{max} = 5\times10^4$–$4\times10^5$ for the quiescent state.

To confirm our knowledge of spectral evolution and rapid variability in blazars more *quantitatively*, we have developed a new time-dependent SSC model, incorporating the radiative cooling and acceleration process, as well as light travel time effects properly. We successully modeled rapid variability and spectral evolution of TeV blazars assuming the physical parameters derived above.

Our present work places a number of *new* observational constraints on the rapid time variability, internal jet structure, and origin of the flare mechanism for TeV γ-ray emitting blazars. However, physical links to other blazar classes, such as LBLs and OVV quasars, still remain unsolved. We need better quality, contemporaneous data over a wide range of observational baands, especially in the hard X-ray and γ-ray regimes, to better understand dynamics operating in all blazar classes. Observations with the next generation of satellites, featuring improved sensitivity at hard X-ray/γ-ray energies, are expected to bring valuable information.

Appendix A

RXTE Observation Log of TeV Blazars

Table A.1: *RXTE* observation log of Mrk 421 (1)

Source Name	OBS-ID [a]	Start (UT)	End (UT)	Exp. (ksec)	Data Mode [b]
Mrk 421	P10345-01-35-00	1996.04.19 02:00	1996.04.19 02:11	0.608	S1/S2/GX1/GX2
	P10345-01-36-00	1996.04.19 07:27	1996.04.19 08:06	2.304	S1/S2/GX1/GX2
	P10345-01-37-00	1996.04.19 12:24	1996.04.19 12:56	1.904	S1/S2/GX1/GX2
	P10345-01-38-00	1996.04.19 16:35	1996.04.19 16:46	0.624	S1/S2/GX1/GX2
	P10345-01-39-00	1996.04.19 19:51	1996.04.19 20:01	0.544	S1/S2/GX1/GX2
	P10345-01-40-00	1996.04.21 01:16	1996.04.21 01:43	1.568	S1/S2/GX1/GX2
	P10345-01-41-00	1996.04.21 05:16	1996.04.21 05:28	0.672	S1/S2/GX1/GX2
	P10345-01-42-00	1996.04.21 09:06	1996.04.21 09:45	2.304	S1/S2/GX1/GX2
	P10345-01-43-00	1996.04.21 14:58	1996.04.21 15:08	0.56	S1/S2/GX1/GX2
	P10345-01-44-00	1996.04.21 21:25	1996.04.21 21:35	0.576	S1/S2/GX1/GX2
	P10345-01-46-00	1996.04.22 14:02	1996.04.22 14:48	2.736	S1/S2/GX1/GX2
	P10345-01-47-00	1996.04.22 18:13	1996.04.22 18:24	0.64	S1/S2/GX1/GX2
	P10345-01-48-00	1996.04.23 00:27	1996.04.23 00:38	0.624	S1/S2/GX1/GX2
	P10345-01-49-00	1996.05.03 04:13	1996.05.03 04:37	1.408	S1/S2/GX1/GX2
	P10345-01-50-00	1996.05.03 10:06	1996.05.03 10:17	0.656	S1/S2/GX1/GX2
	P10345-01-51-00	1996.05.03 13:19	1996.05.03 13:29	0.576	S1/S2/GX1/GX2
	P10345-01-52-00	1996.05.04 00:50	1996.05.04 01:16	1.536	S1/S2/GX1/GX2
	P10345-01-53-00	1996.05.04 05:58	1996.05.04 06:31	1.984	S1/S2/GX1/GX2
	P10345-01-54-00	1996.05.04 08:32	1996.05.04 08:42	0.576	S1/S2/GX1/GX2
	P10345-01-55-00	1996.05.04 18:32	1996.05.04 18:42	0.56	S1/S2/GX1/GX2
	P10345-01-56-00	1996.05.04 21:38	1996.05.04 21:48	0.576	S1/S2/GX1/GX2
	P10345-01-57-00	1996.05.05 04:03	1996.05.05 04:40	2.192	S1/S2/GX1/GX2
	P10345-01-58-00	1996.05.05 10:08	1996.05.05 10:18	0.544	S1/S2/GX1/GX2
	P10345-01-59-00	1996.05.05 13:21	1996.05.05 13:41	1.2	S1/S2/GX1/GX2
	P10345-01-60-00	1996.05.05 21:33	1996.05.05 21:53	1.2	S1/S2/GX1/GX2
	P10345-01-61-00	1996.05.06 05:21	1996.05.06 05:30	0.544	S1/S2/GX1/GX2
	P10345-01-62-00	1996.05.06 10:08	1996.05.06 10:19	0.64	S1/S2/GX1/GX2
	P10345-01-63-00	1996.05.06 14:57	1996.05.06 15:07	0.608	S1/S2/GX1/GX2
	P10345-01-64-00	1996.05.06 23:13	1996.05.06 23:34	1.264	S1/S2/GX1/GX2
	P10345-01-65-00	1996.05.07 05:20	1996.05.07 05:31	0.672	S1/S2/GX1/GX2
	P10345-01-66-00	1996.05.07 10:03	1996.05.07 10:23	1.184	S1/S2/GX1/GX2
	P10345-01-67-00	1996.05.07 15:00	1996.05.07 15:09	0.528	S1/S2/GX1/GX2
	P10345-01-68-00	1996.05.07 21:33	1996.05.07 21:54	1.232	S1/S2/GX1/GX2
	P10345-01-69-00	1996.05.08 06:56	1996.05.08 07:07	0.64	S1/S2/GX1/GX2
	P10345-01-70-00	1996.05.08 13:31	1996.05.08 13:43	0.672	S1/S2/GX1/GX2
	P10345-01-71-00	1996.05.08 18:10	1996.05.08 18:23	0.752	S1/S2/GX1/GX2
	P10345-01-72-00	1996.05.08 23:09	1996.05.08 23:37	1.664	S1/S2/GX1/GX2
	P10345-01-73-00	1996.05.09 05:54	1996.05.09 06:20	1.552	S1/S2/GX1/GX2

Table A.2: *RXTE* observation log of Mrk 421 (2) *continued*

Source Name	OBS-ID [a]	Start (UT)	End (UT)	Exp. (ksec)	Data Mode [b]
Mrk 421	P10345-01-74-00	1996.05.09 11:50	1996.05.09 12:01	0.608	S1/S2/GX1/GX2
	P10345-01-75-00	1996.05.09 15:16	1996.05.09 15:28	0.688	S1/S2/GX1/GX2
	P10345-01-77-00	1996.05.10 06:00	1996.05.10 06:10	0.544	S1/S2/GX1/GX2
	P10345-01-78-00	1996.05.10 08:34	1996.05.10 08:44	0.544	S1/S2/GX1/GX2
	P10345-01-79-00	1996.05.10 15:20	1996.05.10 15:38	1.04	S1/S2/GX1/GX2
	P10345-01-80-00	1996.05.10 21:12	1996.05.10 21:55	2.528	S1/S2/GX1/GX2
	P10345-01-81-00	1996.05.11 06:59	1996.05.11 07:09	0.56	S1/S2/GX1/GX2
	P10345-01-82-00	1996.05.11 12:24	1996.05.11 12:34	0.544	S1/S2/GX1/GX2
	P10345-01-83-00	1996.05.11 18:20	1996.05.11 18:31	0.64	S1/S2/GX1/GX2
	P10345-01-84-00	1996.05.11 21:32	1996.05.11 22:01	1.696	S1/S2/GX1/GX2
	P10345-01-85-00	1996.05.12 06:00	1996.05.12 06:13	0.736	S1/S2/GX1/GX2
	P10345-01-86-00	1996.05.12 11:57	1996.05.12 12:07	0.592	S1/S2/GX1/GX2
	P10345-01-87-00	1996.05.12 18:19	1996.05.12 18:31	0.704	S1/S2/GX1/GX2
	P10345-01-88-00	1996.05.12 19:58	1996.05.12 20:18	1.168	S1/S2/GX1/GX2
	P10345-01-89-00	1996.05.13 02:21	1996.05.13 02:31	0.56	S1/S2/GX1/GX2
	P10345-01-90-00	1996.05.13 08:36	1996.05.13 08:46	0.608	S1/S2/GX1/GX2
	P10345-01-91-00	1996.05.13 13:40	1996.05.13 13:50	0.56	S1/S2/GX1/GX2
	P10345-01-92-00	1996.05.13 18:19	1996.05.13 18:35	0.944	S1/S2/GX1/GX2
	P10345-01-93-00	1996.05.14 05:25	1996.05.14 05:35	0.56	S1/S2/GX1/GX2
	P10345-01-94-00	1996.05.14 08:38	1996.05.14 08:48	0.576	S1/S2/GX1/GX2
	P10345-01-95-00	1996.05.14 15:16	1996.05.14 15:25	0.528	S1/S2/GX1/GX2
	P10345-01-96-00	1996.05.14 23:21	1996.05.14 23:43	1.312	S1/S2/GX1/GX2
	P10345-01-97-00	1996.05.15 06:03	1996.05.15 06:13	0.56	S1/S2/GX1/GX2
	P10345-01-98-00	1996.05.15 11:55	1996.05.15 12:09	0.8	S1/S2/GX1/GX2
	P10345-01-01-10	1996.05.15 15:34	1996.05.15 15:43	0.544	S1/S2/GX1/GX2
	P10345-01-02-10	1996.05.15 22:24	1996.05.15 22:34	0.56	S1/S2/GX1/GX2
	P10345-01-03-10	1996.05.16 08:54	1996.05.16 09:04	0.576	S1/S2/GX1/GX2
	P10345-01-04-10	1996.05.16 12:00	1996.05.16 12:10	0.56	S1/S2/GX1/GX2
	P10345-01-05-10	1996.05.16 18:17	1996.05.16 18:35	1.04	S1/S2/GX1/GX2
	P10345-01-06-10	1996.05.16 21:28	1996.05.16 21:57	1.712	S1/S2/GX1/GX2
	P10345-01-07-10	1996.05.17 01:03	1996.05.17 01:17	0.816	S1/S2/GX1/GX2
	P10345-01-08-10	1996.05.17 07:47	1996.05.17 07:57	0.544	S1/S2/GX1/GX2
	P10345-01-09-10	1996.05.17 13:55	1996.05.17 14:04	0.512	S1/S2/GX1/GX2
	P10345-01-10-10	1996.05.17 22:26	1996.05.17 22:36	0.544	S1/S2/GX1/GX2
	P10345-01-11-10	1996.05.18 05:39	1996.05.18 05:49	0.544	S1/S2/GX1/GX2
	P10345-01-12-10	1996.05.18 14:04	1996.05.18 14:14	0.544	S1/S2/GX1/GX2
	P10345-01-13-10	1996.05.18 19:05	1996.05.18 19:26	1.216	S1/S2/GX1/GX2
	P10345-01-15-10	1996.05.19 01:03	1996.05.19 01:17	0.8	S1/S2/GX1/GX2

Table A.3: *RXTE* observation log of Mrk 421 (3) *continued*

Source Name	OBS-ID [a]	Start (UT)	End (UT)	Exp. (ksec)	Data Mode [b]
Mrk 421	P10345-01-16-10	1996.05.19 05:52	1996.05.19 06:08	0.912	S1/S2/GX1/GX2
	P10345-01-17-10	1996.05.19 17:24	1996.05.19 17:34	0.544	S1/S2/GX1/GX2
	P10345-01-18-10	1996.05.19 21:49	1996.05.19 21:57	0.432	S1/S2/GX1/GX2
	P10345-01-19-10	1996.05.20 06:16	1996.05.20 06:27	0.608	S1/S2/GX1/GX2
	P10345-01-20-10	1996.05.20 12:05	1996.05.20 12:15	0.576	S1/S2/GX1/GX2
	P10345-01-21-10	1996.05.20 19:02	1996.05.20 19:15	0.752	S1/S2/GX1/GX2
	P10345-01-14-10	1996.05.21 01:08	1996.05.21 01:27	1.088	S1/S2/GX1/GX2
	P10341-02-02-00	1996.12.10 21:05	1996.12.10 21:44	2.336	S1/S2/GX1/GX2
	P20341-01-02-01	1997.04.02 03:30	1997.04.02 09:03	19.968	S1/S2/GX1/GX2
	P20341-01-02-00	1997.04.03 05:08	1997.04.03 09:04	14.144	S1/S2/GX1/GX2
	P20341-01-01-00	1997.04.04 05:15	1997.04.04 07:26	7.808	S1/S2/GX1/GX2
	P20341-01-01-01	1997.04.05 05:12	1997.04.05 06:19	4.0	S1/S2/GX1/GX2
	P20341-01-01-02	1997.04.05 06:48	1997.04.05 07:45	3.376	S1/S2/GX1/GX2
	P20341-01-01-03	1997.04.10 05:31	1997.04.10 06:13	2.512	S1/S2/GX1/GX2
	P20341-01-01-04	1997.04.10 06:55	1997.04.10 07:29	2.032	S1/S2/GX1/GX2
	P20341-01-03-00	1997.04.11 05:20	1997.04.11 07:46	8.752	S1/S2/GX1/GX2
	P20341-01-03-01	1997.04.12 05:21	1997.04.12 08:58	12.976	S1/S2/GX1/GX2
	P20341-01-04-00	1997.04.29 05:29	1997.04.29 05:51	1.28	S1/S2/GX1/GX2
	P20341-01-04-01	1997.04.30 05:29	1997.04.30 06:36	3.984	S1/S2/GX1/GX2
	P20341-01-04-02	1997.05.01 21:27	1997.05.01 22:06	2.336	S1/S2/GX1/GX2
	P20341-01-05-00	1997.05.02 05:30	1997.05.02 06:21	3.024	S1/S2/GX1/GX2
	P20341-01-05-01	1997.05.03 03:55	1997.05.03 04:10	0.896	S1/S2/GX1/GX2
	P20341-01-05-02	1997.05.03 05:29	1997.05.03 06:34	3.856	S1/S2/GX1/GX2
	P20341-01-05-03	1997.05.04 03:54	1997.05.04 04:12	1.024	S1/S2/GX1/GX2
	P20341-01-05-04	1997.05.04 05:30	1997.05.04 05:51	1.216	S1/S2/GX1/GX2
	P20341-01-05-05	1997.05.06 02:21	1997.05.06 05:15	10.416	S1/S2/GX1/GX2
	P20341-01-05-06	1997.05.06 05:39	1997.05.06 05:56	0.976	S1/S2/GX1/GX2
	P20341-01-06-00	1997.06.03 05:59	1997.06.03 06:34	2.096	S1/S2/GX1/GX2

Table A.4: *RXTE* observation log of Mrk 501 (1)

Source Name	OBS-ID	Start (UT)	End (UT)	Exp. (ksec)	Data Mode
Mrk 501	P10341-03-01-00	1996.08.01 13:26	1996.08.01 14:01	2.064	S1/S2/GX1/GX2
	P10341-03-02-00	1996.10.22 11:52	1996.10.22 12:26	2.032	S1/S2/GX1/GX2
	P20340-01-01-00	1997.03.18 02:03	1997.03.18 02:54	3.056	S1/S2/GX1/GX2
	P20340-04-01-00	1997.04.03 04:27	1997.04.03 04:55	1.632	S1/S2/GX1/GX2
	P20340-04-02-00	1997.04.03 09:17	1997.04.03 09:33	0.944	S1/S2/GX1/GX2
	P20340-04-03-00	1997.04.04 04:28	1997.04.04 04:44	0.944	S1/S2/GX1/GX2
	P20340-04-04-00	1997.04.04 11:09	1997.04.04 11:34	1.488	S1/S2/GX1/GX2
	P20340-04-05-00	1997.04.05 04:27	1997.04.05 04:59	1.872	S1/S2/GX1/GX2
	P20340-04-06-00	1997.04.05 07:58	1997.04.05 08:19	1.248	S1/S2/GX1/GX2
	P20340-04-07-00	1997.04.06 07:15	1997.04.06 07:31	0.928	S1/S2/GX1/GX2
	P20340-04-08-00	1997.04.06 10:27	1997.04.06 10:42	0.864	S1/S2/GX1/GX2
	P20340-04-09-00	1997.04.07 07:15	1997.04.07 07:30	0.864	S1/S2/GX1/GX2
	P20340-04-10-00	1997.04.07 10:36	1997.04.07 10:52	0.912	S1/S2/GX1/GX2
	P20340-04-11-00	1997.04.08 05:40	1997.04.08 06:08	1.648	S1/S2/GX1/GX2
	P20340-04-12-00	1997.04.08 10:37	1997.04.08 10:53	0.912	S1/S2/GX1/GX2
	P20340-04-13-00	1997.04.09 05:40	1997.04.09 06:08	1.648	S1/S2/GX1/GX2
	P20340-04-14-00	1997.04.09 10:28	1997.04.09 10:43	0.864	S1/S2/GX1/GX2
	P20340-04-15-00	1997.04.10 06:26	1997.04.10 06:42	0.944	S1/S2/GX1/GX2
	P20340-04-16-00	1997.04.10 07:42	1997.04.10 07:57	0.88	S1/S2/GX1/GX2
	P20340-04-17-00	1997.04.11 04:51	1997.04.11 05:07	0.912	S1/S2/GX1/GX2
	P20340-04-18-00	1997.04.11 07:59	1997.04.11 08:38	2.32	S1/S2/GX1/GX2
	P20340-04-19-00	1997.04.12 04:24	1997.04.12 04:39	0.88	S1/S2/GX1/GX2
	P20340-04-20-00	1997.04.12 10:45	1997.04.12 11:03	1.056	S1/S2/GX1/GX2
	P20340-04-21-00	1997.04.13 06:24	1997.04.13 06:53	1.728	S1/S2/GX1/GX2
	P20340-04-22-00	1997.04.13 11:01	1997.04.13 11:54	3.168	S1/S2/GX1/GX2
	P20340-04-23-00	1997.04.14 08:00	1997.04.14 08:16	0.912	S1/S2/GX1/GX2
	P20340-04-24-00	1997.04.14 10:58	1997.04.14 11:40	2.512	S1/S2/GX1/GX2
	P20340-04-25-00	1997.04.15 06:20	1997.04.15 06:41	1.216	S1/S2/GX1/GX2
	P20340-04-26-00	1997.04.15 08:56	1997.04.15 09:12	0.944	S1/S2/GX1/GX2
	P20340-04-27-00	1997.04.16 04:07	1997.04.16 04:25	1.056	S1/S2/GX1/GX2
	P20340-04-28-00	1997.04.16 10:39	1997.04.16 10:51	0.72	S1/S2/GX1/GX2
	P20340-01-02-00	1997.05.02 04:19	1997.05.02 05:18	3.536	S1/S2/GX1/GX2
	P20340-01-03-00	1997.05.02 09:24	1997.05.02 10:11	2.768	S1/S2/GX1/GX2
	P20340-01-04-00	1997.05.03 04:22	1997.05.03 05:17	3.264	S1/S2/GX1/GX2
	P20340-01-05-00	1997.05.04 04:24	1997.05.04 05:18	3.2	S1/S2/GX1/GX2
	P20340-01-06-00	1997.05.04 06:03	1997.05.04 06:25	1.28	S1/S2/GX1/GX2
	P20340-01-07-00	1997.05.05 04:15	1997.05.05 04:42	1.584	S1/S2/GX1/GX2
	P20340-01-08-00	1997.05.05 09:26	1997.05.05 10:12	2.736	S1/S2/GX1/GX2
	P20340-01-09-00	1997.05.06 06:08	1997.05.06 06:45	2.176	S1/S2/GX1/GX2
	P20340-01-10-00	1997.05.06 07:35	1997.05.06 08:36	3.616	S1/S2/GX1/GX2

Table A.5: *RXTE* observation log of Mrk 501 (2) *continued*

Source Name	OBS-ID	Start (UT)	End (UT)	Exp. (ksec)	Data Mode
Mrk 501	P20340-01-11-00	1997.05.07 05:49	1997.05.07 07:00	4.224	S1/S2/GX1/GX2
	P20340-01-12-00	1997.05.07 09:28	1997.05.07 09:50	1.28	S1/S2/GX1/GX2
	P20340-01-13-00	1997.05.08 06:53	1997.05.08 07:01	0.48	S1/S2/GX1/GX2
	P20340-01-14-00	1997.05.08 09:25	1997.05.08 10:17	3.104	S1/S2/GX1/GX2
	P20340-01-15-00	1997.05.09 06:53	1997.05.09 07:04	0.608	S1/S2/GX1/GX2
	P20340-01-16-00	1997.05.09 07:58	1997.05.09 08:40	2.528	S1/S2/GX1/GX2
	P20340-01-17-00	1997.05.10 05:14	1997.05.10 05:30	0.912	S1/S2/GX1/GX2
	P20340-01-18-00	1997.05.10 09:29	1997.05.10 09:59	1.744	S1/S2/GX1/GX2
	P20340-01-19-00	1997.05.11 05:13	1997.05.11 05:29	0.912	S1/S2/GX1/GX2
	P20340-01-20-00	1997.05.11 09:26	1997.05.11 09:42	0.912	S1/S2/GX1/GX2
	P20340-01-21-00	1997.05.12 04:22	1997.05.12 04:44	1.296	S1/S2/GX1/GX2
	P20340-01-22-00	1997.05.12 08:35	1997.05.12 08:45	0.608	S1/S2/GX1/GX2
	P20340-01-23-00	1997.05.13 04:32	1997.05.13 04:46	0.8	S1/S2/GX1/GX2
	P20340-01-24-00	1997.05.13 08:34	1997.05.13 08:46	0.72	S1/S2/GX1/GX2
	P20340-01-25-00	1997.05.14 08:32	1997.05.14 08:47	0.896	S1/S2/GX1/GX2
	P20340-01-26-00	1997.05.14 09:34	1997.05.14 09:51	0.976	S1/S2/GX1/GX2
	P20340-01-27-00	1997.05.15 04:26	1997.05.15 05:08	2.512	S1/S2/GX1/GX2
	P20340-01-28-00	1997.05.15 06:13	1997.05.15 06:49	2.128	S1/S2/GX1/GX2
	P20421-01-01-01	1997.07.11 23:23	1997.07.11 23:51	1.68	S1/S2/GX1/GX2
	P20421-01-01-00	1997.07.12 03:36	1997.07.12 05:09	5.536	S1/S2/GX1/GX2
	P20421-01-02-01	1997.07.12 23:22	1997.07.12 23:51	1.728	S1/S2/GX1/GX2
	P20421-01-02-00	1997.07.13 03:37	1997.07.13 05:09	5.472	S1/S2/GX1/GX2
	P20421-01-03-01	1997.07.13 23:21	1997.07.13 23:49	1.664	S1/S2/GX1/GX2
	P20421-01-03-00	1997.07.14 03:38	1997.07.14 04:48	4.16	S1/S2/GX1/GX2
	P20421-01-04-01	1997.07.14 22:50	1997.07.15 00:07	4.608	S1/S2/GX1/GX2
	P20421-01-04-00	1997.07.15 03:38	1997.07.15 04:55	4.624	S1/S2/GX1/GX2
	P20421-01-05-01	1997.07.15 22:51	1997.07.15 23:51	3.584	S1/S2/GX1/GX2
	P20421-01-05-00	1997.07.16 03:40	1997.07.16 04:55	4.512	S1/S2/GX1/GX2
	P30249-01-01-08	1998.05.25 03:46	1998.05.25 04:22	2.16	S1/S2/GX1/GX2
	P30249-01-01-00	1998.05.25 06:58	1998.05.25 11:08	14.992	S1/S2/GX1/GX2
	P30249-01-01-01	1998.05.25 12:44	1998.05.25 17:42	17.872	S1/S2/GX1/GX2
	P30249-01-01-02	1998.05.25 19:24	1998.05.25 20:11	2.816	S1/S2/GX1/GX2
	P30249-01-01-03	1998.05.25 21:04	1998.05.25 22:20	4.512	S1/S2/GX1/GX2
	P30249-01-01-04	1998.05.26 06:57	1998.05.26 11:08	15.056	31/S2/GX1/GX2
	P30249-01-01-05	1998.05.26 14:23	1998.05.26 17:42	11.936	S1/S2/GX1/GX2
	P30249-01-01-09	1998.05.27 02:06	1998.05.27 02:36	1.808	S1/S2/GX1/GX2
	P30249-01-01-10	1998.05.27 03:45	1998.05.27 04:12	1.6	S1/S2/GX1/GX2
	P30249-01-01-06	1998.05.27 06:55	1998.05.27 11:08	15.168	S1/S2/GX1/GX2
	P30249-01-01-07	1998.05.27 12:44	1998.05.27 15:59	11.696	S1/S2/GX1/GX2

Table A.6: *RXTE* observation log of PKS 2155−304 (1)

Source Name	OBS-ID	Start (UT)	End (UT)	Exp. (ksec)	Data Mode
PKS 2155 −304	P10356-01-01-00	1996.05.16 00:40	1996.05.16 00:50	0.592	S1/S2/GX1/GX2
	P10356-01-02-00	1996.05.16 03:24	1996.05.16 03:47	1.36	S1/S2/GX1/GX2
	P10356-01-03-00	1996.05.16 06:15	1996.05.16 06:40	1.472	S1/S2/GX1/GX2
	P10356-01-04-00	1996.05.16 09:32	1996.05.16 09:42	0.544	S1/S2/GX1/GX2
	P10356-01-05-00	1996.05.16 12:38	1996.05.16 12:48	0.544	S1/S2/GX1/GX2
	P10356-01-06-00	1996.05.16 16:39	1996.05.16 17:09	1.76	S1/S2/GX1/GX2
	P10356-01-07-00	1996.05.16 19:03	1996.05.16 19:14	0.608	S1/S2/GX1/GX2
	P10356-01-08-00	1996.05.16 22:25	1996.05.16 22:41	0.912	S1/S2/GX1/GX2
	P10356-01-09-00	1996.05.17 01:45	1996.05.17 02:16	1.808	S1/S2/GX1/GX2
	P10356-01-10-00	1996.05.17 05:27	1996.05.17 05:49	1.296	S1/S2/GX1/GX2
	P10356-01-11-00	1996.05.17 07:09	1996.05.17 07:19	0.592	S1/S2/GX1/GX2
	P10356-01-12-00	1996.05.17 11:57	1996.05.17 12:14	0.976	S1/S2/GX1/GX2
	P10356-01-13-00	1996.05.17 15:51	1996.05.17 16:01	0.544	S1/S2/GX1/GX2
	P10356-01-14-00	1996.05.17 21:33	1996.05.17 21:58	1.472	S1/S2/GX1/GX2
	P10356-01-15-00	1996.05.18 02:16	1996.05.18 02:25	0.512	S1/S2/GX1/GX2
	P10356-01-16-00	1996.05.18 05:02	1996.05.18 05:11	0.528	S1/S2/GX1/GX2
	P10356-01-17-00	1996.05.18 07:10	1996.05.18 07:20	0.592	S1/S2/GX1/GX2
	P10356-01-18-00	1996.05.18 09:35	1996.05.18 09:45	0.56	S1/S2/GX1/GX2
	P10356-01-45-00	1996.05.18 13:28	1996.05.18 13:36	0.432	S1/S2/GX1/GX2
	P10356-01-20-00	1996.05.18 18:14	1996.05.18 18:37	1.344	S1/S2/GX1/GX2
	P10356-01-21-00	1996.05.18 21:33	1996.05.18 22:15	2.496	S1/S2/GX1/GX2
	P10356-01-19-00	1996.05.18 23:09	1996.05.18 23:55	2.736	S1/S2/GX1/GX2
	P10356-02-01-01	1996.05.19 01:45	1996.05.19 04:11	8.704	S1/S2/GX1/GX2
	P10356-02-01-00	1996.05.19 06:36	1996.05.19 07:31	3.248	S1/S2/GX1/GX2
	P10356-02-01-02	1996.05.19 14:30	1996.05.19 16:56	8.736	S1/S2/GX1/GX2
	P10356-02-01-03	1996.05.19 18:02	1996.05.19 20:34	9.072	S1/S2/GX1/GX2
	P10356-02-01-04	1996.05.19 22:26	1996.05.19 05:48	26.528	S1/S2/GX1/GX2
	P10356-02-01-07	1996.05.20 12:43	1996.05.20 13:45	3.664	S1/S2/GX1/GX2
	P10356-02-01-05	1996.05.20 19:55	1996.05.20 00:40	17.104	S1/S2/GX1/GX2
	P10356-01-23-00	1996.05.21 04:59	1996.05.21 05:07	0.48	S1/S2/GX1/GX2
	P10356-01-24-00	1996.05.21 07:15	1996.05.21 07:39	1.392	S1/S2/GX1/GX2
	P10356-01-25-00	1996.05.21 11:30	1996.05.21 11:44	0.8	S1/S2/GX1/GX2
	P10356-01-26-00	1996.05.21 14:59	1996.05.21 15:34	2.096	S1/S2/GX1/GX2
	P10356-01-27-00	1996.05.21 18:18	1996.05.21 18:55	2.176	S1/S2/GX1/GX2
	P10356-01-28-00	1996.05.21 21:37	1996.05.21 22:01	1.392	S1/S2/GX1/GX2
	P10356-01-29-00	1996.05.22 01:45	1996.05.22 01:55	0.56	S1/S2/GX1/GX2
	P10356-01-31-00	1996.05.22 04:58	1996.05.22 05:23	1.504	S1/S2/GX1/GX2
	P10356-01-30-00	1996.05.22 08:38	1996.05.22 08:48	0.576	S1/S2/GX1/GX2

Table A.7: *RXTE* observation log of PKS 2155−304 (2) *continued*

Source Name	OBS-ID	Start (UT)	End (UT)	Exp. (ksec)	Data Mode
PKS 2155 −304	P10356-01-33-00	1996.05.22 11:50	1996.05.22 12:29	2.32	S1/S2/GX1/GX2
	P10356-01-34-00	1996.05.22 17:35	1996.05.22 17:45	0.592	S1/S2/GX1/GX2
	P10356-01-35-00	1996.05.22 20:02	1996.05.22 20:25	1.376	S1/S2/GX1/GX2
	P10356-01-32-00	1996.05.22 23:15	1996.05.22 23:56	2.448	S1/S2/GX1/GX2
	P10356-01-36-00	1996.05.23 00:51	1996.05.23 01:33	2.512	S1/S2/GX1/GX2
	P10356-01-39-00	1996.05.23 04:56	1996.05.23 05:06	0.592	S1/S2/GX1/GX2
	P10356-01-38-00	1996.05.23 07:19	1996.05.23 07:42	1.344	S1/S2/GX1/GX2
	P10356-01-40-00	1996.05.23 10:31	1996.05.23 10:54	1.328	S1/S2/GX1/GX2
	P10356-01-41-00	1996.05.23 13:21	1996.05.23 13:37	0.928	S1/S2/GX1/GX2
	P10356-01-42-00	1996.05.23 18:21	1996.05.23 18:40	1.136	S1/S2/GX1/GX2
	P10356-01-43-00	1996.05.23 21:44	1996.05.23 22:05	1.216	S1/S2/GX1/GX2
	P10356-01-46-00	1996.05.24 03:32	1996.05.24 03:42	0.592	S1/S2/GX1/GX2
	P10356-01-47-00	1996.05.24 06:26	1996.05.24 06:36	0.56	S1/S2/GX1/GX2
	P10357-01-01-00	1996.05.24 08:02	1996.05.24 08:27	1.456	S1/S2/GX1/GX2
	P10356-01-48-00	1996.05.24 08:27	1996.05.24 08:39	0.72	S1/S2/GX1/GX2
	P10356-01-49-00	1996.05.24 11:44	1996.05.24 11:55	0.624	S1/S2/GX1/GX2
	P10356-01-50-00	1996.05.24 14:27	1996.05.24 14:37	0.544	S1/S2/GX1/GX2
	P10356-01-52-00	1996.05.24 17:39	1996.05.24 17:49	0.56	S1/S2/GX1/GX2
	P10356-01-51-00	1996.05.24 20:05	1996.05.24 20:29	1.408	S1/S2/GX1/GX2
	P10356-01-53-00	1996.05.24 23:18	1996.05.24 23:48	1.792	S1/S2/GX1/GX2
	P10356-01-54-00	1996.05.25 03:23	1996.05.25 03:47	1.424	S1/S2/GX1/GX2
	P10356-01-56-00	1996.05.25 08:55	1996.05.25 09:07	0.704	S1/S2/GX1/GX2
	P10356-01-57-00	1996.05.25 13:17	1996.05.25 13:56	2.32	S1/S2/GX1/GX2
	P10356-01-58-00	1996.05.25 16:41	1996.05.25 17:08	1.6	S1/S2/GX1/GX2
	P10356-01-59-00	1996.05.25 20:06	1996.05.25 20:28	1.312	S1/S2/GX1/GX2
	P10356-01-60-00	1996.05.25 23:20	1996.05.25 23:45	1.504	S1/S2/GX1/GX2
	P10356-01-61-00	1996.05.26 02:30	1996.05.26 02:42	0.72	S1/S2/GX1/GX2
	P10356-01-62-00	1996.05.26 05:43	1996.05.26 05:56	0.784	S1/S2/GX1/GX2
	P10356-01-63-00	1996.05.26 10:04	1996.05.26 10:16	0.704	S1/S2/GX1/GX2
	P10356-01-64-00	1996.05.26 13:16	1996.05.26 13:53	2.192	S1/S2/GX1/GX2
	P10356-01-66-00	1996.05.26 16:15	1996.05.26 16:23	0.464	S1/S2/GX1/GX2
	P10357-01-02-00	1996.05.26 16:23	1996.05.26 17:01	2.272	S1/S2/GX1/GX2
	P10356-01-68-00	1996.05.26 23:20	1996.05.26 23:43	1.376	S1/S2/GX1/GX2
	P10356-01-73-00	1996.05.27 02:33	1996.05.27 02:45	0.72	S1/S2/GX1/GX2
	P10356-01-69-00	1996.05.27 08:59	1996.05.27 09:09	0.592	S1/S2/GX1/GX2
	P10356-01-70-00	1996.05.27 11:38	1996.05.27 11:52	0.8	S1/S2/GX1/GX2
	P10356-01-71-00	1996.05.27 15:00	1996.05.27 15:19	1.104	S1/S2/GX1/GX2
	P10356-01-72-00	1996.05.27 20:09	1996.05.27 20:22	0.752	S1/S2/GX1/GX2
	P10356-01-74-00	1996.05.27 23:22	1996.05.27 23:41	1.136	S1/S2/GX1/GX2

Table A.8: *RXTE* observation log of PKS 2155−304 (3) *continued*

Source Name	OBS-ID	Start (UT)	End (UT)	Exp. (ksec)	Data Mode
PKS 2155 −304	P10356-01-75-00	1996.05.28 03:54	1996.05.28 04:06	0.704	S1/S2/GX1/GX2
	P10357-01-03-00	1996.05.28 14:43	1996.05.28 15:26	2.544	S1/S2/GX1/GX2
	P10357-01-04-00	1996.07.23 09:02	1996.07.23 09:34	1.904	S1/S2/GX1/GX2
	P10357-01-05-00	1996.07.25 15:55	1996.07.25 16:27	1.888	S1/S2/GX1/GX2
	P10357-01-06-00	1996.07.27 15:57	1996.07.27 16:23	1.504	S1/S2/GX1/GX2
	P10357-01-07-00	1996.11.14 07:39	1996.11.14 14:56	26.176	S1/S2/GX1/GX2
	P10357-01-07-01	1996.11.15 15:44	1996.11.15 16:02	1.088	S1/S2/GX1/GX2
	P10356-02-03-00	1996.11.20 09:33	1996.11.20 09:58	1.456	S1/S2/GX1/GX2
	P10356-02-04-00	1996.11.20 17:39	1996.11.20 17:58	1.104	S1/S2/GX1/GX2
	P10356-02-05-00	1996.11.21 07:37	1996.11.21 08:02	1.456	S1/S2/GX1/GX2
	P10356-02-06-00	1996.11.22 03:00	1996.11.22 03:16	0.912	S1/S2/GX1/GX2
	P10356-02-07-00	1996.11.22 14:17	1996.11.22 14:32	0.912	S1/S2/GX1/GX2
	P10356-02-02-00	1996.11.23 10:38	1996.11.23 16:24	20.768	S1/S2/GX1/GX2
	P10356-02-02-01	1996.11.24 07:38	1996.11.24 13:12	20.032	S1/S2/GX1/GX2
	P30253-01-42-00	1997.11.20 22:54	1997.11.20 23:25	1.808	S1/S2/GX1/GX2
	P30253-01-41-00	1997.11.21 15:21	1997.11.21 15:37	0.944	S1/S2/GX1/GX2
	P30253-01-40-00	1997.11.22 17:09	1997.11.22 17:24	0.88	S1/S2/GX1/GX2
	P30253-01-01-00	1998.01.09 03:07	1998.01.09 03:29	1.296	S1/S2/GX1/GX2
	P30253-01-02-00	1998.01.09 12:49	1998.01.09 13:05	0.912	S1/S2/GX1/GX2
	P30253-01-03-00	1998.01.10 03:09	1998.01.10 03:30	1.216	S1/S2/GX1/GX2
	P30253-01-04-00	1998.01.10 12:54	1998.01.10 13:09	0.88	S1/S2/GX1/GX2
	P30253-01-05-00	1998.01.11 07:24	1998.01.11 07:39	0.896	S1/S2/GX1/GX2
	P30253-01-06-00	1998.01.11 12:12	1998.01.11 12:24	0.72	S1/S2/GX1/GX2
	P30253-01-07-00	1998.01.12 05:51	1998.01.12 06:04	0.736	S1/S2/GX1/GX2
	P30253-01-08-00	1998.01.12 14:22	1998.01.12 14:46	1.408	S1/S2/GX1/GX2
	P30253-01-09-00	1998.01.13 03:12	1998.01.13 03:33	1.216	S1/S2/GX1/GX2
	P30253-01-10-00	1998.01.13 14:24	1998.01.13 14:46	1.28	S1/S2/GX1/GX2

[a] proposal ID and observation plan number.

[b] *RXTE* PCA data mode. S1: *standard*-1 mode, S2: *standard*-2 mode, GX1: *GoodXenon*1-16s mode, GX2: *GoodXenon*2-16s mode.

Appendix B

DCF Distributions of Mrk 421 during 1998 Campaign

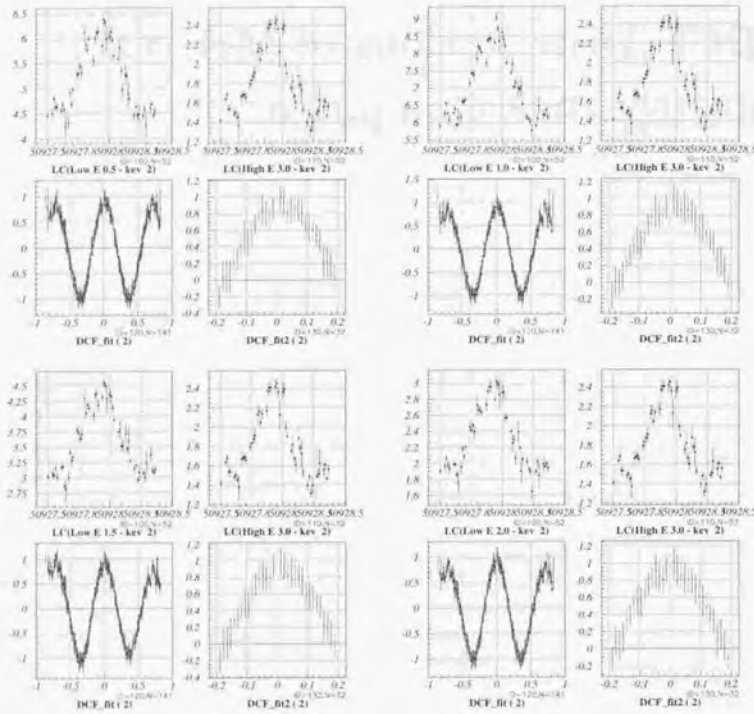

Figure B.1: DCF of time segment 2 for Mrk 421 in 1998.

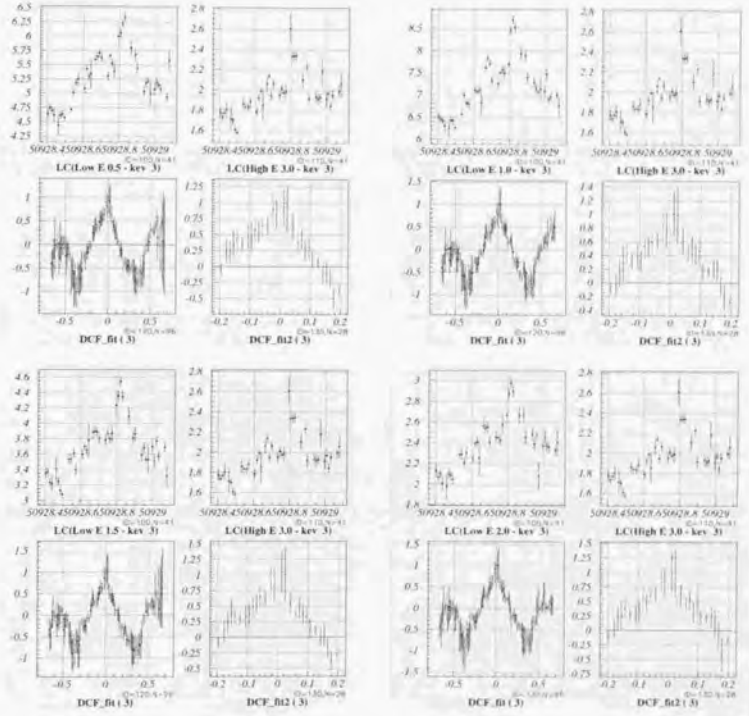

Figure B.2: DCF of time segment 3 for Mrk 421 in 1998.

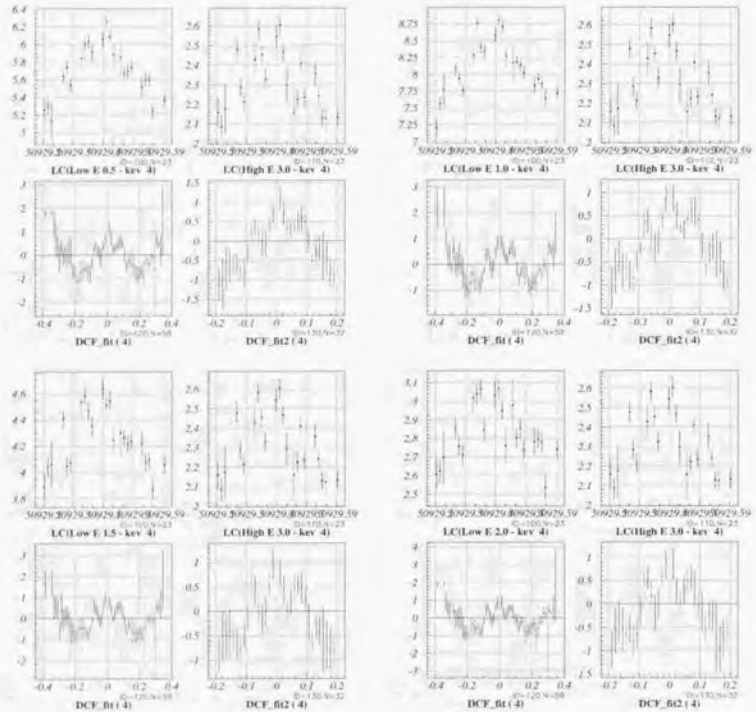

Figure B.3: DCF of time segment 4 for Mrk 421 in 1998.

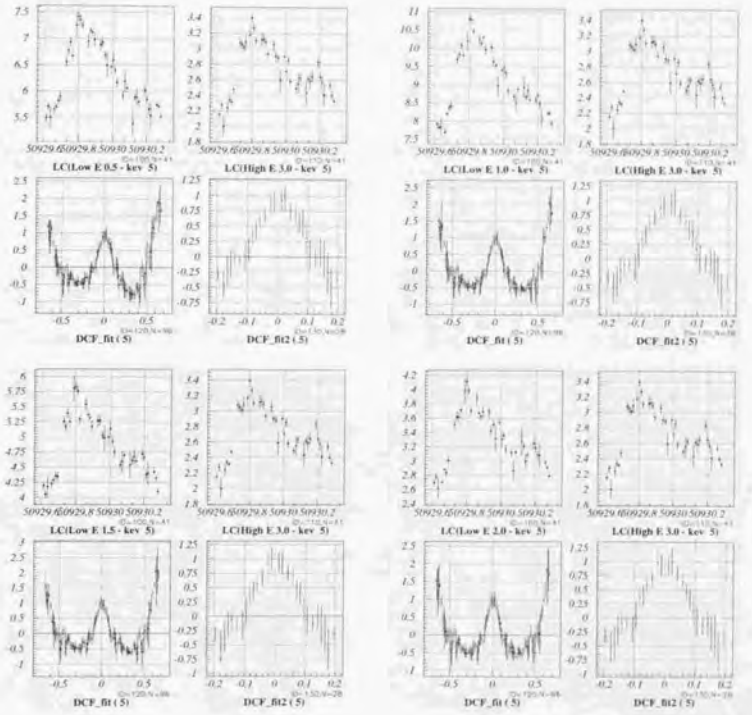

Figure B.4: DCF of time segment 5 for Mrk 421 in 1998.

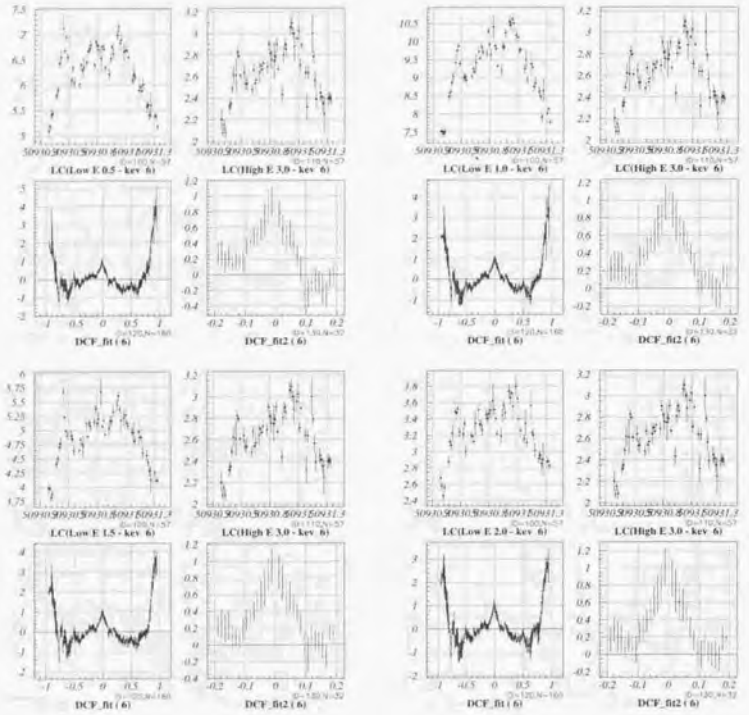

Figure B.5: DCF of time segment 6 for Mrk 421 in 1998.

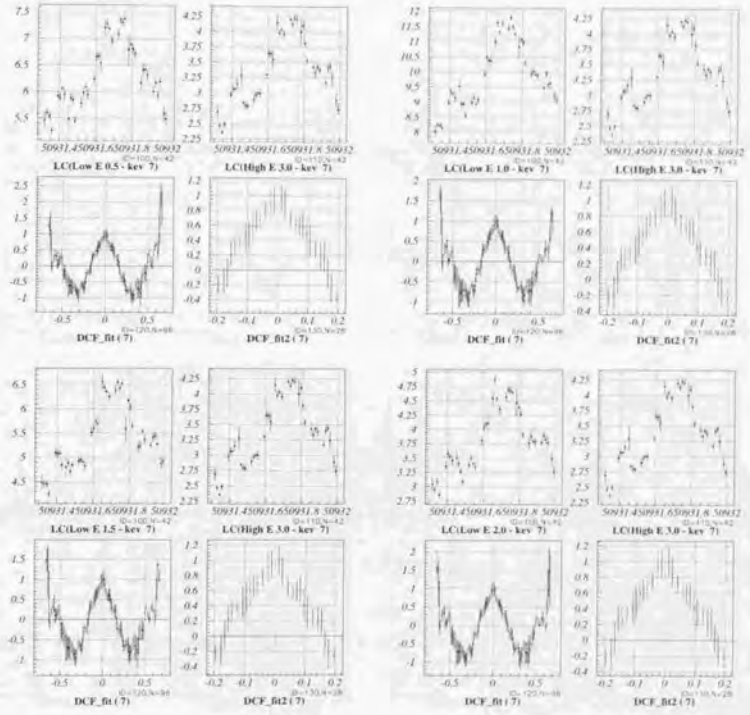

Figure B.6: DCF of time segment 7 for Mrk 421 in 1998.

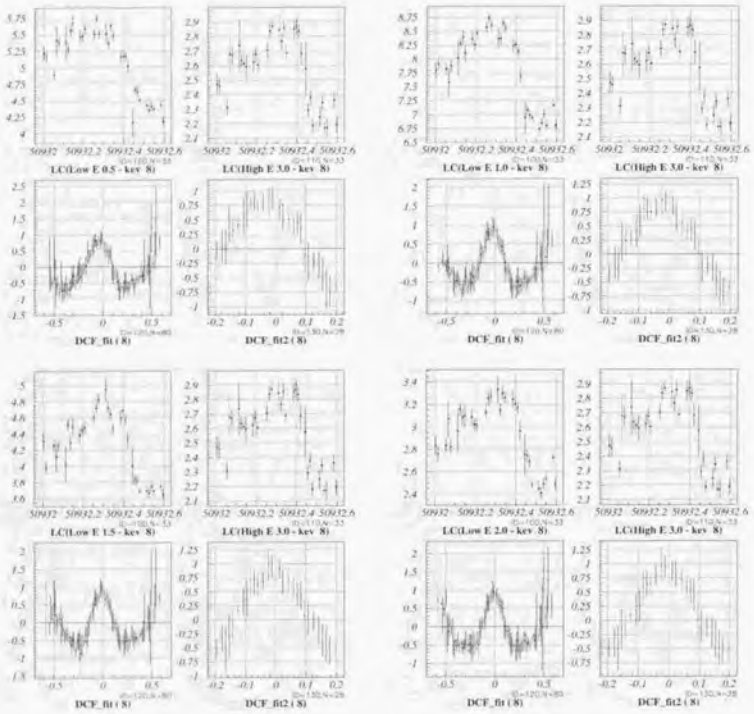

Figure B.7: DCF of time segment 8 for Mrk 421 in 1998.

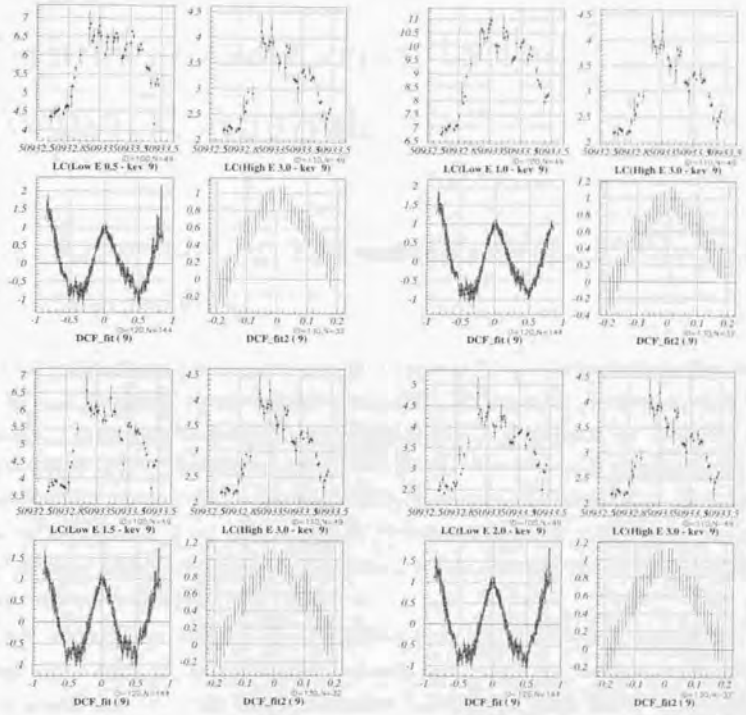

Figure B.8: DCF of time segment 9 for Mrk 421 in 1998.

Appendix C

Estimation of Errors in the Temporal Analysis

C.1 Errors on Lags Estimated from the Monte Calro Simulations

In § 7.2.5, the errors on the lags were simply determined from the uncertainty (1 σ error) of the peak parameter obtained by the minimum χ^2 fitting of the distribution DCF to a Gaussian. More accurately, errors on the lags should be determined by taking the flux uncertainties due to photon statistics into account. The statistical significance of the detection of a lag may not be assessed just by a cross-correlation analysis. In order to test the dependence of our DCF results on photon statistics and estimate the errors on the lags more properly, we apply Monte Calro simulation method which considers the flux randomization (e.g., Zhang et al. 1999).

We assumed that errors on fluxes resulting from the total photon number in a bin (more than a thousand in our case) are normally distributed. We modified each real flux at a certain time ($F(t)$) by adding a random Gaussian deviation based on the quoted error $\sigma_F(t)$ for each data point of the light curves. The modification of each data point is randomly determined from Monte Calro simulations, thus statistically independent of each other. We apply the DCF to each 'randomized' light curves and investigate the distribution of the 'time-lag'. This process was repeated for 2000 times to build up a cross-correlation peak distribution. We defined the errors on the 'lag' as the 68 % (i.e., 1 σ) of the time-lags are included in the range.

In Figure C.1, we show the results of Monte Calro simulation for two time segments of Mrk 421 observation in 1998. Time-region #2 is where the maximum 'soft-lag' was

observed and time-region #8 is the region of an opposite sense ('hard-lag': Figure 7.23). One finds that errors on the lags determined from Monte Calro simulation are exactly consistent with the that determined from the uncertainties of the peak parameter in DCF distribution fitted to a Gaussian function. Thus we conclude that the statistical significance of detection of time-lags is not affected even if we take uncertainty in observed fluxes into account.

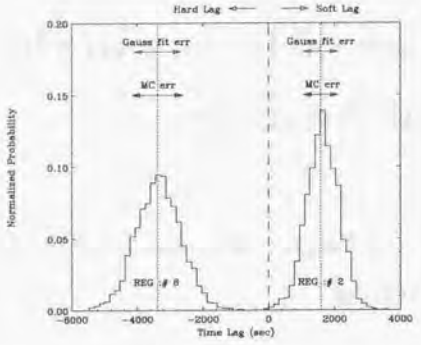

Figure C.1: Errors on time-lags determined from the Monte Calro Simulation (solid arrows). Two examples for Mrk 421 observation in 1998 are shown in the figure. Time-region #2, where the maximum 'soft-lag' was observed and time-region #8, where the maximum 'hard-lag' was observed (see, Figure 7.8, C.2). Lags are calculated for the light curve of 0.5-1.0 keV band as compared to that in 3.0-7.5 keV. Errors are exactly consistent with the previous estimation in which the error was determined from uncertainty of the peak parameter obtained by the minimum χ^2 fitting of the distribution of DCF to a Gaussian (dotted arrows).

C.2 Analysis of De-Trended Light Curves

During 7-day observation of Mrk 421 in 1998, successive occurrence of flares has been observed. These day-by-day flares are superposed on each other, forming an 'offset' in the light curves. Such an offset, or long-term trend, seems to become larger as photon energy increases (Figure 9.2). This is because the amplitude of a flare is larger at increasing photon energy (e.g., § 7.2.2). Thus it is important to verify that these energy-dependent 'offset' do not affect our analysis results. To evaluate the effect quantitatively, we fitted the light curves of Mrk 421 (1998) with a quadratic function, then subtracted the best fit function as a 'trend' (see, Figure C.2 (*left*)). Fittings were performed in various energy

bands from 0.5 keV to 7.5 keV.

Time Lags

Upper right panel of Figure C.2 shows a de-trended light curves in total *ASCA* band (0.5−7.5 keV). Bottom panel shows the time-lags for de-trended light curves in 0.5−1 keV band as compared to that in 3−7.5 keV. Corresponding figure for the original light curve (with 'offset') is Figure C.2 (*left*). One finds that results from de-trended light curves are exactly consistent with that calculated for the original light curves.

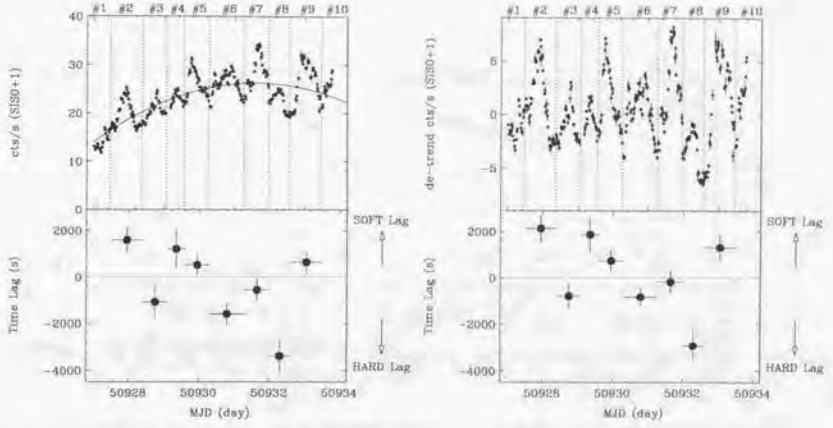

Figure C.2: Time lags of Mrk 421 during 1998 observation. *left* (*upper*): the SIS light curve for total *ASCA* bandpass (0.5−7.5 keV). The best fit quadratic function is shown as a solid line. *left* (*bottom*): time lags of 0.5-1.0 keV band as compared to that in 3.0−7.5 keV. *right* (*upper*): the SIS light curve after subtracting a quadratic trend. *right* (*bottom*): time lags of 0.5-1.0 keV band as compared to that in 3.0−7.5 keV. Results are exactly consistent with that in the left panel.

Time Asymmetry

We next calculate the structure function for these 'de-trended' light curves. For the structure function analysis, however, it is not evident that 'trend (offset)' should be removed or not. Some authors do this, while others argue strong objections (e.g., Smith et al. 1993). Remaining trend in the light curve may suppress the very features one is searching for, in particular, source has periodicity in short time scale. On the other hand, removal of the trend prevents us from investing time scales exceeding the length of the data run (Smith

et al. 1993). This should be carefully determined according to a purpose of the temporal study as well as the nature of time variability in the source.

In any case, we calculate the structure function using de-trended light curves in various energy bands. An example for SF is given in Figure C.3 (*left*). One can see that the slope of SF is unchanged in shorter time scale ($\tau < 1$ day; α 1.1–1.2).

We next measured time asymmetry of the light curve (Figure C.3 *right*). One can see a similar energy depencence with Figure 7.14, even if a quadratic trend is subtracted. We thus conclude that (1) rapid variability in TeV blazars is strong red noise type, and (2) time profile becomes more symmetric at higher energy bands regardless of 'trend' in the light curve.

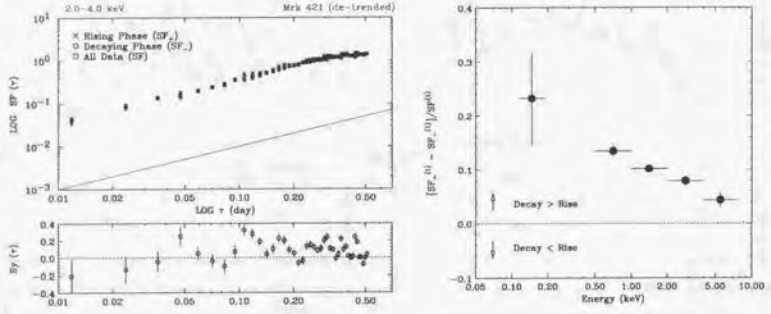

Figure C.3: *left*: Symmetry of the light curves for Mrk 421 in 2.0–4.0 keV. SF from rising phase and decaying phase are separately shown. Dotted line is $SF(\tau) \propto \tau$ to guide eyes. bottom panel shows the symmetry parameter. *right*: Energy dependence of the averaged symmetry parameter $[SF_+ - SF_-]/SF$, which was calculated for the time lags smaller than 0.5 day. We subtracted the best-fit quadratic function as a 'trend' from the original light curves. One can see that our results are not affected even if the 'trend' is subtracted (for comparison, see, Figure 7.14).

Appendix D

ASCA Spectra of TeV blazars

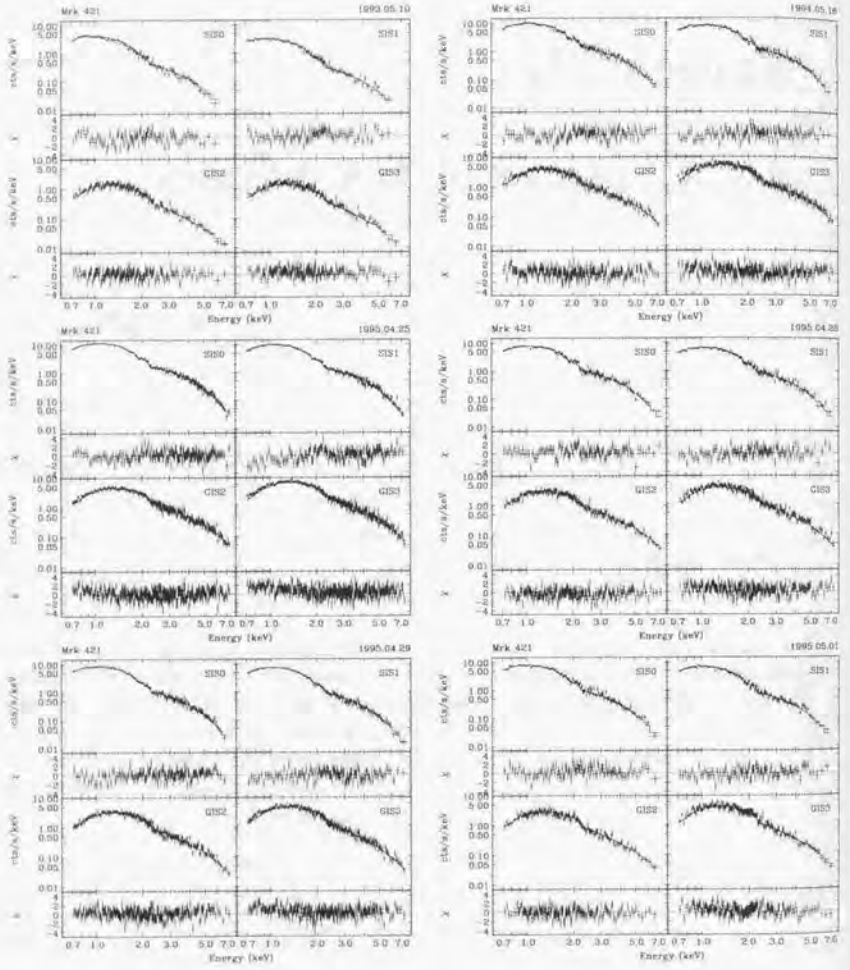

Figure D.1: Energy spectra of Mrk 421 (1).

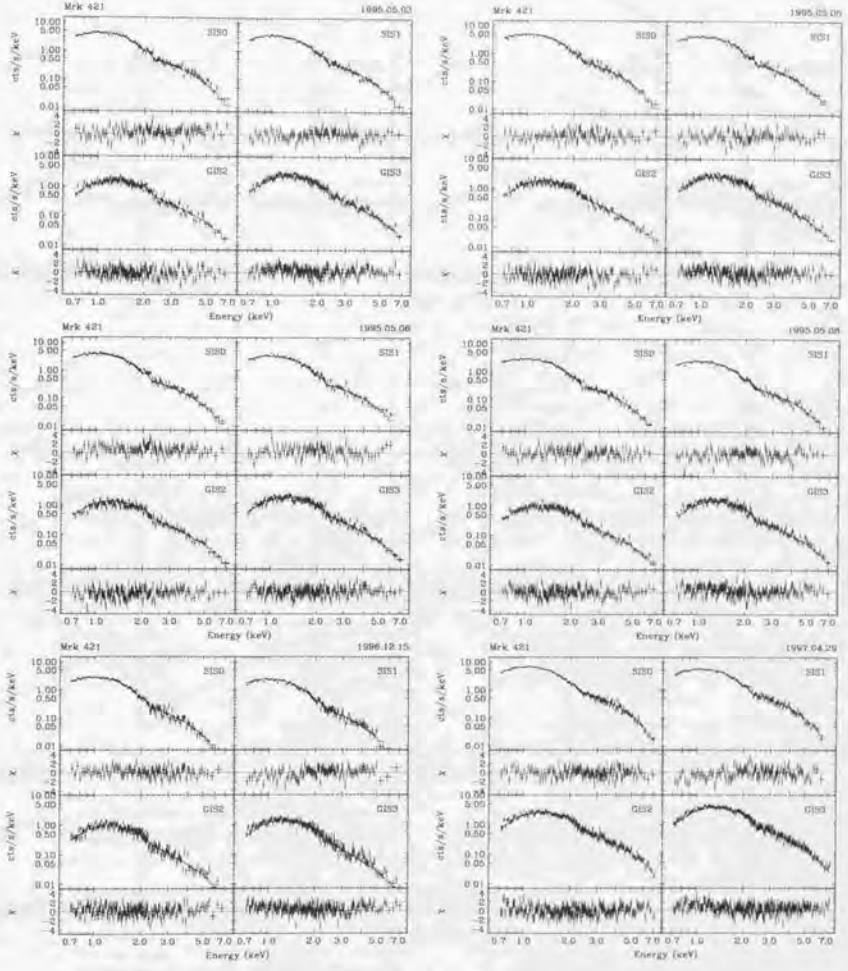

Figure D.2: Energy spectra of Mrk 421 (2).

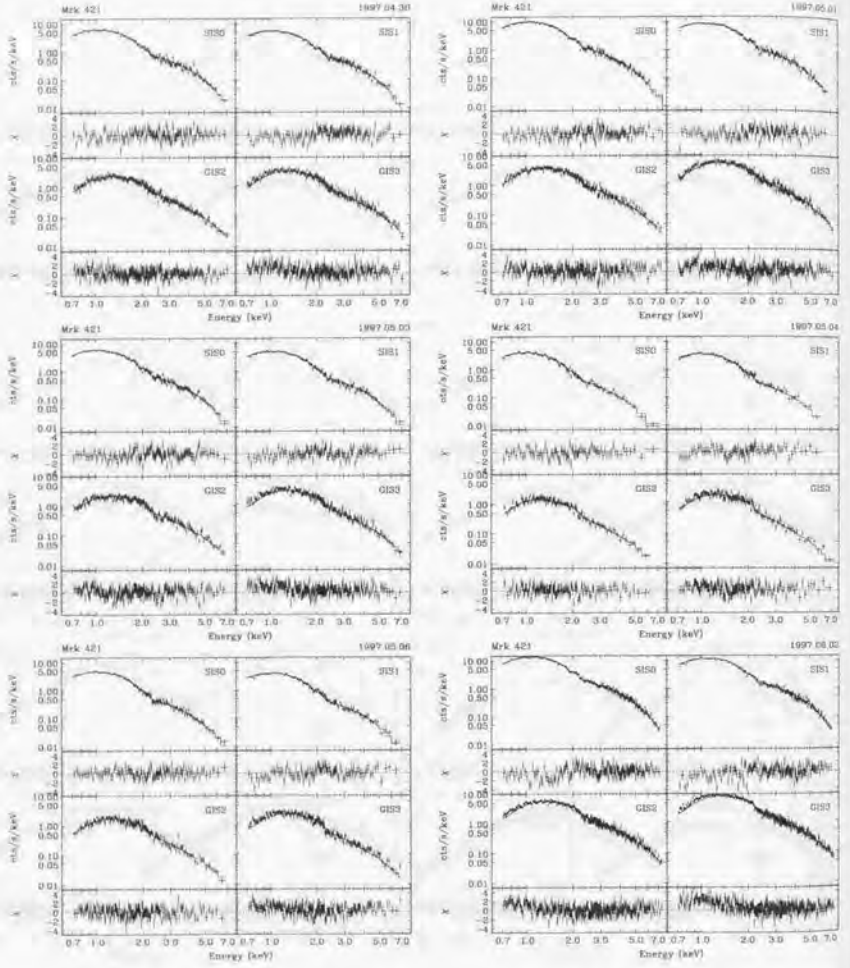

Figure D.3: Energy spectra of Mrk 421 (3).

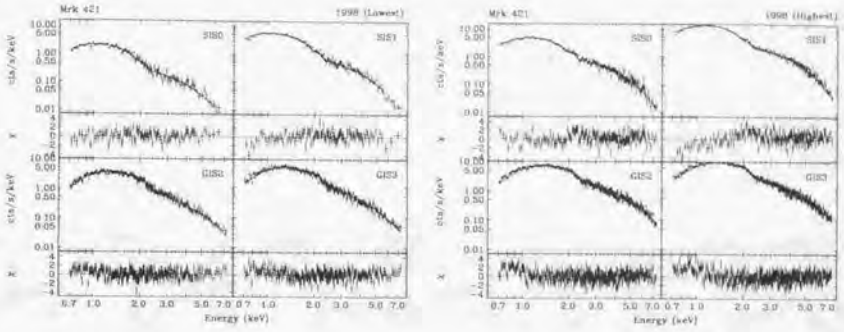

Figure D.4: *ASCA* energy spectra of Mrk 421 (4).

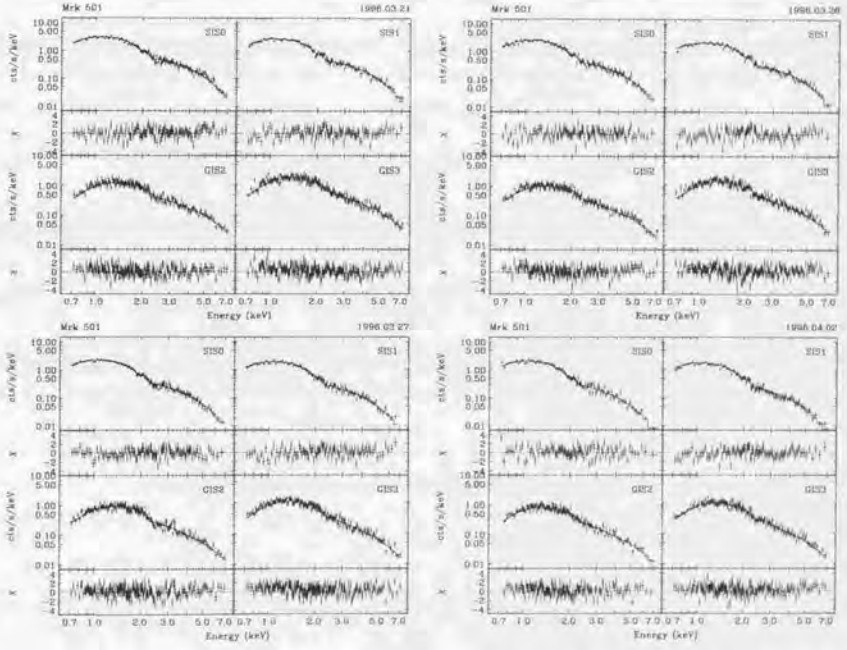

Figure D.5: *ASCA* energy spectra of Mrk 501 (1).

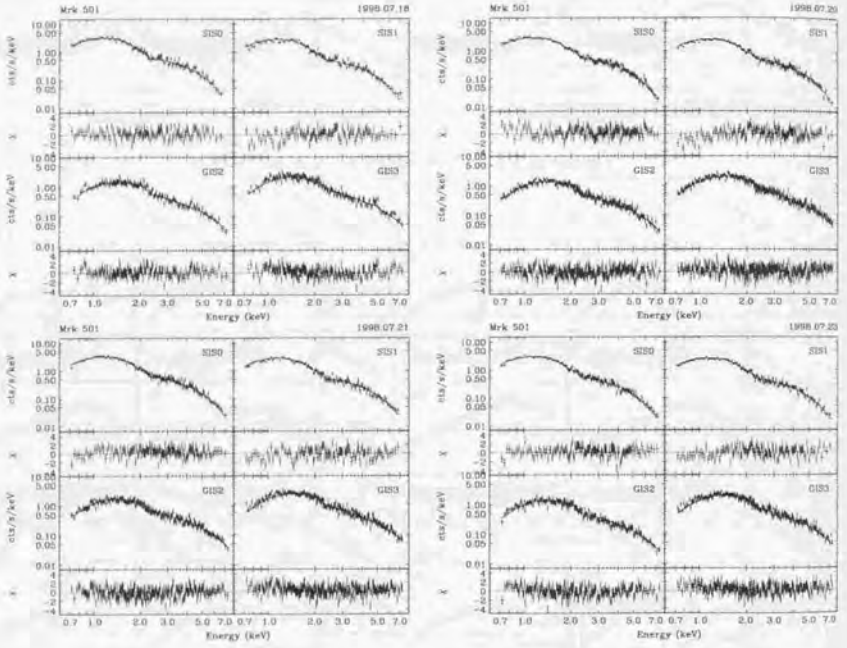

Figure D.6: *ASCA* energy spectra of Mrk 501 (2).

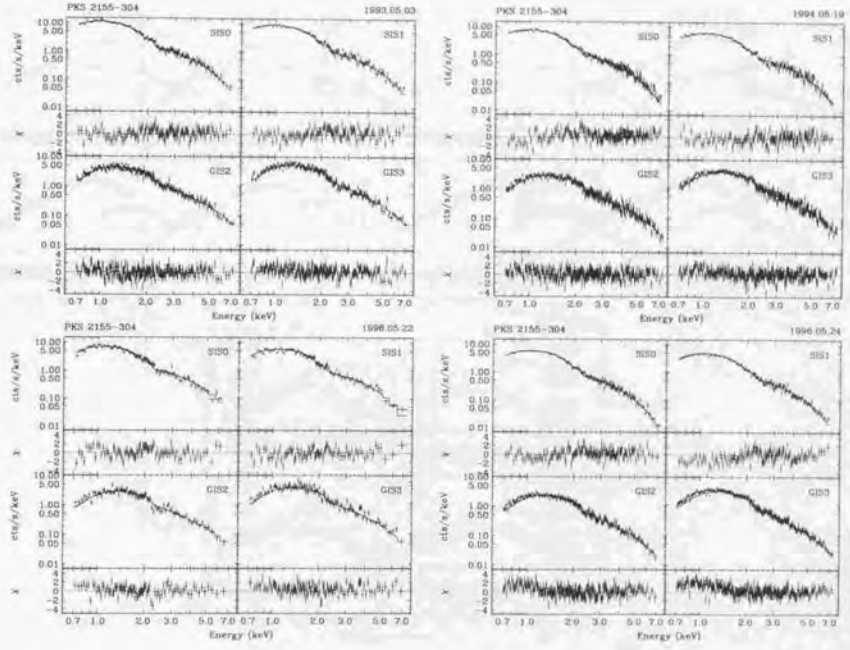

Figure D.7: *ASCA* energy spectra of PKS 2155−304 (1).

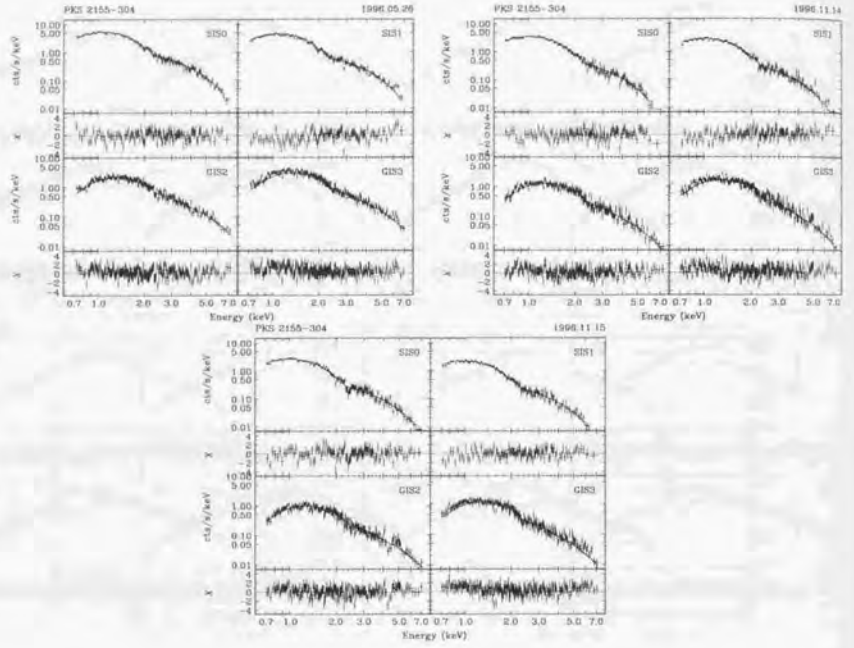

Figure D.8: *ASCA* energy spectra of PKS 2155−304 (2).

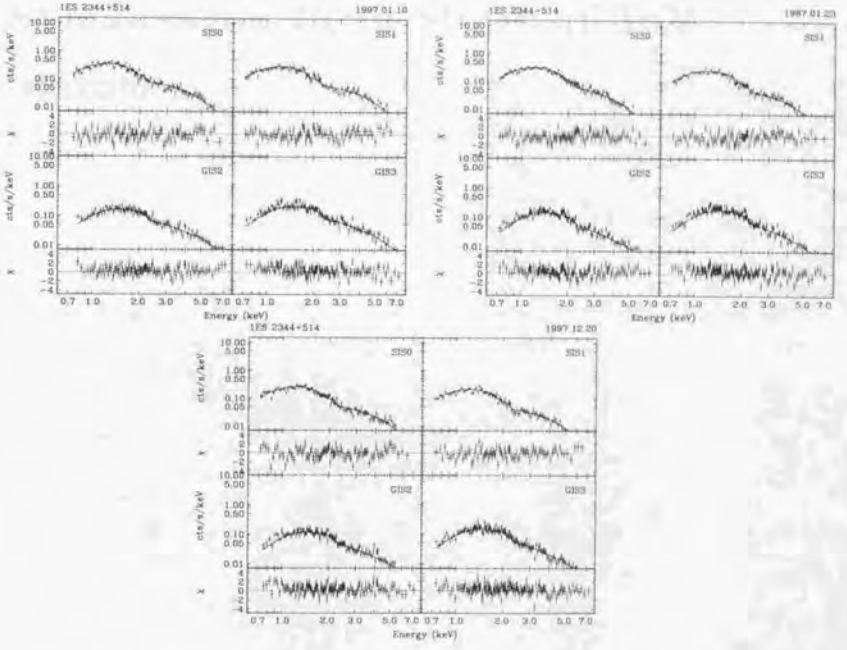

Figure D.9: *ASCA* energy spectra of 1ES 2344+514 (1).

Appendix E

Synchrotron Peak Shifts of TeV blazars

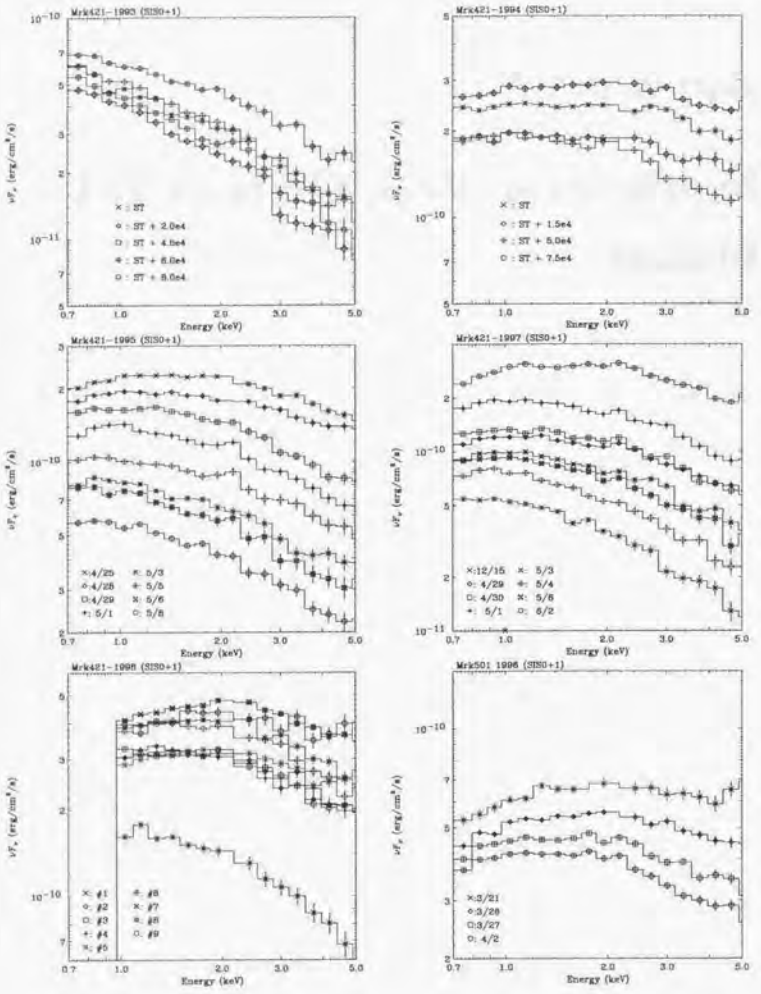

Figure E.1:

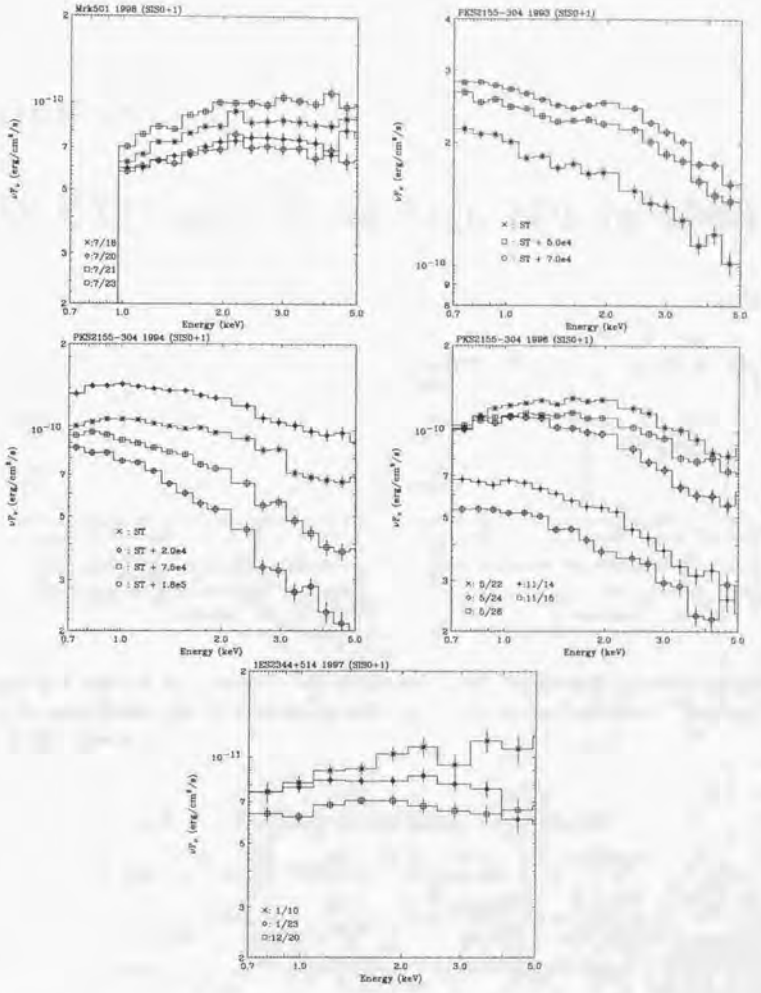

Figure E.2: Synchrotron peak shifts of Mrk 421, Mrk 501, PKS 2155−304 and 1ES 2344+514. Results from different observational seasons are separately shown. 'ST' is the start time of each observation as listed in § 6.1.

Appendix F

HEXTE spectra of Mrk 501 in 1998

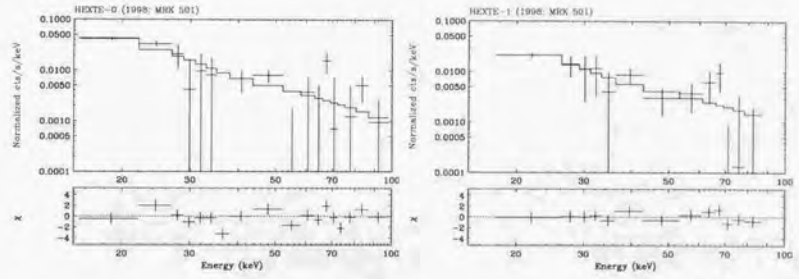

Figure F.1: *RXTE* HEXTE spectra for Mrk 501 obtained in 1998 May, fitted by a power law function. Data for total exposure (net 60 ksec) are summed. *left*: energy spectra for cluster-0, *right*: energy spectra for cluster-1.

Table F.1: Results of spectral fitting of HEXTE data

Detector	cluster	Photon Index	Flux (20-50keV) 10^{-12} erg/cm^2/s	χ^2 (d.o.f)
HEXTE	0	$2.17^{+0.25}_{-0.21}$	$23.6^{+26.7}_{-11.4}$	1.95(16)
HEXTE	1	$1.93^{+0.36}_{-0.29}$	$22.9^{+47.2}_{-14.0}$	0.67(11)

Data from 1998 05/25 to 05/27 were used for the fit (60 ksec in total). Fitting model is just a power law, because the Galactic absorption is negligibly small in this energy band. All errors are 1 σ.

Appendix G

Spectral Fit Results of *RXTE* Observations

Table G.1: Fit results of *RXTE* spectra of Mrk 421 (1)

Target	Start MJD	Stop MJD	Int. time (ksec)	N_H 10^{20}/cm^2	Photon Index	Flux (2-10keV) 10^{-12} erg/cm^2/s	χ^2 (dof)
Mrk 421	50192.084	50192.090	0.56	1.45fix	$3.08^{+0.05}_{-0.05}$	$73.38^{+1.27}_{-1.27}$	0.73(45)
	50192.315	50192.318	0.26	1.45fix	$2.95^{+0.06}_{-0.06}$	$88.21^{+1.96}_{-1.95}$	0.58(45)
	50192.516	50192.522	0.50	1.45fix	$2.92^{+0.04}_{-0.04}$	$92.03^{+1.42}_{-1.41}$	0.75(45)
	50194.053	50194.056	0.27	1.45fix	$2.90^{+0.04}_{-0.04}$	$129.30^{+2.09}_{-2.12}$	0.88(45)
	50194.219	50194.227	0.66	1.45fix	$2.87^{+0.03}_{-0.03}$	$120.30^{+1.32}_{-1.29}$	1.29(45)
	50194.381	50194.385	0.37	1.45fix	$2.66^{+0.03}_{-0.03}$	$145.50^{+1.88}_{-1.84}$	0.82(45)
	50194.892	50194.899	0.54	1.45fix	$2.65^{+0.02}_{-0.02}$	$187.00^{+1.59}_{-1.68}$	0.68(45)
	50195.584	50195.590	0.48	1.45fix	$2.77^{+0.03}_{-0.03}$	$159.80^{+1.66}_{-1.76}$	0.85(45)
	50196.019	50196.026	0.59	1.45fix	$2.74^{+0.02}_{-0.02}$	$173.70^{+1.58}_{-1.50}$	0.56(45)
	50206.176	50206.182	0.53	1.45fix	$2.11^{+0.01}_{-0.01}$	$445.70^{+2.15}_{-2.18}$	1.62(45)
	50206.425	50206.428	0.21	1.45fix	$2.41^{+0.03}_{-0.03}$	$215.60^{+2.69}_{-2.75}$	0.65(45)
	50207.248	50207.254	0.50	1.45fix	$2.76^{+0.03}_{-0.03}$	$119.10^{+1.47}_{-1.53}$	0.71(45)
	50207.356	50207.362	0.53	1.45fix	$2.79^{+0.04}_{-0.04}$	$97.01^{+1.41}_{-1.40}$	0.61(45)
	50207.772	50207.778	0.53	1.45fix	$2.63^{+0.02}_{-0.02}$	$216.40^{+1.75}_{-1.73}$	0.86(45)
	50207.901	50207.907	0.53	1.45fix	$2.31^{+0.01}_{-0.01}$	$458.10^{+2.25}_{-2.25}$	1.96(45)
	50208.169	50208.184	1.30	1.45fix	$2.52^{+0.01}_{-0.01}$	$206.90^{+1.11}_{-1.05}$	1.27(45)
	50208.426	50208.428	0.21	1.45fix	$2.36^{+0.02}_{-0.02}$	$375.00^{+3.45}_{-3.48}$	1.35(45)
	50208.556	50208.569	1.14	1.45fix	$2.27^{+0.01}_{-0.01}$	$556.40^{+1.65}_{-1.69}$	3.44(45)†
	50209.223	50209.228	0.46	1.45fix	$2.56^{+0.02}_{-0.02}$	$258.70^{+2.05}_{-1.96}$	0.78(45)
	50209.426	50209.429	0.24	1.45fix	$2.65^{+0.03}_{-0.03}$	$247.30^{+2.85}_{-2.84}$	0.78(45)
	50209.623	50209.629	0.51	1.45fix	$2.52^{+0.01}_{-0.01}$	$350.80^{+2.00}_{-2.13}$	1.09(45)
	50210.223	50210.229	0.50	1.45fix	$2.31^{+0.01}_{-0.01}$	$377.20^{+2.19}_{-2.14}$	1.34(45)
	50210.427	50210.432	0.42	1.45fix	$2.52^{+0.02}_{-0.02}$	$246.30^{+1.99}_{-2.08}$	0.96(45)
	50210.625	50210.630	0.50	1.45fix	$2.76^{+0.03}_{-0.03}$	$164.30^{+1.71}_{-1.61}$	0.84(45)
	50210.902	50210.906	0.32	1.45fix	$2.77^{+0.03}_{-0.03}$	$198.50^{+2.23}_{-2.22}$	0.53(45)
	50211.280	50211.286	0.46	1.45fix	$2.85^{+0.03}_{-0.03}$	$176.60^{+1.85}_{-1.85}$	0.72(45)
	50211.363	50211.371	0.64	1.45fix	$2.76^{+0.02}_{-0.02}$	$172.60^{+1.52}_{-1.44}$	1.06(45)
	50211.757	50211.765	0.69	1.45fix	$2.66^{+0.02}_{-0.02}$	$173.10^{+1.44}_{-1.43}$	0.91(45)
	50211.964	50211.972	0.64	1.45fix	$2.75^{+0.02}_{-0.02}$	$199.00^{+1.54}_{-1.59}$	0.99(45)
	50212.245	50212.258	1.09	1.45fix	$2.97^{+0.02}_{-0.02}$	$193.10^{+1.24}_{-1.26}$	1.09(45)
	50212.493	50212.500	0.56	1.45fix	$2.86^{+0.02}_{-0.02}$	$192.30^{+1.66}_{-1.71}$	0.65(45)

Table G.2: Fit results of Mrk 421 (2) *continued*

Target	Start MJD	Stop MJD	Int. time (ksec)	N_H 10^{20}/cm^2	Photon Index	Flux (2-10keV) 10^{-12} erg/cm^2/s	χ^2 (dof)
Mrk 421	50212.636	50212.644	0.64	1.45fix	$2.90^{+0.02}_{-0.02}$	$186.40^{+1.54}_{-1.50}$	0.65(45)
	50213.250	50213.256	0.50	1.45fix	$2.84^{+0.03}_{-0.03}$	$169.60^{+1.73}_{-1.71}$	0.75(45)
	50213.358	50213.363	0.42	1.45fix	$2.83^{+0.03}_{-0.03}$	$171.20^{+1.91}_{-1.98}$	0.66(45)
	50213.639	50213.651	1.01	1.45fix	$2.83^{+0.02}_{-0.02}$	$149.10^{+1.11}_{-1.16}$	0.71(45)
	50213.892	50213.904	1.06	1.45fix	$2.88^{+0.06}_{-0.06}$	$114.10^{+2.54}_{-2.45}$	0.57(45)
	50214.292	50214.297	0.43	1.45fix	$2.78^{+0.03}_{-0.03}$	$153.70^{+1.80}_{-1.72}$	0.65(45)
	50214.517	50214.522	0.50	1.45fix	$2.81^{+0.02}_{-0.02}$	$193.80^{+1.80}_{-1.78}$	0.92(45)
	50214.764	50214.770	0.53	1.45fix	$2.77^{+0.02}_{-0.02}$	$195.40^{+1.73}_{-1.70}$	0.70(45)
	50214.897	50214.903	0.50	1.45fix	$2.83^{+0.02}_{-0.02}$	$184.20^{+1.74}_{-1.75}$	0.99(45)
	50215.250	50215.258	0.67	1.45fix	$2.56^{+0.01}_{-0.01}$	$282.80^{+1.75}_{-1.67}$	1.29(45)
	50215.498	50215.504	0.53	1.45fix	$2.53^{+0.02}_{-0.02}$	$256.90^{+1.86}_{-1.86}$	0.96(45)
	50215.763	50215.769	0.54	1.45fix	$2.62^{+0.02}_{-0.02}$	$222.80^{+1.74}_{-1.80}$	0.79(45)
	50215.832	50215.836	0.34	1.45fix	$2.64^{+0.02}_{-0.02}$	$225.50^{+2.28}_{-2.20}$	0.81(45)
	50216.098	50216.104	0.54	1.45fix	$2.74^{+0.03}_{-0.02}$	$166.40^{+1.61}_{-1.62}$	0.55(45)
	50216.360	50216.364	0.38	1.45fix	$2.64^{+0.03}_{-0.03}$	$160.10^{+1.89}_{-1.85}$	0.81(45)
	50216.569	50216.576	0.54	1.45fix	$2.69^{+0.02}_{-0.02}$	$172.20^{+1.63}_{-1.54}$	0.85(45)
	50216.763	50216.768	0.48	1.45fix	$2.57^{+0.03}_{-0.02}$	$171.20^{+1.70}_{-1.69}$	0.68(45)
	50217.227	50217.232	0.42	1.45fix	$2.72^{+0.03}_{-0.03}$	$175.10^{+1.85}_{-1.87}$	0.72(45)
	50217.361	50217.366	0.46	1.45fix	$2.62^{+0.02}_{-0.02}$	$193.00^{+1.80}_{-1.75}$	1.13(45)
	50217.972	50217.977	0.43	1.45fix	$2.83^{+0.04}_{-0.03}$	$125.80^{+1.70}_{-1.62}$	0.65(45)
	50218.252	50218.258	0.53	1.45fix	$2.69^{+0.03}_{-0.03}$	$140.70^{+1.53}_{-1.50}$	0.66(45)
	50218.497	50218.505	0.77	1.45fix	$2.99^{+0.03}_{-0.03}$	$96.96^{+1.17}_{-1.16}$	1.35(45)
	50218.648	50218.654	0.51	1.45fix	$3.09^{+0.05}_{-0.05}$	$86.68^{+1.45}_{-1.44}$	0.62(45)
	50219.371	50219.377	0.56	1.45fix	$3.12^{+0.04}_{-0.05}$	$85.98^{+1.34}_{-1.32}$	1.02(45)
	50219.500	50219.506	0.53	1.45fix	$3.10^{+0.04}_{-0.04}$	$89.69^{+1.38}_{-1.39}$	1.02(45)
	50219.763	50219.766	0.27	1.45fix	$3.03^{+0.06}_{-0.06}$	$91.51^{+1.93}_{-1.93}$	0.71(45)
	50219.897	50219.907	0.94	1.45fix	$2.98^{+0.04}_{-0.03}$	$85.59^{+1.04}_{-1.03}$	0.57(45)
	50220.044	50220.050	0.58	1.45fix	$3.14^{+0.05}_{-0.05}$	$76.40^{+1.32}_{-1.32}$	0.84(45)
	50220.324	50220.330	0.51	1.45fix	$3.14^{+0.06}_{-0.06}$	$65.07^{+1.30}_{-1.30}$	0.97(45)
	50220.580	50220.585	0.48	1.45fix	$3.00^{+0.05}_{-0.05}$	$80.02^{+1.42}_{-1.40}$	0.48(45)
	50221.236	50221.241	0.50	1.45fix	$2.92^{+0.04}_{-0.03}$	$118.50^{+1.57}_{-1.48}$	0.83(45)
	50221.586	50221.592	0.53	1.45fix	$2.89^{+0.04}_{-0.04}$	$102.90^{+1.47}_{-1.38}$	0.77(45)
	50221.800	50221.809	0.74	1.45fix	$3.04^{+0.04}_{-0.04}$	$79.83^{+1.16}_{-1.15}$	0.69(45)
	50222.044	50222.052	0.70	1.45fix	$3.10^{+0.04}_{-0.04}$	$80.06^{+1.19}_{-1.19}$	0.78(45)
	50222.244	50222.255	0.90	1.45fix	$3.07^{+0.04}_{-0.04}$	$77.83^{+1.03}_{-1.01}$	0.76(45)
	50223.261	50223.267	0.50	1.45fix	$3.11^{+0.05}_{-0.05}$	$81.07^{+1.46}_{-1.39}$	0.61(45)
	50223.503	50223.510	0.54	1.45fix	$3.13^{+0.04}_{-0.04}$	$101.70^{+1.42}_{-1.46}$	0.91(45)
	50224.047	50224.053	0.50	1.45fix	$2.62^{+0.03}_{-0.03}$	$165.60^{+1.65}_{-1.66}$	0.61(45)
	50427.884	50427.905	1.81	1.45fix	$3.04^{+0.08}_{-0.08}$	$20.73^{+0.54}_{-0.55}$	0.70(45)
	50540.147	50540.164	1.47	1.45fix	$2.79^{+0.03}_{-0.03}$	$96.46^{+0.93}_{-0.93}$	0.50(45)
	50540.214	50540.236	1.89	1.45fix	$2.74^{+0.02}_{-0.02}$	$96.22^{+0.81}_{-0.81}$	0.71(45)
	50540.281	50540.294	1.14	1.45fix	$2.71^{+0.03}_{-0.03}$	$97.67^{+1.04}_{-1.04}$	0.61(45)
	50540.294	50540.307	1.15	1.45fix	$2.71^{+0.03}_{-0.03}$	$95.90^{+1.03}_{-1.02}$	0.47(45)
	50540.348	50540.362	1.25	1.45fix	$2.58^{+0.02}_{-0.02}$	$117.20^{+1.00}_{-1.05}$	0.69(45)
	50540.362	50540.376	1.23	1.45fix	$2.52^{+0.02}_{-0.02}$	$125.40^{+0.99}_{-1.07}$	0.68(45)

Table G.3: Fit results of Mrk 421 (3) — *continued*

Target	Start MJD	Stop MJD	Int. time (ksec)	N_H 10^{20}/cm^2	Photon Index	Flux (2-10keV) 10^{-12} erg/cm^2/s	χ^2 (dof)
Mrk 421	50541.215	50541.236	1.79	1.45fix	$2.67^{+0.02}_{-0.02}$	$124.70^{+0.88}_{-0.89}$	0.87(45)
	50541.349	50541.363	1.22	1.45fix	$2.64^{+0.03}_{-0.03}$	$100.90^{+1.01}_{-0.97}$	0.73(45)
	50541.363	50541.377	1.22	1.45fix	$2.62^{+0.03}_{-0.02}$	$105.00^{+1.02}_{-0.98}$	0.58(45)
	50542.219	50542.237	1.58	1.45fix	$2.74^{+0.03}_{-0.03}$	$92.02^{+0.88}_{-0.87}$	0.59(45)
	50542.219	50542.237	1.58	1.45fix	$2.74^{+0.03}_{-0.03}$	$92.02^{+0.88}_{-0.87}$	0.59(45)
	50542.284	50542.296	1.09	1.45fix	$2.77^{+0.04}_{-0.04}$	$76.83^{+1.02}_{-1.02}$	0.45(45)
	50542.296	50542.309	1.09	1.45fix	$2.71^{+0.03}_{-0.03}$	$81.43^{+1.00}_{-1.00}$	0.61(45)
	50543.218	50543.238	1.71	1.45fix	$2.99^{+0.03}_{-0.03}$	$88.31^{+0.87}_{-0.88}$	0.58(45)
	50543.284	50543.297	1.06	1.45fix	$2.91^{+0.03}_{-0.03}$	$87.75^{+1.10}_{-1.09}$	0.61(45)
	50543.297	50543.309	1.07	1.45fix	$2.96^{+0.04}_{-0.04}$	$86.62^{+1.10}_{-1.08}$	0.57(45)
	50543.318	50543.322	0.32	1.45fix	$2.98^{+0.06}_{-0.06}$	$86.55^{+2.01}_{-1.99}$	0.52(45)
	50548.229	50548.242	1.09	1.45fix	$3.00^{+0.02}_{-0.02}$	$141.60^{+1.22}_{-1.31}$	1.05(45)
	50548.248	50548.258	0.85	1.45fix	$2.98^{+0.03}_{-0.03}$	$140.90^{+1.43}_{-1.43}$	0.63(45)
	50548.289	50548.311	1.92	1.45fix	$2.97^{+0.02}_{-0.02}$	$140.00^{+0.93}_{-0.98}$	0.78(45)
	50549.223	50549.236	1.14	1.45fix	$2.98^{+0.01}_{-0.01}$	$451.50^{+1.90}_{-1.99}$	2.13(45)†
	50549.236	50549.249	1.15	1.45fix	$2.96^{+0.02}_{-0.02}$	$450.70^{+1.96}_{-1.96}$	2.00(45)†
	50549.249	50549.262	1.15	1.45fix	$2.97^{+0.02}_{-0.02}$	$443.50^{+1.88}_{-1.94}$	2.27(45)†
	50549.289	50549.312	1.97	1.45fix	$2.92^{+0.01}_{-0.01}$	$410.90^{+1.43}_{-1.36}$	2.53(45)†
	50549.318	50549.323	0.45	1.45fix	$2.92^{+0.02}_{-0.02}$	$406.40^{+1.86}_{-1.78}$	0.69(45)
	50550.223	50550.245	1.89	1.45fix	$2.92^{+0.02}_{-0.01}$	$180.00^{+1.03}_{-1.03}$	0.97(45)
	50550.247	50550.263	1.38	1.45fix	$2.94^{+0.02}_{-0.02}$	$181.50^{+1.24}_{-1.19}$	0.87(45)
	50550.290	50550.302	1.04	1.45fix	$2.94^{+0.02}_{-0.02}$	$185.10^{+1.42}_{-1.40}$	1.03(45)
	50550.302	50550.314	1.07	1.45fix	$2.95^{+0.02}_{-0.02}$	$182.70^{+1.41}_{-1.37}$	0.80(45)
	50550.318	50550.329	0.99	1.45fix	$2.91^{+0.02}_{-0.02}$	$184.40^{+1.43}_{-1.44}$	0.94(45)
	50550.357	50550.373	1.41	1.45fix	$2.88^{+0.02}_{-0.02}$	$200.20^{+1.26}_{-1.19}$	1.03(45)
	50567.229	50567.243	1.25	1.45fix	$3.02^{+0.02}_{-0.02}$	$130.10^{+1.14}_{-1.16}$	0.74(45)
	50568.229	50568.242	1.15	1.45fix	$2.90^{+0.02}_{-0.02}$	$123.30^{+1.16}_{-1.18}$	0.99(45)
	50568.242	50568.257	1.25	1.45fix	$2.92^{+0.03}_{-0.03}$	$125.00^{+1.35}_{-1.35}$	0.55(45)
	50569.896	50569.901	0.46	1.45fix	$2.93^{+0.03}_{-0.03}$	$194.60^{+2.13}_{-2.14}$	0.77(45)
	50569.905	50569.920	1.26	1.45fix	$2.95^{+0.02}_{-0.02}$	$194.10^{+1.28}_{-1.33}$	0.65(45)
	50570.229	50570.243	1.20	1.45fix	$2.96^{+0.02}_{-0.02}$	$176.90^{+1.24}_{-1.34}$	1.21(45)
	50570.243	50570.258	1.30	1.45fix	$2.95^{+0.02}_{-0.02}$	$174.10^{+1.52}_{-1.47}$	0.79(45)
	50571.163	50571.173	0.86	1.45fix	$2.91^{+0.03}_{-0.03}$	$110.50^{+1.31}_{-1.26}$	0.64(45)
	50571.229	50571.244	1.30	1.45fix	$2.99^{+0.03}_{-0.03}$	$101.10^{+1.05}_{-1.05}$	0.54(45)
	50571.244	50571.259	1.31	1.45fix	$3.00^{+0.03}_{-0.03}$	$96.33^{+1.02}_{-1.02}$	0.78(45)
	50572.163	50572.174	0.99	1.45fix	$3.20^{+0.06}_{-0.06}$	$54.73^{+0.98}_{-1.07}$	0.63(45)
	50572.229	50572.243	1.17	1.45fix	$3.23^{+0.06}_{-0.05}$	$55.97^{+1.02}_{-1.01}$	0.57(45)
	50574.098	50574.106	0.69	1.45fix	$2.99^{+0.05}_{-0.05}$	$81.04^{+1.34}_{-1.32}$	0.46(45)
	50574.163	50574.177	1.15	1.45fix	$3.04^{+0.04}_{-0.04}$	$76.21^{+1.05}_{-1.04}$	0.42(45)
	50574.177	50574.190	1.15	1.45fix	$3.04^{+0.04}_{-0.04}$	$76.68^{+1.03}_{-1.04}$	0.60(45)
	50574.235	50574.247	0.96	1.45fix	$3.02^{+0.04}_{-0.04}$	$76.14^{+1.15}_{-1.15}$	0.58(45)
	50602.249	50602.261	1.02	1.45fix	$2.69^{+0.01}_{-0.01}$	$403.50^{+1.81}_{-1.85}$	1.53(45)
	50602.261	50602.273	1.02	1.45fix	$2.74^{+0.02}_{-0.02}$	$403.10^{+3.04}_{-2.95}$	2.05(45)†

†: Photon spectrum is not well represented by a power law function, however, the cutoff power law function is statistically acceptable as we see in Table G.11.

Table G.4: Fit results of *RXTE* spectra of Mrk 501 (1)

Target	Start MJD	Stop MJD	Int. time (ksec)	N_H 10^{20}/cm^2	Photon Index	Flux (2-10keV) 10^{-12} erg/cm^2/s	χ^2 (dof)
Mrk 501	50296.571	50296.583	1.07	1.73fix	$2.45^{+0.02}_{-0.02}$	$111.50^{+0.98}_{-0.93}$	0.81(45)
	50378.501	50378.517	1.42	1.73fix	$2.17^{+0.01}_{-0.01}$	$154.10^{+0.98}_{-0.88}$	0.86(45)
	50525.087	50525.089	0.19	1.73fix	$2.00^{+0.02}_{-0.02}$	$299.00^{+3.19}_{-3.20}$	0.78(45)
	50525.119	50525.120	0.13	1.73fix	$1.97^{+0.03}_{-0.03}$	$302.70^{+3.99}_{-3.89}$	0.66(45)
	50541.194	50541.204	0.85	1.73fix	$2.07^{+0.01}_{-0.01}$	$328.70^{+1.67}_{-1.58}$	0.74(45)
	50541.387	50541.397	0.91	1.73fix	$2.10^{+0.01}_{-0.01}$	$296.40^{+1.48}_{-1.52}$	0.88(45)
	50542.195	50542.197	0.16	1.73fix	$1.99^{+0.03}_{-0.03}$	$299.10^{+3.55}_{-3.58}$	0.56(45)
	50542.464	50542.474	0.82	1.73fix	$2.03^{+0.01}_{-0.01}$	$318.10^{+1.57}_{-1.54}$	0.84(45)
	50543.195	50543.207	1.04	1.73fix	$2.06^{+0.01}_{-0.01}$	$319.20^{+1.41}_{-1.50}$	1.00(45)
	50543.332	50543.341	0.77	1.73fix	$2.05^{+0.01}_{-0.01}$	$315.90^{+1.68}_{-1.67}$	1.13(45)
	50544.302	50544.311	0.75	1.73fix	$1.88^{+0.01}_{-0.01}$	$373.50^{+1.72}_{-1.77}$	1.10(45)
	50544.435	50544.445	0.83	1.73fix	$1.90^{+0.01}_{-0.01}$	$366.20^{+1.66}_{-1.64}$	0.98(45)
	50545.302	50545.311	0.78	1.73fix	$2.02^{+0.01}_{-0.01}$	$291.90^{+1.58}_{-1.59}$	0.86(45)
	50545.442	50545.452	0.86	1.73fix	$2.01^{+0.01}_{-0.01}$	$283.40^{+1.50}_{-1.47}$	0.71(45)
	50546.236	50546.240	0.38	1.73fix	$2.04^{+0.02}_{-0.02}$	$248.40^{+2.38}_{-2.09}$	0.64(45)
	50546.250	50546.255	0.45	1.73fix	$2.02^{+0.02}_{-0.02}$	$245.40^{+1.95}_{-1.98}$	0.62(45)
	50546.442	50546.452	0.86	1.73fix	$2.02^{+0.01}_{-0.01}$	$244.70^{+1.46}_{-1.46}$	0.82(45)
	50547.236	50547.241	0.45	1.73fix	$1.95^{+0.02}_{-0.02}$	$255.50^{+1.97}_{-1.96}$	0.66(45)
	50547.249	50547.255	0.51	1.73fix	$1.98^{+0.02}_{-0.02}$	$254.50^{+1.89}_{-1.81}$	0.70(45)
	50547.436	50547.446	0.82	1.73fix	$1.93^{+0.01}_{-0.01}$	$264.50^{+1.46}_{-1.46}$	0.62(45)
	50548.268	50548.275	0.62	1.73fix	$1.87^{+0.01}_{-0.01}$	$312.90^{+1.77}_{-1.78}$	1.27(45)
	50548.321	50548.330	0.85	1.73fix	$1.88^{+0.01}_{-0.01}$	$321.20^{+1.56}_{-1.54}$	0.81(45)
	50549.202	50549.208	0.54	1.73fix	$1.90^{+0.01}_{-0.01}$	$319.10^{+1.67}_{-1.69}$	0.78(45)
	50549.332	50549.342	0.82	1.73fix	$1.90^{+0.01}_{-0.01}$	$302.80^{+1.57}_{-1.54}$	0.77(45)
	50550.183	50550.193	0.85	1.73fix	$1.89^{+0.01}_{-0.01}$	$306.80^{+1.65}_{-1.70}$	0.92(45)
	50550.448	50550.451	0.26	1.73fix	$1.85^{+0.02}_{-0.02}$	$427.50^{+3.10}_{-3.19}$	1.47(45)
	50550.453	50550.460	0.54	1.73fix	$1.85^{+0.01}_{-0.01}$	$428.90^{+2.22}_{-2.27}$	1.00(45)
	50551.266	50551.276	0.82	1.73fix	$1.81^{+0.01}_{-0.01}$	$531.80^{+1.94}_{-1.86}$	1.11(45)
	50551.459	50551.469	0.90	1.73fix	$1.77^{+0.01}_{-0.01}$	$535.20^{+1.83}_{-1.88}$	1.13(45)
	50552.333	50552.342	0.78	1.73fix	$1.89^{+0.03}_{-0.03}$	$436.90^{+1.85}_{-1.76}$	1.18(45)
	50552.457	50552.469	1.02	1.73fix	$1.81^{+0.01}_{-0.01}$	$421.70^{+1.59}_{-1.54}$	0.81(45)
	50553.264	50553.276	1.06	1.73fix	$1.84^{+0.01}_{-0.01}$	$435.40^{+1.58}_{-1.54}$	0.91(45)
	50553.372	50553.382	0.88	1.73fix	$1.93^{+0.06}_{-0.06}$	$414.20^{+12.62}_{-12.65}$	1.08(45)
	50554.171	50554.183	1.02	1.73fix	$1.71^{+0.01}_{-0.01}$	$603.10^{+1.78}_{-1.81}$	1.23(45)
	50554.443	50554.451	0.66	1.73fix	$1.72^{+0.01}_{-0.01}$	$659.20^{+2.34}_{-2.31}$	1.15(45)
	50570.179	50570.182	0.27	1.73fix	$1.96^{+0.02}_{-0.02}$	$263.30^{+2.52}_{-2.60}$	0.89(45)
	50570.392	50570.402	0.85	1.73fix	$2.03^{+0.01}_{-0.01}$	$265.00^{+1.49}_{-1.48}$	0.57(45)
	50571.182	50571.188	0.50	1.73fix	$1.90^{+0.01}_{-0.01}$	$304.60^{+1.95}_{-2.00}$	0.83(45)
	50572.183	50572.188	0.40	1.73fix	$1.78^{+0.01}_{-0.01}$	$383.20^{+2.42}_{-2.35}$	0.90(45)
	50572.252	50572.260	0.67	1.73fix	$1.80^{+0.01}_{-0.01}$	$384.90^{+2.89}_{-2.81}$	0.86(45)

Table G.5: Fit results of Mrk 501 (2) – *continued*

Target	Start MJD	Stop MJD	Int. time (ksec)	N_H 10^{20}/cm^2	Photon Index	Flux (2-10keV) 10^{-12} erg/cm^2/s	χ^2 (dof)
Mrk 501	50573.177	50573.189	1.01	1.73fix	$1.91^{+0.01}_{-0.01}$	$293.70^{+1.38}_{-1.40}$	0.80(45)
	50573.393	50573.403	0.86	1.73fix	$1.89^{+0.01}_{-0.01}$	$292.10^{+1.47}_{-1.52}$	0.95(45)
	50574.256	50574.262	0.51	1.73fix	$1.92^{+0.02}_{-0.01}$	$276.60^{+1.89}_{-1.92}$	0.64(45)
	50574.316	50574.333	1.46	1.73fix	$1.88^{+0.01}_{-0.01}$	$291.80^{+1.18}_{-1.12}$	0.57(45)
	50575.243	50575.262	1.55	1.73fix	$1.77^{+0.01}_{-0.01}$	$415.30^{+1.28}_{-1.24}$	0.81(45)
	50575.394	50575.404	0.85	1.73fix	$1.72^{+0.01}_{-0.01}$	$480.70^{+1.75}_{-1.85}$	1.06(45)
	50576.392	50576.405	1.14	1.73fix	$1.80^{+0.01}_{-0.01}$	$365.90^{+1.56}_{-1.54}$	0.88(45)
	50577.332	50577.335	0.30	1.73fix	$1.82^{+0.01}_{-0.01}$	$422.50^{+2.94}_{-2.85}$	0.91(45)
	50578.393	50578.406	0.96	1.73fix	$1.82^{+0.01}_{-0.01}$	$433.00^{+1.62}_{-1.67}$	1.16(45)
	50579.393	50579.403	0.88	1.73fix	$1.83^{+0.01}_{-0.01}$	$459.30^{+1.74}_{-1.78}$	0.85(45)
	50580.183	50580.194	0.93	1.73fix	$1.83^{+0.01}_{-0.01}$	$495.10^{+1.74}_{-1.80}$	1.45(45)
	50581.189	50581.194	0.50	1.73fix	$1.86^{+0.01}_{-0.01}$	$503.50^{+2.43}_{-2.47}$	1.13(45)
	50582.399	50582.409	0.91	1.73fix	$1.84^{+0.01}_{-0.01}$	$393.70^{+1.62}_{-1.62}$	0.60(45)
	50583.187	50583.196	0.77	1.73fix	$1.79^{+0.01}_{-0.01}$	$397.50^{+1.73}_{-1.80}$	0.97(45)
	50583.259	50583.267	0.67	1.73fix	$1.80^{+0.01}_{-0.01}$	$399.30^{+1.92}_{-1.87}$	1.12(45)
	50640.982	50640.991	0.80	1.73fix	$1.98^{+0.01}_{-0.01}$	$628.50^{+2.22}_{-2.21}$	1.66(45)
	50641.151	50641.166	1.30	1.73fix	$1.96^{+0.01}_{-0.01}$	$619.90^{+1.65}_{-1.70}$	2.57(45)†
	50641.176	50641.191	1.28	1.73fix	$1.96^{+0.01}_{-0.01}$	$614.10^{+1.66}_{-1.70}$	2.44(45)†
	50641.982	50641.991	0.78	1.73fix	$1.90^{+0.01}_{-0.01}$	$596.70^{+2.10}_{-2.15}$	1.49(45)
	50642.151	50642.166	1.30	1.73fix	$1.88^{+0.01}_{-0.01}$	$581.60^{+1.57}_{-1.64}$	1.46(45)
	50642.175	50642.191	1.36	1.73fix	$1.86^{+0.01}_{-0.01}$	$597.10^{+1.56}_{-1.60}$	1.71(45)
	50642.982	50642.991	0.78	1.73fix	$1.85^{+0.01}_{-0.01}$	$569.60^{+2.03}_{-2.08}$	1.32(45)
	50643.152	50643.168	1.39	1.73fix	$1.85^{+0.01}_{-0.01}$	$521.70^{+1.42}_{-1.52}$	1.69(45)
	50643.175	50643.191	1.42	1.73fix	$1.85^{+0.01}_{-0.01}$	$521.10^{+1.49}_{-1.42}$	1.84(45)
	50643.982	50643.991	0.77	1.73fix	$1.89^{+0.01}_{-0.01}$	$582.80^{+2.15}_{-2.07}$	1.08(45)
	50644.152	50644.169	1.42	1.73fix	$1.90^{+0.01}_{-0.01}$	$611.80^{+1.55}_{-1.60}$	2.07(45)†
	50644.172	50644.192	1.66	1.73fix	$1.90^{+0.00}_{-0.01}$	$611.90^{+1.50}_{-1.41}$	1.56(45)
	50644.983	50644.992	0.75	1.73fix	$1.94^{+0.01}_{-0.01}$	$689.50^{+2.35}_{-2.26}$	1.51(45)
	50645.152	50645.171	1.60	1.73fix	$1.95^{+0.01}_{-0.01}$	$700.70^{+1.61}_{-1.56}$	3.53(45)†
	50645.173	50645.192	1.63	1.73fix	$1.90^{+0.01}_{-0.01}$	$686.00^{+1.53}_{-1.53}$	3.45(45)†
	50958.166	50958.173	0.58	1.73fix	$2.11^{+0.03}_{-0.03}$	$106.20^{+1.31}_{-1.40}$	0.63(45)
	50958.332	50958.351	1.62	1.73fix	$2.08^{+0.02}_{-0.02}$	$100.50^{+0.79}_{-0.76}$	0.69(45)
	50958.358	50958.372	1.25	1.73fix	$2.11^{+0.02}_{-0.02}$	$100.50^{+0.89}_{-0.88}$	0.77(45)
	50958.399	50958.411	1.02	1.73fix	$2.09^{+0.02}_{-0.02}$	$100.00^{+1.02}_{-0.95}$	0.49(45)
	50958.411	50958.423	1.01	1.73fix	$2.11^{+0.02}_{-0.02}$	$99.20^{+0.98}_{-0.98}$	0.54(45)
	50958.427	50958.439	1.07	1.73fix	$2.11^{+0.02}_{-0.02}$	$99.67^{+0.96}_{-0.95}$	0.57(45)
	50958.532	50958.545	1.09	1.73fix	$2.05^{+0.02}_{-0.02}$	$99.28^{+0.95}_{-0.94}$	0.99(45)
	50958.545	50958.558	1.10	1.73fix	$2.11^{+0.02}_{-0.02}$	$102.10^{+0.90}_{-0.97}$	0.66(45)
	50958.569	50958.573	0.29	1.73fix	$2.04^{+0.05}_{-0.05}$	$97.01^{+1.85}_{-1.85}$	0.70(45)
	50958.599	50958.612	1.15	1.73fix	$2.06^{+0.02}_{-0.02}$	$103.30^{+0.98}_{-0.88}$	0.90(45)

Table G.6: Fit results of Mrk 501 (3) – *continued*

Target	Start MJD	Stop MJD	Int. time (ksec)	N_H 10^{20}/cm^2	Photon Index	Flux (2-10keV) 10^{-12} erg/cm^2/s	χ^2 (dof)
Mrk 501	50958.612	50958.626	1.18	1.73fix	$2.08^{+0.02}_{-0.02}$	$103.80^{+0.94}_{-0.89}$	0.71(45)
	50958.675	50958.696	1.81	1.73fix	$2.06^{+0.02}_{-0.02}$	$108.10^{+0.73}_{-0.75}$	0.64(45)
	50958.704	50958.706	0.21	1.73fix	$2.11^{+0.05}_{-0.03}$	$105.70^{+2.22}_{-2.23}$	0.52(45)
	50958.815	50958.827	1.04	1.73fix	$2.08^{+0.02}_{-0.02}$	$107.80^{+0.99}_{-0.98}$	0.63(45)
	50958.827	50958.839	1.06	1.73fix	$2.07^{+0.02}_{-0.02}$	$122.30^{+0.98}_{-1.06}$	0.94(45)
	50958.885	50958.906	1.79	1.73fix	$2.07^{+0.02}_{-0.02}$	$112.50^{+0.74}_{-0.80}$	0.68(45)
	50959.291	50959.306	1.31	1.73fix	$2.11^{+0.02}_{-0.02}$	$113.30^{+0.90}_{-0.89}$	0.47(45)
	50959.333	50959.354	1.81	1.73fix	$2.11^{+0.02}_{-0.02}$	$111.30^{+0.79}_{-0.72}$	0.93(45)
	50959.356	50959.373	1.42	1.73fix	$2.13^{+0.02}_{-0.02}$	$111.20^{+0.93}_{-0.88}$	0.61(45)
	50959.400	50959.423	1.97	1.73fix	$2.11^{+0.02}_{-0.02}$	$110.10^{+0.76}_{-0.69}$	0.71(45)
	50959.427	50959.439	1.04	1.73fix	$2.12^{+0.02}_{-0.02}$	$108.10^{+0.96}_{-1.04}$	0.64(45)
	50959.599	50959.613	1.18	1.73fix	$2.14^{+0.02}_{-0.02}$	$105.70^{+0.94}_{-0.92}$	0.75(45)
	50959.613	50959.627	1.20	1.73fix	$2.15^{+0.02}_{-0.02}$	$105.20^{+0.93}_{-0.91}$	0.93(45)
	50959.637	50959.639	0.21	1.73fix	$2.15^{+0.05}_{-0.05}$	$103.40^{+2.25}_{-2.24}$	0.64(45)
	50959.675	50959.696	1.84	1.73fix	$2.16^{+0.02}_{-0.02}$	$108.70^{+0.71}_{-0.79}$	0.87(45)
	50959.704	50959.706	0.14	1.73fix	$2.19^{+0.06}_{-0.06}$	$108.00^{+2.69}_{-2.70}$	0.68(45)
	50960.096	50960.106	0.86	1.73fix	$2.17^{+0.02}_{-0.02}$	$120.50^{+1.11}_{-1.20}$	0.95(45)
	50960.166	50960.172	0.58	1.73fix	$2.16^{+0.03}_{-0.03}$	$113.50^{+1.34}_{-1.41}$	0.72(45)
	50960.289	50960.306	1.44	1.73fix	$2.22^{+0.02}_{-0.02}$	$103.30^{+0.86}_{-0.83}$	0.54(45)
	50960.333	50960.353	1.78	1.73fix	$2.18^{+0.02}_{-0.02}$	$104.50^{+0.74}_{-0.78}$	0.55(45)
	50960.356	50960.372	1.41	1.73fix	$2.19^{+0.02}_{-0.02}$	$103.40^{+0.83}_{-0.87}$	0.60(45)
	50960.400	50960.422	1.87	1.73fix	$2.16^{+0.02}_{-0.02}$	$103.20^{+0.74}_{-0.72}$	1.23(45)
	50960.427	50960.439	1.01	1.73fix	$2.19^{+0.02}_{-0.02}$	$104.30^{+0.99}_{-1.04}$	0.68(45)
	50960.533	50960.546	1.12	1.73fix	$2.19^{+0.02}_{-0.02}$	$100.90^{+0.91}_{-0.99}$	0.79(45)
	50960.546	50960.559	1.14	1.73fix	$2.19^{+0.02}_{-0.02}$	$102.10^{+0.95}_{-0.92}$	0.62(45)
	50960.569	50960.572	0.27	1.73fix	$2.16^{+0.05}_{-0.05}$	$97.14^{+1.94}_{-1.92}$	0.86(45)
	50960.599	50960.613	1.15	1.73fix	$2.14^{+0.02}_{-0.02}$	$100.10^{+0.96}_{-0.89}$	0.69(45)
	50960.613	50960.627	1.18	1.73fix	$2.19^{+0.02}_{-0.02}$	$103.50^{+0.93}_{-0.91}$	0.80(45)
	50960.636	50960.639	0.24	1.73fix	$2.11^{+0.05}_{-0.05}$	$96.44^{+2.03}_{-2.02}$	0.65(45)

†: Phton spectrum is not well represented by a power law function, however, the cutoff power law function is statistically acceptable as we see in Table G.11.

Table G.7: Fit results of *RXTE* spectra of PKS 2155−304 (1)

Target	Start MJD	Stop MJD	Int. time (ksec)	N_H 10^{20}/cm^2	Photon Index	Flux (2-10keV) 10^{-12} erg/cm^2/s	χ^2 (dof)
PKS 2155	50219.027	50219.034	0.56	1.77fix	$2.68^{+0.04}_{-0.04}$	$79.96^{+1.27}_{-1.26}$	0.66(45)
−304	50219.150	50219.157	0.56	1.77fix	$2.50^{+0.04}_{-0.04}$	$91.32^{+1.28}_{-1.27}$	0.48(45)
	50219.260	50219.264	0.29	1.77fix	$2.52^{+0.05}_{-0.05}$	$85.06^{+1.71}_{-1.71}$	0.67(45)
	50219.397	50219.403	0.50	1.77fix	$2.56^{+0.04}_{-0.04}$	$88.86^{+1.32}_{-1.31}$	0.68(45)
	50219.527	50219.533	0.48	1.77fix	$2.56^{+0.04}_{-0.04}$	$85.71^{+1.33}_{-1.32}$	0.84(45)
	50219.694	50219.700	0.53	1.77fix	$2.44^{+0.03}_{-0.03}$	$108.50^{+1.36}_{-1.32}$	0.43(45)
	50219.940	50219.944	0.37	1.77fix	$2.83^{+0.20}_{-0.19}$	$118.60^{+8.60}_{-8.61}$	0.92(45)
	50220.080	50220.094	1.13	1.77fix	$2.46^{+0.02}_{-0.02}$	$110.50^{+1.06}_{-1.02}$	0.85(45)
	50220.227	50220.235	0.74	1.77fix	$2.35^{+0.02}_{-0.02}$	$129.90^{+1.14}_{-1.22}$	0.91(45)
	50220.298	50220.302	0.40	1.77fix	$2.39^{+0.03}_{-0.03}$	$134.70^{+1.65}_{-1.60}$	0.74(45)
	50220.498	50220.502	0.38	1.77fix	$2.38^{+0.03}_{-0.03}$	$148.40^{+1.72}_{-1.70}$	0.92(45)
	50220.661	50220.667	0.45	1.77fix	$2.31^{+0.02}_{-0.02}$	$176.10^{+1.69}_{-1.64}$	0.74(45)
	50220.898	50220.903	0.43	1.77fix	$2.50^{+0.03}_{-0.03}$	$116.90^{+1.51}_{-1.60}$	0.83(45)
	50221.094	50221.100	0.48	1.77fix	$2.39^{+0.03}_{-0.03}$	$120.60^{+1.48}_{-1.44}$	0.95(45)
	50221.298	50221.303	0.43	1.77fix	$2.54^{+0.04}_{-0.03}$	$107.30^{+1.51}_{-1.46}$	0.78(45)
	50221.399	50221.405	0.53	1.77fix	$2.55^{+0.03}_{-0.03}$	$107.20^{+1.39}_{-1.31}$	0.55(45)
	50221.561	50221.566	0.40	1.77fix	$2.57^{+0.04}_{-0.04}$	$94.03^{+1.48}_{-1.48}$	0.51(45)
	50221.760	50221.766	0.53	1.77fix	$2.54^{+0.04}_{-0.03}$	$96.19^{+1.30}_{-1.30}$	0.61(45)
	50221.898	50221.904	0.54	1.77fix	$2.54^{+0.03}_{-0.03}$	$105.30^{+1.37}_{-1.31}$	0.78(45)
	50221.964	50221.971	0.54	1.77fix	$2.48^{+0.03}_{-0.03}$	$107.40^{+1.35}_{-1.31}$	0.73(45)
	50222.081	50222.104	1.98	1.77fix	$2.51^{+0.02}_{-0.02}$	$114.00^{+0.68}_{-0.75}$	0.78(45)
	50222.151	50222.171	1.70	1.77fix	$2.48^{+0.02}_{-0.02}$	$115.00^{+0.75}_{-0.78}$	0.67(45)
	50222.275	50222.290	1.26	1.77fix	$2.47^{+0.02}_{-0.02}$	$112.20^{+0.88}_{-0.87}$	0.44(45)
	50222.290	50222.305	1.28	1.77fix	$2.48^{+0.02}_{-0.02}$	$113.50^{+0.83}_{-0.92}$	1.15(45)
	50222.604	50222.618	1.20	1.77fix	$2.53^{+0.02}_{-0.02}$	$121.40^{+0.96}_{-0.91}$	0.89(45)
	50222.618	50222.632	1.18	1.77fix	$2.55^{+0.02}_{-0.02}$	$123.20^{+1.00}_{-0.90}$	0.56(45)
	50222.663	50222.681	1.49	1.77fix	$2.54^{+0.02}_{-0.02}$	$126.30^{+0.82}_{-0.86}$	0.78(45)
	50222.681	50222.698	1.52	1.77fix	$2.49^{+0.02}_{-0.02}$	$128.40^{+0.86}_{-0.81}$	0.69(45)
	50222.752	50222.767	1.34	1.77fix	$2.49^{+0.02}_{-0.02}$	$131.00^{+0.95}_{-0.86}$	0.96(45)
	50222.801	50222.813	1.07	1.77fix	$2.43^{+0.02}_{-0.02}$	$148.80^{+1.05}_{-1.06}$	0.64(45)
	50222.813	50222.826	1.09	1.77fix	$2.43^{+0.02}_{-0.02}$	$156.50^{+1.33}_{-1.24}$	1.10(45)
	50222.826	50222.839	1.09	1.77fix	$2.43^{+0.02}_{-0.02}$	$161.50^{+1.06}_{-1.07}$	1.07(45)
	50222.941	50222.959	1.57	1.77fix	$2.48^{+0.02}_{-0.02}$	$174.70^{+1.15}_{-1.18}$	1.12(45)
	50222.959	50222.972	1.07	1.77fix	$2.52^{+0.02}_{-0.02}$	$174.20^{+1.11}_{-1.14}$	0.79(45)
	50223.012	50223.026	1.22	1.77fix	$2.53^{+0.02}_{-0.02}$	$174.70^{+1.23}_{-1.19}$	0.96(45)
	50223.026	50223.039	1.14	1.77fix	$2.52^{+0.02}_{-0.02}$	$173.30^{+1.10}_{-1.07}$	1.29(45)
	50223.082	50223.094	1.02	1.77fix	$2.57^{+0.02}_{-0.02}$	$167.60^{+1.14}_{-1.15}$	0.95(45)
	50223.094	50223.105	1.02	1.77fix	$2.58^{+0.02}_{-0.02}$	$169.30^{+1.14}_{-1.14}$	1.01(45)
	50223.152	50223.172	1.76	1.77fix	$2.55^{+0.01}_{-0.01}$	$162.50^{+0.82}_{-0.88}$	1.11(45)
	50223.222	50223.239	1.46	1.77fix	$2.54^{+0.01}_{-0.01}$	$177.00^{+0.94}_{-0.98}$	1.03(45)

Table G.8: Fit results of PKS 2155−304 (2) - *continued*

Target	Start MJD	Stop MJD	Int. time (ksec)	N_H 10^{20}/cm^2	Photon Index	Flux (2-10keV) 10^{-12} erg/cm^2/s	χ^2 (dof)
PKS 2155	50223.531	50223.548	1.42	1.77fix	$2.51^{+0.01}_{-0.01}$	$209.50^{+1.06}_{-1.00}$	1.41(45)
−304	50223.548	50223.564	1.44	1.77fix	$2.49^{+0.01}_{-0.01}$	$206.80^{+1.04}_{-1.01}$	0.75(45)
	50223.829	50223.839	0.85	1.77fix	$2.48^{+0.02}_{-0.02}$	$210.10^{+1.34}_{-1.33}$	0.86(45)
	50223.872	50223.890	1.60	1.77fix	$2.49^{+0.01}_{-0.01}$	$193.10^{+1.11}_{-1.07}$	0.78(45)
	50223.890	50223.907	1.41	1.77fix	$2.48^{+0.01}_{-0.01}$	$188.40^{+1.00}_{-1.00}$	0.98(45)
	50223.942	50223.959	1.44	1.77fix	$2.45^{+0.02}_{-0.01}$	$179.20^{+1.06}_{-1.14}$	0.98(45)
	50223.959	50223.973	1.26	1.77fix	$2.45^{+0.01}_{-0.01}$	$183.90^{+1.06}_{-1.03}$	1.21(45)
	50224.012	50224.027	1.30	1.77fix	$2.46^{+0.02}_{-0.02}$	$192.50^{+1.56}_{-1.05}$	1.00(45)
	50224.207	50224.212	0.45	1.77fix	$2.59^{+0.02}_{-0.02}$	$178.20^{+1.76}_{-1.79}$	0.83(45)
	50224.302	50224.307	0.40	1.77fix	$2.61^{+0.03}_{-0.03}$	$155.80^{+1.76}_{-1.76}$	0.84(45)
	50224.479	50224.488	0.77	1.77fix	$2.53^{+0.02}_{-0.02}$	$192.60^{+1.45}_{-1.35}$	0.86(45)
	50224.624	50224.630	0.54	1.77fix	$2.43^{+0.02}_{-0.02}$	$207.40^{+1.68}_{-1.65}$	0.74(45)
	50224.763	50224.769	0.51	1.77fix	$2.52^{+0.02}_{-0.02}$	$213.30^{+1.78}_{-1.77}$	0.87(45)
	50224.901	50224.908	0.59	1.77fix	$2.50^{+0.02}_{-0.02}$	$214.30^{+1.61}_{-1.64}$	0.77(45)
	50225.207	50225.224	1.47	1.77fix	$2.56^{+0.01}_{-0.01}$	$186.40^{+0.94}_{-1.01}$	1.51(45)
	50225.359	50225.366	0.56	1.77fix	$2.56^{+0.02}_{-0.02}$	$179.20^{+1.56}_{-1.55}$	1.13(45)
	50225.493	50225.496	0.29	1.77fix	$2.49^{+0.03}_{-0.03}$	$213.00^{+2.31}_{-2.27}$	0.71(45)
	50225.734	50225.739	0.42	1.77fix	$2.44^{+0.02}_{-0.02}$	$211.50^{+1.93}_{-1.94}$	0.90(45)
	50225.834	50225.841	0.61	1.77fix	$2.46^{+0.02}_{-0.02}$	$194.40^{+1.55}_{-1.52}$	0.92(45)
	50225.968	50225.975	0.59	1.77fix	$2.52^{+0.02}_{-0.02}$	$203.40^{+1.62}_{-1.58}$	1.02(45)
	50226.035	50226.042	0.61	1.77fix	$2.54^{+0.02}_{-0.02}$	$215.70^{+1.65}_{-1.61}$	1.06(45)
	50226.205	50226.212	0.54	1.77fix	$2.66^{+0.02}_{-0.02}$	$205.10^{+1.65}_{-1.72}$	0.92(45)
	50226.305	50226.309	0.37	1.77fix	$2.56^{+0.02}_{-0.02}$	$205.10^{+2.04}_{-2.01}$	1.05(45)
	50226.438	50226.442	0.35	1.77fix	$2.61^{+0.03}_{-0.03}$	$182.70^{+1.98}_{-2.04}$	0.79(45)
	50226.556	50226.562	0.51	1.77fix	$2.54^{+0.02}_{-0.02}$	$162.60^{+1.58}_{-1.62}$	0.78(45)
	50226.764	50226.771	0.54	1.77fix	$2.69^{+0.03}_{-0.03}$	$132.80^{+1.46}_{-1.47}$	0.66(45)
	50226.906	50226.910	0.35	1.77fix	$2.66^{+0.04}_{-0.04}$	$130.10^{+1.77}_{-1.80}$	0.59(45)
	50227.147	50227.153	0.56	1.77fix	$2.78^{+0.03}_{-0.03}$	$137.10^{+1.50}_{-1.50}$	0.52(45)
	50227.269	50227.271	0.22	1.77fix	$2.67^{+0.05}_{-0.05}$	$113.90^{+2.21}_{-2.14}$	0.65(45)
	50227.336	50227.351	1.36	1.77fix	$2.70^{+0.02}_{-0.02}$	$119.30^{+0.91}_{-0.90}$	0.67(45)
	50227.353	50227.360	0.58	1.77fix	$2.72^{+0.03}_{-0.03}$	$125.90^{+1.42}_{-1.37}$	0.67(45)
	50227.489	50227.495	0.51	1.77fix	$2.64^{+0.03}_{-0.03}$	$141.30^{+1.49}_{-1.54}$	0.74(45)
	50227.603	50227.608	0.48	1.77fix	$2.65^{+0.03}_{-0.03}$	$145.50^{+1.63}_{-1.54}$	0.66(45)
	50227.736	50227.742	0.46	1.77fix	$2.57^{+0.03}_{-0.03}$	$134.10^{+1.59}_{-1.65}$	0.77(45)
	50227.837	50227.843	0.51	1.77fix	$2.63^{+0.03}_{-0.03}$	$139.10^{+1.56}_{-1.52}$	0.74(45)
	50227.974	50227.977	0.30	1.77fix	$2.71^{+0.04}_{-0.04}$	$134.10^{+1.96}_{-2.02}$	0.68(45)
	50228.141	50228.157	1.38	1.77fix	$2.71^{+0.02}_{-0.02}$	$130.40^{+0.85}_{-0.94}$	0.89(45)
	50228.371	50228.377	0.54	1.77fix	$2.73^{+0.03}_{-0.03}$	$136.70^{+1.54}_{-1.49}$	0.55(45)
	50228.553	50228.561	0.66	1.77fix	$2.62^{+0.02}_{-0.02}$	$142.10^{+1.34}_{-1.36}$	0.62(45)
	50228.695	50228.701	0.53	1.77fix	$2.67^{+0.03}_{-0.03}$	$146.70^{+1.54}_{-1.53}$	0.59(45)

Table G.9: Fit results of PKS 2155−304 (3) *continued*

Target	Start MJD	Stop MJD	Int. time (ksec)	$N_{\rm H}$ 10^{20}/cm^2	Photon Index	Flux (2-10keV) 10^{-12} erg/cm^2/s	χ^2 (dof)
PKS 2155	50228.837	50228.843	0.54	1.77fix	$2.64^{+0.03}_{-0.03}$	$140.40^{+1.54}_{-1.45}$	1.20(45)
−304	50228.972	50228.978	0.53	1.77fix	$2.62^{+0.03}_{-0.03}$	$135.50^{+1.61}_{-1.52}$	0.63(45)
	50229.104	50229.111	0.66	1.77fix	$2.54^{+0.02}_{-0.02}$	$194.30^{+1.49}_{-1.49}$	0.84(45)
	50229.238	50229.245	0.61	1.77fix	$2.60^{+0.02}_{-0.02}$	$174.10^{+1.49}_{-1.52}$	0.56(45)
	50229.419	50229.427	0.66	1.77fix	$2.50^{+0.02}_{-0.02}$	$164.40^{+1.37}_{-1.40}$	0.70(45)
	50229.553	50229.560	0.64	1.77fix	$2.51^{+0.02}_{-0.02}$	$163.90^{+1.42}_{-1.39}$	0.66(45)
	50229.677	50229.682	0.45	1.77fix	$2.50^{+0.03}_{-0.03}$	$158.80^{+1.76}_{-1.66}$	0.71(45)
	50229.684	50229.702	1.57	1.77fix	$2.48^{+0.01}_{-0.01}$	$158.60^{+0.88}_{-0.90}$	0.50(45)
	50229.972	50229.979	0.59	1.77fix	$2.47^{+0.02}_{-0.02}$	$142.00^{+1.41}_{-1.38}$	0.67(45)
	50230.106	50230.112	0.53	1.77fix	$2.48^{+0.03}_{-0.02}$	$152.10^{+1.52}_{-1.51}$	0.57(45)
	50230.375	50230.379	0.34	1.77fix	$2.34^{+0.03}_{-0.03}$	$152.20^{+1.83}_{-1.90}$	0.91(45)
	50230.485	50230.493	0.70	1.77fix	$2.33^{+0.02}_{-0.03}$	$159.40^{+1.32}_{-1.31}$	0.50(45)
	50230.625	50230.631	0.50	1.77fix	$2.38^{+0.02}_{-0.02}$	$158.30^{+1.59}_{-1.51}$	0.79(45)
	50230.839	50230.845	0.45	1.77fix	$2.26^{+0.02}_{-0.02}$	$194.50^{+1.74}_{-1.77}$	0.47(45)
	50230.973	50230.979	0.51	1.77fix	$2.38^{+0.03}_{-0.03}$	$140.80^{+1.45}_{-1.50}$	0.52(45)
	50231.162	50231.170	0.66	1.77fix	$2.20^{+0.02}_{-0.02}$	$131.00^{+1.27}_{-1.21}$	0.75(45)
	50231.613	50231.632	1.58	1.77fix	$2.33^{+0.01}_{-0.01}$	$146.60^{+0.82}_{-0.86}$	0.66(45)
	50287.376	50287.393	1.42	1.77fix	$2.88^{+0.05}_{-0.05}$	$43.82^{+0.69}_{-0.68}$	0.61(45)
	50289.663	50289.680	1.49	1.77fix	$3.08^{+0.07}_{-0.07}$	$29.40^{+0.66}_{-0.66}$	0.45(45)
	50291.665	50291.681	1.42	1.77fix	$3.13^{+0.14}_{-0.14}$	$21.01^{+0.91}_{-0.91}$	0.45(45)
	50401.319	50401.332	1.10	1.77fix	$2.99^{+0.06}_{-0.06}$	$43.68^{+0.81}_{-0.81}$	0.50(45)
	50401.338	50401.343	0.40	1.77fix	$2.84^{+0.08}_{-0.08}$	$47.32^{+1.33}_{-1.32}$	0.37(45)
	50401.372	50401.385	1.09	1.77fix	$3.02^{+0.05}_{-0.05}$	$46.47^{+0.82}_{-0.81}$	0.51(45)
	50401.385	50401.398	1.10	1.77fix	$2.91^{+0.05}_{-0.05}$	$44.68^{+0.80}_{-0.80}$	0.58(45)
	50401.398	50401.411	1.12	1.77fix	$2.94^{+0.05}_{-0.05}$	$45.68^{+0.80}_{-0.80}$	0.52(45)
	50401.439	50401.452	1.10	1.77fix	$3.01^{+0.05}_{-0.05}$	$46.18^{+0.81}_{-0.81}$	0.69(45)
	50401.452	50401.464	1.10	1.77fix	$2.88^{+0.05}_{-0.05}$	$46.01^{+0.81}_{-0.80}$	0.48(45)
	50401.464	50401.477	1.10	1.77fix	$3.04^{+0.05}_{-0.05}$	$46.99^{+0.82}_{-0.82}$	0.60(45)
	50401.506	50401.520	1.22	1.77fix	$2.97^{+0.04}_{-0.04}$	$52.92^{+0.78}_{-0.79}$	0.48(45)
	50401.520	50401.534	1.22	1.77fix	$2.88^{+0.04}_{-0.04}$	$53.11^{+0.79}_{-0.79}$	0.71(45)
	50401.537	50401.544	0.62	1.77fix	$2.91^{+0.06}_{-0.06}$	$56.98^{+1.13}_{-1.12}$	0.69(45)
	50401.572	50401.587	1.28	1.77fix	$2.83^{+0.03}_{-0.03}$	$64.66^{+0.78}_{-0.78}$	0.70(45)
	50401.587	50401.602	1.28	1.77fix	$2.83^{+0.04}_{-0.04}$	$61.19^{+0.79}_{-0.79}$	0.76(45)
	50401.606	50401.611	0.40	1.77fix	$2.97^{+0.07}_{-0.07}$	$61.17^{+1.41}_{-1.41}$	0.59(45)
	50402.657	50402.667	0.86	1.77fix	$2.55^{+0.06}_{-0.06}$	$44.94^{+0.89}_{-0.88}$	0.93(45)
	50407.398	50407.413	1.30	1.77fix	$2.91^{+0.04}_{-0.04}$	$54.67^{+0.76}_{-0.77}$	0.56(45)
	50407.741	50407.746	0.50	1.77fix	$2.71^{+0.05}_{-0.05}$	$64.80^{+1.25}_{-1.25}$	0.82(45)
	50408.317	50408.334	1.42	1.77fix	$2.81^{+0.03}_{-0.03}$	$79.85^{+0.80}_{-0.80}$	0.78(45)
	50409.125	50409.135	0.88	1.77fix	$2.89^{+0.04}_{-0.04}$	$65.19^{+0.97}_{-0.98}$	0.55(45)

Table G.10: Fit results of PKS 2155−304 (4) *continued*

Target	Start MJD	Stop MJD	Int. time (ksec)	$N_{\rm H}$ 10^{20}/cm^2	Photon Index	Flux (2-10keV) 10^{-12} erg/cm^2/s	χ^2 (dof)
PKS 2155	50409.601	50409.605	0.34	1.77fix	$2.77^{+0.05}_{-0.05}$	$92.78^{+1.59}_{-1.68}$	0.47(45)
−304	50410.443	50410.448	0.50	1.77fix	$2.88^{+0.05}_{-0.04}$	$87.17^{+1.38}_{-1.38}$	0.64(45)
	50410.452	50410.467	1.23	1.77fix	$2.77^{+0.03}_{-0.03}$	$86.01^{+0.88}_{-0.87}$	0.54(45)
	50410.467	50410.481	1.23	1.77fix	$2.84^{+0.03}_{-0.03}$	$88.73^{+0.88}_{-0.87}$	0.39(45)
	50410.531	50410.548	1.42	1.77fix	$2.80^{+0.02}_{-0.03}$	$89.04^{+0.81}_{-0.80}$	0.66(45)
	50410.601	50410.614	1.12	1.77fix	$2.85^{+0.03}_{-0.03}$	$98.98^{+0.94}_{-0.94}$	0.70(45)
	50410.672	50410.681	0.82	1.77fix	$2.84^{+0.03}_{-0.03}$	$106.80^{+1.10}_{-1.09}$	0.74(45)
	50411.318	50411.333	1.30	1.77fix	$2.78^{+0.03}_{-0.03}$	$79.42^{+0.83}_{-0.84}$	0.81(45)
	50411.333	50411.348	1.31	1.77fix	$2.82^{+0.03}_{-0.04}$	$82.02^{+0.83}_{-0.83}$	0.44(45)
	50411.376	50411.389	1.10	1.77fix	$2.84^{+0.03}_{-0.03}$	$89.27^{+0.94}_{-0.93}$	0.61(45)
	50411.389	50411.402	1.09	1.77fix	$2.77^{+0.03}_{-0.03}$	$88.75^{+0.95}_{-0.94}$	0.58(45)
	50411.402	50411.414	1.10	1.77fix	$2.82^{+0.03}_{-0.03}$	$89.72^{+0.92}_{-0.93}$	0.76(45)
	50411.454	50411.467	1.20	1.77fix	$2.77^{+0.03}_{-0.03}$	$92.74^{+0.91}_{-0.90}$	0.59(45)
	50411.467	50411.481	1.20	1.77fix	$2.85^{+0.03}_{-0.03}$	$95.06^{+0.90}_{-0.90}$	0.87(45)
	50411.532	50411.548	1.42	1.77fix	$2.76^{+0.02}_{-0.02}$	$96.35^{+0.83}_{-0.82}$	0.90(45)
	50772.955	50772.969	1.25	1.77fix	$3.02^{+0.01}_{-0.02}$	$247.00^{+1.43}_{-1.54}$	1.09(45)
	50773.639	50773.650	0.91	1.77fix	$3.01^{+0.02}_{-0.02}$	$241.10^{+1.77}_{-1.67}$	0.56(45)
	50774.721	50774.724	0.30	1.77fix	$2.96^{+0.04}_{-0.04}$	$183.90^{+2.64}_{-2.55}$	0.79(45)
	50822.130	50822.133	0.32	1.77fix	$3.02^{+0.12}_{-0.11}$	$47.28^{+1.81}_{-1.70}$	0.36(45)
	50822.137	50822.141	0.29	1.77fix	$3.06^{+0.12}_{-0.12}$	$48.06^{+1.51}_{-1.88}$	0.66(45)
	50822.534	50822.544	0.88	1.77fix	$2.83^{+0.08}_{-0.08}$	$35.45^{+0.98}_{-0.96}$	0.63(45)
	50823.131	50823.142	0.88	1.77fix	$3.15^{+0.10}_{-0.10}$	$32.22^{+1.03}_{-1.02}$	0.42(45)
	50823.537	50823.546	0.74	1.77fix	$2.90^{+0.10}_{-0.09}$	$33.68^{+1.06}_{-1.04}$	0.56(45)
	50824.308	50824.318	0.86	1.77fix	$3.55^{+0.18}_{-0.17}$	$21.38^{+1.08}_{-1.06}$	0.61(45)
	50824.508	50824.514	0.50	1.77fix	$3.22^{+0.20}_{-0.19}$	$20.48^{+1.27}_{-1.24}$	0.41(45)
	50825.244	50825.252	0.70	1.77fix	$2.87^{+0.06}_{-0.06}$	$52.84^{+1.15}_{-1.14}$	0.83(45)
	50825.608	50825.613	0.40	1.77fix	$3.17^{+0.08}_{-0.08}$	$62.33^{+1.71}_{-1.70}$	0.69(45)
	50826.133	50826.144	0.88	1.77fix	$3.19^{+0.07}_{-0.06}$	$50.46^{+1.12}_{-1.11}$	0.86(45)
	50826.609	50826.613	0.40	1.77fix	$3.26^{+0.10}_{-0.10}$	$54.50^{+1.73}_{-1.70}$	0.62(45)

Table G.11: Fit results of TeV blazars with a cutoff power law function

Target	Start MJD	Stop MJD	Int. time (ksec)	$N_{\rm H}$ 10^{20}/cm^2	E_c (keV)	Photon Index	Flux (2-10keV) 10^{-12} erg/cm^2/s	χ^2 (dof)
Mrk 421	50208.556	50208.569	1.14	1.45fix	$1.86^{+0.17}_{-0.17}$	$2.62^{+0.03}_{-0.03}$	$541.80^{+24.6}_{-23.2}$	0.63(44)
	50549.223	50549.236	1.14	1.45fix	$2.23^{+0.30}_{-0.29}$	$3.42^{+0.06}_{-0.06}$	$428.80^{+18.8}_{-34.6}$	0.76(44)
	50549.236	50549.249	1.15	1.45fix	$2.11^{+0.29}_{-0.29}$	$3.37^{+0.06}_{-0.06}$	$429.23^{+37.4}_{-34.1}$	0.74(44)
	50549.249	50549.262	1.15	1.45fix	$2.25^{+0.29}_{-0.28}$	$3.42^{+0.06}_{-0.06}$	$421.07^{+37.8}_{-43.9}$	0.87(44)
	50549.289	50549.312	1.97	1.45fix	$2.06^{+0.23}_{-0.23}$	$3.33^{+0.05}_{-0.05}$	$392.05^{+25.6}_{-25.1}$	0.65(44)
	50602.261	50602.273	1.02	1.45fix	$2.20^{+0.30}_{-0.30}$	$3.15^{+0.06}_{-0.06}$	$384.60^{+33.6}_{-30.9}$	0.78(44)
Mrk 501	50641.151	50641.166	1.30	1.73fix	$1.29^{+0.16}_{-0.16}$	$2.18^{+0.03}_{-0.03}$	$607.38^{+23.3}_{-22.1}$	1.01(44)
	50641.176	50641.191	1.28	1.73fix	$1.20^{+0.16}_{-0.16}$	$2.16^{+0.03}_{-0.03}$	$602.35^{+23.1}_{-22.1}$	1.10(44)
	50644.152	50644.169	1.42	1.73fix	$0.94^{+0.15}_{-0.15}$	$2.06^{+0.03}_{-0.03}$	$602.70^{+21.5}_{-20.4}$	1.11(44)
	50645.152	50645.171	1.90	1.73fix	$1.29^{+0.13}_{-0.13}$	$2.17^{+0.03}_{-0.03}$	$686.61^{+21.8}_{-20.9}$	1.26(44)
	50645.173	50645.192	1.63	1.73fix	$1.32^{+0.13}_{-0.13}$	$2.18^{+0.02}_{-0.02}$	$671.84^{+21.5}_{-20.8}$	1.02(44)

Appendix H

RXTE Spectra of TeV Blazars

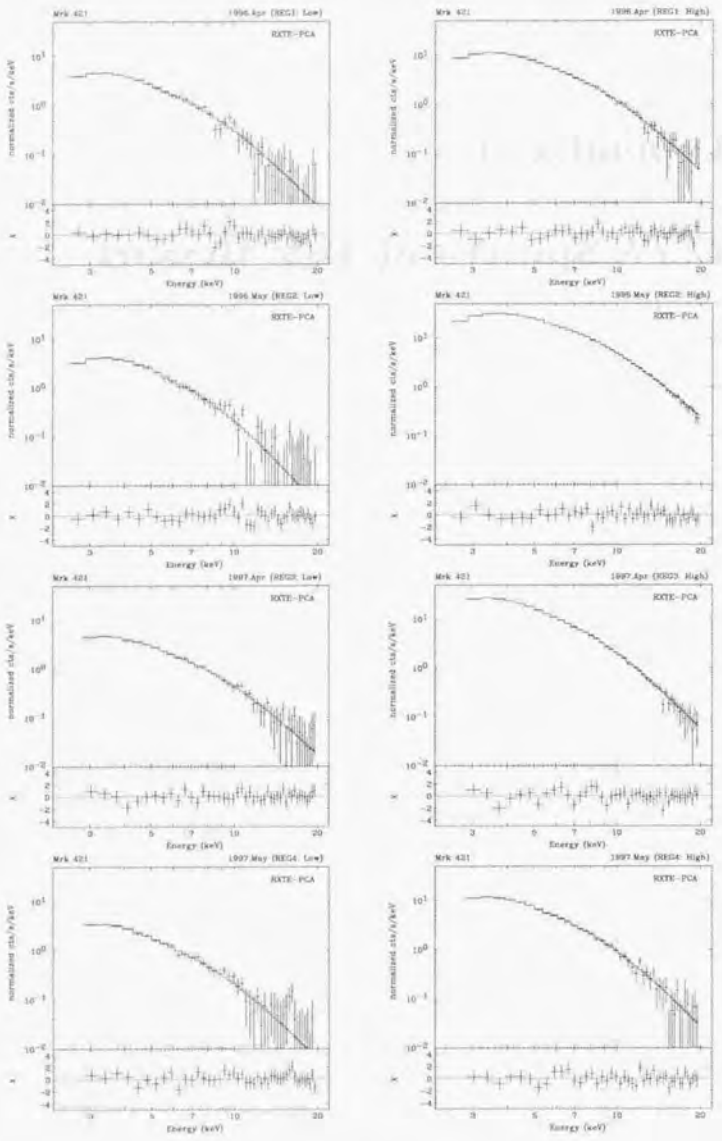

Figure H.1:

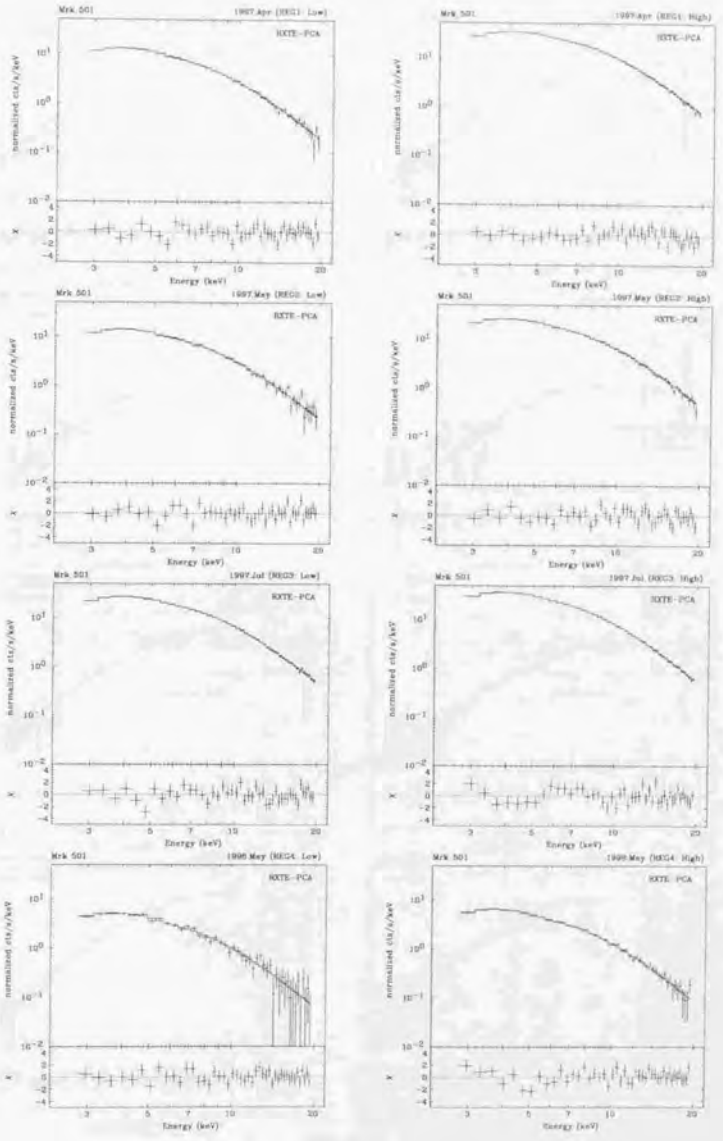

Figure H.2:

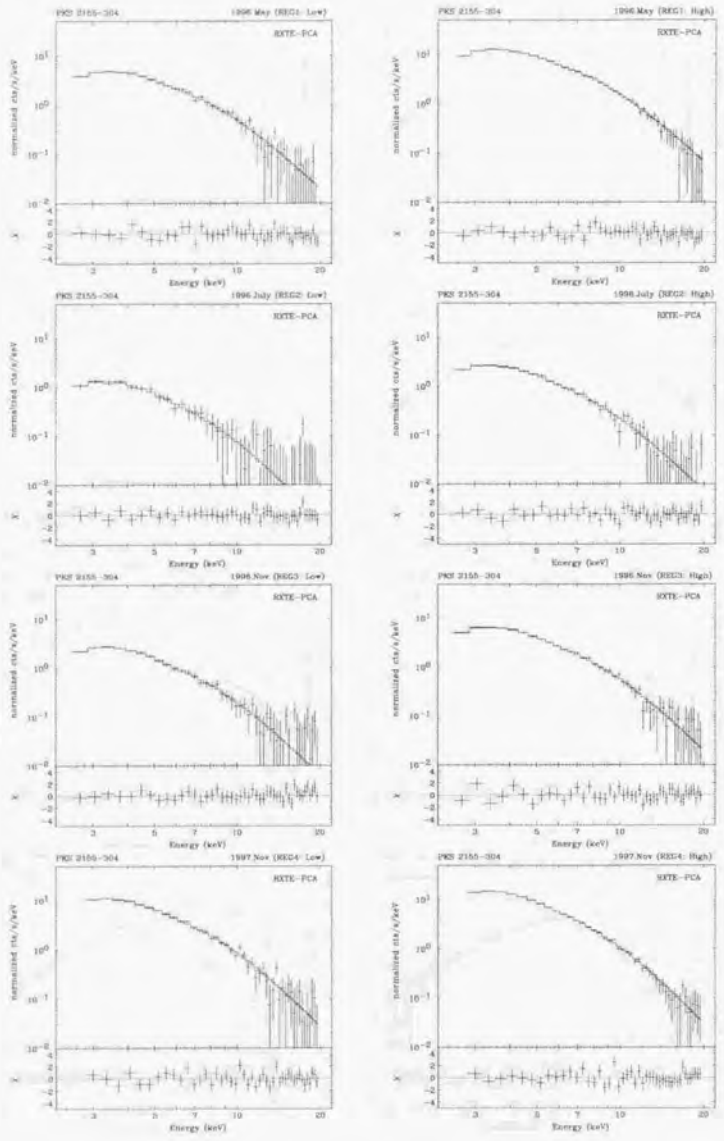

Figure H.3:

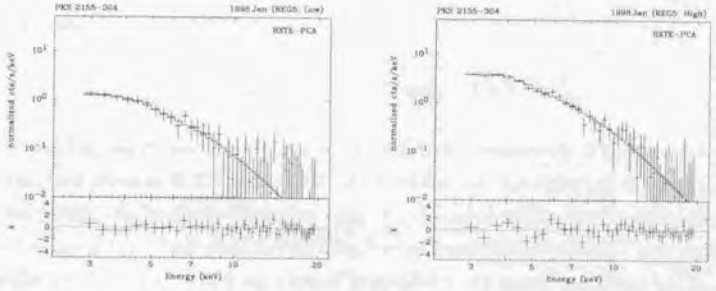

Figure H.4:

Appendix I

Homogeneous SSC model

I.1 Solution for a Spherical Geometry

We start from the equation (11.1)

$$F(\nu) = \frac{1}{4\pi d_L^2} \int d^3\vec{r} \;\; [4\pi j_\nu(\vec{r}) \exp(-\int \alpha_\nu(\vec{r'}) ds')], \tag{I.1}$$

where j_ν and α_ν are emission and absorption coefficients respectively. For the synchrotron case, they are given in (3.37) and (3.40). We consider here the spherical source of radius R. The sphere can be divided into the sum of cylindrical shells, whose center-lines are aligned to the z axis. Each shell is very thin, having equal thickness dx. Those shells can be further cut into rings, which are aligned in parallel to xy-plane. Each ring has an equal width in height (dl) in the z direction. We first consider the emission from the each 'ring', summing up to a single 'cylinder' next, and finally all the contribution from cylindrical shells are added to calculate the emission from the entire sphere. The schematic view of the cross section of the homogeneous sphere is given in Figure I.1.

We start from the relations

$$r(\alpha)\sin\alpha = R\sin\theta, \tag{I.2}$$

$$dl = r(\alpha)\cos\alpha - r(\alpha + d\alpha)\cos(\alpha + d\alpha). \tag{I.3}$$

Both equations yield,

$$dl = \frac{R\sin\theta}{\sin^2\alpha} d\alpha. \tag{I.4}$$

Similarly, dx is simply given by

$$dx = R\sin(\theta + d\theta) - R\sin\theta = R\cos\theta d\theta. \tag{I.5}$$

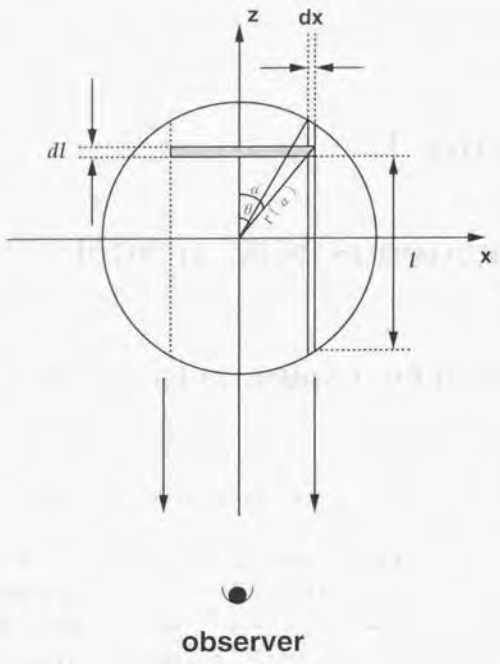

Figure I.1: Schematic view of the cross section of a homogeneous sphere. The shaded part represent a 'ring'.

We obtain the ring volume dV

$$dV = 2\pi R\sin\theta dx dl = 2\pi R^3\sin^2\theta\cos\theta d\theta\frac{d\alpha}{\sin^2\alpha}. \tag{I.6}$$

The photon flux emitted from this ring will be absorbed by a factor $\exp(-\alpha_\nu l)$ before escaping from the sphere. Assuming that only photons emitted in the solid angle $\Omega \sim \Omega + d\Omega$ can be observed, we can calculate the luminosity from the ring in $d\Omega$

$$dS_\nu(\alpha,\theta,d\Omega) = j_\nu d\Omega h\nu dV\exp(-\alpha_\nu l) = G(\theta)\frac{d\alpha}{\sin^2\alpha}\exp[-\alpha_\nu K(\alpha)], \tag{I.7}$$

where

$$G(\theta) \equiv j_\nu d\Omega h\nu 2\pi R^3\sin^2\theta\cos\theta d\theta\exp[-\alpha_\nu R\cos\theta], \tag{I.8}$$

$$K(\alpha) = \frac{\cos\alpha}{\sin\alpha}R\sin\theta. \tag{I.9}$$

Note that, there is a relation

$$\frac{d}{d\alpha}[\exp(-\alpha_\nu K(\alpha))] = \alpha_\nu R\frac{\sin\theta}{\sin^2\alpha}\exp[-\alpha_\nu K(\alpha)]. \tag{I.10}$$

Next we consider the emission from a single cylindrical shell. Integral of $dS_\nu(\alpha,\theta,d\Omega)$ over α yields the solution

$$dS_\nu(\theta,d\Omega) = \int_\theta^{\pi-\theta}\frac{G(\theta)}{\alpha_\nu R\sin\theta}\frac{d}{d\alpha}[\exp(-\alpha_\nu K(\alpha))]d\alpha = CJ(\theta), \tag{I.11}$$

where

$$C = \frac{1}{\alpha_\nu R}j_\nu d\Omega h\nu 2\pi R^3, \tag{I.12}$$

$$J(\theta) = \sin\theta\cos\theta d\theta[1-\exp(-2\alpha_\nu R\cos\theta)]. \tag{I.13}$$

Finally, contributions from each cylindrical shell are summed up, and integrated over the solid angle. We have the total luminosity from the sphere S_ν,

$$S_\nu = 4\pi\int_0^{\pi/2}dS_\nu(\theta) = \frac{8\pi^2 j_\nu h\nu R^2}{\alpha_\nu}\int_0^1 t[1-\exp(-2\alpha_\nu Rt)]dt \tag{I.14}$$

This yields straightforwardly the observed flux at distance $d_{\rm L}$

$$L(\nu) = \frac{S_\nu}{4\pi d_{\rm L}^2} = 4\pi^2R^2\frac{j_\nu}{\alpha_\nu}(1-\frac{2}{\tau_\nu^2}[1-e^{-\tau_\nu}(\tau_\nu+1)]), \tag{I.15}$$

where τ_ν is the optical depth in the blob along the line of sight and expressed as $\tau_\nu = 2\alpha_\nu R$.

I.2 Correction Factor; $C_{\rm corr}$

We calculate the correction factor in equation (11.3), based on the formulae given in Gould (1979). In a homogeneous model, the electron population is assumed to be *homogeneous* over the source. This results in the synchrotron emissivity j_ν is also homogeneous, however, the number density of photons $n(\epsilon_0)$ should vary depending on the position in the source.

Gould (1979) showed that in a homogeneous source, the number density changes with the radial distance from the center ξ ($\xi \equiv r/R$) as

$$n(\xi) \propto \Phi(\xi), \tag{I.16}$$

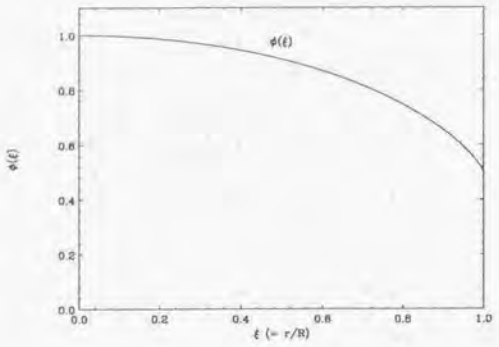

Figure I.2: Function $\Phi(\xi)$, which represents the *density* of synchrotron photon distribution in a homogeneous source ($n(\xi) \propto \Phi(\xi)$). ξ is defined as $\xi \equiv r/R$, and r is the radial distance from the center.

where

$$\Phi(\xi) = \frac{1}{4\xi}(1-\xi^2)\ln|\frac{1+\xi}{1-\xi}| + \frac{1}{2}, \tag{I.17}$$

and illustrated in Figure I.2.

The total number of synchrotron self-Compton (SSC) photons produced per unit time per interval of $d\epsilon$ is proportional to integral I, such that

$$\frac{dN_\epsilon}{dtd\epsilon} \propto I \equiv 4\int_0^1 d\xi\xi^2\Phi(\xi) = 1 \tag{I.18}$$

(see, equation (20) and (22) in Gould 1979).

We approximate $n(\xi)$ at the center of the source, which corresponds to

$$\Phi(\xi) \sim \Phi(0) = 1. \tag{I.19}$$

In this case, the integral $I_{\rm approx}$ is replaced by

$$I_{\rm approx} = 4\int_0^1 d\xi\xi^2\Phi(0) = 4\int_0^1 d\xi\xi^2 = \frac{4}{3}. \tag{I.20}$$

which makes misreading of absolute SSC flux by a factor of 4/3 from the accurate solution. The invert of this factor, i.e., 0.75, should be multiplied to correct the soft photon density for inverse Compton scattering. We thus correct $n(\epsilon_0)$ by a factor $C_{\rm corr}$ ($\equiv 0.75$), yielding

$$n(\epsilon_0) = \frac{4\pi}{hc\epsilon_0}C_{\rm corr}\frac{j_\nu}{\alpha_\nu}(1-e^{-\alpha_\nu R}), \tag{I.21}$$

Appendix J

Numerical Approach to the Kinetic Equation

In general, the kinetic equations of electrons, given in equation (3.55), can not be solved analytically except for very simple cases which do not involve the non-linear processes (e.g., Kardashev 1962). In §4, we derived the approximate solution for time evolution of electrons in the *accelerating region*, while numerical approach was necessary for *emitting region*, because of the high non-linearity of inverse Compton process in the Klein-Nishina regime (equation (3.54)).

We solved the equation (11.7) adopting a fully implicit difference scheme proposed by Chang & Cooper (1970). This method was developed in the study of Fokker-Planck equations which describes an infinite, isotropic, fully ionized plasma. This equation have the form

$$\frac{\partial u}{\partial t} = \frac{1}{A(x)}\frac{\partial}{\partial x}[B(x,t)u + C(x,t)\frac{\partial u}{\partial x}], \tag{J.1}$$

in the domain $0 \leq t \leq t_0$, $0 \leq x \leq \infty$, with A, B, and C are all positive functions. The quantity x usually represents a velocity variable and $u(x,t)$ is the single particle distribution function. The merits of their method are as follows:

(1) particle number is always conserved,

(2) solution is always positive, and never fall in negative values,

(3) significantly reduces the number of mesh points in calculation, with no loss of accuracy.

However, for our purposes, some modifications are required because we are including the additional injection/escape terms, while no diffusion term ($C(x,t)[\partial u/\partial x]$).

We first define the energy mesh points of electrons with equal logarithmic resolution;

$$\gamma_j = \gamma_{\rm min}(\frac{\gamma_{\rm inf}}{\gamma_{\rm min}})^{\frac{j}{j_{\rm max}}} \qquad (0 \leq j \leq j_{\rm max}), \tag{J.2}$$

where $j_{\rm max}$ is the number of the mesh and $\gamma_{\rm inf}$ is the maximum Lorentz factor of electrons to be used in the calculation. Since we are assuming exponential cut-off at $\gamma = \gamma_{\rm max}$ for the injection function $Q(\gamma, t)$ (see, e.g., equation (11.20)), $\gamma_{\rm inf}$ is taken to be much larger than $\gamma_{\rm max}$. As a default, we used $j_{\rm max} = 50$ for $\gamma_{\rm inf} = 10^7 - 10^8$.

The kinetic equation in the emission region is given by equation (11.7)

$$\frac{\partial N(\gamma,t)}{\partial t} = \frac{\partial}{\partial \gamma}[\dot{\gamma} N(\gamma,t)] + Q(\gamma,t) - \frac{N(\gamma,t)}{t_{\rm esc}}, \tag{J.3}$$

where

$$\dot{\gamma} = \dot{\gamma}_{\rm sync} + \dot{\gamma}_{\rm SSC}. \tag{J.4}$$

For the numerical calculation, this can be written as

$$\frac{N_j^{n+1} - N_j^n}{\Delta t} = \frac{\dot{\gamma}_{j+1/2}^n N_{j+1}^{n+1} - \dot{\gamma}_{j-1/2}^n N_j^{n+1}}{\gamma_{j+1/2} - \gamma_{j-1/2}} + Q_j^n - \frac{N_j^{n+1}}{t_{\rm esc}} \tag{J.5}$$

where

$$N_j^n = N(\gamma_j, n\Delta t), \tag{J.6}$$

and quantities with the subscript $j+1/2$ are calculated at half grid points. Δt is the time-step of the calculation. We can rewrite this equation conveniently in the form (Chaiberge & Ghisellini, 1999)

$$V3_j N_{j+1}^{n+1} + V2_j N_j^{n+1} + V1_j N_{j-1}^{n+1} = S_j^n \qquad (1 \leq j \leq j_{\rm max}), \tag{J.7}$$

where

$$V1_j = 0, \tag{J.8}$$

$$V2_j = 1 + \frac{\Delta t}{\gamma_{j+1/2} - \gamma_{j-1/2}} \dot{\gamma}_{j-1/2}^n + \frac{\Delta t}{t_{\rm esc}}. \tag{J.9}$$

$$V3_j = -\frac{\Delta t}{\gamma_{j+1/2} - \gamma_{j-1/2}} \dot{\gamma}_{j+1/2}^n, \tag{J.10}$$

$$S_j^n = N_j^n + Q_j^n \Delta t. \tag{J.11}$$

This can be written in a tridiagonal matrix and can be solved numerically (e.g., Press et al. 1989)

$$\begin{pmatrix} V2_0 & V3_0 & 0 & \cdot & \cdot & 0 \\ V1_1 & V2_1 & V3_1 & 0 & \cdot & \cdot \\ \cdot & \cdot & \cdot & \cdot & \cdot & \cdot \\ \cdot & \cdot & \cdot & \cdot & \cdot & \cdot \\ \cdot & \cdot & \cdot & \cdot & \cdot & \cdot \\ \cdot & \cdot & 0 & V1_{j_{\rm max}-1} & V2_{j_{\rm max}-1} & V3_{j_{\rm max}-1} \\ \cdot & \cdot & 0 & 0 & V1_{j_{\rm max}} & V2_{j_{\rm max}} \end{pmatrix} \begin{pmatrix} N_0^{n+1} \\ N_1^{n+1} \\ \cdot \\ \cdot \\ \cdot \\ N_{j_{\rm max}-1}^{n+1} \\ N_{j_{\rm max}}^{n+1} \end{pmatrix} = \begin{pmatrix} S_0^n \\ S_1^n \\ \cdot \\ \cdot \\ \cdot \\ S_{j_{\rm max}-1}^n \\ S_{j_{\rm max}}^n \end{pmatrix}. \tag{J.12}$$

To obtain a number conserving solution, we have to set the boundary condition in the absence of *sources* (injection term) or *sinks* (escape term) for each trial. This can be written

$$\sum_{j=1}^{j_{\rm max}} (\frac{\dot{\gamma}_{j+1/2}^n N_{j+1}^{n+1} - \dot{\gamma}_{j-1/2}^n N_j^{n+1}}{\gamma_{j+1/2} - \gamma_{j-1/2}}) \equiv 0. \tag{J.13}$$

Summarizing our numerical approach, we first define the electron population $N_j^0 = N(\gamma_j, 0)$ as an initial condition. Next we calculate for this electron population, synchrotron loss $\dot{\gamma}_{\rm sync}$ and inverse Compton loss $\dot{\gamma}_{\rm IC}$ by using equation (3.34) and (3.54). We then obtain $\dot{\gamma}_{j-1/2}$ and $\dot{\gamma}_{j+1/2}$, which can be used to produce $V1_j$, $V2_j$ and $V3_j$ (equation (J.9) and (J.10)). The tridiagonal matrix (equation (J.12)) is solved numerically to obtain the electron population at time Δt; $N_j^1 = N(\gamma_j, \Delta t)$. The iteration of above prescription gives the electron population at an arbitrary time t.

Bibliography

[1] Aharonian, F., et al. 1997, A&A, 327, L5

[2] Aharonian, F., et al. 1999a, A & A, 349, 29

[3] Aharonian, F., et al. 1999b, A & A, 350, 757

[4] Angel, J. R. P., & Stockman, H. S., 1980, Annu. Rev. Astron. Astrophysics, 18, 321

[5] Antonucci, R., & Miller, J. 1985, ApJ, 297, 621

[6] Antonucci, R. 1993, Ann. Rev. Astr. Astrophys, 31, 473

[7] Band, D. L., & Grindlay, J. E. 1985, ApJ, 298, 128

[8] Band, D. L., & Grindlay, J. E. 1986, ApJ, 308, 576

[9] Bednarek, W. 1993, ApJ, 402, L29

[10] Bednarek, W., & Protheroe, R. J. 1997, MNRAS, 292, 646

[11] Bednarek, W., & Protheroe, R. J. 1999, MNRAS, submitted, astro-ph/9902050

[12] Belobodorov, A. M., Stern, B & Svensson, R., 1998, ApJ, 508, L25

[13] Blandford, R. D., & Königl, A. 1979, ApJ, 232, 34

[14] Blandford, R. D., & Rees, M. J., 1978, In "Pittsburgh Conference on BL Lac objects", 328, niv Pittsburgh Press

[15] Blandford, R. D., & Eichler, D., Phys. Rep., 1987, 154, 1

[16] Blandford, R. D., & Levinson, A. 1995, ApJ, 441, 79

[17] Blumenthal, G. R., & Gould, R. J. 1970, Rev. Mod. Phys., 42, 237

[18] Bradbury, S. M. 1997, A&A, 320, L5

[19] Buckley, J. H., et al. 1996, ApJ, 472, L9

[20] Burke, B. E., et al. 1991, IEEE Trans. ED-38, 1096

[21] Catanese, M., et al. 1997, ApJ, 487, L143

[22] Catanese, M., et al. 1998, ApJ, 501, 616

[23] Cawley, M. F., & Weekes, T. C. 1995, Exp. Astron., 6, 7

[24] Celloti, A., & Ghisellini, G. 1998, BL Lac Phenomenam June 22-26, Turku, Finland

[25] Chadwick, P. M., et al. 1999, ApJ, 513, 161

[26] Chang, J. S., & Cooper, G. 1970, Journal of Computational Physics, 6, 1

[27] Chiaberge, M., & Ghisellini, G. 1999, MNRAS, 306, 551

[28] Chiappetti, L., et al. 1999, ApJ, 521, 552, astro-ph/9810263

[29] Comastri, A., et al. 1995, MNRAS, 277, 297

[30] Comastri, A., et al. 1997, ApJ, 480, 534

[31] Dar, A., & Laor.,A. 1997, ApJ, 478, L5

[32] Dermer, C. D., & Schlickeiser, R. 1993, ApJ, 416, 458

[33] Dermer, C. D. 1995, ApJ, 446, L63

[34] Dermer, C. D. 1998, ApJ, 501, L157

[35] Dotani, T., et al. 1997, ApJL, 485, L87

[36] Dondi, L.,& Ghisellini, G. 1995, MNRAS, 273, 583

[37] Edelson, R. A. 1987, ApJ, 313, 651

[38] Edelson, R., & Krolik, J. 1988, ApJ, 333, 646

[39] Edelson, R., et al. 1995, ApJ, 438, 120

[40] Elvis, M., et al. 1989, AJ, 97(3), 777

[41] Elvis, M., et al. 1992, ApJS, 80, 257

[42] Fanaroff, B. & Riley, J. 1974 MNRAS, 167, 31

[43] Fabian, A. C., 1979, Proc. R. Soc. London, 366, 449

[44] Fichtel, C. E., et al. 1994, ApJS, 94, 551

[45] Fossati, G., et al. 1998, MNRAS, 299, 433

[46] Funk, B., et al. 1998, Astroparticle Physics, 9, 97

[47] Gaidos, J. A., et al. 1996, Nature, 383, 319

[48] Gaisser, T. K., Cosmic Rays and Prticle Physics, Cambridge University Press, 1990

[49] Gehrels, N. 1997, IL NUOVO CIMENTO, 112 B, 11

[50] Georganopoulos, M., & Marscher, A. P. 1999, ApJ, 506, L11

[51] George, I. M., Warrick, R. S., & Bromage, G. E. 1988, MNRAS, 232, 793

[52] Ghisellini, G., & Maraschi, L. 1989, ApJ, 340, 181

[53] Ghisellini, G., & Maraschi, L. 1996, Blazar Continuum Variability, ASP conferences Series, Vol. 110

[54] Ghisellini, G., & Madau, P., 1996, MNRAS, 280, 67

[55] Ghisellini, G., et al. 1997, A & A, 327, 61

[56] Ghisellini, G., et al. 1998, MNRAS, 301, 451

[57] Ghisellini, G., 1999, Astronomische Nachrichten, proceedings of fourth *ASCA* symposium

[58] Giommi, P., et al. 1990, ApJ, 356, 432

[59] Giommi, P., et al. 1998, A&A, 333, L5

[60] Giommi, P., et al. 1999, MNRAS, in press

[61] Giovannini, G., et al. 1998, in the proceedings of "BL Lac phenomenon" Turku, Finland

[62] Gould, R. J., et al. 1979, A&A, 76, 306

[63] Gregory, P. C.,& Condon, J. J., 1991, ApJS, 75, 1011

[64] Hartman, R. C., et al. 1996, ApJ, 461, 698

[65] Hartman, R. C., et al. 1999, ApJS, 123, 79

[66] Hayashida, K., et al. 1998, ApJ, 500, 642

[67] Hewitt, A & Burbidge, G. 1993, ApJS, 87, 451

[68] Hughes, P. A., Aller, H. D.,& Aller, M. F., 1992, ApJ, 396, 469

[69] Inoue, S., & Takahara, F. 1996, ApJ, 463, 555

[70] Jahoda, K., et al. 1996, SPIE, 2808, 59

[71] Jahoda, K., et al. 1999,"On Orbit Perormance of the Rossi X-ray Timing Explore Proportional Counter Array", http://lheawww.gsfc.nasa.gov/docs/xray/xte/pca

[72] Jones, F. C. 1968, Phys. Rev., 167, 1159

[73] Jones, T. W., O'Dell, S. L., & Stein, W. A. 1974, ApJ, 188, 353

[74] Kardashev, N. S. 1962, Soviet Astronomy-AJ, 6, 317

[75] Kataoka, J., et al. 1999a, ApJ, 514, 138

[76] Kataoka, J., et al. 1999b, Astroparticle Physics, 11, 149

[77] Kataoka, J., et al. 2000, ApJ, 528, 243

[78] Kawaguchi, T., et al. 1998, ApJ, 504, 671

[79] Kerrick, A. D., et al. 1995, ApJ, 438, L59

[80] Kirk, J. G., Rieger, F. M. & Mastichiadis, A. 1998, A&A, 333, 452

[81] Kohmura, H., et al. 1994, PASJ, 46, 131

[82] Königl, A. 1981, ApJ, 243, 700

[83] Kubo, H., Ph. D. Thesis, University of Tokyo

[84] Kubo, H., et al. 1998, ApJ, 504, 693

[85] Lamer, G., & Wagner, S. J. 1998, A & A, 331, L13

[86] Lin, D. J., et al. 1992, ApJ, 442, 96

[87] Macomb, D. J., et al. 1995, ApJ, 449, L99

[88] Macomb, D. J., et al. 1996, ApJ, 459, L111 (Erratum)

[89] Madejski, G. M., et al. 1999, ApJ, 521, 145

[90] Mannheim, K., & Biermann, P. L., 1992, A & A, 253, L21

[91] Mannheim, K., A & A, 1993, 269, 67

[92] Makino, F. et al. 1987, ApJ, 313, 662

[93] Makino, F., Fink, H. H., & Clavel, J. 1992, in Frontiers of X-ray Astronomy, Universal Academy Press, Y.Tanaka & K.Koyam

[94] Makino, F., et al. 1996, in Röntgenstrahlung from the Universe, eds. H. U. Zimmermann, J. Trümper and H. Yorke, MPE Report 263, p.413.

[95] Makino, F., et al. 1998, in the proceedings of "BL Lac phenomenon" Turku, Finland

[96] Makishima, K, et al. 1996, PASJ, 48, 171

[97] Maraschi, L, et al. 1994, ApJ, 435, L91

[98] Maraschi, L, et al. 1999a, Proceedings of the 32nd COSPAR Meeting, Nagoya, astro-ph/9902059

[99] Maraschi, L, et al. 1999b, ApJL, in press

[100] Marscher, A. P. 1980, ApJ, 235, 386

[101] Marscher, A. P., & Travis, J. P. 1996, A&AS, 120, 537

[102] Marscher, A. P., 1999, Astroparticle Physics, 11, 19

[103] Mastichiadis, A., & Kirk, J. G. 1997, A&A, 320, 19

[104] Mattox, J. R., et al. 1993, ApJ, 410, 609

[105] Mattox, J. R., et al. 1997, ApJ, 476, 692

[106] McEnergy, J. E., et al. 1997, in proceedings of 25 ICRC (Durban), astro-ph/9706125

[107] Miyoshi, M., et al. 1995, Nature, 373, 127

[108] Mukherjee, R., et al. 1997, ApJ, 490, 116

[109] Morrison, R, & McCammon, D. 1983, ApJ, 270, 119

[110] Ohashi, T., et al. 1996, PASJ, 48, 157

[111] Osterbrock, D. E. 1981, ApJ, 249, 462

[112] Ormes, in Current Perspectives in High Energy Astrophysics, NASA 1391, 1996

[113] Padovani, P., & Giommi, P. 1995, ApJ, 444, 567

[114] Paltani, S., et al. 1997, 327, 539

[115] Patanik, A. R., 1992, 254, 655

[116] Perlman, E. S., et al. 1996, ApJS, 104, 251

[117] Petry, D., et al. 1996, A&A, 311, L13

[118] Petry, D., 1997, PhD thesis, Max-Planck-Institute for Physics, Munich, report MPI-PhE/97-27

[119] Pian, E., et al. 1998, ApJ, 492, L17

[120] Piner, B, G., et al. 1999, ApJ, in press

[121] Press, W, H., et al. 1992, Numerical Recipes in C, Cambridge University Press

[122] Protheroe, R. J., in Towards the Millennium in Astrophysics: Problems and Prospects, Erice 1996, astro-ph/961212

[123] Punch, M., et al. 1992, Nature, 358, 477

[124] Quinn, J., et al. 1996, ApJ, 456, L83

[125] Quinn, J., et al. 1999, ApJ, 518, 693

[126] Rees, M. J., 1984, Annu. Rev. Astron. Astrophys., 22, 471

[127] Rephaeli, Y., 1979, ApJ, 227, 364

[128] Rodriguez-pascual, P. M., 1997, ApJS, 110, 9

[129] Rybicki,G. B., & Lightman, A. P. 1979, Radiative Processes in Astrophysics (New York: Wiley)

[130] Samuelson, F. W., et al. 1998, ApJ, 501, L17

[131] Sembay, S., et al. 1993, ApJ, 404, 112

[132] Sikora, M., Begelman, M. C., & Rees, M. J. 1994, ApJ, 421, 153

[133] Sikora, M. 1994, ApJS, 90, 923

[134] Sikora, M. & Madejski, G. M., Moderski, R., & Poutanen, J, 1997, ApJ, 484, 108

[135] Simonetti, J, H., Cordes, J, M., & Heeschen, D. S., 1985, ApJ, 296, 46

[136] Smith, A. G., et al. 1993, AJ, 105, 437

[137] Sreekumar, P., & Vestrand, W. T., 1997, IAU Circular, 6774

[138] Stark, A. A., et al. 1992, ApJS, 79, 77

[139] Stecker, F. W., de Jager, O. C., & Salamon, M. H. 1992, ApJ, 390, L49

[140] Stecker, F. W., de Jager, O. C. 1998, A & A, 334, L85

[141] Stein, W. A., O'Dell, S. L., & Strittmatter, R., 1976, Annu. Rev. Astron. Astrophysics, 14, 173

[142] Tagliaferri, G., et al. 1991, ApJ, 380, 78

[143] Takahashi, T., et al. 1994, IAU Circular, 5993

[144] Takahashi, T., et al. 1995, IAU Circular, 6167

[145] Takahashi, T., Tashiro, M., Madejski, M., Kubo, H., Kamae, T., Kataoka, J., et al. 1996, ApJ, 470, L89

[146] Takahashi, T., et al. 1998, IAU Circular, 6888

[147] Takahashi, T., et al. 1999, Astroparticle Physics, 11, 177

[148] Tanaka, Y., Inoue, H., and Holt, S. S. 1994, PASJ, 46, L73

[149] Tanaka, Y., et al. 1995, Nature, 375, 659

[150] Tanihata, C., Takahashi, T., Kataoka, J. et al. 1999, submitted to ApJ

[151] Tashiro, M., et al. 1992, Ph. D. Thesis, University of Tokyo

[152] Tashiro, M., et al. 1995, PASJ, 47, 131

[153] Tavecchio, F., Maraschi, L., & Ghisellini, G. 1998, ApJ, 509, 608

[154] Thompson, D. J., et al. 1993, ApJS, 86, 629

[155] Toor, A., & Seward, F. D. 1974, AJ, 79, 995

[156] Treves, A., et al. 1989, ApJ, 341, 733

[157] Ulrich, M. -H., Maraschi, L., & Urry, C. M. 1997, ARAA, 35, 445

[158] Urry, C. M., 1984, PhD Thsis, Johns Hopkins University

[159] Urry, C. M., & Padovani, P., 1995, PASP, 715, 803

[160] Urry, C. M., et al. 1997, ApJ, 486, 799

[161] Urry, C. M. 1998, Proc. of BL Lac Phenomenon, Takalo

[162] Vermeulen, R. C., & Cohen, M. H. 1994, ApJ, 430, 467

[163] Veron-Cetti, M.P. & Veron, P. 1993, ESO Sci. Rep. 13, 1

[164] Vestrand, W. T., Stacy, J. G., & Sreekumar, P. 1995, ApJ, 454, L93

[165] Wagner, S. J., et al. 1993, A & A, 271, 344

[166] von Montigny, C., et al. 1995, ApJ, 440, 525

[167] Yamashita, A. 1997, IEEE Trans Nucl. Sci., 44, 847

[168] Yamashita, A. 1999, Nuclear Instruments And Methods In Physics Research Sect. A Vol. 436 (1), 68

[169] Zhang, Y. H., et al. 1999, ApJ, 527, 719

Acknowledgment

I am deeply grateful to Prof. Tadayuki Takahashi for his guidance and support through the five years of my graduate course. His comments were always fresh, and I was very often 'accelerated' by his ideas. I would like to thank Prof. Greg Madejski for his constructive comments and discussion on this thesis and continuous encouragement. I thank Prof. Fumiyoshi Makino and Prof. Hajime Inoue, who were always worrying about my thesis and gave me a lot of new ideas. I thank Dr. Hidetoshi Kubo, for his guidance through my graduate course. I also thank Ms. Chiharu Tanihata for her cheerful encouragement, and Dr. Makoto Tashiro for the collaboration of *ASCA* analysis.

I would like to thank Dr. P. Edwards and Mr. P. Hilton in ISAS for careful reading and suggestions to improve this thesis. For the analysis of *RXTE* data, I must thank Dr. A. Smale and Ms. T. Jaffe in GSFC for their technical guidance.

I thank Prof. Fumio Takahara and Dr. Susumu Inoue for suggesting many theoretical interpretations and discussion of the observational results. I must thank Prof. Masaaki Kusunose and Prof. John Kirk for giving me careful advises and comments on the time dependent SSC code.

Many observations presented in this thesis are based on the collaborations with other wavelengths, in particular, EGRET and *Whipple* . I would like to thank Prof. J. Mattox for the collaboration of the EGRET analysis of Mrk 501 data. I learned many about blazars from the very basics, when he stayed in ISAS during the summer of 1997. I also thank Dr. R. Hartman and Dr. P. Sreekumar who are always very kind to me. The Mrk 501 paper could not be published without their helps.

I would like to thank many people in the *Whipple* collaboration. I really thank Dr. J. Quinn, who always encourages me and provides me with nice insights. All the TeV data of Mrk 501 used in this thesis come from his excellent papers. Moreover, he took me to the top of the Mount Hopskins in Arizona, where *Whipple* observatory locates! I thank Prof. T. Weekes and Dr. C. Masterson for their support during my stay and very kindly taught me about the very high-energy astrophysics. I also appreciate Dr. M. Catanese for his collaboration of the analysis of Mrk 421 data.

I also thank Prof. M. Urry for inviting me to the STScI. She noticed me an importance of the light travel time effects. I would like to thank Prof. S. Wagner for his helpful discussion on the emission mechanism of blazars. He introduced me many analysis techniques including the structure function. Dr. S. Paltani is also thanked for noticing me the properties of rapid variability in blazars.

Finally to my family – I thank my parents, an elder brother and three cats (!) for supporting my school life.